Elucidation of Surface Plasmon Resonance, Size and Structure of $Cu@Cu_xO$ and $Ag@Ag_xO_y$ Nanoparticles Synthesized by Pulsed Laser Ablation in Liquid, Dynamics of the Process and Applications

DOCTOR OF PHILOSOPHY

by

PRAHLAD KUMAR BARUAH

DEPARTMENT OF PHYSICS

INDIAN INSTITUTE OF TECHNOLOGY GUWAHATI

GUWAHATI-781039, INDIA

March 2019

Elucidation of Surface Plasmon Resonance, Size and Structure of $Cu@Cu_xO$ and $Ag@Ag_xO_y$ Nanoparticles Synthesized by Pulsed Laser Ablation in Liquid, Dynamics of the Process and Applications

A Thesis submitted in partial fulfillment of the requirements for the award of the degree of

DOCTOR OF PHILOSOPHY

by

PRAHLAD KUMAR BARUAH

DEPARTMENT OF PHYSICS

INDIAN INSTITUTE OF TECHNOLOGY GUWAHATI

GUWAHATI-781039, INDIA

March 2019

Dedicated to my Parents

Prahlad Kumar Baruah
Registration No. 126121027
Department of Physics
Indian Institute of Technology Guwahati
Guwahati-781039, Assam, India

Statement

I hereby declare that the matter embodied in this thesis is the result of investigations carried out by me at the Department of Physics, Indian Institute of Technology Guwahati, Guwahati, India, under the supervision of **Prof. Alika Khare and Dr. Ashwini Kumar Sharma**. This thesis has not been submitted to any other university, institute or elsewhere for the award of any degree, diploma or associate-ship.

Date: ……. **Prahlad Kumar Baruah**

भारतीय प्रौद्योगिकी संस्थान गुवाहाटी
Indian Institute of Technology Guwahati
Department of Physics
Guwahati-781039, Assam State, INDIA
Phone: +91 361 258250, 2690321 to 328 (extn. 2750),
Fax: +91 361 2582749

Date:

Certificate

This is to certify that work contained in the thesis entitled **'Elucidation of Surface Plasmon Resonance, Size and Structure of Cu@Cu_xO and Ag@Ag_xO_y Nanoparticles Synthesized by Pulsed Laser Ablation in Liquid, Dynamics of the Process and Applications'** by **Mr Prahlad Kumar Baruah** (Roll no 126121027), a student of Department of Physics, Indian Institute of Technology Guwahati, for the award of degree of Doctor of Philosophy, has been carried out under our supervision and the same has not been submitted elsewhere for the award of any other degree.

Alika Khare
Email: alika@iitg.ac.in

Ashwini Kumar Sharma
aksharma@iitg.ac.in

Acknowledgements

First and foremost, I would like to express my deepest gratitude to my research supervisors, Prof. Alika Khare and Dr. Ashwini Kumar Sharma for their inspiration, guidance and persistent support which helped in shaping the present thesis. I acknowledge the freedom to try anything new which was provided during the course of my Ph. D. work.

I would like to extend my sincere appreciation to my doctoral committee members; Prof. Bosanta Ranjan Boruah, Prof. Girish S. Setlur and Prof. Latha Rangan for the invaluable suggestions and critical assessments which helped in improving the present research work. I am indebted to Prof. Latha Rangan and her students, Ishani and Anuma for providing the karanjin crystals and the facilities to conduct the antibacterial studies.

My sincere gratitude also goes to the present and former Heads of the Department of Physics, Prof. Subhradip Ghosh, Prof. Poulose Poulose and Prof. Saurabh Basu and all the other faculty members of the Department for their support at various stages of my research work. I acknowledge the Central Instruments Facility (CIF) and Mechanical Engineering Department, IIT Guwahati for the instrumental facilities provided. I would like to thank Dr. Sidananda Sarma, Mr. Basab, Mr. Hemanta, Himaku, Mrs. Leoni and all other staff members at the Department of Physics, IIT Guwahati. I must also thank Mr. Madhurjya Borah, Mr. Chandan Borgohain, Mr. Sujit Deb and all other staff members at the CIF, IIT Guwahati. I would like to thank MHRD, India and IIT Guwahati for providing financial assistance during my Ph.D. tenure.

I would like to thank my lab seniors, Dr. Abu, Dr. Satchi, Dr. Indrajeet, Dr. Shanta, Dr. Partha and Dr. Gyan for their help and support. I would also like to thank Dr. Arpita Nath for the useful discussions which helped me immensely. My labmates Rahul, Eshita, Gobinda, Sasmita, Sumit, and Nagendra deserve special appreciation for their love and support throughout my stay here at IIT Guwahati. I am thankful to Dr. Gyan for his help in the Raman and PL measurements and to Eshita and Sundarlal for helping me in the Raman and profilometer measurements, respectively. I am indebted to my friends and juniors, Rahul, Koushik, Ram, Nitin, Deepanjali, Shibananda, Dhriti, Pratap, Apurba, Joy, Indu, Ranjan and others for their support and for standing by me during the difficult stages of my Ph.D. life.

My special gratitude goes to my family for their role in my life. I would like to thank my mother, Mrs. Rita Baruah and sister, Nandini for their unconditional support and blessings. I thank my father, Late Arun Kumar Baruah whose blessings and love I have always felt at every moment of my life. Special thanks to my uncle, Prof. Prabin Kumar Bora, my aunt, Dr. Sabita Baruah Bora and my cousin, Jonak for everything that they have done for me. This acknowledgement would remain incomplete without mentioning the support of my in-laws, my cousins and others including Dr. A. Rajesh, and my entire Gakkai family. Last, but not the least, I would like to express special appreciation to my lovely wife, Niharika for being my biggest strength and for supporting me whole-heartedly at every step of my life.

Abstract

In the present thesis, nanoparticles of copper and silver have been synthesized by pulsed laser ablation of the respective targets in distilled water. The surface plasmon resonance, size and the structure of the nanoparticles have been simultaneously controlled by the laser ablation duration, incident laser energy and the background liquid viz., distilled water and two organic solvents, methanol and 2-propanol. In addition, the intriguing dynamics of the process of pulsed laser ablation in liquid is studied via shadowgraphy and beam deflection techniques. The dynamics of the cavitation bubbles and also the shock waves generated during the process exhibited the extreme condition of pressure ~ 10^{10} Pa and temperature ~ 3000 K. An attempt to correlate the dynamical behavior of the shock waves to understand the nucleation of nanoparticles is also undertaken in the reported work. The synthesized nanoparticles of copper and silver have been successfully tested to be an excellent surface enhanced Raman scattering substrate for a bioactive furanoflavonoid, karanjin, having medicinal properties. The surface enhanced Raman scattering intensity is found to be dependent on the particle size, concentration, aggregation and also on the degree of oxidation of the nanoparticles. The antibacterial properties of the nanoparticles have been used to act as a protective coating for three locally available natural silks viz., Pat, Eri and Muga which have commercial importance. The bactericidal efficacy of the nanoparticles has also been used in the treatment of filter paper for the annihilation of bacteria in contaminated water.

Contents

List of Figures

List of Tables

Abbreviations

ATCC: American Type Culture Collection

CCD: Charge Coupled Device

CFU: Colony Forming Unit

DMSO: Dimethyl Sulphoxide

DNA: Deoxyribonucleic Acid

DSO: Digital Storage Oscilloscope

DW: Distilled Water

EDX: Energy Dispersive X-ray

FESEM: Field Emission Scanning Electron Microscope

HRTEM: High Resolution Transmission Electron Microscope

Fig.: Figure

IFFT: Inverse Fast Fourier Transform

IB: Inter band

LIBS: Laser Induced Breakdown Spectroscopy

LSPR: Localized Surface Plasmon Resonance

MEF: Metal Enhanced Fluorescence

MTCC: Microbial Type Culture Collection and Gene Bank

NP: Nanoparticle

NPs: Nanoparticles

Nd:YAG: Neodymium-doped Yttrium Aluminium Garnet

PL: Photoluminescence

PLAL: Pulsed Laser Ablation in Liquid

PLD: Pulsed Laser Deposition

RD: Radiative Decay

R-P: Rayleigh-Plesset

RR: Radiative Recombination

SAED: Selected Area Electron Diffraction

SERS: Surface Enhanced Raman Scattering

SPR: Surface Plasmon Resonance

SW: Shock Wave

TEM: Transmission Electron Microscope

TTL: Transistor-Transistor Logic

UV-Vis: Ultra Violet-Visible

viz.: Namely

WHO: World Health Organization

w. r. t.: with respect to

XRD: X-Ray Diffraction

Symbols

~	Approximately
Ag	Silver
Au	Gold
Å	Angstrom
α	Internal energy devoted to thermal energy
α'	Polarizability
α_{met}	Polarizability of metal
α_{mol}	Polarizability of molecule
c	Speed of light
cm	Centimetre
Cu	Copper
d	Lattice spacing
E_a	Activation energy
E_0	Incident electric field
E_1	Enhanced local field
ε'	Dielectric function
ε_1	Real part of dielectric function
ε_2	Imaginary part of dielectric function
ε_b	Interband contribution to dielectric function
ε_D	Drude contribution to dielectric function
°C	Degree Celsius
$\Delta\mu$	Chemical potential difference
f	Focal length
GPa	Giga Pascal
GW	Gigawatt
ΔG_m	Gibbs free energy difference per mole
g	Gram
γ	Electron scattering rate; damping constant
γ_s	Surface energy
γ_0	Bulk damping constant
γ'	Ratio of the heat capacity
h	Plank's constant
I_o	Incident intensity
J	Joule
k_B	Boltzmann constant
K	Kelvin
kV	Kilo volt
K	Total extinction coefficient
λ	Wavelength of light
MHz	Mega hertz
m	Mass
mg	Milligram
mK	Millikelvin
mL	Millilitre
mm	Millimetre
mol	Mole
μ	Dipole moment
µL	Microlitre
µm	Micrometer
µs	Microsecond
Ni	Nickel

n	Number of particles
nm	Nanometre
ns	Nanosecond
Ω	Ohm
P, p	Pressure
P_0	Initial pressure
P_h	Hydrostatic pressure
Pa	Pascal
P_B	Bubble pressure
P_l	Liquid pressure
P_S	Shock wave pressure
p_{sat}	Saturated vapor pressure
R	Bubble radius
R_f	Retardation factor
R_T	Raman intensity of karanjin treated with nanoparticles
R_U	Raman intensity of untreated karanjin
r	Particle radius
r^*	Size of critical nucleus
ρ	Density of water
Si	Silicon
σ	Standard deviation
σ'	Surface tension
T	Temperature
T_B	Temperature of the bubble
T_0	Initial temperature
t	Time
t_l	Laser pulse duration
τ	Nucleation time
η	Viscosity
V	Volume
V_m	Molar volume
ΔV	Molar volume difference
v	Electron velocity at Fermi energy
v_s	Shock wave velocity
v_p	Particle velocity
W	Watt
wt%	Weight percentage
ω	Angular frequency of light
ω_0	Frequency of incident light
ω_1	Frequency of molecule
ω_p	Plasma frequency
Z	Reduced shock impedance
ζ	Lattice spacing in growth direction

Chapter 1

Introduction

Laser ablation of a solid in gaseous medium or in liquid is a technique that has been successfully implemented in many applications like laser cutting, laser micromachining, thin film deposition, nanoparticle (NP) synthesis, etc. [1-5]. The mechanism of ablation of a solid target upon laser irradiation is very complex. The focusing of a high power laser onto a solid target in the presence of gaseous medium or in liquid results in the formation of plasma [6-9]. The huge pressure difference between the laser-produced plasma plume and the surrounding medium results in the expansion of the plasma plume. For nanosecond laser ablation, during the laser pulse, the plasma expansion is isothermal but the expansion becomes adiabatic after the termination of the laser pulse [10, 11]. As the plasma expands, it undergoes collisions among the ambient atoms and molecules which results in its cooling. Under suitable optimum conditions of temperature and pressure, the plasma species may nucleate to form nanostructures or nanoparticles (NPs) either on a substrate placed a few centimetres away from the target in vacuum/gas or in a liquid if the target is immersed in it [3, 7, 9]. Laser ablation of a target in gaseous medium has been the basis of pulsed laser deposition (PLD) which has proved to be an excellent technique for the fabrication of thin films of any material and of any composition [3, 12]. In the last two decades, pulsed laser ablation of a target immersed in liquid has paved a new method for the fabrication of NPs with desired properties [4, 7, 13]. In 1987, the pioneering work on pulsed laser ablation of a solid in liquid was reported by Patil and co-workers [14]. They synthesized metastable phase of iron oxides by ablating an iron target in water. The major difference between laser induced breakdown of the target in vacuum or gaseous medium and that of in liquid is the strong confinement of the plasma by the surrounding liquid which

generates a localized region of high pressure of the order of a few GPa or more [7]. Fabbro *et al.* reported that during the laser heating, the amplitude of pressure generated at the interface of the solid and the liquid is about ten times greater than that obtained under vacuum or in the presence of gaseous ambient [15]. Since the beginning of the 21st century, there has been a boom in the synthesis of NPs by the method of pulsed laser ablation in liquid, commonly known as PLAL [4, 9, 13, 16]. The flexibility and simplicity associated with PLAL has led to its ever-growing importance.

1.1 Mechanism of laser ablation of a solid immersed in liquid

Laser irradiation onto a target immersed in liquid leads to the increase in the temperature of the target surface and on achieving the ablation threshold of the material being irradiated, a very well-known phase transition occurs from solid-liquid, liquid-vapor and vapor-plasma [7-9]. However, it should be noted that the actual processes taking place in laser produced plasma are rather complex and in addition to thermal vaporization, phase explosion may also occur [17, 18]. The processes involved in the laser ablation of a solid in liquid are listed in Fig.1.1 and the entire mechanism is pictorially represented in Fig. 1.2.

As the focused laser beam falls on the target, the interaction leads to the generation of the seed electrons via multiphoton ionization and focal heating resulting in the formation of plasma of the target material in the focal region and also of the surrounding liquid in its neighbourhood [19]. The generated free electrons absorb the incoming photons from the laser beam via inverse Bremsstrahlung process. This leads to the gain in kinetic energy of the electrons and they simultaneously collide with the other species present in the neighbourhood of the focal volume. During this process, generation of more electrons occurs as a result of impact ionization. This results in a cascade ionization, leading to the attainment of extremely high pressure, density and temperature conditions.

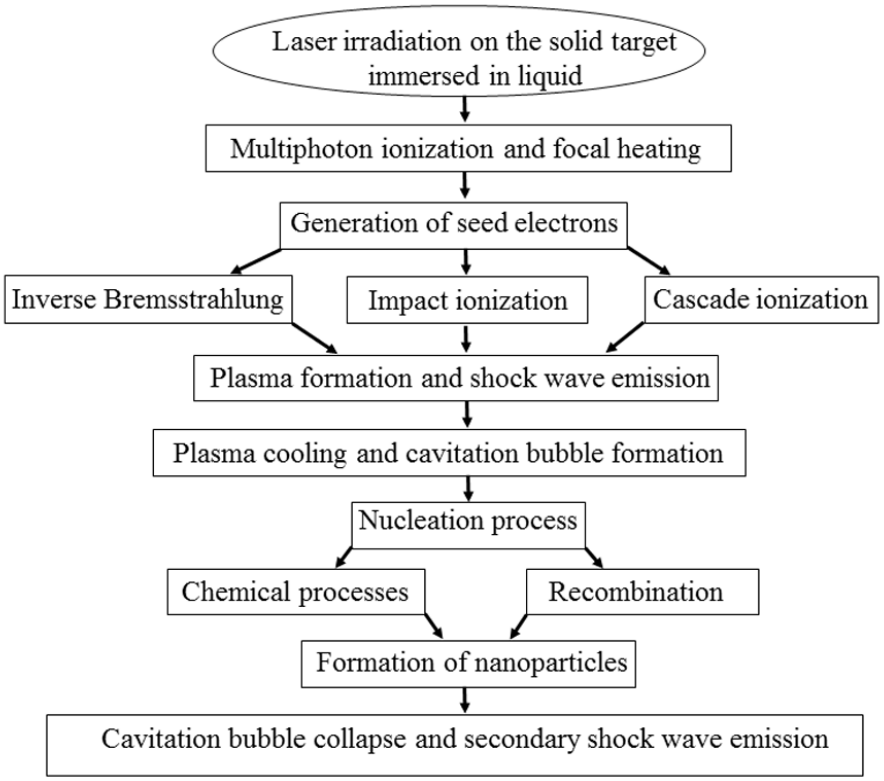

Figure 1.1 *Processes involved in the laser ablation of a solid in liquid.*

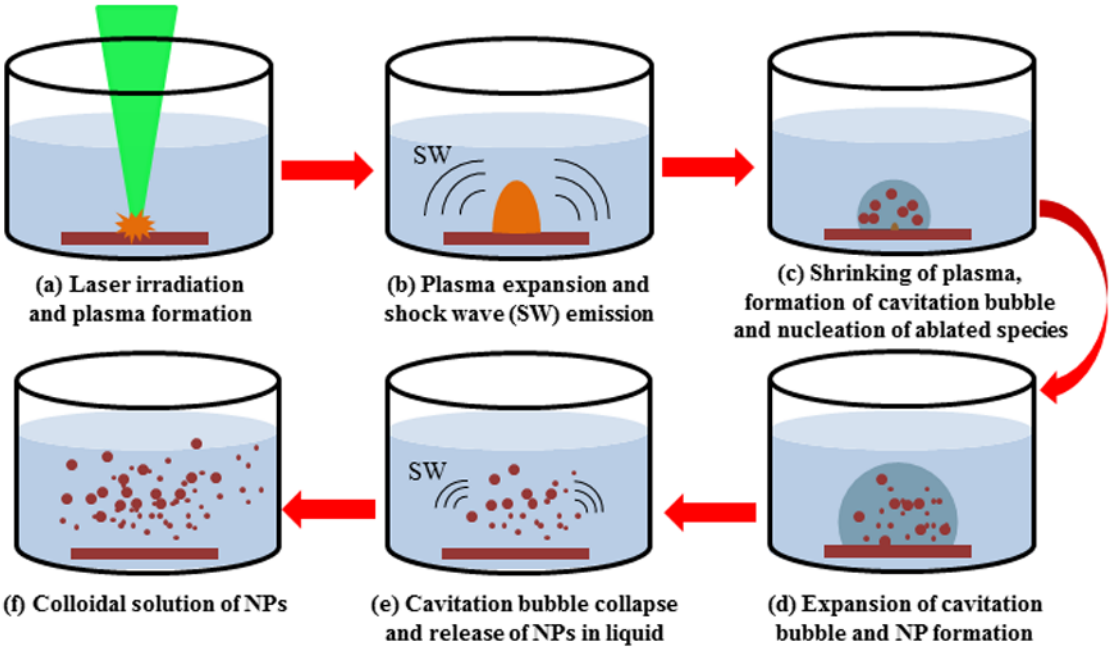

Figure 1.2 *Schematic representation of the entire mechanism of laser ablation of a solid in liquid.*

There are three main chemical processes taking place during laser ablation of a solid in liquid [7]. The first one being the chemical reaction among the various species in the target plasma itself. Another reaction takes place between the target plasma and the surrounding liquid plasma. Finally, there is forceful ejection of the target plasma into the surrounding liquid. The various stakeholders in these processes are schematically shown in Fig. 1.3.

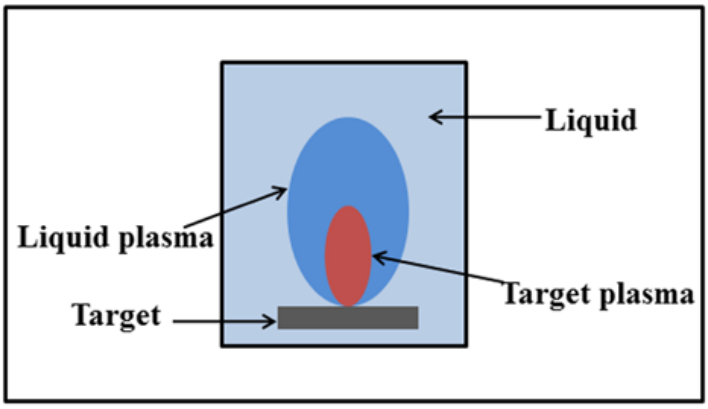

Figure 1.3 *Participants in the chemical processes in laser ablation of a solid in liquid.*

The plasma formed is confined by the surrounding liquid curtailing the free expansion of the plasma unlike those of under vacuum or in presence of gaseous medium [20]. As a result, the propagation of the plasma gets delayed and there is emission of primary shock waves (SWs) in the vicinity of the target as shown in Fig. 1.2(b). Once the laser pulse is over, the plasma starts cooling down and the hot plasma is replaced by vaporized fluid. At this stage, there are rapid pressure variations and the vaporized fluid forms a bubble or cavity called the cavitation bubble [21]. Inside the cavitation bubble, condensation of the ablated species leads to its nucleation which ultimately results in the formation of NPs (Fig. 1.2(c) and 1.2(d)) [22]. The properties of the NPs depend on various chemical reactions and recombination processes occurring among the participating species [9, 23].

The cavitation bubble exhibits interesting dynamical nature. The bubble expands due to the inertia of the vaporized species present inside as shown in Fig. 1.2(d). This

expansion brings about a state inside the bubble wherein the pressure becomes less than the hydrostatic pressure of the surrounding liquid [24]. To maintain the pressure, the bubble compresses and the pressure inside the bubble increases as compared to that of the ambient. This leads to the collapse of the bubble and there is an emission of excess energy in the form of secondary SWs in the surrounding liquid. The collapse of the bubble initiates the growth of a new bubble which again collapses in the similar manner. This process, called the bubble oscillation, continues till all the energy of the bubble is dissipated in the liquid ambient [25]. The collapse of each bubble results in the release of NPs in the surrounding liquid and is accompanied by the emission of SWs (Fig. 1.2(e)). The final outcome of the processes described is the colloidal solution of the NPs as depicted in Fig. 1.2(f).

The dynamical behaviour of the initial SWs and the cavitation bubbles determines the properties of the final product in the form of NPs in the process of laser ablation in liquid and hence the understanding of these highly transient processes is of utmost importance.

1.2 Importance/applications of laser ablation of solid in liquid

Laser ablation in liquid has been successfully implemented in the field of engineering, medical sciences, lithography, laser induced breakdown spectroscopy (LIBS) and fabrication of various micro/nanostructures, etc. [4, 9, 26-28]. In the engineering domain, high power laser is widely used as an effective tool for cutting, drilling, etching, machining, surface coating, surface cleaning, etc. [26, 27]. While laser ablation in air is suitable for most of these applications, but when it comes to machining, micromachining in particular, there are various undesired effects like deposition of recast layer, debris and increased roughness in the machined substrate [26, 27]. These problems have been successfully negated by carrying out the laser machining in a liquid ambient [26, 27]. The liquid medium carries away the excessive heat from the target faster than in air owing to the higher thermal

conductivity of the liquid as compared to that of air. This results in the generation of surface with smooth morphology. Moreover, the ablated species and also the debris are carried away by the liquid whereas in the case of ablation in air these get deposited on the target surface itself.

The laser-target-liquid interaction is being applied in the field of medical sciences too [29, 30]. However, the complexities involved in the process led to the delay in its efficient use in various medical procedures. Today, the role of lasers in ophthalmic dissection, dissection of various cellular organelles and also in fragmentation of kidney stones, etc. has become indispensable [30-33]. The importance of laser ablation in liquid in the research related to medical sciences lies in the fact that most of the tissues in the human body have a dominant quantity of water [30]. Hence, understanding of the processes involved in laser ablation in liquid is crucial in order to avoid adverse effects during non-invasive laser surgery.

The process of laser ablation has also been applied to the field of spectroscopy [8]. LIBS is a powerful spectroscopic technique developed for analysing the elemental composition in materials [6, 8, 34-36]. Laser induced plasma emits characteristic line spectrum of atoms/ions/molecules of constituent species making it feasible to identify and quantify the composition of the target under consideration. Although LIBS in air is an established technique for the elemental analysis, the same in liquid has certain limitations [37]. The confinement effect of the liquid and the shortened lifetime of the plasma results in the decrease of the signal to noise ratio and it becomes difficult to distinguish the LIBS signal from the background arising due to the Bremsstrahlung processes and other noises [37, 38]. Also, due to the confinement, the alignment for the detection becomes very critical. However, the prospects of LIBS in liquid has increased with improvements being

made in this field. Application of dual pulse in LIBS to increase the signal strength has made the detection of trace elements in liquid easy and reliable [39, 40].

Among many areas in which the process of laser ablation in liquid has been successfully applied, the most phenomenal impact of this process has been in the field of NP synthesis. The reasons for the "numero uno" status associated to PLAL in the synthesis of NPs over the years is discussed in the following section.

1.3 Nanoparticle synthesis by PLAL

In the last few decades, the importance of NPs has increased at an unprecedented rate due to its application in the field of medicines, industries, agriculture, etc. [41-44]. With the increasing demand for NPs, a large number of techniques for its synthesis have been invented including chemical, biological and physical techniques [45-47]. Chemical methods such as chemical reduction, sol gel, polyol, etc. have been used for the synthesis of nanomaterials with huge success [48-50]. In the last decade, biological methods for the synthesis of NPs have proved to be excellent green techniques. In biological methods, microorganisms such as fungi, bacteria, plant extracts, etc. are used in the synthesis of NPs [46, 51]. However, the adverse effect on the environment due to the use of chemical reagents in the chemical methods and the longer reaction time and low yield of NPs in most of the biological methods have kept researchers on their toes, looking for alternative methods [52, 53].

Among various available methods, PLAL is one of the best and simplest techniques for the synthesis of NPs [4, 7, 13, 16, 54]. The high purity of the sample and stable handling of the colloidal NPs makes it very advantageous over other techniques. The NPs formed remain suspended in the surrounding liquid and can be easily transported for further analysis. Most importantly, the technique does not necessarily demand the use of any

chemical reagent even in the form of surfactants or stabilizers making PLAL an environment-friendly technique [54].

Depending on the target and its affinity towards the surrounding liquid, a variety of NPs can be synthesized. The properties of the NPs can be tuned by varying the laser parameters viz., the laser wavelength, pulse duration, fluence, exposure time, etc. [55-58]. The focusing conditions of the laser beam can also be varied to alter the NP properties [57, 59]. It has also been found that the properties of the surrounding liquid can also tailor the characteristics of the NPs [60, 61]. The beauty of PLAL lies in the fact that NPs of any solid material can be synthesized. As such, the list of various NPs that have been successfully synthesized by PLAL is an exhaustive one [16]. Another factor which is responsible for the popularity of PLAL has been the low cost associated with the technique. Barring the initial investment in the laser system, which is high, PLAL is a more cost effective technique as compared to its chemical counterparts. Of course, the scale of NP production is one area in which PLAL is a bit lagging but there have been significant improvements even in this direction [62]. The NPs synthesized via PLAL have shown potential applications in biomedicine, pseudo-capacitors, optoelectronics, catalysis, toxicity reduction, surface enhanced Raman scattering (SERS), etc. [16, 63-67].

1.4 Importance of noble metal NPs

With every stride in nanotechnology, the importance of NPs has increased drastically. Metal NPs, noble metal NPs in particular, have huge potential due to their remarkable optical, electronic and catalytic properties as compared to those of bulk materials [68-70]. These properties have led to its imperative role in many fields, especially in sensing applications like nano biosensors, metal enhanced fluorescence (MEF), SERS, etc. [71-75]. Among many interesting properties of noble metal NPs, the most notable is the localized surface plasmon resonance (LSPR) associated with it [76, 77].

The mechanism of generation of LSPR is schematically represented in Fig. 1.4. When an external electromagnetic radiation is incident on the NPs, it interacts with the free electrons present in the NPs. If the size of the NPs is smaller than the wavelength of the incident light it leads to a collective oscillation of the electrons and have a displacement of the electron cloud. A restoring force from Coulombic attraction results in the oscillation of the electron cloud with respect to the nuclei. At a particular frequency of oscillation, resonance occurs and a dipolar field is created outside the NPs [76, 77]. The generation of this field is the source of strong enhancement of electromagnetic field around the surface of the NPs which is the backbone of LSPR and SERS based plasmonic applications [71, 72].

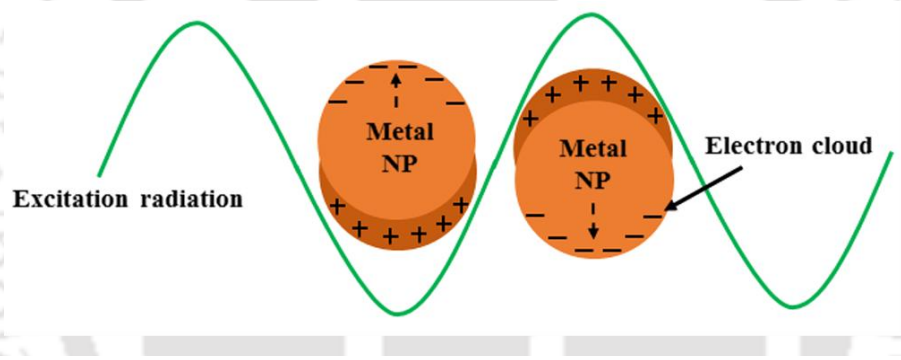

Figure 1.4 *Schematic representation of the generation of LSPR in noble metals.*

The LSPR of metallic NPs is explained by the Mie theory [78, 79]. Starting from the Maxwell equations, Mie went on to describe the optical properties of small spherical metal particles. For particle size much smaller than the wavelength of the incident light ($R << \lambda$), the absorption is caused mainly by the electric dipole oscillations, and the total extinction coefficient κ in the quasi-static regime is given by [80]

$$\kappa = \frac{18\pi n V \varepsilon'^{3/2}}{\lambda} \frac{\varepsilon_2}{[\varepsilon_1 + 2\varepsilon']^2 + \varepsilon_2^2} \tag{1.1}$$

where n is the number of particles, V is the volume, λ is the wavelength of the incident light, ε' is the dielectric constant of the surrounding medium and, ε_1 and ε_2 are the real and

imaginary parts, respectively of the dielectric constant, $\varepsilon(\omega)$, of the material where ω is the angular frequency of light. If ε_2 is small or weakly dependent on ω then the plasmon resonance condition is roughly fulfilled when $\varepsilon_1(\omega) = -2\varepsilon'$. When this condition is satisfied, a resonance enhancement is experienced by the polarizability. As a result of this enhanced polarizability, the scattering and absorption capability of metallic NPs increases. This is the origin of the SPR.

Among the noble metal NPs, gold (Au), silver (Ag) and copper (Cu) are mostly used in plasmonic applications [81-84]. Au due to its chemical inertness and biocompatibility has been in high demand in many applications especially the ones involving biomolecules [85]. Some of the applications of gold NPs in biomedical field include its use as biolabels, its enhanced immunosensing when used in conjugation with protein, targeted drug delivery, etc. [86-88]. Besides these, recently, laser induced explosion of Au NPs has come up as a new prospect for the treatment of cancer [89]. Ag is another very important noble metal and is known to exhibit the strongest plasmonic response which has led to it being the preferred choice in many plasmonic applications [83, 90-92]. These applications include its use as SERS substrate, in plasmonic color printing, plasmonic sensors, etc. [83, 91-93]. Luminescence enhancement property of Ag NPs is used to enhance the sensitivity of radiation detector [94]. In addition to these, NPs of Ag and its oxide have excellent antimicrobial properties which has facilitated its use in many industries including health and textile [95, 96]. In spite of all the advantages associated with Ag NPs, the cyto-toxicity of these NPs has been a matter of concern for environmentalists across the globe [97]. Efforts to reduce the cytotoxicity of Ag NPs is on the rise with sulfidation of the NPs being a viable option [98].

Application of Cu NPs in plasmonics is comparatively limited due to its reactive nature. But the low cost of copper has been a motivating factor for researchers to explore

its potential in plasmonic applications [84, 99-101]. Cu NPs are finding applications as SERS substrate, in enhancing the light harvesting properties in solar cells, as photocatalysts, calorimetric sensors, etc. [99, 102-105]. Recently, there have been several reports on the applications of metal oxide NPs [106, 107]. Cu has a natural tendency for oxidation. As a result, the oxidation of Cu which was considered as a setback earlier has turned out to be a dramatically interesting topic. Cu oxide semiconductors possessing narrow bandgaps are being extensively used in renewable energy production [108]. Cu_2O thin films are used as hole-transport layers in perovskite solar cells and CuO nanostructures are being used as electrode materials in supercapacitors [109, 110]. Both Cu_2O and CuO have potential applications as gas sensors and their photocatalytic activities are found to be excellent [111, 112]. NPs of both Cu as well its oxides are reported to have enhanced antimicrobial properties against pathogenic bacteria [95, 113]. Composites of Cu with polymer have been used in medical devices, food packaging, medical implants, bandage, water disinfectant, etc. [114].

Among various applications of noble metal NPs, its use as LSPR based sensors has been a major breakthrough [72, 77]. SERS is one such vibrational spectroscopic technique utilizing the LSPR property of noble metals to enhance the intensity of intrinsically weak Raman signal obtained from a sample by several orders of magnitude [74, 115, 116]. In terms of identification of various species, although traditional Raman spectroscopy is a very efficient technique, it suffers from the disadvantage of poor signal due to the low cross-section for Raman scattering [117]. This demerit associated with Raman spectroscopy has been negated efficiently by the advent of SERS. The virtue of SERS in the identification of various species and obtaining the structural information is widely acclaimed. This is reflected in the application of SERS in the fields of material science, biomedical engineering, electrochemistry, etc. [74, 75, 118, 119]. Even though many

advances have been made in the search for high-performance SERS substrates since its discovery, more than 35 years ago, but till date the quest for more reliable and low cost SERS substrates is on [120, 121]. While fabrication of some very good SERS substrates requires extremely sophisticated techniques to create periodic nanostructures, there have been successful endeavours towards developing cheaper substrates [122-124]. Development of SERS has led to its successful implementation in single molecule detection, biomolecular sensing and trapping, detection of proteins, nucleic acids, deoxyribonucleic acid (DNA), etc. [115].

1.5 The present work

In view of the above discussion, it is evident that PLAL is a very advantageous technique for the synthesis of NPs. Keeping the importance of noble metal NPs in mind, in the present work, NPs of Cu and Ag have been synthesized by pulsed laser ablation in distilled water (DW). Incident laser energy and ablation duration have been used to alter the properties of the NPs. The role of the confining liquid on the properties of the NPs synthesized via PLAL is investigated by carrying out the synthesis of Cu NPs in two organic solvents, methanol and 2-propanol. The results obtained in these solvents are compared with those obtained for the NPs synthesized in DW. The study of the effect of the confining liquid on the NPs is complemented with a correlative study of the laser produced crater on the target surface in various ambients.

The formation of NPs via PLAL is influenced by the dynamics of the processes involved in PLAL viz., the cavitation bubble and SWs. These processes are studied using shadowgraphy and beam deflection techniques. The thermodynamics of the peculiar dynamics of the cavitation bubbles have been derived analytically. A thermodynamic nucleation model has been used to study the nucleation of Cu@Cu_2O NPs.

The synthesized NPs have been successfully applied as excellent SERS substrate for a bioactive furanoflavonoid, karanjin having medicinal properties [125, 126]. A comparison between the SERS capability of Cu and Ag NPs in the sensing of karanjin is also done. As both Cu and Ag NPs have excellent antimicrobial properties, the synthesized NPs are used as an effective antibacterial protective layer on three natural silks. The synthesized NPs have also been applied to check its viability on the treatment of filter paper for annihilation of bacteria from contaminated water.

Organisation of the present thesis

The entire thesis has been divided into eight chapters as briefed below.

Chapter 1, "Introduction" presents the overview of the literature survey on pulsed laser ablation of a solid, the mechanism of PLAL and its application in NP synthesis, and importance of noble metal NPs.

Chapter 2, "Experimental Details" describes various experimental setup used in the present thesis work. The PLAL setup for the synthesis of the NPs, shadowgraphy and beam deflection setup for the investigation of the dynamics of the cavitation bubble and SWs are illustrated and explained. The preparation of the NP samples for SERS studies on karanjin and also the details of the antibacterial study on silk and filter paper are elucidated. In addition, the basic information of the instruments used for the characterization of the NPs is also included in this chapter.

Chapter 3, "Synthesis and Characterization of Cu@Cu_xO Nanoparticles" describes the effect of incident laser energy and ablation duration on the size, SPR and structural features of the Cu@Cu_xO (x=1, 2) NPs synthesized via PLAL.

Chapter 4, "Synthesis and Characterization of Ag@Ag_xO_y Nanoparticles" discusses the effect of incident laser energy and ablation duration on the size, SPR and

structural features of the $Ag@Ag_xO_y$ (x=1, 2; y=0, 1, 3) NPs synthesized by PLAL. The photoluminescence of the Ag NPs and its possible origin is also discussed in this chapter.

Chapter 5, "Role of Confining Liquids on the Properties of Nanoparticles Synthesized via PLAL" involves the investigations on the effect of confining liquid on the properties of NPs synthesized via PLAL. The variation in the properties of NPs synthesized via PLAL in various solvents is correlated to the changes occurring on the laser produced crater on the target surface in different ambients.

Chapter 6, "Dynamics of the Process of Laser Ablation in Liquid: Cavitation Bubbles and Shock Waves" involves the investigation of the cavitation bubble and SWs using the shadowgraphy and beam deflection techniques. The temperature and pressure derived from the dynamics of the cavitation bubble and SWs and its correlation with the nucleation of $Cu@Cu_2O$ NPs synthesized via pulsed laser ablation of Cu in DW is elaborately discussed.

Chapter 7, "SERS and Antibacterial Activities of PLAL Synthesized Nanoparticles of $Cu@Cu_xO$ and $Ag@Ag_xO_y$" demonstrates the SERS capability of Cu as well as Ag NPs on karanjin. The antibacterial activity of the NPs and its use as a protective layer for Eri, Pat and Muga silks is discussed. Treatment of filter paper with the synthesized NPs in order to check its antibacterial efficacy for the annihilation of bacteria in contaminated water is also discussed in this chapter.

Finally, the thesis is concluded in ***Chapter 8*** with possible future scope.

References

[1] K. Sugioka, M. Meunier, A. Piqué, Laser precision microfabrication, Springer, 2010.
[2] T.C. Chong, M.H. Hong, L.P. Shi, Laser precision engineering: from microfabrication to nanoprocessing, Laser & Photonics Reviews, **4** (2010) 123-143.

[3] D.B. Chrisey, G.K. Hubler, Pulsed laser deposition of thin films, Wiley-Interscience, 1994.

[4] Z. Yan, D.B. Chrisey, Pulsed laser ablation in liquid for micro-/nanostructure generation, Journal of Photochemistry and Photobiology C: Photochemistry Reviews, **13** (2012) 204-223.

[5] L.J. Radziemski, Review of selected analytical applications of laser plasmas and laser ablation, 1987-1994, Microchemical Journal, **50** (1994) 218-234.

[6] L.J. Radziemski, D.A. Cremers, Laser-induced plasmas and applications, Marcel Dekker, 1989.

[7] G. Yang, Laser ablation in liquids: Applications in the synthesis of nanocrystals, Progress in Materials Science, **52** (2007) 648-698.

[8] J.P. Singh, S.N. Thakur, Laser-induced breakdown spectroscopy, Elsevier, 2007.

[9] G. Yang, Laser ablation in liquids: principles and applications in the preparation of nanomaterials, CRC Press, 2012.

[10] R.K. Singh, J. Narayan, Pulsed-laser evaporation technique for deposition of thin films: Physics and theoretical model, Physical Review B, **41** (1990) 8843.

[11] S. Harilal, C. Bindhu, R.C. Issac, V. Nampoori, C. Vallabhan, Electron density and temperature measurements in a laser produced carbon plasma, Journal of Applied Physics, **82** (1997) 2140-2146.

[12] P.P. Dey, A. Khare, Nonlinear optical and optical limiting response of PLD nc-Si thin films, Journal of Materials Chemistry C, **5** (2017) 12211-12220.

[13] H. Zeng, X.W. Du, S.C. Singh, S.A. Kulinich, S. Yang, J. He, W. Cai, Nanomaterials via laser ablation/irradiation in liquid: a review, Advanced Functional Materials, **22** (2012) 1333-1353.

[14] P. Patil, D. Phase, S. Kulkarni, S. Ghaisas, S. Kulkarni, S. Kanetkar, S. Ogale, V. Bhide, Pulsed-laser–induced reactive quenching at liquid-solid interface: Aqueous oxidation of iron, Physical review letters, **58** (1987) 238.

[15] R. Fabbro, J. Fournier, P. Ballard, D. Devaux, J. Virmont, Physical study of laser-produced plasma in confined geometry, Journal of Applied Physics, **68** (1990) 775-784.

[16] D. Zhang, B. Gökce, S. Barcikowski, Laser synthesis and processing of colloids: fundamentals and applications, Chemical reviews, **117** (2017) 3990-4103.

[17] J.H. Yoo, O.V. Borisov, X. Mao, R.E. Russo, Existence of phase explosion during laser ablation and its effects on inductively coupled plasma-mass spectroscopy, Analytical Chemistry, **73** (2001) 2288-2293.

[18] R. Kelly, A. Miotello, Does normal boiling exist due to laser-pulse or ion bombardment?, Journal of Applied Physics, **87** (2000) 3177-3179.

[19] A. Vogel, K. Nahen, D. Theisen, J. Noack, Plasma formation in water by picosecond and nanosecond Nd: YAG laser pulses. I. Optical breakdown at threshold and superthreshold irradiance, IEEE Journal of Selected Topics in Quantum Electronics, **2** (1996) 847-860.

[20] L. Berthe, R. Fabbro, P. Peyre, L. Tollier, E. Bartnicki, Shock waves from a water-confined laser-generated plasma, Journal of Applied Physics, **82** (1997) 2826-2832.

[21] A. Vogel, W. Lauterborn, R. Timm, Optical and acoustic investigations of the dynamics of laser-produced cavitation bubbles near a solid boundary, Journal of Fluid Mechanics, **206** (1989) 299-338.

[22] P. Wagener, S. Ibrahimkutty, A. Menzel, A. Plech, S. Barcikowski, Dynamics of silver nanoparticle formation and agglomeration inside the cavitation bubble after pulsed laser ablation in liquid, Physical Chemistry Chemical Physics, **15** (2013) 3068-3074.

[23] M. Dell'Aglio, R. Gaudiuso, O. De Pascale, A. De Giacomo, Mechanisms and processes of pulsed laser ablation in liquids during nanoparticle production, Applied Surface Science, **348** (2015) 4-9.

[24] R. Zhao, R.-q. Xu, Z.-h. Shen, J. Lu, X.-w. Ni, Experimental investigation of the collapse of laser-generated cavitation bubbles near a solid boundary, Optics & Laser Technology, **39** (2007) 968-972.

[25] P. Gregorcic, J. Mozina, A beam-deflection probe as a method for optodynamic measurements of cavitation bubble oscillations, Measurement Science and Technology, **18** (2007) 2972.

[26] A. Kruusing, Underwater and water-assisted laser processing: part 1—general features, steam cleaning and shock processing, Optics and lasers in engineering, **41** (2004) 307-327.

[27] A. Kruusing, Underwater and water-assisted laser processing: Part 2—Etching, cutting and rarely used methods, Optics and lasers in engineering, **41** (2004) 329-352.

[28] S. Owa, H. Nagasaka, Immersion Lithography; its potential performance and issues, Optical Microlithography XVI, International Society for Optics and Photonics, 2003, pp. 724-734.

[29] A. Vogel, Nonlinear absorption: intraocular microsurgery and laser lithotripsy, Physics in Medicine & Biology, **42** (1997) 895.

[30] A. Vogel, V. Venugopalan, Mechanisms of pulsed laser ablation of biological tissues, Chemical reviews, **103** (2003) 577-644.

[31] A. Vogel, P. Schweiger, A. Frieser, M.N. Asiyo, R. Birngruber, Intraocular Nd: YAG laser surgery: Light-tissue interaction, damage range, and reduction of collateral effects, IEEE J. Quantum Electron, **26** (1990) 2240-2260.

[32] S.P. Dretler, Laser lithotripsy: a review of 20 years of research and clinical applications, Lasers in surgery and medicine, **8** (1988) 341-356.

[33] B. Azadgoli, R.Y. Baker, Laser applications in surgery, Annals of translational medicine, **4** (2016).

[34] D.W. Hahn, N. Omenetto, Laser-induced breakdown spectroscopy (LIBS), part II: review of instrumental and methodological approaches to material analysis and applications to different fields, Applied spectroscopy, **66** (2012) 347-419.

[35] G. Galbács, A critical review of recent progress in analytical laser-induced breakdown spectroscopy, Analytical and bioanalytical chemistry, **407** (2015) 7537-7562.

[36] E. Mal, R. Junjuri, M.K. Gundawar, A. Khare, Optimization of temporal window for application of calibration free-laser induced breakdown spectroscopy (CF-LIBS) on copper alloys in air employing a single line, Journal of Analytical Atomic Spectrometry, (2019).

[37] O. Samek, D.C. Beddows, J. Kaiser, S.V. Kukhlevsky, M. Liska, H.H. Telle, A.J. Whitehouse, Application of laser-induced breakdown spectroscopy to in situ analysis of liquid samples, Optical Engineering, **39** (2000) 2248-2263.

[38] J.-S. Huang, H.-T. Liu, K.-C. Lin, Laser-induced breakdown spectroscopy in analysis of Al3+ liquid droplets: On-line preconcentration by use of flow-injection manifold, Analytica chimica acta, **581** (2007) 303-308.

[39] A. De Giacomo, M. Dell'Aglio, F. Colao, R. Fantoni, V. Lazic, Double-pulse LIBS in bulk water and on submerged bronze samples, Applied Surface Science, **247** (2005) 157-162.

[40] K. Rifai, S. Laville, F. Vidal, M. Sabsabi, M. Chaker, Quantitative analysis of metallic traces in water-based liquids by UV-IR double-pulse laser-induced breakdown spectroscopy, Journal of Analytical Atomic Spectrometry, **27** (2012) 276-283.

[41] A.C. Anselmo, S. Mitragotri, Nanoparticles in the clinic, Bioengineering & translational medicine, **1** (2016) 10-29.

[42] L. Zhang, F. Gu, J. Chan, A. Wang, R. Langer, O. Farokhzad, Nanoparticles in medicine: therapeutic applications and developments, Clinical pharmacology & therapeutics, **83** (2008) 761-769.

[43] C.S. Santos, B. Gabriel, M. Blanchy, O. Menes, D. García, M. Blanco, N. Arconada, V. Neto, Industrial applications of nanoparticles–a prospective overview, Materials Today: Proceedings, **2** (2015) 456-465.

[44] R. Prasad, V. Kumar, K.S. Prasad, Nanotechnology in sustainable agriculture: present concerns and future aspects, African Journal of Biotechnology, **13** (2014) 705-713.

[45] S. Iravani, H. Korbekandi, S. Mirmohammadi, B. Zolfaghari, Synthesis of silver nanoparticles: chemical, physical and biological methods, Research in pharmaceutical sciences, **9** (2014) 385-406.

[46] S. Ahmed, M. Ahmad, B.L. Swami, S. Ikram, A review on plants extract mediated synthesis of silver nanoparticles for antimicrobial applications: a green expertise, Journal of advanced research, **7** (2016) 17-28.

[47] C. Dhand, N. Dwivedi, X.J. Loh, A.N.J. Ying, N.K. Verma, R.W. Beuerman, R. Lakshminarayanan, S. Ramakrishna, Methods and strategies for the synthesis of diverse nanoparticles and their applications: a comprehensive overview, Rsc Advances, **5** (2015) 105003-105037.

[48] T.M.D. Dang, T.T.T. Le, E. Fribourg-Blanc, M.C. Dang, Synthesis and optical properties of copper nanoparticles prepared by a chemical reduction method, Advances in Natural Sciences: Nanoscience and Nanotechnology, **2** (2011) 015009.

[49] I.A. Rahman, V. Padavettan, Synthesis of silica nanoparticles by sol-gel: size-dependent properties, surface modification, and applications in silica-polymer nanocomposites—a review, Journal of nanomaterials, 2012 (2012) 8.

[50] A. Reverberi, N. Kuznetsov, V. Meshalkin, M. Salerno, B. Fabiano, Systematical analysis of chemical methods in metal nanoparticles synthesis, Theoretical Foundations of Chemical Engineering, **50** (2016) 59-66.

[51] N. Durán, P.D. Marcato, M. Durán, A. Yadav, A. Gade, M. Rai, Mechanistic aspects in the biogenic synthesis of extracellular metal nanoparticles by peptides, bacteria, fungi, and plants, Applied microbiology and biotechnology, **90** (2011) 1609-1624.

[52] K.N. Thakkar, S.S. Mhatre, R.Y. Parikh, Biological synthesis of metallic nanoparticles, Nanomedicine: nanotechnology, biology and medicine, **6** (2010) 257-262.

[53] S.S. Shankar, A. Ahmad, M. Sastry, Geranium leaf assisted biosynthesis of silver nanoparticles, Biotechnology progress, **19** (2003) 1627-1631.

[54] S. Barcikowski, V. Amendola, G. Marzun, C. Rehbock, S. Reichenberger, D. Zhang, B. Gökce, Handbook of laser synthesis of colloids, DuEPublico, 2016.

[55] D. Reyes-Contreras, M. Camacho-López, M.A. Camacho-López, S. Camacho-López, R.I. Rodríguez-Beltrán, M. Mayorga-Rojas, Influence of the per pulse laser fluence on the optical

properties of carbon nanoparticles synthesized by laser ablation of solids in liquids, Optics & Laser Technology, **74** (2015) 48-52.

[56] D. Werner, S. Hashimoto, Controlling the pulsed-laser-induced size reduction of Au and Ag nanoparticles via changes in the external pressure, laser intensity, and excitation wavelength, Langmuir, **29** (2013) 1295-1302.

[57] K.A. Elsayed, H. Imam, M.A. Ahmed, R. Ramadan, Effect of focusing conditions and laser parameters on the fabrication of gold nanoparticles via laser ablation in liquid, Optics & Laser Technology, **45** (2013) 495-502.

[58] V. Amendola, M. Meneghetti, What controls the composition and the structure of nanomaterials generated by laser ablation in liquid solution?, Physical chemistry chemical physics : PCCP, **15** (2013) 3027-3046.

[59] A. Nath, A. Khare, Size induced structural modifications in copper oxide nanoparticles synthesized via laser ablation in liquids, Journal of Applied Physics, **110** (2011) 043111.

[60] R.M. Tilaki, A. Iraji zad, S.M. Mahdavi, Size, composition and optical properties of copper nanoparticles prepared by laser ablation in liquids, Applied Physics A, **88** (2007) 415-419.

[61] P. Liu, H. Wang, X. Li, M. Rui, H. Zeng, Localized surface plasmon resonance of Cu nanoparticles by laser ablation in liquid media, Rsc Advances, **5** (2015) 79738-79745.

[62] R. Streubel, G. Bendt, B. Gökce, Pilot-scale synthesis of metal nanoparticles by high-speed pulsed laser ablation in liquids, Nanotechnology, **27** (2016) 205602.

[63] C. Streich, L. Akkari, C. Decker, J. Bormann, C. Rehbock, A. Müller-Schiffmann, F.C. Niemeyer, L. Nagel-Steger, D. Willbold, B. Sacca, Characterizing the effect of multivalent conjugates composed of Aβ-specific ligands and metal nanoparticles on neurotoxic fibrillar aggregation, ACS nano, **10** (2016) 7582-7597.

[64] M. Rui, X. Li, L. Gan, T. Zhai, H. Zeng, Ternary Oxide Nanocrystals: Universal Laser-Hydrothermal Synthesis, Optoelectronic and Electrochemical Applications, Advanced Functional Materials, **26** (2016) 5051-5060.

[65] B.M. Hunter, J.D. Blakemore, M. Deimund, H.B. Gray, J.R. Winkler, A.M. Müller, Highly active mixed-metal nanosheet water oxidation catalysts made by pulsed-laser ablation in liquids, Journal of the American Chemical Society, **136** (2014) 13118-13121.

[66] D. Tiedemann, U. Taylor, C. Rehbock, J. Jakobi, S. Klein, W.A. Kues, S. Barcikowski, D. Rath, Reprotoxicity of gold, silver, and gold–silver alloy nanoparticles on mammalian gametes, Analyst, **139** (2014) 931-942.

[67] M. Vinod, K.G. Gopchandran, Au, Ag and Au:Ag colloidal nanoparticles synthesized by pulsed laser ablation as SERS substrates, Progress in Natural Science: Materials International, **24** (2014) 569-578.

[68] A. Zaleska-Medynska, M. Marchelek, M. Diak, E. Grabowska, Noble metal-based bimetallic nanoparticles: the effect of the structure on the optical, catalytic and photocatalytic properties, Advances in colloid and interface science, **229** (2016) 80-107.

[69] Z. Fan, H. Zhang, Crystal phase-controlled synthesis, properties and applications of noble metal nanomaterials, Chemical Society Reviews, **45** (2016) 63-82.

[70] M. Rai, A.P. Ingle, I. Gupta, A. Brandelli, Bioactivity of noble metal nanoparticles decorated with biopolymers and their application in drug delivery, International Journal of Pharmaceutics, **496** (2015) 159-172.

[71] M. Li, S.K. Cushing, N. Wu, Plasmon-enhanced optical sensors: a review, Analyst, **140** (2015) 386-406.

[72] E. Petryayeva, U.J. Krull, Localized surface plasmon resonance: nanostructures, bioassays and biosensing—a review, Analytica chimica acta, **706** (2011) 8-24.

[73] C.D. Geddes, Metal-enhanced fluorescence, Physical chemistry chemical physics : PCCP, **15** (2013) 19537.

[74] B. Sharma, R.R. Frontiera, A.-I. Henry, E. Ringe, R.P. Van Duyne, SERS: Materials, applications, and the future, Materials Today, **15** (2012) 16-25.

[75] A. Hakonen, P.O. Andersson, M.S. Schmidt, T. Rindzevicius, M. Käll, Explosive and chemical threat detection by surface-enhanced Raman scattering: A review, Analytica chimica acta, **893** (2015) 1-13.

[76] K.A. Willets, R.P. Van Duyne, Localized surface plasmon resonance spectroscopy and sensing, Annual review of physical chemistry, **58** (2007) 267-297.

[77] K.M. Mayer, J.H. Hafner, Localized surface plasmon resonance sensors, Chemical reviews, **111** (2011) 3828-3857.

[78] C.F. Bohren, D.R. Huffman, Absorption and scattering of light by small particles, John Wiley & Sons, 2008.

[79] G. Mie, Contributions to the optics of turbid media, particularly of colloidal metal solutions, Annalen der Physik, **25** (1908) 377-445.

[80] S. Link, M.A. El-Sayed, Spectral properties and relaxation dynamics of surface plasmon electronic oscillations in gold and silver nanodots and nanorods, The Journal of Physical Chemistry B, **103** (1999) 8410-8426.

[81] J. Castillo, J. Chirinos, H. Gutiérrez, M. La Cruz, Surface plasmon resonance sensor based on golden nanoparticles and cold vapour generation technique for the detection of mercury in aqueous samples, Optics & Laser Technology, **94** (2017) 34-39.

[82] Y. Zhang, Q. Zhang, X. Ouyang, D.Y. Lei, A.P. Zhang, H.-Y. Tam, Ultrafast Light-Controlled Growth of Silver Nanoparticles for Direct Plasmonic Color Printing, ACS nano, **12** (2018) 9913-9921.

[83] C.-Y. Li, M. Meng, S.-C. Huang, L. Li, S.-R. Huang, S. Chen, L.-Y. Meng, R. Panneerselvam, S.-J. Zhang, B. Ren, "Smart" Ag nanostructures for plasmon-enhanced spectroscopies, Journal of the American Chemical Society, **137** (2015) 13784-13787.

[84] S. Ezugwu, H. Ye, G. Fanchini, Three-dimensional scanning near field optical microscopy (3D-SNOM) imaging of random arrays of copper nanoparticles: implications for plasmonic solar cell enhancement, Nanoscale, **7** (2015) 252-260.

[85] X. Zhang, Gold nanoparticles: recent advances in the biomedical applications, Cell biochemistry and biophysics, **72** (2015) 771-775.

[86] H. Daraee, A. Eatemadi, E. Abbasi, S. Fekri Aval, M. Kouhi, A. Akbarzadeh, Application of gold nanoparticles in biomedical and drug delivery, Artificial cells, nanomedicine, and biotechnology, **44** (2016) 410-422.

[87] C. Parolo, A. de la Escosura-Muñiz, E. Polo, V. Grazú, J.M. De La Fuente, A. Merkoçi, Design, preparation, and evaluation of a fixed-orientation antibody/gold-nanoparticle conjugate as an immunosensing label, ACS applied materials & interfaces, **5** (2013) 10753-10759.

[88] A. Kumar, X. Zhang, X.-J. Liang, Gold nanoparticles: emerging paradigm for targeted drug delivery system, Biotechnology advances, **31** (2013) 593-606.

[89] N.S. Abadeer, C.J. Murphy, Recent progress in cancer thermal therapy using gold nanoparticles, The Journal of Physical Chemistry C, **120** (2016) 4691-4716.

[90] X. Li, J. Li, X. Zhou, Y. Ma, Z. Zheng, X. Duan, Y. Qu, Silver nanoparticles protected by monolayer graphene as a stabilized substrate for surface enhanced Raman spectroscopy, Carbon, **66** (2014) 713-719.

[91] G. Schmidl, J. Dellith, H. Schneidewind, D. Zopf, O. Stranik, A. Gawlik, S. Anders, V. Tympel, C. Katzer, F. Schmidl, Formation and characterization of silver nanoparticles embedded in optical transparent materials for plasmonic sensor surfaces, Materials Science and Engineering: B, **193** (2015) 207-216.

[92] S. Nishanthi, S. Iyyapushpam, B. Sundarakannan, E. Subramanian, D.P. Padiyan, Plasmonic silver nanoparticles loaded titania nanotube arrays exhibiting enhanced photoelectrochemical and photocatalytic activities, Journal of Power Sources, **274** (2015) 885-893.

[93] M. Canamares, J. Garcia-Ramos, S. Sanchez-Cortes, M. Castillejo, M. Oujja, Comparative SERS effectiveness of silver nanoparticles prepared by different methods: A study of the enhancement factor and the interfacial properties, Journal of colloid and interface science, **326** (2008) 103-109.

[94] E.J. Guidelli, A.P. Ramos, O. Baffa, Silver nanoparticle films for metal enhanced luminescence: toward development of plasmonic radiation detectors for medical applications, Sensors and Actuators B: Chemical, **224** (2016) 248-255.

[95] S.M. Dizaj, F. Lotfipour, M. Barzegar-Jalali, M.H. Zarrintan, K. Adibkia, Antimicrobial activity of the metals and metal oxide nanoparticles, Materials Science and Engineering: C, **44** (2014) 278-284.

[96] T. Yuranova, A. Rincon, A. Bozzi, S. Parra, C. Pulgarin, P. Albers, J. Kiwi, Antibacterial textiles prepared by RF-plasma and vacuum-UV mediated deposition of silver, Journal of Photochemistry and Photobiology A: Chemistry, **161** (2003) 27-34.

[97] S. Prabhu, E.K. Poulose, Silver nanoparticles: mechanism of antimicrobial action, synthesis, medical applications, and toxicity effects, International nano letters, **2** (2012) 32.

[98] C. Levard, E.M. Hotze, G.V. Lowry, G.E. Brown Jr, Environmental transformations of silver nanoparticles: impact on stability and toxicity, Environmental science & technology, **46** (2012) 6900-6914.

[99] M. Dendisová-Vyškovská, V. Prokopec, M. Člupek, P. Matějka, Comparison of SERS effectiveness of copper substrates prepared by different methods: what are the values of enhancement factors?, Journal of Raman Spectroscopy, **43** (2012) 181-186.

[100] P. Shen, Y. Liu, Y. Long, L. Shen, B. Kang, High-performance polymer solar cells enabled by copper nanoparticles-induced plasmon resonance enhancement, The Journal of Physical Chemistry C, **120** (2016) 8900-8906.

[101] X. Li, X. Ren, Y. Zhang, W.C. Choy, B. Wei, An all-copper plasmonic sandwich system obtained through directly depositing copper NPs on a CVD grown graphene/copper film and its application in SERS, Nanoscale, **7** (2015) 11291-11299.

[102] F. Parveen, B. Sannakki, M.V. Mandke, H.M. Pathan, Copper nanoparticles: Synthesis methods and its light harvesting performance, Solar Energy Materials and Solar Cells, **144** (2016) 371-382.

[103] X. Guo, C. Hao, G. Jin, H.Y. Zhu, X.Y. Guo, Copper nanoparticles on graphene support: an efficient photocatalyst for coupling of nitroaromatics in visible light, Angewandte Chemie International Edition, **53** (2014) 1973-1977.

[104] K.B.A. Ahmed, M. Sengan, S. Kumar, A. Veerappan, Highly selective colorimetric cysteine sensor based on the formation of cysteine layer on copper nanoparticles, Sensors and Actuators B: Chemical, **233** (2016) 431-437.

[105] Y.-T. Hwang, W.-H. Chung, Y.-R. Jang, H.-S. Kim, Intensive plasmonic flash light sintering of copper nanoinks using a band-pass light filter for highly electrically conductive electrodes in printed electronics, ACS applied materials & interfaces, **8** (2016) 8591-8599.

[106] P. Gao, D. Liu, Facile synthesis of copper oxide nanostructures and their application in non-enzymatic hydrogen peroxide sensing, Sensors and Actuators B: Chemical, **208** (2015) 346-354.

[107] M. Karami, M. Akhavan-Behabadi, M.R. Dehkordi, S. Delfani, Thermo-optical properties of copper oxide nanofluids for direct absorption of solar radiation, Solar Energy Materials and Solar Cells, **144** (2016) 136-142.

[108] X. Liu, J. Chen, P. Liu, H. Zhang, G. Li, T. An, H. Zhao, Controlled growth of CuO/Cu2O hollow microsphere composites as efficient visible-light-active photocatalysts, Applied Catalysis A: General, **521** (2016) 34-41.

[109] S. Chatterjee, A.J. Pal, Introducing Cu2O thin films as a hole-transport layer in efficient planar perovskite solar cell structures, The Journal of Physical Chemistry C, **120** (2016) 1428-1437.

[110] S. Shinde, H. Dhaygude, D.-Y. Kim, G. Ghodake, P. Bhagwat, P. Dandge, V. Fulari, Improved synthesis of copper oxide nanosheets and its application in development of supercapacitor and antimicrobial agents, Journal of Industrial and Engineering Chemistry, **36** (2016) 116-120.

[111] J. Zhang, J. Liu, Q. Peng, X. Wang, Y. Li, Nearly monodisperse Cu2O and CuO nanospheres: preparation and applications for sensitive gas sensors, Chemistry of materials, **18** (2006) 867-871.

[112] J. Choi, H. Oh, S.-W. Han, S. Ahn, J. Noh, J.B. Park, Preparation and characterization of graphene oxide supported Cu, Cu2O, and CuO nanocomposites and their high photocatalytic activity for organic dye molecule, Current Applied Physics, **17** (2017) 137-145.

[113] A.K. Chatterjee, R. Chakraborty, T. Basu, Mechanism of antibacterial activity of copper nanoparticles, Nanotechnology, **25** (2014) 135101.

[114] L. Tamayo, M. Azócar, M. Kogan, A. Riveros, M. Páez, Copper-polymer nanocomposites: An excellent and cost-effective biocide for use on antibacterial surfaces, Materials Science and Engineering: C, **69** (2016) 1391-1409.

[115] S. Schlücker, Surface-Enhanced raman spectroscopy: Concepts and chemical applications, Angewandte Chemie International Edition, **53** (2014) 4756-4795.

[116] P.L. Stiles, J.A. Dieringer, N.C. Shah, R.P. Van Duyne, Surface-enhanced Raman spectroscopy, Annu. Rev. Anal. Chem., **1** (2008) 601-626.

[117] M. Wrona, J. Salafranca, C. Nerín, Fast assessment of oxo-biodegradable polyethylene film oxidation by surface-enhanced Raman scattering with in situ formation of a silver nanoparticle substrate, Journal of Materials Chemistry C, **5** (2017) 463-469.

[118] J.F. Li, Y.F. Huang, Y. Ding, Z.L. Yang, S.B. Li, X.S. Zhou, F.R. Fan, W. Zhang, Z.Y. Zhou, B. Ren, Shell-isolated nanoparticle-enhanced Raman spectroscopy, Nature, **464** (2010) 392.

[119] Y. Cao, J. Zhang, Y. Yang, Z. Huang, N.V. Long, C. Fu, Engineering of SERS substrates based on noble metal nanomaterials for chemical and biomedical applications, Applied Spectroscopy Reviews, **50** (2015) 499-525.

[120] B. Sharma, M.F. Cardinal, S.L. Kleinman, N.G. Greeneltch, R.R. Frontiera, M.G. Blaber, G.C. Schatz, R.P. Van Duyne, High-performance SERS substrates: Advances and challenges, MRS bulletin, **38** (2013) 615-624.

[121] J.F. Betz, W.Y. Wei, Y. Cheng, I.M. White, G.W. Rubloff, Simple SERS substrates: powerful, portable, and full of potential, Physical Chemistry Chemical Physics, **16** (2014) 2224-2239.

[122] H. Zhang, M. Liu, F. Zhou, D. Liu, G. Liu, G. Duan, W. Cai, Y. Li, Physical deposition improved SERS stability of morphology controlled periodic micro/nanostructured arrays based on colloidal templates, Small, **11** (2015) 844-853.

[123] B.B. Xu, Y.L. Zhang, W.Y. Zhang, X.Q. Liu, J.N. Wang, X.L. Zhang, D.D. Zhang, H.B. Jiang, R. Zhang, H.B. Sun, Silver-coated rose petal: green, facile, low-cost and sustainable fabrication of a SERS substrate with unique superhydrophobicity and high efficiency, Advanced Optical Materials, **1** (2013) 56-60.

[124] L. Polavarapu, L.M. Liz-Marzán, Towards low-cost flexible substrates for nanoplasmonic sensing, Physical Chemistry Chemical Physics, **15** (2013) 5288-5300.

[125] A. Singh, I. Jahan, M. Sharma, L. Rangan, A. Khare, A.N. Panda, Structural Characterization, In Silico Studies and In Vitro Antibacterial Evaluation of a Furanoflavonoid from Karanj, Planta Medica Letters, **3** (2016) e91-e95.

[126] W.S. Eipeson, J. Manjunatha, P. Srinivas, T.S. Kanya, Extraction and recovery of karanjin: A value addition to karanja (Pongamia pinnata) seed oil, Industrial Crops and Products, **32** (2010) 118-122.

Chapter 2

Experimental Details

2.1 Introduction

Pulsed laser ablation in liquid (PLAL) is a versatile technique for the synthesis of nanoparticles (NPs) [1-5]. In this technique, properties of the NPs can be easily tuned by varying the laser parameters and properties of the surrounding liquid medium [6-8]. In the present thesis, NPs of copper (Cu) and silver (Ag) have been synthesized by the ablation of the respective targets in distilled water (DW) as a function of laser energy and ablation duration. In order to study the influence of the surrounding liquid, Cu NPs have also been synthesized in two organic solvents. The laser ablated crater on the surface of Cu in various ambients is analysed to understand the oxidation taking place on the target surface as well as its impact on the NPs. In the process of laser ablation in liquid, the dynamics of the laser produced cavitation bubbles and shock waves (SWs) in liquid play a very important role and hence these two phenomena have been studied using the shadowgraphy and beam deflection technique [9-11(a)]. The synthesized NPs of Cu and Ag have been tested for its viability as a substrate for surface enhanced Raman scattering (SERS) in the sensing of a furanoflavonoid, karanjin. The antibacterial properties of the synthesized NPs have also been applied to act as a protective layer for natural silks and in the treatment of filter paper for the annihilation of bacteria in contaminated water.

In this chapter, the experimental details regarding the synthesis of NPs and the formation of laser produced crater are elaborately discussed. The various techniques employed for the characterization of the NPs as well as the laser ablated crater are briefly stated. A lucid description of the shadowgraphy and beam deflection setup to study the dynamics of laser ablation is provided. The experimental details for testing the viability of

Cu and Ag NPs as SERS substrate and the antibacterial agent have also been detailed in this chapter.

2.2 Experimental details for synthesis of nanoparticles

The NPs of Cu and Ag were prepared via pulsed laser ablation of the respective Cu and Ag targets (99.9% pure) in DW. Cu NPs were also synthesized in two organic solvents, methanol and 2-propanol. In each case, the target was cleaned by ultra-sonication in acetone followed by rinsing with propanol. It was then placed at the bottom of a cell filled with ~ 8 mL of the liquid. The schematic and the photograph of the experimental setup for the generation of NPs by PLAL are shown in Fig. 2.1 and 2.2, respectively. The laser beam from the 2nd harmonic of a Q-switched Nd:YAG laser (Litron LPY7864-10G) having pulse duration of 7 ns was used for ablating the target. The laser was operated at a repetition rate of 10 Hz. The laser beam was steered by a set of optical components (shown in Fig. 2.2) and then finally focused using a 25 cm focal length lens onto the target immersed in the liquid.

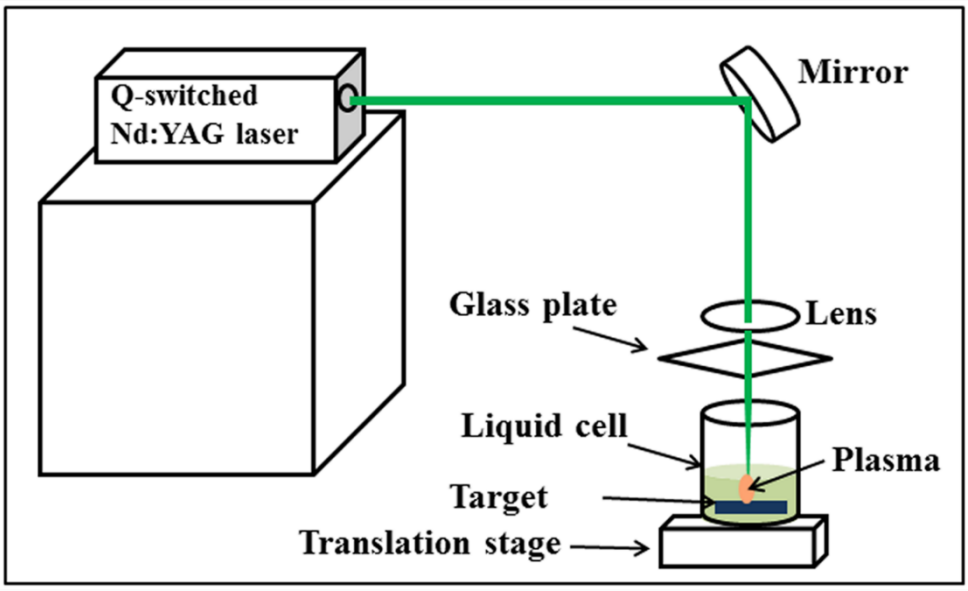

Figure 2.1 *Schematic of the experimental setup for PLAL.*

To avoid the drilling of the target due to repeated laser shots, the liquid cell containing the target was translated with the help of a programmable motorized

translational stage at a scan speed of 125 μm per second. Laser ablation is accompanied by a cracking sound and the intensity of the sound can be a good indicator of the uniform ablation [11(b)]. During the synthesis of NPs by laser ablation, in the present work, it was found that the intensity of the cracking sound was almost uniform throughout the experiment, indicating efficient and uniform ablation. The colloidal solution was also manually stirred frequently during the ablation process to disperse the floating layer of NPs formed during ablation and to ensure uniform laser ablation on shot-to-shot basis.

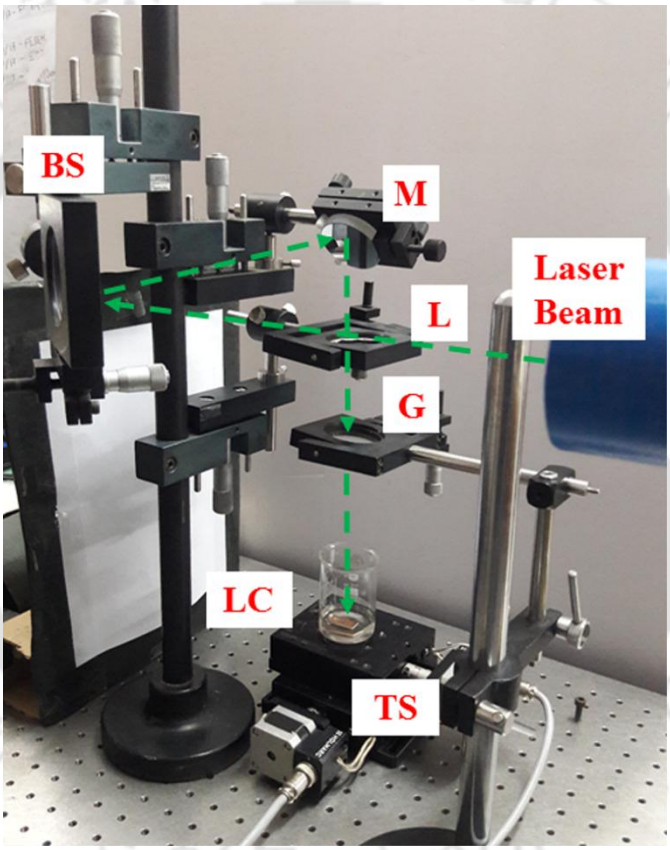

Figure 2.2 *Photograph of the PLAL setup; BS: beam splitter, M: mirror, L: lens, G: glass plate, LC: liquid cell, TS: translation stage.*

To study the effect of laser ablation duration and incident laser energy on the properties of the NPs, the experiment was conducted for three different duration of laser ablation at a fixed laser energy and then by keeping the ablation time fixed, the experiment was performed at three different laser energies.

Cu NP samples C1-C3 were synthesized in DW by varying the ablation duration for 15, 30 and 60 minutes, respectively while keeping the laser energy fixed at 30 mJ. Then, in line with sample C3, samples C4 and C5 were synthesized at laser energies of 50 and 70 mJ, respectively for a fixed ablation duration of 60 minutes. Thus, C1-C3 formed the set of samples for studying the effect of laser ablation duration and C3-C5 formed another set of samples for the effect of incident laser energy on the properties of Cu NPs. The details of the samples are summarized in table 2.1.

Table 2.1 *Details of Cu NPs synthesized in DW.*

Sample	Laser energy (mJ)	Duration (minutes)
C1	30	**15**
C2	30	**30**
C3	**30**	**60**
C4	**50**	60
C5	**70**	60

Similarly, for the case of Ag NPs, samples A1-A3, synthesized in DW by varying the ablation duration for 5, 15 and 30 minutes, respectively at fixed incident laser energy of 30 mJ, formed the series for studying the effect of ablation duration. Samples A4 and A5 were prepared at incident laser energy of 50 and 70 mJ, respectively for a duration of 30 minutes and hence samples A3-A5 formed the series for studying the variation in incident laser energy. The reason for choosing lesser duration in the case of Ag NPs will be discussed in section 4.3.2. The details of these Ag NPs are listed in table 2.2.

Table 2.2 *Details of Ag NP samples synthesized in DW.*

Sample	Laser energy (mJ)	Duration (minutes)
A1	30	**5**
A2	30	**15**
A3	**30**	**30**
A4	**50**	30
A5	**70**	30

Cu NP samples were also synthesized in methanol (M1-M3) and 2-propanol (P1-P3) by varying the ablation duration as 15, 30 and 60 minutes, respectively at a fixed incident laser energy of 30 mJ. The details of these samples M1-M3 and P1-P3 are summarized in table 2.3.

Table 2.3 *Details of Cu NP samples synthesized in methanol and 2-propanol.*

Sample	Laser energy (mJ)	Duration (minutes)
M1, P1	30	**15**
M2, P2	30	**30**
M3, P3	30	**60**

The laser ablation fluence impinging on the target was assessed from the focal spot (area ~ 3×10^{-3} cm^2) as depicted in Fig. 2.3. It was observed to be ~ 10, 16 and 22 J/cm^2 corresponding to laser energy of 30, 50 and 70 mJ, respectively.

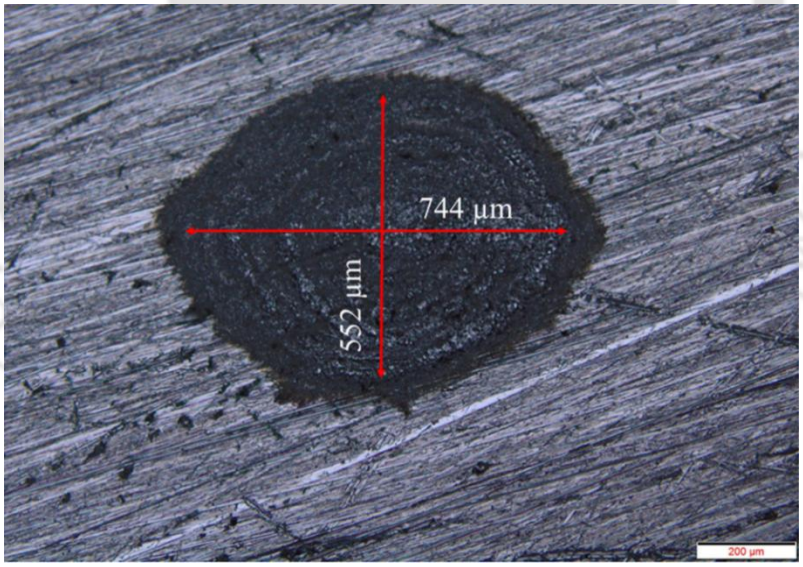

Figure 2.3 *Laser focal spot size on Ag target using a 25 cm focal length lens at 30 mJ laser energy.*

2.3 Laser produced crater formation

In order to investigate the structural and morphological changes of the laser irradiated target surface in various ambients and to correlate it with the properties of NPs thus formed, laser ablation of the Cu surface was performed in air, DW, methanol and 2-

propanol. For this, the ablation was carried out under similar conditions as was employed for the synthesis of NPs, section 2.2, with the only difference being that the target was not translated during ablation and repeated shots of laser were fired at the same spot in order to produce a prominent crater.

2.4 Characterization of nanoparticles and crater

The synthesized NPs and also the laser produced crater were subjected to a variety of characterization techniques. These techniques are briefly discussed in the following subsections.

2.4.1 Transmission electron microscope

The transmission electron microscope (TEM; JEOL JEM 2100, 2100F) operated at a voltage of 200 kV was used to study the shape and size of the NPs. The selected area electron diffraction (SAED) patterns and the high resolution TEM (HRTEM) gave information about its structural features. For this, the colloidal solution of the NPs was drop casted onto carbon coated copper grids and were subjected to TEM analysis. The TEM images were analysed by using the built-in "Gatan digital micrograph" software.

2.4.2 UV-visible spectrophotometer

The surface plasmon resonance (SPR) of the NPs was studied by recording the absorption spectra of the colloidal solutions using a UV-Visible spectrophotometer (Shimadzu UV-3101 PC). For this, the as-prepared colloidal solutions of the NPs were transferred in quartz cuvette (Dimension: 1 cm × 1 cm × 5 cm) for recording the spectra and the baseline correction was applied for each and every sample against the respective solvent in which the NPs were synthesized.

2.4.3 Raman spectrophotometer

In order to unveil the various oxide phases formed, the NPs were subjected to a Raman spectrophotometer (Horiba Jobin Vyon LabRam HR800) using a holographic grating of

1800 grooves/mm. For this, the colloidal solutions of NPs were drop casted onto glass coverslips and dried. The Raman spectra were then recorded at an excitation wavelength of 488 nm of Argon ion laser. The different regions of the crater were also probed with the laser to ascertain the formation of oxide under various ambients. The spectral resolution of the Raman spectrophotometer is less than 1 cm^{-1}.

2.4.4 X-ray diffractometer

The samples were also investigated by the X-ray diffractometer (Rigaku, TTRAX III) operated at a wavelength of 1.5407 Å of Cu-Kα line to identify the crystalline phases of the NPs. For this, the NP solutions were drop casted onto silicon (Si) wafers and dried and then exposed to the X-rays. The grazing angle of incidence of the X-rays was maintained between 1-2° and the step size is 0.03°.

2.4.5 Photoluminescence spectrometer

The photoluminescence (PL) spectra of the colloidal samples were recorded using an excitation wavelength of 300 nm at room temperature. The colloidal solutions were taken in quartz cuvette (Dimension: 1 cm × 1 cm × 5 cm) and a steady state fluorescence spectrometer (Edinburgh Instruments, FS920) equipped with Xenon lamp was used to record the PL spectra. The spectral resolution of the spectrometer is 0.1 nm.

2.4.6 Optical microscope

To measure the dimension of the craters produced as a result of ablation carried out in the different ambients, the ablated samples were subjected to an optical microscope (Olympus BX51M) having a minimum adjustment gradation of 1 µm.

2.4.7 Surface profilometer

In order to assess the mass ablation rate, the volume of the crater formed in various ambients was estimated from a non-contact high precision optical profilometer having field view of 0.825 mm × 0.825 mm (Taylor Hobson, Talysurf CCI lite).

2.4.8 Field emission scanning electron microscope

The morphological changes in the central and peripheral regions of the laser produced crater were investigated using the Field emission scanning electron microscope (FESEM; Zeiss, Sigma), operated at an accelerating voltage of 2 to 5 kV. The NP treated filter paper and the bacteria used in the antibacterial study were also subjected to the FESEM. Prior to loading the samples in the vacuum column of FESEM, the samples were coated with a very thin layer of gold to avoid the charging effect during measurement.

2.4.9 Energy dispersive X-ray

The oxygen content in different regions of the laser produced crater could be a good indicator for the oxidation taking place on the surface of the target during ablation. Hence, the various regions of the craters were probed with the Energy Dispersive X-ray (EDX) spectrometer (Oxford Instruments) attached to the FESEM.

2.5 Experimental details for the study of cavitation bubbles and shock waves

Once the laser beam is incident onto the target immersed in liquid, plasma formation of the target commences and is followed by the release of SWs and subsequent formation of the cavitation bubbles [5, 9, 10, 12]. The properties of the NPs produced via PLAL are influenced by the SWs and the cavitation bubbles [9, 12-14]. The dynamics of these two very important phenomena were studied via shadowgraphy and beam deflection technique as elaborated in the following subsections.

2.5.1 Shadowgraphy technique

The principle of the shadowgraphy technique lies in the ability of the probe beam to cast the shadow of any obstacle lying in its path onto a camera. The study of the cavitation bubble dynamics using this technique involves capturing of the bubble images at different times relative to the laser pulse [10, 15, 16].

The schematic and the photograph of the experimental setup for recording the images of the cavitation bubbles via shadowgraphy are shown in Fig 2.4 and 2.5, respectively.

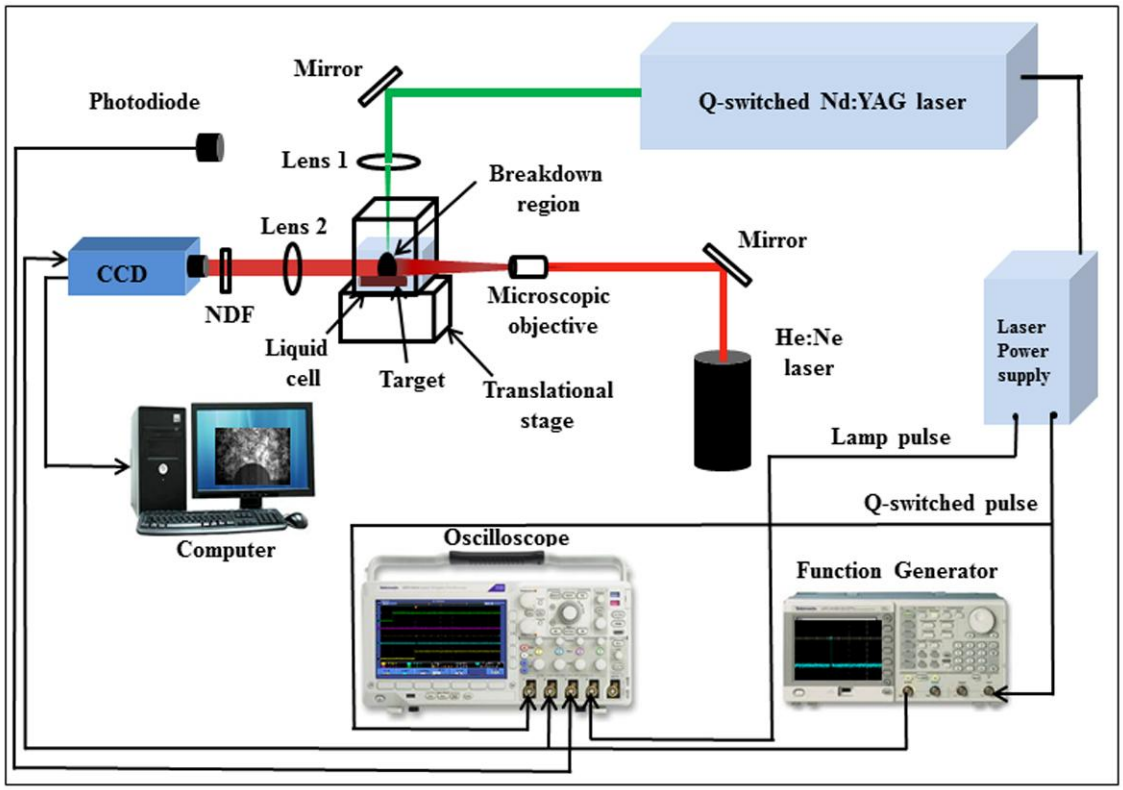

Figure 2.4 *Schematic of the shadowgraphy setup.*

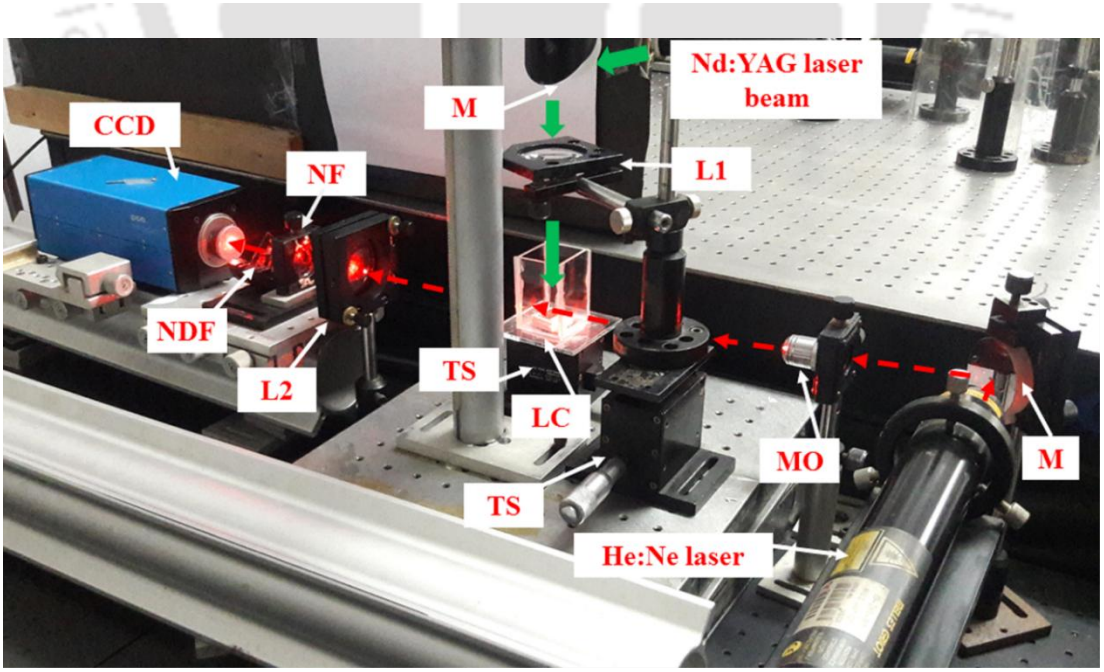

Figure 2.5 *Photograph of the shadowgraphy setup; CCD: Charge coupled device, NDF: Neutral density filter, NF: Notch filter, M: mirror, MO: Microscopic objective, L: lens, LC: liquid cell, TS: translation stage.*

The second harmonic of a Q-switched Nd:YAG laser (Spectra-Physics, INDI-HG) having a pulse duration of 7 ns and operated in the single shot mode was focused onto a Cu target for the ablation and formation of laser induced plasma followed by NPs. The Cu target was placed at the bottom of a liquid cell (LC; Dimension: 5 cm × 5 cm × 10 cm) made of glass as shown in Fig. 2.5. The LC was filled with water to a height of ~ 8 mm above the target. The laser beam was steered suitably using a set of optical components (in Fig. 2.4 and 2.5, only one mirror of the final stage is shown) and finally focused using a convex lens (L1) of focal length 10 cm on the target. To record the dynamics of cavitation bubbles via shadowgraphy, a probe laser beam from a cw He:Ne laser (Melles Griot, 05-LHR-991, Power:30 mW, λ=632.8 nm) was aligned in a direction perpendicular to the direction of plasma or the pump Nd:YAG laser beam focused onto the target in the vicinity of the ablated region. For proper illumination of the bubbles, the probe beam was expanded using a 10X microscopic objective as shown in Fig. 2.4. This expanded probe beam after passing through the breakdown region was imaged onto a fast gated charge coupled device (CCD) camera (PCO Sensicam qe) using a convex lens (L2) of focal length 10 cm to record shadowgraphic images of the bubble in the 1:1 configuration.

In order to record the temporal evolution of the bubbles, the CCD camera was triggered appropriately at different intervals of time w. r. t. the laser pulse. The triggering scheme was monitored on a digital storage oscilloscope (DSO; DPO3034; 300 MHz, 2.5 GS/s) and is depicted in Fig. 2.6. Fig 2.6(a) shows the time delay between the lamp pulse of the laser and the Q-switched pulse which is ~ 183 µs. The Q-switched pulse from the laser power supply triggered the function generator (Tektronix AFG3102, 1GS/s, 100 MHz) from which a delayed trigger pulse w. r. t. the laser signal was generated. This generated pulse was used to trigger the CCD. Fig. 2.6(b) shows the Q-switched pulse, the laser pulse and the generated trigger pulse from the function generator. Thus,

shadowgraphic images of the bubbles were captured as a function of time w. r. t. the laser pulse by delaying the output of the function generator.

In this way, the temporal evolution of the cavitation bubbles were recorded. The exposure time of the CCD camera was kept fixed at 2 µs and a neutral density filter (NDF; optical density 1.3) was used in front of the camera to avoid its saturation. The experiment was performed at three laser fluences of ~ 10, 16 and 22 J/cm^2, which is same as that of used for the synthesis of NPs discussed in section 2.2.

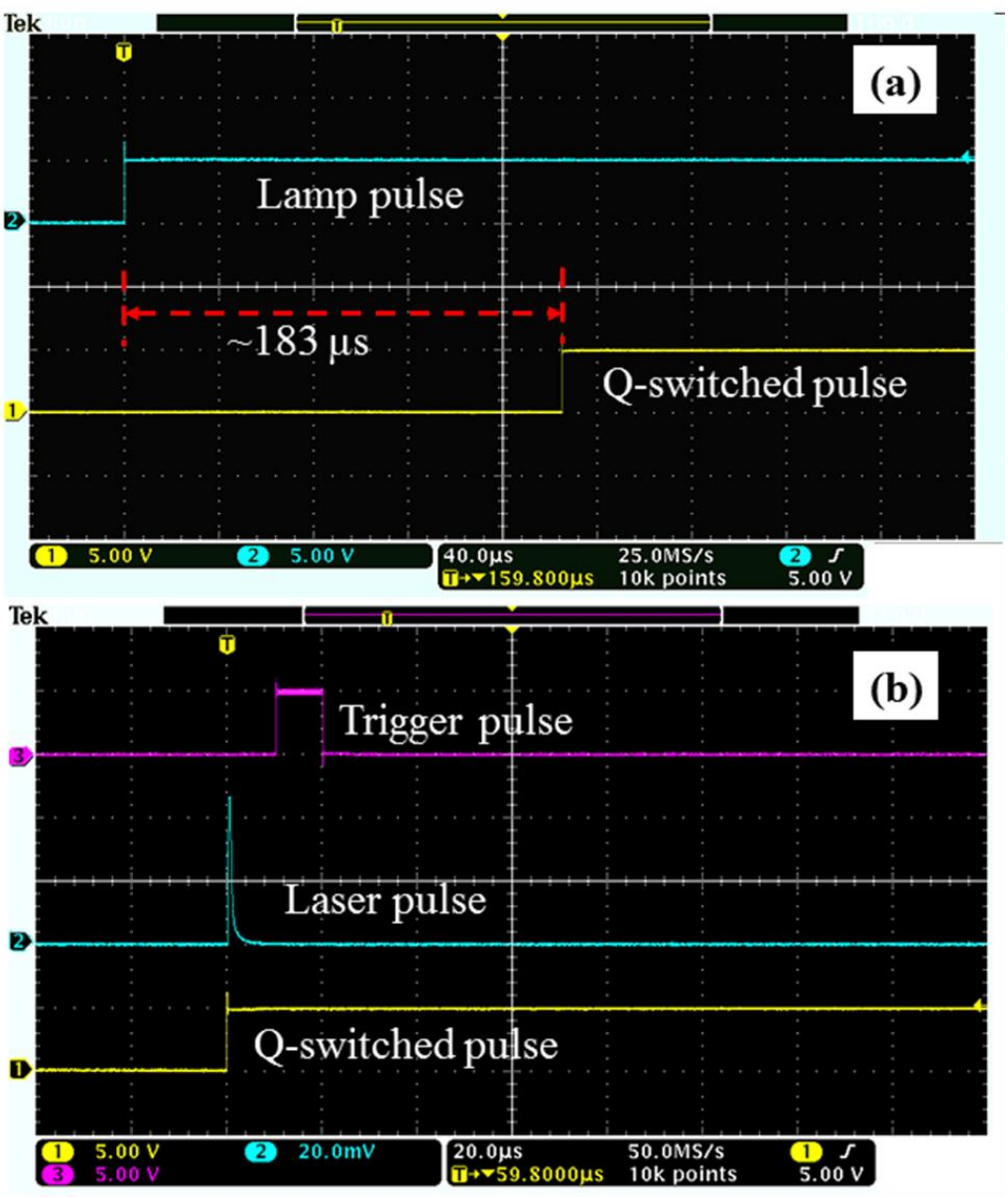

Figure 2.6 *Oscilloscope trace of* **(a)** *the Lamp pulse and Q-switched pulse of the laser;* **(b)** *scheme used for triggering the CCD.*

2.5.2 Laser beam deflection technique

The principle of the beam deflection technique involves the deflection of a probe beam due to a refractive index gradient of the medium lying in its path. This deflection of the probe beam is recorded by a position-sensitive detector [10, 17]. Using this technique, the entire time evolution of the SW and cavitation bubble can be obtained in a single shot of laser [18].

The schematic and the photograph of the beam deflection setup employed for the study of the cavitation bubbles and the SWs are shown in Fig. 2.7 and Fig. 2.8, respectively. The basic arrangement for the generation of laser induced plasma of the target in DW is same as that of described in section 2.5.1, shadowgraphy technique. The only difference is in the way the probe beam is launched and detected. In the laser beam deflection technique, a photodiode is used as the detector replacing the CCD camera of the shadowgraphy setup.

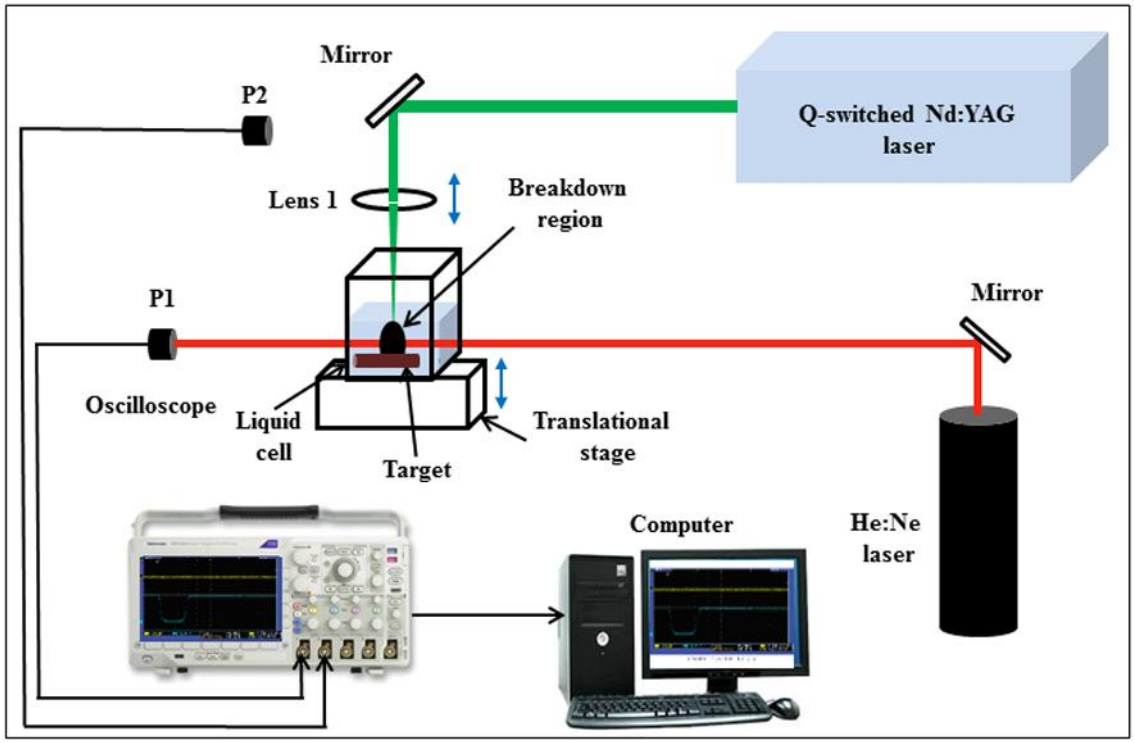

Figure 2.7 *Schematic of the beam deflection setup.*

In the beam deflection setup, the He:Ne laser beam (probe beam) is directly made to fall onto a photodiode, P1 (Model: 13 DSI 001) which is aligned so that the

centre of the beam falls on it giving the maximum signal. The size of the probe beam is 0.65 mm (beam diameter $1/e^2$) and the active region of the photodiode is 0.31 mm^2. The photodiode signal is displayed onto a DSO (through a 50 Ω terminator) interfaced to a computer. The DSO was triggered with the Nd:YAG laser pulse (employed for the generation of laser induced plasma) through another identical photodiode (P2). For this, a scattered signal at 532 nm of the incident laser was made to fall on P2 and displayed on the other channel of the DSO along with the signal from P1.

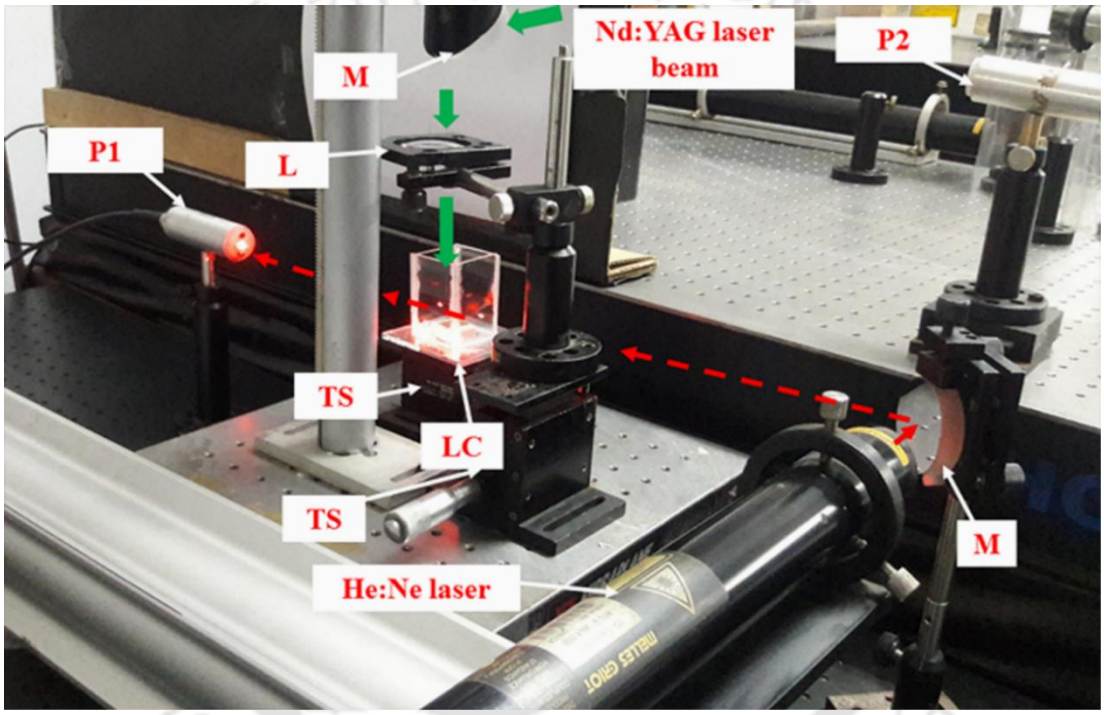

Figure 2.8 *Photograph of the beam deflection setup; P: Photodiode, M: mirror, L: lens, LC: liquid cell, TS: translation stage.*

As the probe beam passes through the breakdown region, the formation of the cavitation bubbles and the SWs induces deflection in the probe He: Ne beam due to the change in the refractive index of the surrounding medium resulting in the change in the intensity of the probe beam falling on P1 and hence there is a modulation in its signal. One such signal from the beam deflection setup along with the laser pulse recorded at a distance of 1 mm from the target in the direction of plasma expansion is shown in Fig. 2.9. Careful analysis of this deflection in the probe beam can give information about the

dynamic behaviour of the bubbles and the SWs. In the Fig. 2.9(a), the primary and secondary cavitation bubbles are marked in the beam deflection signal. The trigger pulse is also shown in this figure. The expanded view of the beam deflection signal (circled in red) in the initial stage is shown in Fig. 2.9(b). The small deflection in this signal corresponds to the SW emitted immediately after the plasma formation. A detailed analysis of the SWs using beam deflection setup is given in chapter 6.

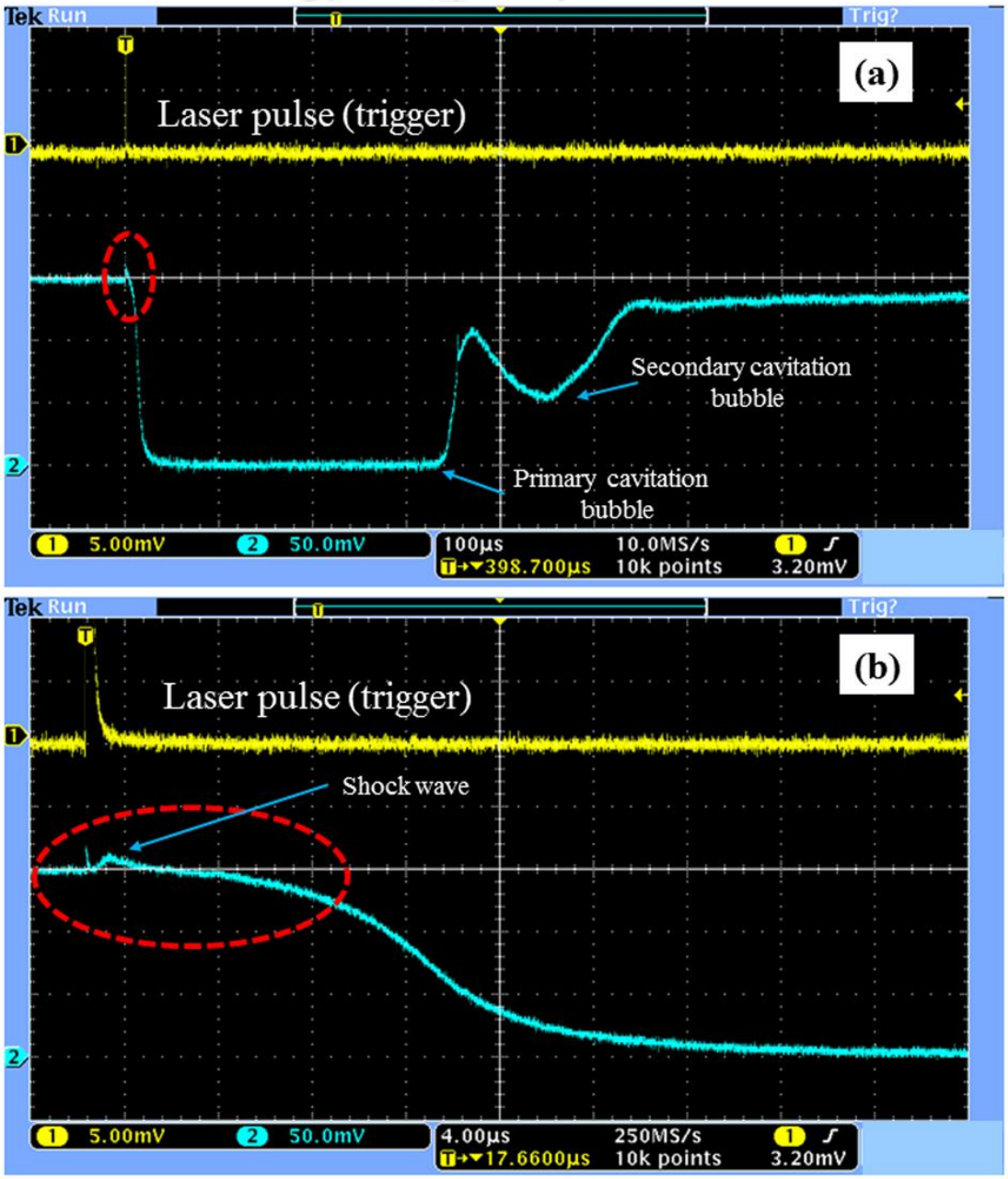

Figure 2.9 (a) *DSO trace showing the modulation in the beam deflection signal,* **(b)** *the same in an expanded scale.*

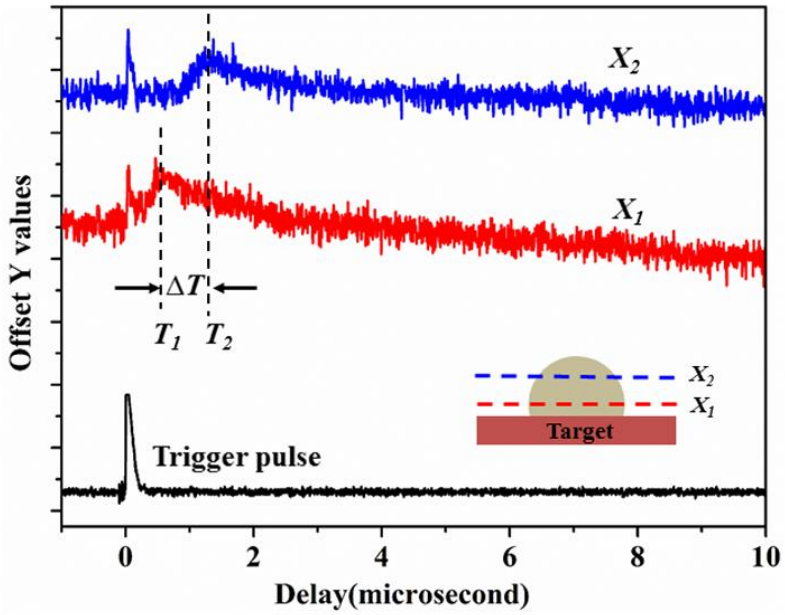

Figure 2.10 *Beam deflection signal as a function of time at different positions from the target; the inset shows the positions schematically.*

The measurement of the SW velocity using this technique can be performed by considering the modulation in the He:Ne probe beam at different positions w. r. t. the target surface as shown in Fig. 2.10. For this, the target as well as the lens, L1, were moved simultaneously along the direction of the source Nd:YAG laser beam and the deflection was recorded as a function of distance from the target. Fig. 2.10 shows the expanded view of the signal recorded at two distances from the target, say X_1 and X_2. As shown in the Fig. 2.10, ΔT is the difference between the delay time T_1 and T_2, w. r. t. the trigger pulse at positions X_1 and X_2, respectively. From ΔT and ΔX, the velocity of the SW can be measured easily.

2.6 Experimental details for the application of the nanoparticles

The NPs synthesized via PLAL technique were tested for its viability as SERS substrate as well as its antibacterial activity. The experimental details for these applications of the PLAL synthesized NPs are presented in the following subsections.

2.6.1 Surface enhanced Raman scattering (SERS) application of PLAL synthesized nanoparticles of Cu and Ag

The SERS activity of both Cu as well as Ag NPs was tested on a bioactive furanoflavonoid, karanjin. In order to check the SERS capability of the Cu NPs, samples C3-C5, as listed in table 2.1, for which a uniform size distribution was obtained were used as the substrate. For the Ag NPs, all the five samples, A1-A5 (listed in table 2.2) having uniform size distribution were used.

2.6.1.1 Preparation of karanjin

Karanjin was isolated from ethyl acetate crude extract by column chromatography using hexane-ethyl acetate eluent system [19]. The compound was purified and the retardation factor, R_f value of karanjin was found to be 0.44 in 15% hexane-ethyl acetate eluent system. After crystallization, white needle-shaped crystals were obtained. The crystals were washed with hexane and binary solvent mixture (ethyl acetate and hexane). Finally, the karanjin crystals were dissolved in dimethyl sulphoxide (DMSO) to obtain a concentration of ~ 2 mg/mL.

2.6.1.2 SERS measurements

To test the SERS response, 10 µL of karanjin solution was mixed with 500 µL of each of the synthesized samples of Cu and Ag NPs separately. After addition, the solutions were sonicated to ensure the uniform mixing and then drop casted onto Si wafers, dried and subjected to the Raman spectrophotometer with an excitation wavelength of 488 nm to record the Raman spectra. The Raman spectra of pure karanjin and that of karanjin treated with the different samples of the NPs were recorded over various location on each of the samples. The presence of the NPs in the proximity of the analyte, karanjin, was verified using the TEM.

2.6.2 Antibacterial applications of PLAL synthesized nanoparticles of Cu and Ag

Delicate materials such as silk are very important in the textile industry and there is a need to devise methods to protect such materials against bacterial contamination. There is a similar need to devise easy and convenient methods to rid drinking water, especially during emergencies, from harmful pathogenic bacteria. In the present work, the antibacterial activity of the Cu and Ag NPs was tested to act as a protective layer for natural silk and also in the treatment of filter paper for the annihilation of bacteria from contaminated drinking water. For these studies, the samples C5 and A5, listed in table 2.1 and 2.2, respectively, were taken pertaining to their high concentration.

2.6.2.1 Natural silk treated with nanoparticles

The effect of treatment of Cu and Ag NPs on three common silks, viz., Eri, Pat and Muga which are locally available in the North-eastern part of India, were studied to check its antibacterial activity. These silks are woven from the silkworms *Philosomia ricini*, *Bombyx mori* and *Antheraea assamensis*, respectively.

2.6.2.1.1 Preparation of silk pellets

The threads of Eri, Pat and Muga silk were purchased from local market and shredded into very fine pieces separately. The stages of the preparation of the pellets is pictorially represented in Fig. 2.11.

The fine pieces of each and every type of silk were ground separately in a mortar and a pestle until all the pieces were smudged thoroughly which gave the appearance of a cotton-like texture. These samples were put in a KBr Die maker and a pressure of about 60 kg/cm^2 was applied on it to make their pellet.

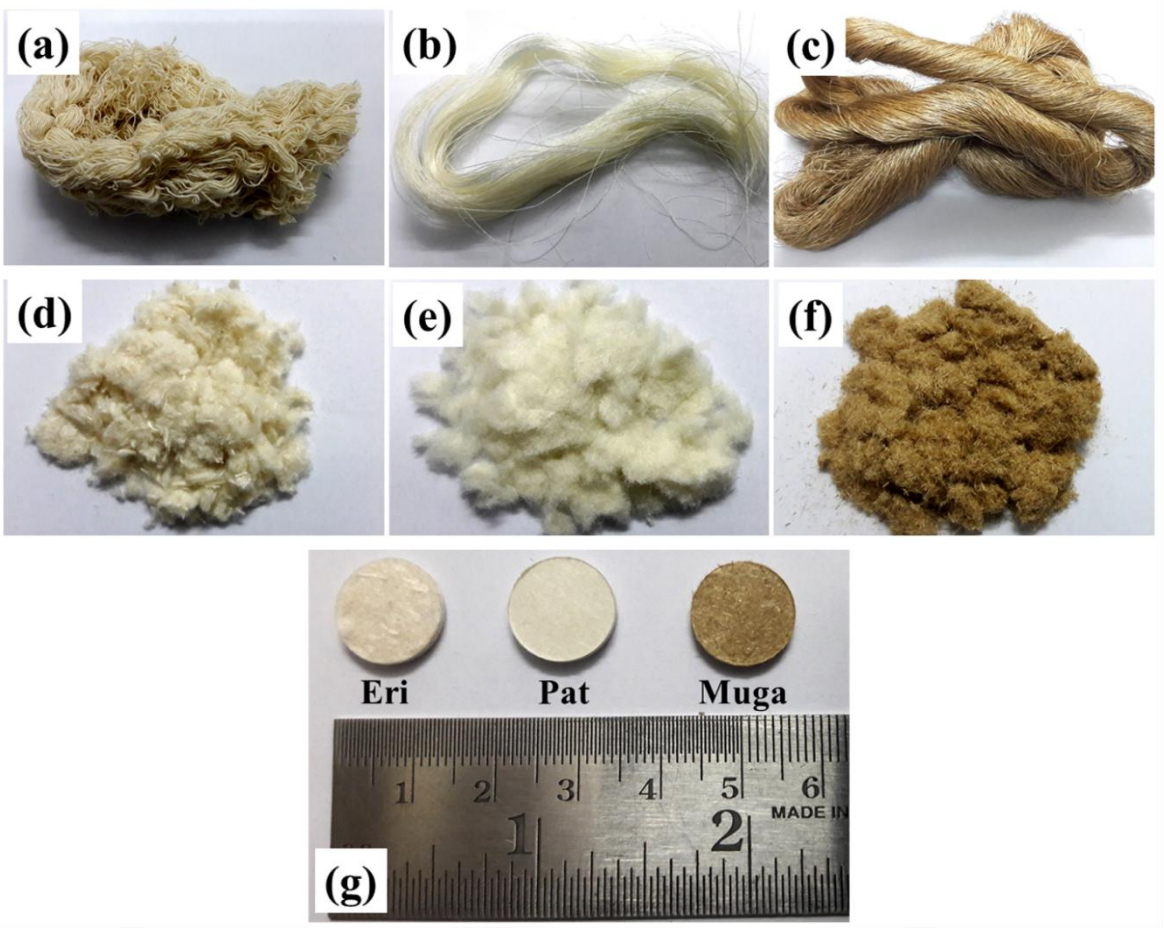

Figure 2.11 (a)-(c) *Threads of Eri, Pat and Muga silk*; **(d)-(f)** *cut and ground pieces of the respective silk threads*; **(g)** *final form of the silk pellets.*

2.6.2.1.2 Agar diffusion test for bactericidal testing on nanoparticle treated silk

The prepared pellets of the silks were dipped in the colloidal solutions of the NP samples C5 and A5 separately for its attachment to the silk. The antibacterial activities of the silk pellets were tested on gram positive, *Staphylococcus aureus* (ATCC 6538) bacteria using agar diffusion method. The agar was poured in petri plates and solidified in laminar air flow. Bacterial culture of 100 µl was spread on the agar using a spreader and the NP treated silk pellets were placed in it.

In order to confirm the validity of the results obtained in the Agar test, the following standard procedure was adopted. Two wells were made in agar after the bacteria was spread and water was poured in one of them as negative control and 10 µL of Kanamycin (antibiotic, 25 µg/mL) was put in the other as positive control. These petri

plates were incubated at 37°C for 24 hours. In general, no inhibition zone around the negative control and maximum inhibition zone around the positive control after incubation is expected for a correct test. In order to compare the antibacterial activity of Cu and Ag NPs, the entire procedure was repeated separately for untreated silk pellets.

2.6.2.2 Antibacterial efficacy of filter paper treated with nanoparticles

The antibacterial activity of the NPs was also tested in the treatment of filter paper for the annihilation of bacteria in contaminated water.

2.6.2.2.1 Preparation of Cu and Ag nanoparticle treated filter paper

The efficiency of the method of treatment of the filter papers with the synthesized NPs of Cu and Ag in removing the bacteria from contaminated water was tested in the following way. The cellulose filter papers (Whatman Grade 1, 98% alpha-cellulose content) were placed in two separate borosilicate glass petri plates. The colloidal solutions each of Cu and Ag NP samples, C5 and A5 were uniformly poured over the separate filter papers until the papers were completely dipped in the solution. The petri plates were then heated by placing on a hot plate in order to evaporate the water from it. A small piece of each dried filter paper was then subjected to FESEM to confirm the adhesion of the NPs onto the papers.

2.6.2.2.2 Antibacterial test on nanoparticle treated filter paper

To examine the bactericidal efficacy of the NPs attached to the cellulose filter papers, two common pathogenic bacteria, one gram positive, *Staphylococcus aureus*, and a gram negative bacteria, *Escherichia coli* (MTCC 723) were used. The NP treated papers were folded in the form of a cone and placed on a filter funnel. Active log phase culture (Optical density 0.6 corresponding to approximately 10^6 cells CFU) was diluted 10 fold with autoclaved distilled water and 5 mL of such bacteria contaminated water was passed through the filters. A small amount of each filtrate was then distributed uniformly on petri plates containing nutrient agar to check for the growth of colonies of bacteria.

Also, the bacteria that came in contact with the NPs were scooped from the filter paper and were inoculated in fresh nutrient media. The growth kinetics of the bacteria in these solutions were observed for 24 hours at an interval of 2 hours by measuring the optical density at 600 nm. For comparison, the same procedure was also adopted for untreated filter paper. To ascertain the condition of the bacteria upon coming into contact with the NPs, the bacteria that were passed through NP treated filter papers as well as the ones that were passed through untreated filter papers were subjected to the FESEM.

2.7 Conclusion

In this chapter, the experimental setup for the synthesis of NPs via PLAL and the formation of laser induced crater is described in detail. In addition, various characterization tools adopted for the analysis of the NPs have also been summarized. The experimental details with regard to the study of the dynamics of the process of cavitation bubbles and SWs is elucidated. Finally, the details of the application of the synthesized NPs in the SERS and antibacterial studies have been outlined.

References

[1] G. Yang, Laser ablation in liquids: applications in the synthesis of nanocrystals, Progress in Materials Science, **52** (2007) 648-698.

[2] H. Zeng, X.W. Du, S.C. Singh, S.A. Kulinich, S. Yang, J. He, W. Cai, Nanomaterials via laser ablation/irradiation in liquid: a review, Advanced Functional Materials, **22** (2012) 1333-1353.

[3] Z. Yan, D.B. Chrisey, Pulsed laser ablation in liquid for micro-/nanostructure generation, Journal of Photochemistry and Photobiology C: Photochemistry Reviews, **13** (2012) 204-223.

[4] D. Zhang, B. Gökce, S. Barcikowski, Laser synthesis and processing of colloids: fundamentals and applications, Chemical reviews, **117** (2017) 3990-4103.

[5] G. Yang, Laser ablation in liquids: principles and applications in the preparation of nanomaterials, CRC Press, 2012.

[6] V. Amendola, M. Meneghetti, What controls the composition and the structure of nanomaterials generated by laser ablation in liquid solution?, Physical Chemistry Chemical Physics, **15** (2013) 3027-3046.

[7] C.G. Moura, R.S.F. Pereira, M. Andritschky, A.L.B. Lopes, J.P. de Freitas Grilo, R.M. do Nascimento, F.S. Silva, Effects of laser fluence and liquid media on preparation of small Ag nanoparticles by laser ablation in liquid, Optics & Laser Technology, **97** (2017) 20-28.

[8] E. Solati, M. Mashayekh, D. Dorranian, Effects of laser pulse wavelength and laser fluence on the characteristics of silver nanoparticle generated by laser ablation, Applied Physics A, **112** (2013) 689-694.

[9] S. Reich, P. Schönfeld, P. Wagener, A. Letzel, S. Ibrahimkutty, B. Gökce, S. Barcikowski, A. Menzel, T. dos Santos Rolo, A. Plech, Pulsed laser ablation in liquids: Impact of the bubble dynamics on particle formation, Journal of colloid and interface science, **489** (2017) 106-113.

[10] J. Chen, X. Li, Y. Gu, H. Wang, X. Song, H. Zeng, Probing mesoscopic process of laser ablation in liquid by integrated method of optical beam deflection and time-resolved shadowgraphy, Journal of colloid and interface science, **489** (2017) 38-46.

[11(a)] A. Nath, A. Khare, Transient evolution of multiple bubbles in laser induced breakdown in water, Laser and Particle Beams, **29** (2011) 1-9.

[11(b)] C.H. Bae, S.H. Nam, S.M. Park, Formation of silver nanoparticles by laser ablation of a silver target in NaCl solution, Applied Surface Science, **197** (2002) 628-634.

[12] M. Dell'Aglio, R. Gaudiuso, O. De Pascale, A. De Giacomo, Mechanisms and processes of pulsed laser ablation in liquids during nanoparticle production, Applied Surface Science, **348** (2015) 4-9.

[13] S. Ibrahimkutty, P. Wagener, T. dos Santos Rolo, D. Karpov, A. Menzel, T. Baumbach, S. Barcikowski, A. Plech, A hierarchical view on material formation during pulsed-laser synthesis of nanoparticles in liquid, Scientific reports, **5** (2015) 16313.

[14] R. Tanabe, T.T. Nguyen, T. Sugiura, Y. Ito, Bubble dynamics in metal nanoparticle formation by laser ablation in liquid studied through high-speed laser stroboscopic videography, Applied Surface Science, **351** (2015) 327-331.

[15] T. Tsuji, Y. Tsuboi, N. Kitamura, M. Tsuji, Microsecond-resolved imaging of laser ablation at solid–liquid interface: investigation of formation process of nano-size metal colloids, Applied Surface Science, **229** (2004) 365-371.

[16] J. Lam, J. Lombard, C. Dujardin, G. Ledoux, S. Merabia, D. Amans, Dynamical study of bubble expansion following laser ablation in liquids, Applied Physics Letters, **108** (2016) 074104.

[17] P. Gregorcic, J. Mozina, A beam-deflection probe as a method for optodynamic measurements of cavitation bubble oscillations, Measurement Science and Technology, **18** (2007) 2972.

[18] P. Gregorčič, R. Petkovšek, J. Možina, Investigation of a cavitation bubble between a rigid boundary and a free surface, Journal of Applied Physics, **102** (2007) 094904.

[19] A. Singh, I. Jahan, M. Sharma, L. Rangan, A. Khare, A.N. Panda, Structural Characterization, In Silico Studies and In Vitro Antibacterial Evaluation of a Furanoflavonoid from Karanj, Planta Medica Letters, **3** (2016) e91-e95.

Chapter 3

Synthesis and Characterization of $Cu@Cu_xO$ Nanoparticles

3.1 Introduction

Copper (Cu) nanoparticles (NPs) exhibit localized surface plasmon resonance (LSPR) in the visible region of the electromagnetic spectrum which has led to its implementation in many plasmonic applications [1-3]. Both Cu as well as its oxides have been found to be extremely useful. Some of these applications include plasmonic sensor, photocatalyst, ink-jet printed electronic, gas sensor, etc. [2, 4-8]. The plasmonic response of the NPs are highly dependent on the size, structure and also on the surrounding medium [9, 10]. Hence, tailoring the properties of plasmonic NPs has been an active area of research. Size and structure of the NPs can be controlled by various techniques [11, 12], but considering the versatility of the technique of pulsed laser ablation in liquid (PLAL), as discussed in section 1.3 with the large pool of adjustable parameters including laser wavelength, pulse duration, laser energy, surrounding liquid medium, etc., PLAL has gone a long way in this direction [13, 14]. Using the technique of PLAL, Muniz-Miranda *et al.* reported the characterization of Cu NPs synthesized as a function of laser wavelength [15]. It was reported that laser wavelength of 1064 nm is more efficient in particle production while 532 nm results in reduced particle size due to photo-fragmentation. The work of Santillan *et al.* elaborately discusses the formation of core-shell Cu oxide NPs synthesized by femtosecond laser ablation of Cu in acetone and water [16]. Nath *et al.* varied the laser focussing conditions and were able to achieve structural modification of Cu oxide NPs [17]. However, no definite control over the size and surface plasmon resonance (SPR) have been reported till date. Although there are few more reports on the effect of laser

parameters on the properties of Cu NPs, but a proper correlative study on the SPR and its size and also on the oxidation of Cu NPs is not well documented [18]. This motivates the work described in the present chapter which emphasises on the determination of a set of laser parameters so as to obtain a good control over the particle size, plasmonic response and stoichiometry of Cu@Cu_xO NPs.

Starting exactly from this, Cu@Cu_xO NPs were synthesized by pulsed laser ablation of a Cu target immersed in distilled water (DW). The choice of DW as the liquid was made in order to avoid any unwanted impurities in the synthesized NPs. Laser ablation duration and incident laser energy were varied to tune the properties of the NPs. An attempt to correlate the SPR behaviour of these NPs and its size was undertaken. The process of oxidation of the synthesized NPs during its synthesis and its dependence on the various parameters have also been reported.

3.2 Experimental details

The NPs of Cu were synthesized by the pulsed laser ablation of Cu in DW, as described in section 2.2. Five samples of Cu NPs were synthesized by varying the laser ablation duration as well as its energy. These are listed in table 3.1.

Table 3.1 *Nanoparticle samples prepared under different conditions.*

Sample	Laser energy (mJ)	Duration (minutes)
C1	30	**15**
C2	30	**30**
C3	**30**	**60**
C4	**50**	60
C5	**70**	60

The first three samples C1-C3 were prepared by varying the ablation duration for 15, 30 and 60 minutes, respectively while keeping the laser energy fixed at 30 mJ. Then, in line

with sample C3, samples C4 and C5 were prepared at laser energies of 50 and 70 mJ, respectively for a fixed ablation duration of 60 minutes. Here, the reason for fixing the ablation as 60 minutes will be discussed in section 3.3.3. Thus, samples C1-C3 form a series for studying the effect of ablation duration and that of C3-C5 form another set of samples for the effect of incident laser energy on the properties of Cu NPs.

In order to ascertain the mass ablation rate as a function of incident laser energy, the laser ablation of the target was carried out at laser energies of 30, 50 and 70 mJ, respectively. For this, repeated shots of laser were fired at the same location for one minute to produce a prominent crater for the ease of measurement. For the characterization of Cu@Cu_xO NPs the colloidal solution of the samples (C1-C5) were drop casted onto carbon coated Cu grids for the transmission electron microscope (TEM) measurements. For the Raman analysis, the colloidal solutions were drop casted onto glass coverslips and the Raman spectra were recorded at an excitation wavelength of 488 nm. The samples were also drop casted onto Silicon wafer and subjected to X-ray diffractometer.

3.3 Results and discussion

3.3.1 Formation of the nanoparticles

The change in color of the colloidal solution of as-synthesized Cu NPs synthesized via PLAL is clearly displayed in Fig. 3.1. The coloration of water confirms the formation of Cu NPs. The color of the colloidal solution turns darker with the increase in laser ablation duration from the samples C1-C3 implying an increase in the concentration of the Cu NPs, which is mainly due to the fact that more material is ablated from the target with prolonged laser exposure.

In the case of 2nd set of samples, C3-C5, synthesized with increasing incident laser energies, the color of the colloidal solution is observed to become darker from sample C3 to C5. This indicates that the irradiation of the target with higher laser energy facilitates higher degree of ablation of the Cu target and hence an increase in the concentration of NPs. An idea

of the extent of ablation as a function of incident laser energy can be obtained from the estimated mass ablation rate as described in the next section.

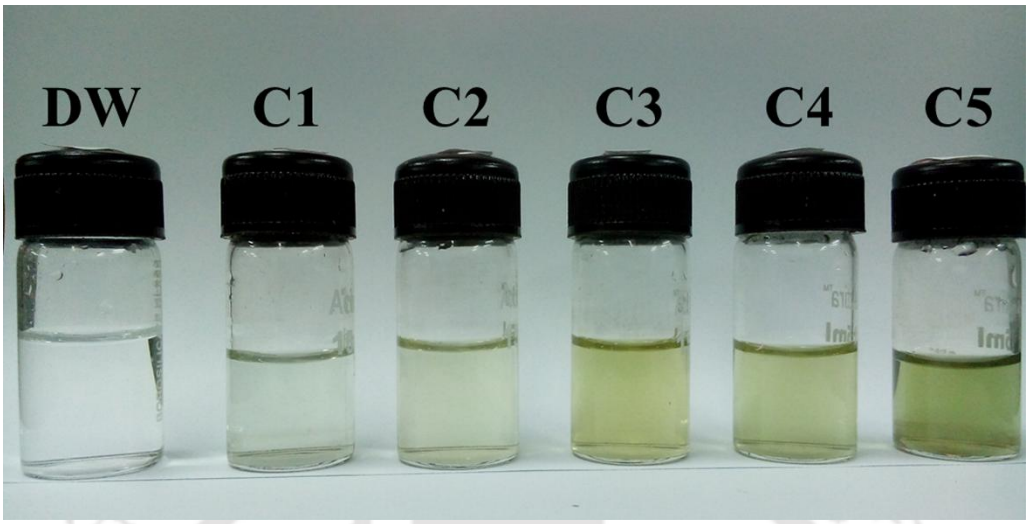

Figure 3.1 *Change in color of the colloidal solution of Cu NPs.*

3.3.2 Estimation of mass ablation rate

The ablation of target via laser, leaves behind its imprint in the form of crater in the focal region. The dimensions of the crater formed can be used to estimate the mass ablated upon incidence of the laser beam. The depth profiles of the crater were extracted along a line that joins two diametrically opposite points on the boundary of the crater as depicted in Fig. 3.2, as an example. Fig. 3.3(a)-(c) show the average depth profile of the crater obtained at laser energies of 30, 50 and 70 mJ, respectively. An increase in the depth of the crater with the increase in incident laser energy is evident from the depth profiles.

The integrated ablated volume of the crater was measured from the surface profilometer. The volumes of the crater produced at 30, 50 and 70 mJ are found to be 5.03×10^6, 7.22×10^6 and 8.75×10^6 μm^3, respectively. This volume was eventually used to assess the mass of the material ablated from the target and hence the mass ablation rate (mass ablated per laser shot).

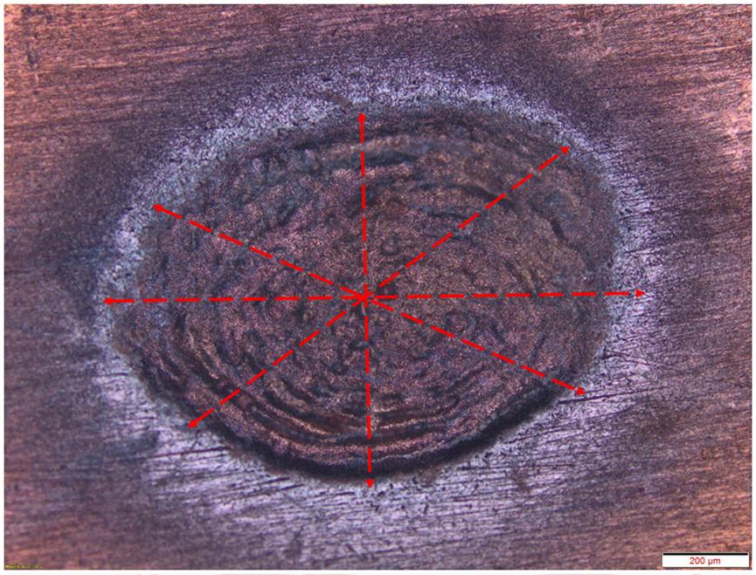

Figure 3.2 *Optical micrograph of a laser produced crater showing lines joining diametrically opposite points for extraction of depth profiles.*

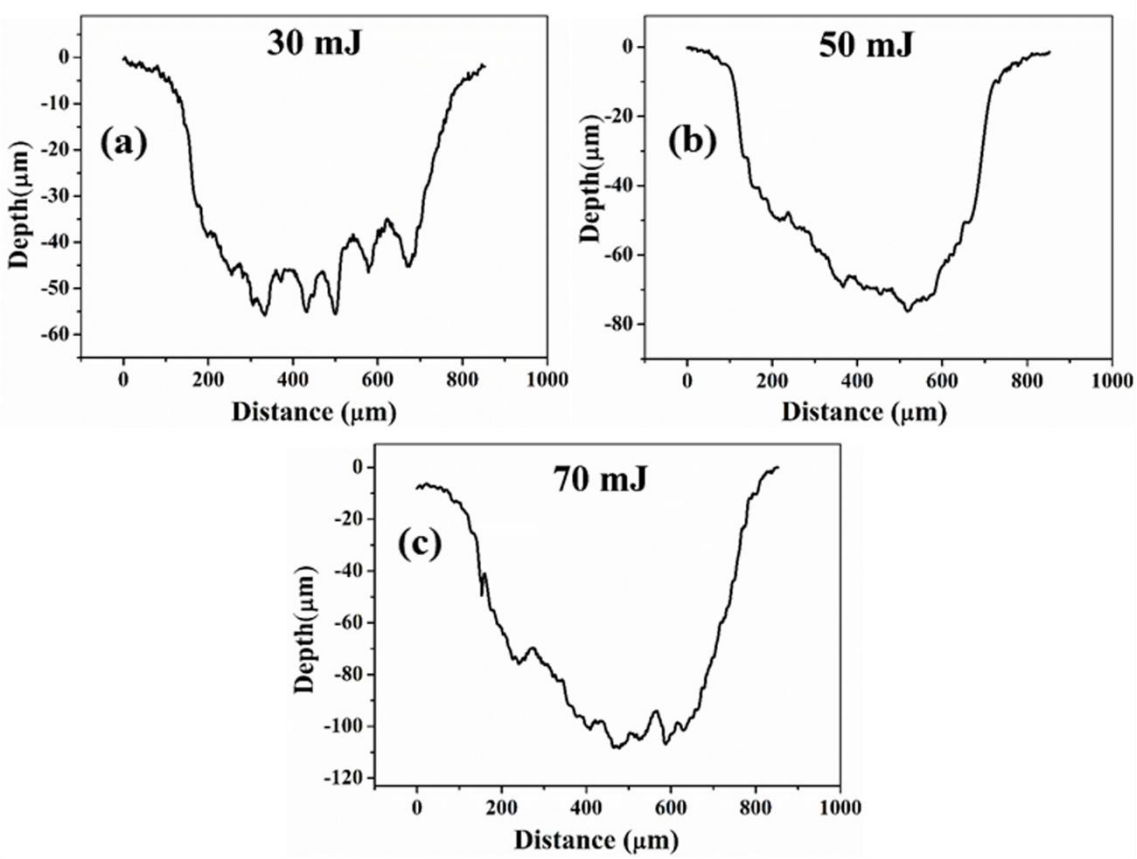

Figure 3.3 *Depth profiles of crater produced at* **(a)** *30 mJ,* **(b)** *50 mJ and* **(c)** *70 mJ.*

The plot of the ablation rate (μg/shot) versus the incident laser energy, Fig. 3.4, shows that the ablation rate increases with the increase in laser energy. The increased ablation rate is

responsible for the release of more material at high fluence from the Cu target into the surrounding liquid and therefore the concentration of the synthesized NPs increases.

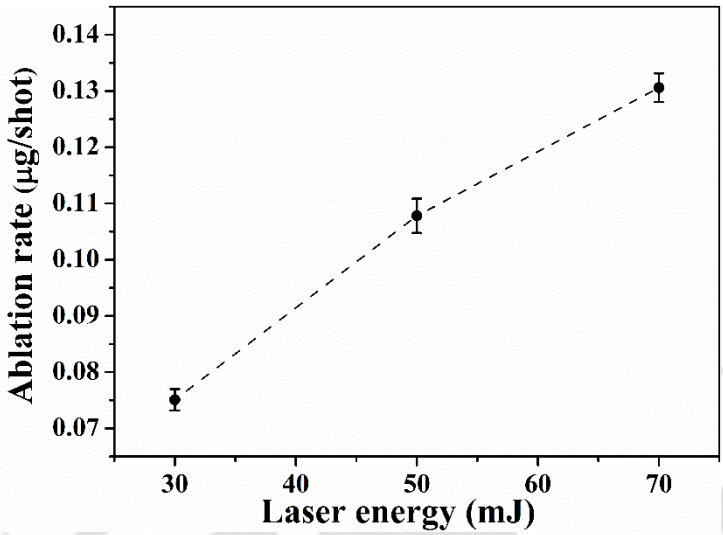

Figure 3.4 *Variation of ablation rate as a function of incident laser.*

3.3.3 Particle size analysis by transmission electron microscope

The TEM images of samples C1-C5 are shown in Fig. 3.5(a)-(e), respectively along with the particle size distribution for C3-C5 in the respective insets. For sample C1, the shape of the particles is nearly spherical and dominated by bigger particles having size in the range of 40-50 nm along with appearance of small sized particles. For C2, the particles are in agglomerated form with a mixture of mostly small and a few large sized particles. This gives an idea that the larger particles already formed initially are fragmented due to the incidence of repeated laser pulse for longer duration of time. However, for C1 and C2, the observed high agglomeration among the particles makes it difficult to obtain the precise size distribution of the particles. In Fig. 3.5(c), for sample C3, it is observed that with the increase in laser ablation duration upto 60 minutes, the particles formed are much more distinct compared to previous two samples. The particle size distribution is shown in the inset and the average size is found to be ~ 20 nm.

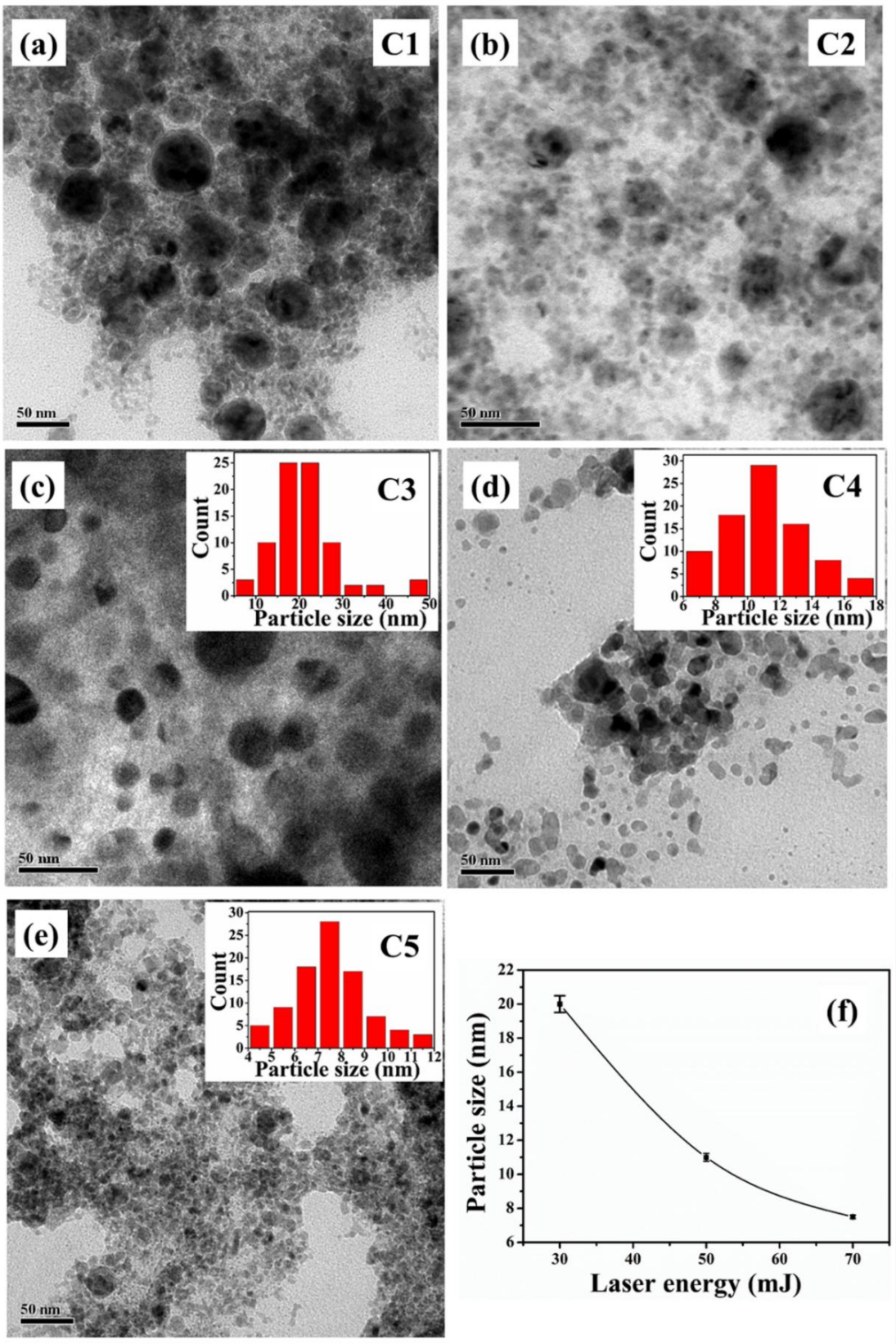

Figure 3.5 (a)-(e) *TEM image of samples C1-C5 with the particle size distribution shown in the inset for C3-C5,* **(f)** *Variation of average particle size with the increase in incident laser energy.*

Thus, the size of the NPs decreases with the increase in laser ablation duration. This may be due to the redistribution of the size of the particles through longer interaction with the laser beam [19]. For longer ablation duration, as the number of laser pulses hitting the target increases, the number of NPs formed is increased. After sometime, this number becomes sufficiently high and the NPs obstruct the laser beam reaching the target further. At this stage, the laser energy is absorbed by the already formed NPs resulting in its heating. As a result of this, there is an increase in the temperature of the particles followed by its melting and fragmentation into small sized particles [20]. Thus, distinct particles are formed with nearly uniform distribution for an ablation time of 60 minutes.

From Fig. 3.5(d) and (e), the average particle size of samples C4 and C5 is found to be ~ 11 and 7 nm, respectively. This decrease in the average size of the NPs with the increase in the incident laser energy is represented graphically in Fig. 3.5(f). From the particle size analysis via TEM, it is observed that there is a decrease in the average particle size with the increase in laser energy which can be attributed to three main reasons. Firstly, the larger kinetic energy of the particles at higher incident laser energy increases collision among the initially formed larger particles in the condensation process leading to a decrease in size [21]. Secondly, the size reduction may occur due to the melting and subsequent vaporization of the initially formed larger NPs. The large absorption of laser energy by the NPs and less heat dissipation to the surrounding liquid medium leads to rise in temperature in the particles which is expected to be more probable for higher laser energies [22]. Finally, fragmentation of NPs may also occur due to the accumulation of photo-ejected electrons near the surface of the NPs facilitating the disintegration of the initially formed NPs because of charging [23]. Normally it is difficult to pin point the exact process of fragmentation of the NPs to smaller size at high energy as all the three processes are equally probable.

3.3.4 Structural and compositional studies

3.3.4.1 SAED and HRTEM analysis

The SAED patterns of the samples C1-C5 are shown in Fig 3.6(a)-(e), respectively.

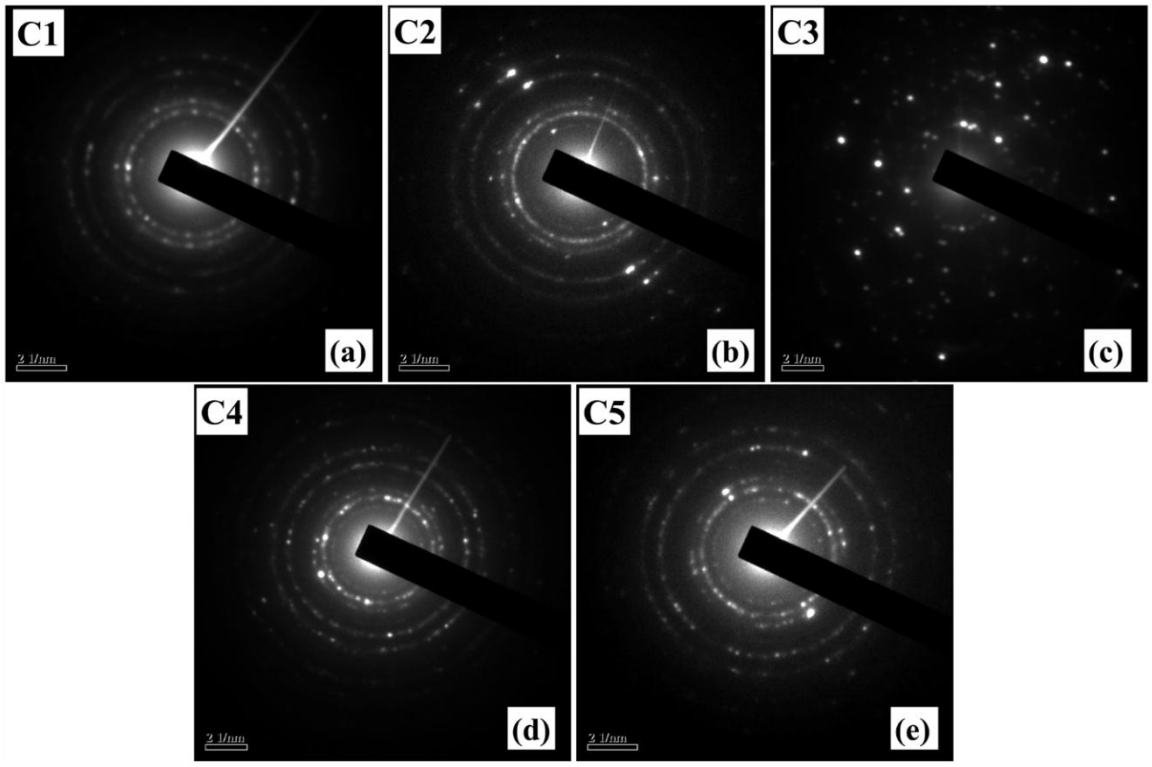

Figure 3.6 (a)-(e) *SAED patterns of samples C1-C5, respectively.*

Table 3.2 *Lattice d-spacing of synthesized NPs calculated from SAED patterns along with the corresponding planes.*

		Observed in sample				
***hkl* plane**	***d* (nm)**	**C1**	**C2**	**C3**	**C4**	**C5**
Cu(111)	0.20	✓	✓	✓	✓	✓
$Cu_2O(220)$	0.16	✓	-	-	-	-
$Cu_2O(211)$	0.17	-	✓	-	-	-
$Cu_2O(111)$	0.24	✓	✓	✓	-	-
$Cu_2O(110)$	0.32	✓	✓	-	✓	✓
$CuO(11\bar{3})$	0.15	-	-	✓	✓	-
CuO(200)	0.23	-	-	-	✓	✓

For a bird's eye view, the inter-planar spacings denoted by the *d*-values along with the corresponding lattice planes for samples C1-C5 are listed in table 3.2. From the table, it is observed that for samples C1 and C2, there is formation of Cu as well as Cu_2O phase of NPs, with the latter phase being the dominant one. On the other hand, for sample C3, in addition to Cu and Cu_2O there is an emergence of CuO phase. The presence of CuO for higher ablation duration at fixed laser energy indicates that the Cu NPs get more oxidized with longer duration of laser ablation in DW.

Another intriguing feature observed in the SAED pattern of C3 is an increased crystallinity which is obvious from the distinct diffraction pattern of Fig 3.6(c). The reason for this is unknown but in order to ensure that the recorded pattern is from the Cu NPs itself and not from any impurity, the high resolution TEM (HRTEM) image was also recorded and is shown in Fig. 3.7(a). From the HRTEM and its Inverse Fast Fourier Transform (IFFT) of a selected area for the sample C3, the *d*-value is found to be ~ 0.20 nm corresponding to Cu(111) plane. Thus, the presence of any impurity in the sample is ruled out.

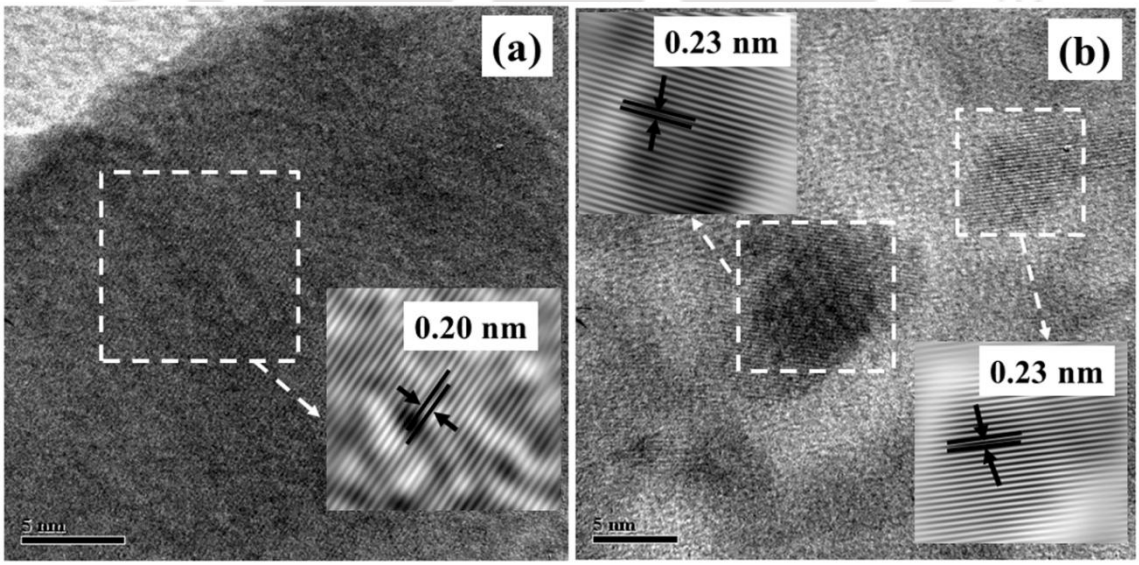

Figure 3.7 *HRTEM image with the IFFT of selected region of samples* **(a)** *C3* and **(b)** *C5*.

For samples C4 and C5, the respective SAED patterns confirm the presence of both Cu_2O and CuO phase along with Cu. The HRTEM image along with the IFFT of selected areas for the sample C5 is shown in Fig. 3.7(b). From this, the *d*-value is found to be ~ 0.23 nm which corresponds to CuO(200) substantiating the diffraction pattern.

The increased duration of ablation as well as increase in laser energy induces the formation of a more oxidized CuO phase of NPs in addition to oxygen deficient phase Cu_2O. Thus, the SAED analysis confirms the formation of Cu@Cu_xO(x=1, 2) NPs in the samples. This is indeed an interesting observation and in order to further confirm it, the synthesized NPs were subjected to Raman spectrophotometer which is expected to throw more light onto the formation of Cu_2O and CuO phases.

3.3.4.2 Raman studies

The Raman spectrum of sample C1, Fig. 3.8(a), shows sharp peaks at 109, 151, and 218 cm^{-1} along with a faint broad peak around 500-550 cm^{-1}. The first three peaks are the clear fingerprints of Cu_2O and are attributed to Γ_{12^-}, $\Gamma_{15^-}^{(1)}$ and $2\Gamma_{12^-}$ bands while the broad peak corresponds to the active Raman mode (T_{2g}) [24, 25].

For sample C2, Fig. 3.8(b), the observed Raman peaks of Cu_2O phase are slightly shifted at 149 and 221 cm^{-1}. Thus, for samples C1 and C2, Raman spectra confirms the formation of Cu_2O and there is no trace of CuO phase, complementing the SAED analysis. For the sample C3, the peaks in Raman shift are at 147, 218 and 292 cm^{-1} as demonstrated in Fig. 3.8(c). While the first two peaks correspond to Cu_2O, the small third peak at 292 cm^{-1} attributed to A_g mode indicates the appearance of CuO [25]. For sample C4, the Raman spectrum in Fig. 3.8(d) shows a small peak at 149 cm^{-1} of Cu_2O with two distinct peaks at 292 and 340 cm^{-1} corresponding to the A_g and B_g modes of CuO, respectively. In the Raman spectrum of sample C5 (Fig. 3.8(e)), two sharp and distinct peaks at 292 and 340 cm^{-1} both corresponding to CuO

are observed but Cu_2O peak is completely absent. This is in slight contradiction with the SAED pattern for sample C5 which showed the presence of Cu_2O phase in addition to CuO phase. The absence of Cu_2O phase in the Raman spectrum is due to its presence in a less detectable amount as most of the Cu atoms ablated from the target gets oxidized to CuO at the high incident laser energy.

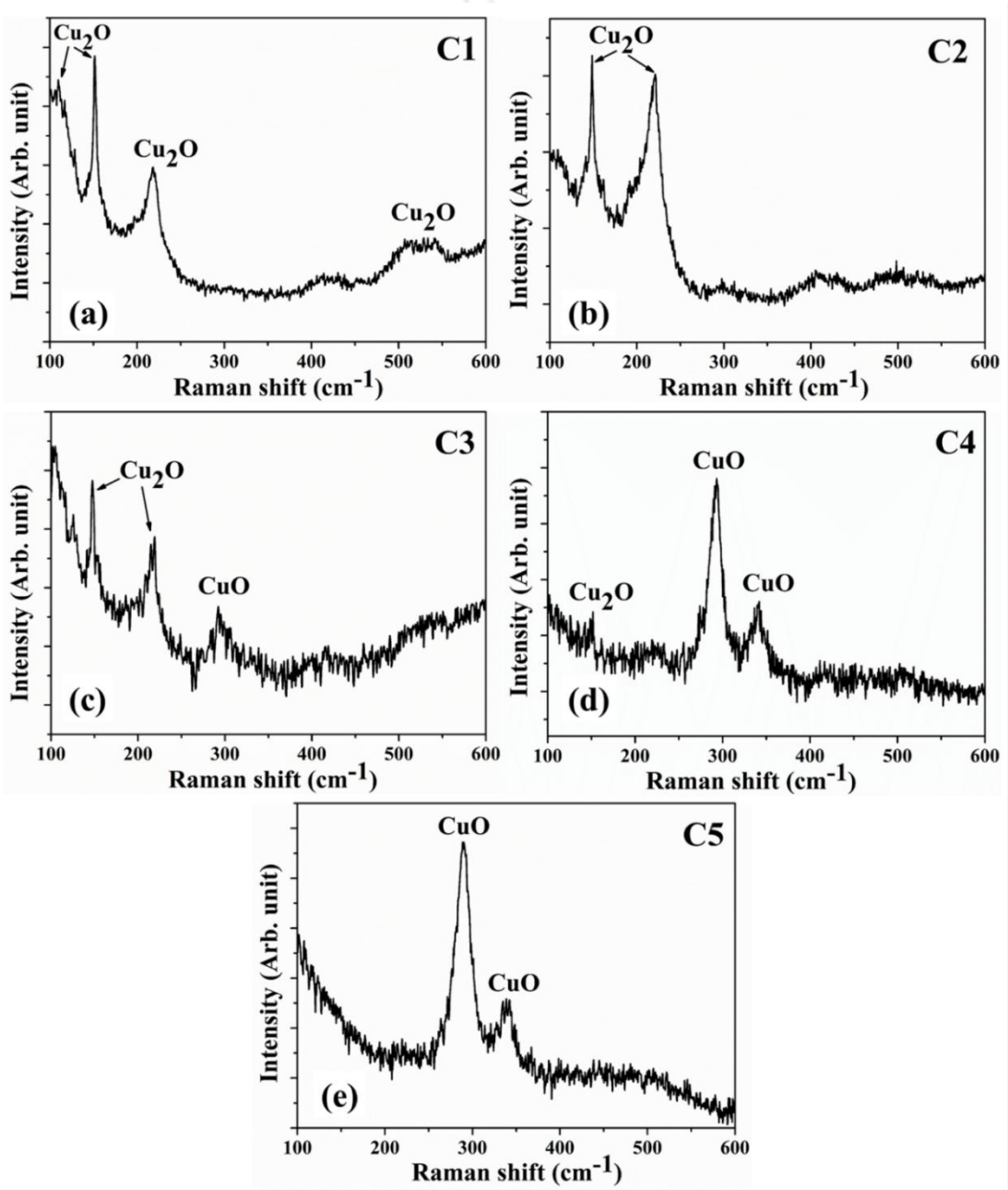

Figure 3.8 (a)-(e) *Raman spectra of Cu NPs samples C1-C5.*

Thus, it is seen that there is presence of Cu_2O and CuO phases of Cu in the samples and depending on the synthesis conditions, a particular phase is found to be dominating. In order to understand the origin of these oxide phases of Cu in a better way, it is important to note their vibrational modes. The zone-center modes for Cu_2O are represented by [25]

$$\Gamma_{Cu_2O} = A_{2u}+E_u+3T_{1u}+T_{2u}+T_{2g} \quad (3.1)$$

Among these various modes, two T_{1u} modes are infrared active, T_{2g} is Raman active, and the others are silent. The Raman active mode (T_{2g} symmetry) involves the relative motion of oxygen ions. For CuO, the zone-center modes are represented by [25, 26]

$$\Gamma_{CuO} = A_g+2B_g+4A_u+5B_u \quad (3.2)$$

Of these, there are three acoustic modes (A_u+2B_u), three Raman active modes (A_g+2B_g) and six IR-active modes (3A_u+3B_u).

Although the mechanism of oxidation of Cu NPs is complex, still from the above study it is observed that for lesser ablation duration, the NPs formed have oxygen deficient Cu_2O as the dominant phase. With the increase in laser ablation duration, there is an appearance of CuO phase in addition to Cu_2O due to more oxidation owing to various chemical processes taking place in PLAL for longer duration. Further, the increase in laser energy, for higher duration of ablation time, corresponds to increased kinetic energy during ablation among the ablated species. Hence, a regime which has higher temperature and pressure due to stronger coupling between the laser beam and the Cu target is formed along with increase in dissociation of water molecule forming higher amount of oxygen ion. These conditions favour the formation of NPs which have the presence of strong CuO phase. Thus, it can be concluded that the stoichiometry of NPs of Cu@Cu_xO can be easily controlled in PLAL by ablation of the Cu target in terms of exposure duration and incident laser energy.

3.3.4.3 XRD analysis

The X-ray diffraction (XRD) patterns for samples, C1-C5 are shown in Fig. 3.9. The observed peak at ~ 44° corresponds to (111) plane of fcc structure of metallic Cu [27]. The presence of this peak in the XRD spectra is in accordance with the SAED patterns but the XRD could not detect any oxide phase of Cu as obtained by the SAED and Raman. This is due to the fact that the oxide layer in the NPs is very thin and hence could not be detected by the XRD. The high resolution of SAED due to the electrons as compared to X-rays is responsible for the detection of even the minutest oxide layer in the SAED patterns of the NPs [28]. The intensity of the peak is found to increase for samples C1-C5 as the concentration of the NPs increases.

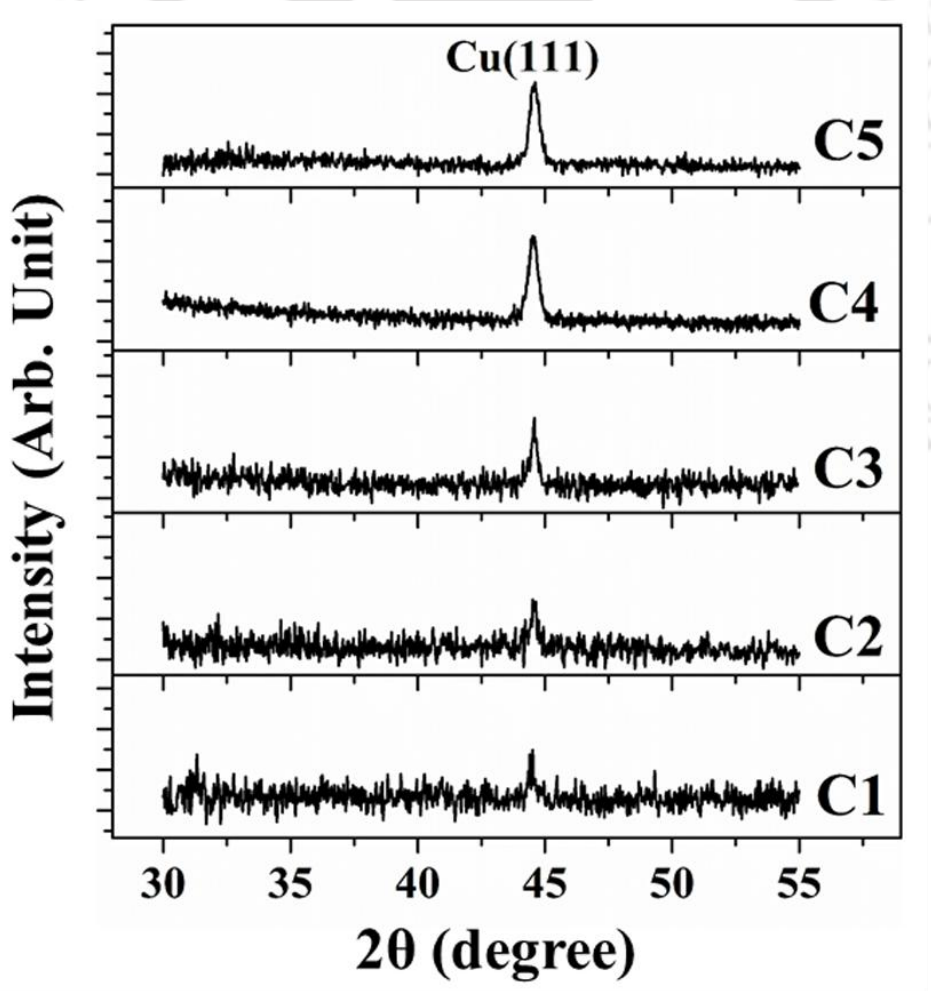

Figure 3.9 *XRD patterns of the samples C1-C5.*

3.3.5 Surface plasmon resonance of the NPs

Fig. 3.10(a)-(e) show the absorption spectra which clearly displays the SPR peak of Cu NPs in the range of 617-641 nm for the samples C1-C5. The SPR peak of Cu usually lies in the range of 550-600 nm [29]. The red shift in the SPR peak in the present case is due to the formation of both Cu as well as Cu oxide NPs due to partial oxidation of Cu in DW during the ablation process [30].

The SPR peak absorbance of the colloidal solutions is found to increase from C1 to C3 which is due to the increase in concentration of the NPs formed with the increase in ablation duration. On closely observing the SPR peak, a blue-shift is seen with the increase in ablation duration from C1-C3. The shift of SPR peak towards shorter wavelength, from ~ 641 to 626 nm, for higher laser ablation duration is due to reduction in size of the NPs as confirmed by the TEM analysis discussed in section 3.3.3 [31, 32]. The SPR bandwidth is also found to increase from ~ 127 to 165 nm. It is worth mentioning here that the SPR peak position and the plasmon bandwidth have been determined by fitting the experimental absorbance plots with a Bi-Gaussian function which is normally employed for asymmetric peaks [33]. The general form of the Bi-Gaussian function is:

$$y = y_0 + H\exp\{-0.5\left(\frac{x - x_c}{w_1}\right)^2\}; x < x_c \tag{3.3}$$

$$y = y_0 + H\exp\{-0.5\left(\frac{x - x_c}{w_2}\right)^2\}; x \geq x_c \tag{3.4}$$

where H, y_0, x_c, w_1 and w_2 are respectively the height, base, centre and widths of the distribution.

From the absorption spectra of the samples C3-C5, the SPR peak position is found to be slightly blue-shifted for samples C3-C5. The peak position is ~ 626 nm for the sample C3 while for that of C4 and C5 the peak positions are at ~ 620 and 617 nm, respectively. SPR bandwidth is found to increase from ~ 165 to 209 nm for samples C3 to C5, respectively. The

blue-shift of the SPR peak position and the broadening of the SPR bandwidth with the increase in laser energy is in accord with the observed decrease in the size of the NPs formed.

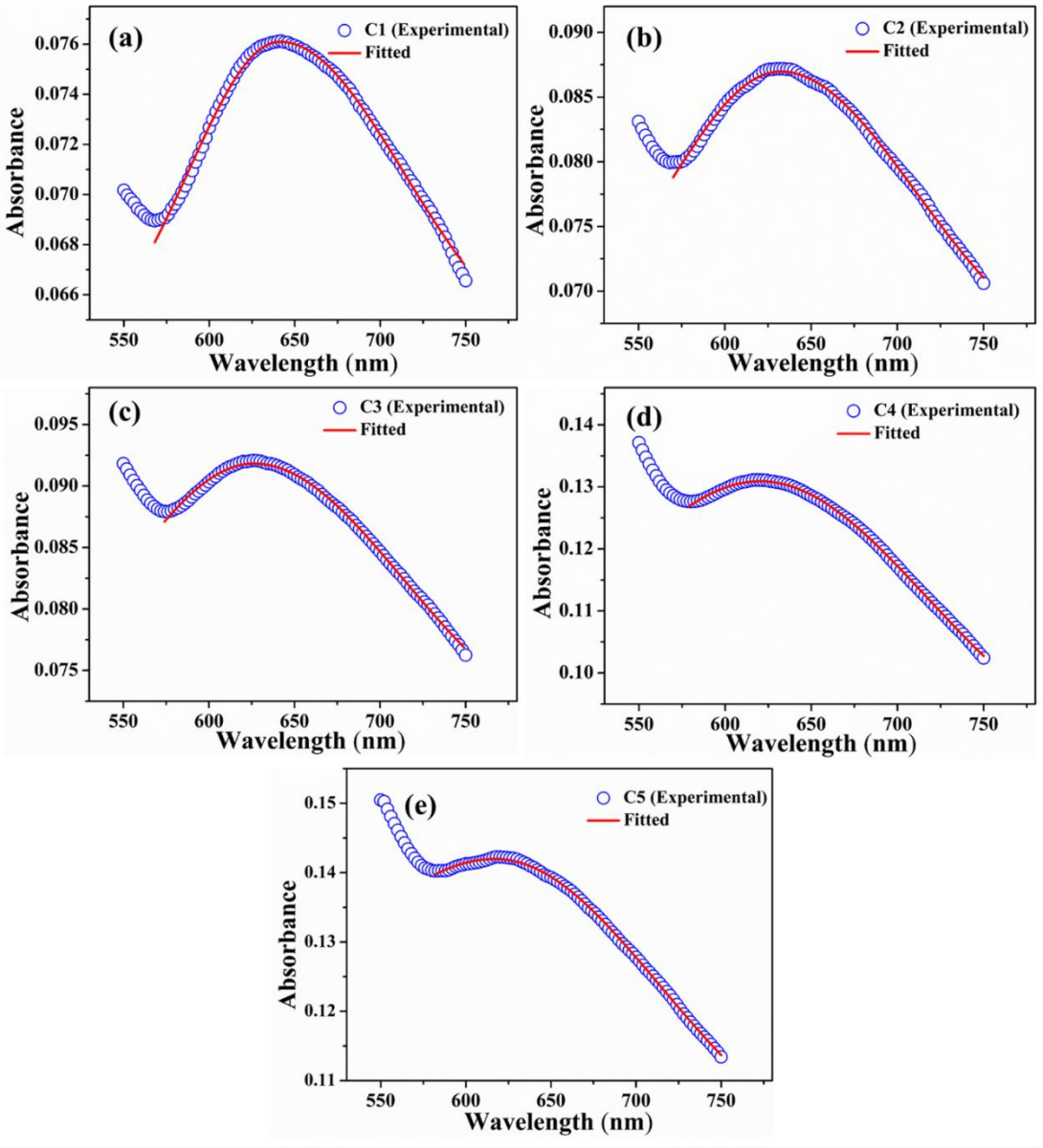

Figure 3.10 (a)-(e) *Absorption spectra of the colloidal solution of samples C1-C5 along with the corresponding curve fitted using Bi-Gaussian function.*

According to Mie theory, there is a peak-shift in an absorption spectrum with the change in the size distribution of the particles [22, 34, 35]. A blue-shift in the plasmonic peak generally refers to the reduction in size of the NPs. However, there are reports of both blue as well as red-shift of the peak with the increase in size of the NPs [22, 35, 36]. These contradicting reports have been explained by theoretical models considering changes of the band structure in

the particles, environmental changes, etc. [35]. For smaller particles, the blue-shift in the SPR peak may be attributed to the quantum size effect [32]. But, for this to be effective the size of the NPs under consideration should be below its excitonic Bohr radius. The NPs formed in the present case also contain oxidized phase which is confirmed by the SAED patterns of samples C1-C5, discussed in section 3.3.4.1. The excitonic Bohr radius of Cu oxide NPs are reported to lie in between 6.6 and 28.7 nm [37]. The average particle size of the samples are actually found to be in this range, confirming that the blue-shift of the SPR peak position is due to the reduction in size of the NPs especially for samples C3-C5 where the size distribution is reasonably uniform.

The broadening in the plasmon bandwidth can be understood starting from the Mie theory [34, 36]. Mie started from the Maxwell equations and went on to describe the optical properties of small spherical metal particles. In the quasi-static approximation, the absorption in particles much smaller than the wavelength of light is caused mainly by the electric dipole oscillations and the total extinction coefficient is given by equation 1.1 described in chapter 1 [34, 36]. If the imaginary part ε_2 of the dielectric constant $\varepsilon(\omega)$ of the material is small or weakly dependent on ω then the plasmon resonance condition is roughly fulfilled when $\varepsilon_1(\omega) = -2\varepsilon'$ where ε' is the dielectric constant of the surrounding medium.

Although within the dipole approximation, the plasmon absorption is size-independent, experimentally there have been many reports on the increase in plasmon bandwidth with the decrease in particle size [36, 38, 39]. This behaviour can be explained by assuming a size-dependent material dielectric function $\varepsilon(\omega, r)$. The dielectric function $\varepsilon(\omega, r)$ is considered to be a combination of two parts viz., an interband part which represents the response of the *d* electrons and a Drude term, $\varepsilon_D(\omega)$ which considers the free conduction electrons. $\varepsilon_D(\omega)$ is given by [36, 39]

$$\varepsilon_D(\omega) = 1 - \frac{\omega_p^2}{\omega^2 + i\gamma\omega} \tag{3.5}$$

where ω_p is the bulk plasmon frequency and γ is the damping constant. For a perfect free electron gas in the limit $\gamma << \omega$, γ equals the plasmon bandwidth. In the case of a small particle, the mean free path of conduction electrons is bounded by the particle's boundaries. Hence, γ becomes dependent on the radius r of the particle and is given by [36, 40]

$$\gamma(r) = \gamma_0 + \frac{av_F}{r} \tag{3.6}$$

where γ_0 is the bulk damping constant, v_F is the velocity of the electrons at the Fermi energy, and a carries the details of the scattering process. The broadening in the plasmon bandwidth may also be attributed to the decrease in the mean free path of the conduction electrons due to collisions with the particle surfaces [32, 38]. This may also be viewed as the size confinement of the conduction band electrons in the NPs and is caused by the scattering of the electrons on the NP surface causing broadening of the plasmonic peak with the reduction in the size of NPs.

The SPR peak position, bandwidth and the average NP size for the samples C1-C5 are listed in table 3.3.

Table 3.3 *SPR peak position, bandwidth and average NP size for the samples C1-C5.*

Sample	SPR peak position (nm)	SPR peak width (nm)	Average particle size (nm)
C1	641	127	-
C2	633	146	-
C3	626	165	20
C4	620	194	11
C5	617	209	7

3.4 Conclusion

$Cu@Cu_xO(x=1, 2)$ NPs were synthesized by pulsed laser ablation of a pure Cu target in DW. The structural features of the NPs as revealed by the SAED and Raman studies suggest that more oxidized phases of Cu NPs are favourably formed with the increase in laser ablation duration and laser energy. The blue-shift in the plasmonic peak and broadening in the bandwidth indicates a reduction in the size of the NPs which is confirmed by the TEM studies. These results have been explained using the quantum size effect as well as Mie theory. Thus, simultaneous control over the size, SPR and oxidation state of the synthesized NPs has been established by varying the laser ablation duration and laser energy.

References

[1] P. Liu, H. Wang, X. Li, M. Rui, H. Zeng, Localized surface plasmon resonance of Cu nanoparticles by laser ablation in liquid media, RSC Advances, **5** (2015) 79738-79745.

[2] M. Dendisová-Vyškovská, V. Prokopec, M. Člupek, P. Matějka, Comparison of SERS effectiveness of copper substrates prepared by different methods: what are the values of enhancement factors?, Journal of Raman Spectroscopy, **43** (2012) 181-186.

[3] S. Ezugwu, H. Ye, G. Fanchini, Three-dimensional scanning near field optical microscopy (3D-SNOM) imaging of random arrays of copper nanoparticles: implications for plasmonic solar cell enhancement, Nanoscale, **7** (2015) 252-260.

[4] X. Li, X. Ren, Y. Zhang, W.C. Choy, B. Wei, An all-copper plasmonic sandwich system obtained through directly depositing copper NPs on a CVD grown graphene/copper film and its application in SERS, Nanoscale, **7** (2015) 11291-11299.

[5] X. Guo, C. Hao, G. Jin, H.Y. Zhu, X.Y. Guo, Copper nanoparticles on graphene support: an efficient photocatalyst for coupling of nitroaromatics in visible light, Angewandte Chemie International Edition, **53** (2014) 1973-1977.

[6] K. Sugioka, M. Meunier, A. Piqué, Laser precision microfabrication, Springer, 2010.

[7] J. Zhang, J. Liu, Q. Peng, X. Wang, Y. Li, Nearly monodisperse Cu_2O and CuO nanospheres: preparation and applications for sensitive gas sensors, Chemistry of materials, **18** (2006) 867-871.

[8] K.B. Ayaz Ahmed, M. Sengan, S.K. P, A. Veerappan, Highly selective colorimetric cysteine sensor based on the formation of cysteine layer on copper nanoparticles, Sensors and Actuators B: Chemical, **233** (2016) 431-437.

[9] K. L. Kelly, E. Coronado, L.L. Zhao, G.C. Schatz, The optical properties of metal nanoparticles: the influence of size, shape, and dielectric environment, The Journal of Physical Chemistry B, **107** (2003) 668-677.

[10] M.A. Mahmoud, M. Chamanzar, A. Adibi, M.A. El-Sayed, Effect of the dielectric constant of the surrounding medium and the substrate on the surface plasmon resonance spectrum and sensitivity factors of highly symmetric systems: silver nanocubes, Journal of the American Chemical Society, **134** (2012) 6434-6442.

[11] T. Hinotsu, B. Jeyadevan, C. Chinnasamy, K. Shinoda, K. Tohji, Size and structure control of magnetic nanoparticles by using a modified polyol process, Journal of Applied Physics, **95** (2004) 7477-7479.

[12] Y.M. Mohan, K. Vimala, V. Thomas, K. Varaprasad, B. Sreedhar, S. Bajpai, K.M. Raju, Controlling of silver nanoparticles structure by hydrogel networks, Journal of colloid and interface science, **342** (2010) 73-82.

[13] D. Zhang, B. Gökce, S. Barcikowski, Laser synthesis and processing of colloids: fundamentals and applications, Chemical reviews, **117** (2017) 3990-4103.

[14] Z. Yan, D.B. Chrisey, Pulsed laser ablation in liquid for micro-/nanostructure generation, Journal of Photochemistry and Photobiology C: Photochemistry Reviews, **13** (2012) 204-223.

[15] M. Muniz-Miranda, C. Gellini, A. Simonelli, M. Tiberi, F. Giammanco, E. Giorgetti, Characterization of copper nanoparticles obtained by laser ablation in liquids, Applied Physics A, **110** (2013) 829-833.

[16] J. Santillán, F. Videla, M. Fernández van Raap, D. Schinca, L. Scaffardi, Analysis of the structure, configuration, and sizing of Cu and Cu oxide nanoparticles generated by fs laser ablation of solid target in liquids, Journal of Applied Physics, **113** (2013) 134305.

[17] A. Nath, A. Khare, Size induced structural modifications in copper oxide nanoparticles synthesized via laser ablation in liquids, Journal of Applied Physics, **110** (2011) 043111.

[18] R. M. Tilaki, A. Iraji zad, S. M. Mahdavi, Size, composition and optical properties of copper nanoparticles prepared by laser ablation in liquids, Applied Physics A, **88** (2007) 415-419.

[19] R. Mahfouz, F.J. Cadete Santos Aires, A. Brenier, B. Jacquier, J.C. Bertolini, Synthesis and physico-chemical characteristics of nanosized particles produced by laser ablation of a nickel target in water, Applied Surface Science, **254** (2008) 5181-5190.

[20] M.H. Mahdieh, B. Fattahi, Effects of water depth and laser pulse numbers on size properties of colloidal nanoparticles prepared by nanosecond pulsed laser ablation in liquid, Optics & Laser Technology, **75** (2015) 188-196.

[21] A.F.M.Y. Haider, S. Sengupta, K.M. Abedin, A.I. Talukder, Fabrication of gold nanoparticles in water by laser ablation technique and their characterization, Applied Physics A, **105** (2011) 487-495.

[22] A. Takami, H. Kurita, S. Koda, Laser-Induced Size Reduction of Noble Metal Particles, Journal of Physical Chemistry B, **103** (1999) 1226-1232.

[23] P.V. Kamat, M. Flumiani, G.V. Hartland, Picosecond dynamics of silver nanoclusters. Photoejection of electrons and fragmentation, The Journal of Physical Chemistry B, **102** (1998) 3123-3128.

[24] L. Yang, J. Lv, Y. Sui, W. Fu, X. Zhou, J. Ma, S. Su, W. Zhang, P. Lv, D. Wu, Y. Mu, H. Yang, Fabrication of Cu2O/Ag composite nanoframes as surface-enhanced Raman scattering substrates in a successive one-pot procedure, CrystEngComm, **16** (2014) 2298-2304.

[25] A.S. Zoolfakar, R.A. Rani, A.J. Morfa, A.P. O'Mullane, K. Kalantar-zadeh, Nanostructured copper oxide semiconductors: a perspective on materials, synthesis methods and applications, Journal of Materials Chemistry C, **2** (2014) 5247-5270.

[26] L. Debbichi, M.C. Marco de Lucas, J.F. Pierson, P. Krüger, Vibrational Properties of CuO and Cu4O3from First-Principles Calculations, and Raman and Infrared Spectroscopy, The Journal of Physical Chemistry C, **116** (2012) 10232-10237.

[27] T.M.D. Dang, T.T.T. Le, E. Fribourg-Blanc, M.C. Dang, The influence of solvents and surfactants on the preparation of copper nanoparticles by a chemical reduction method, Advances in Natural Sciences: Nanoscience and Nanotechnology, **2** (2011) 025004.

[28] D.B. Williams, C.B. Carter, Diffraction in TEM, in: Transmission Electron Microscopy: A Textbook for Materials Science, Springer US, Boston, MA, 2009, pp. 197-209.

[29] P. Khanna, S. Gaikwad, P. Adhyapak, N. Singh, R. Marimuthu, Synthesis and characterization of copper nanoparticles, Materials Letters, **61** (2007) 4711-4714.

[30] P.V. Kazakevich, A.V. Simakin, V.V. Voronov, G.A. Shafeev, Laser induced synthesis of nanoparticles in liquids, Applied Surface Science, **252** (2006) 4373-4380.

[31] S. Link, M.A. El-Sayed, Shape and size dependence of radiative, non-radiative and photothermal properties of gold nanocrystals, International Reviews in Physical Chemistry, **19** (2000) 409-453.

[32] K.B. Mogensen, K. Kneipp, Size-Dependent Shifts of Plasmon Resonance in Silver Nanoparticle Films Using Controlled Dissolution: Monitoring the Onset of Surface Screening Effects, The Journal of Physical Chemistry C, **118** (2014) 28075-28083.

[33] T.S. Buys, K. de Clerk, Bi-Gaussian Fitting of Skewed Peaks, Analytical Chemistry, **44** (1972) 1273-1275.

[34] G. Mie, Contributions to the optics of turbid media, particularly of colloidal metal solutions, Annalen der Physik, **25** (1908) 377-445.

[35] U. Kreibig, M. Vollmer, Optical properties of metal clusters, Springer Science & Business Media, 2013.

[36] S. Link, M.A. El-Sayed, Spectral properties and relaxation dynamics of surface plasmon electronic oscillations in gold and silver nanodots and nanorods, The Journal of Physical Chemistry B, **103** (1999) 8410-8426.

[37] S. Dagher, Y. Haik, A.I. Ayesh, N. Tit, Synthesis and optical properties of colloidal CuO nanoparticles, Journal of Luminescence, **151** (2014) 149-154.

[38] U. Kreibig, C.V. Fragstein, The limitation of electron mean free path in small silver particles, Zeitschrift für Physik, **224** (1969) 307-323.

[39] U. Kreibig, Kramers Kronig Analysis of the Optical Properties of Small Silver Particles Zeitschrift für Physik B, **234** (1970) 307-318.

[40] U. Kreibig, L. Genzel, Optical absorption of small metallic particles, Surface Science, **156** (1985) 678-700.

Chapter 4

Synthesis and Characterization of $Ag@Ag_xO_y$ Nanoparticles

4.1 Introduction

Among the noble metals, silver (Ag) is known to exhibit the strongest plasmonic response and is preferred in many plasmonic applications including sensing devices, color printing, photovoltaics devices, etc. [1-4]. The photoluminescence (PL) of Ag nanoparticles (NPs) has also paved a way for its successful application in solar cells, bio-imaging, etc. [5]. During the past two decades, a large effort has been made to synthesize plasmonic nanomaterials with precise control over its properties [6, 7].

There are several reports on the variation in the properties of the NPs by changing the laser parameters in pulsed laser ablation in liquid (PLAL) technique [8-10]. But depending on the synthesis conditions, there is ambiguity in the available literature pertaining to the size of the NPs. While there have been report on the formation of larger Ag NPs with the increase in laser fluence from 14 to 22 J/cm^2, a decrease in the size of the NPs with the increase in the laser fluence from 1 to 3 J/cm^2 is also observed [11, 12]. Very recently, Moura *et al*. obtained smaller NPs almost of the same order of size, 7 to 19 nm, using very high laser fluence [13]. Although Mahfouz *et al.* had reported a slight decrease in the size of Ni NPs with increase in the number of laser shots, the effect of the change in the laser ablation duration on the properties of the NPs is not explored much [14]. Thus, active research in the field of tuning the properties, especially the size of the NPs as well as its crystalline phase and structure by varying the laser parameters is still wide open.

In the preceding chapter, the properties of Cu NPs were successfully tuned by the variation of the laser ablation duration and incident laser energy. In order to substantiate the effect of these two process parameters on the NPs and to confirm the absence of any ambiguity as discussed above, Ag NPs have also been synthesized by varying the laser ablation duration and incident laser energy. In addition to the importance of Ag NPs in various applications, as already stated, the reason for the choice of Ag in this work is to compare the efficiency of the Cu NPs with regard to Ag which is considered a superior plasmonic material. The applications of the synthesized Cu and Ag NPs will be discussed in chapter 7 of the present thesis. An attempt to correlate the size and the SPR of the Ag NPs is made. Along with the structural elucidation of the synthesized NPs, the PL properties of these NPs are also investigated.

4.2 Experimental details

Similar to the synthesis of Cu NPs, NPs of Ag were synthesized by the pulsed laser ablation of Ag in DW. The experimental details of the process of synthesis is illustrated in section 2.1. The samples prepared under various conditions are listed in table 4.1.

Table 4.1 *Nanoparticle samples prepared under different conditions.*

Sample	Laser energy (mJ)	Duration (minutes)
A1	30	**5**
A2	30	**10**
A3	**30**	**30**
A4	**50**	30
A5	**70**	30

To study the effect of laser ablation duration, three samples A1-A3 were synthesized by varying the ablation duration as 5, 15 and 30 minutes, respectively at fixed laser energy of 30 mJ. The reason for choosing lesser duration in the case of Ag NPs will be discussed in section 4.3.2. In line with sample A3, samples A4 and A5 were prepared at

laser energies of 50 and 70 mJ, respectively for an ablation duration of 30 minutes in order to study the effect of incident laser energy on the NPs. Samples A1-A3 form the set of samples to study the effect of laser ablation duration and samples A3-A5 form another set for the effect of incident laser energy on the synthesized Ag NPs. For the estimation of the mass ablation rate and the characterization of the NPs, the same procedure as adopted for the NPs of Cu in chapter 3 was followed.

4.3 Results and discussion

4.3.1 Formation of the nanoparticles

The observed change in color of the samples A1-A5 as depicted in Fig. 4.1 confirms the formation of NPs of Ag.

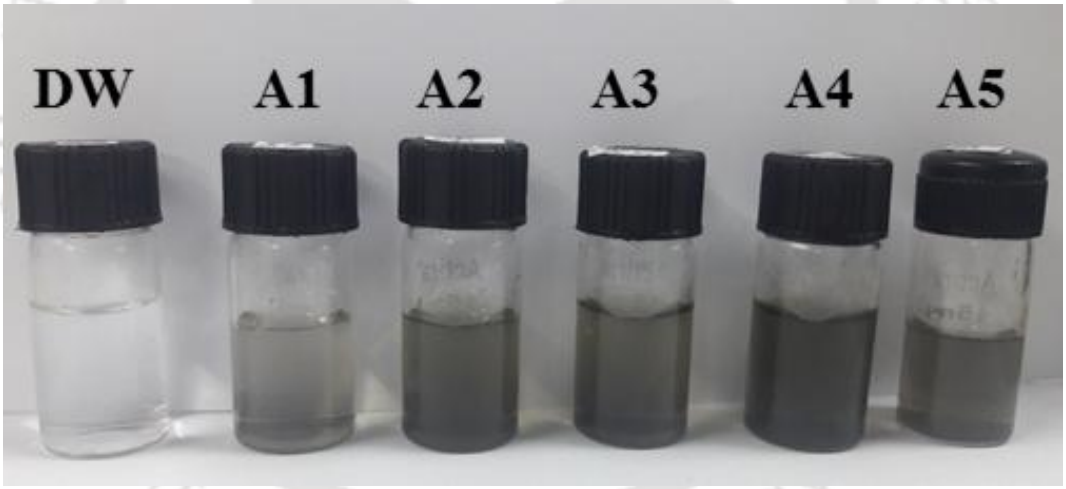

Figure 4.1 *Change in color of the colloidal solution of Ag NPs.*

The darkening of the color of the colloidal solutions from A1-A5 implies the increase in the concentration of the NPs with the increase in laser ablation duration and also with the increase in incident laser energy. The increase in the concentration of the NPs with the ablation duration is attributed to the ablation of more target material with the prolonged exposure to laser while the increase with the laser energy is due to the higher extent of ablation for higher energies. As in the case of Cu, the mass ablation rate as function of

incident laser energy was also estimated for Ag to gain an idea about the extent of ablation and is discussed in the following section.

4.3.2 Estimation of mass ablation rate

The average depth profiles of the craters obtained at laser energies of 30, 50 and 70 mJ, respectively are shown in Fig. 4.2(a)-(c). Similar to the case of Cu, the profiles were extracted along a line joining two diametrically opposite points on the boundary of the crater. Here also, with the increase in incident laser energy there is an increase in the depth of the crater.

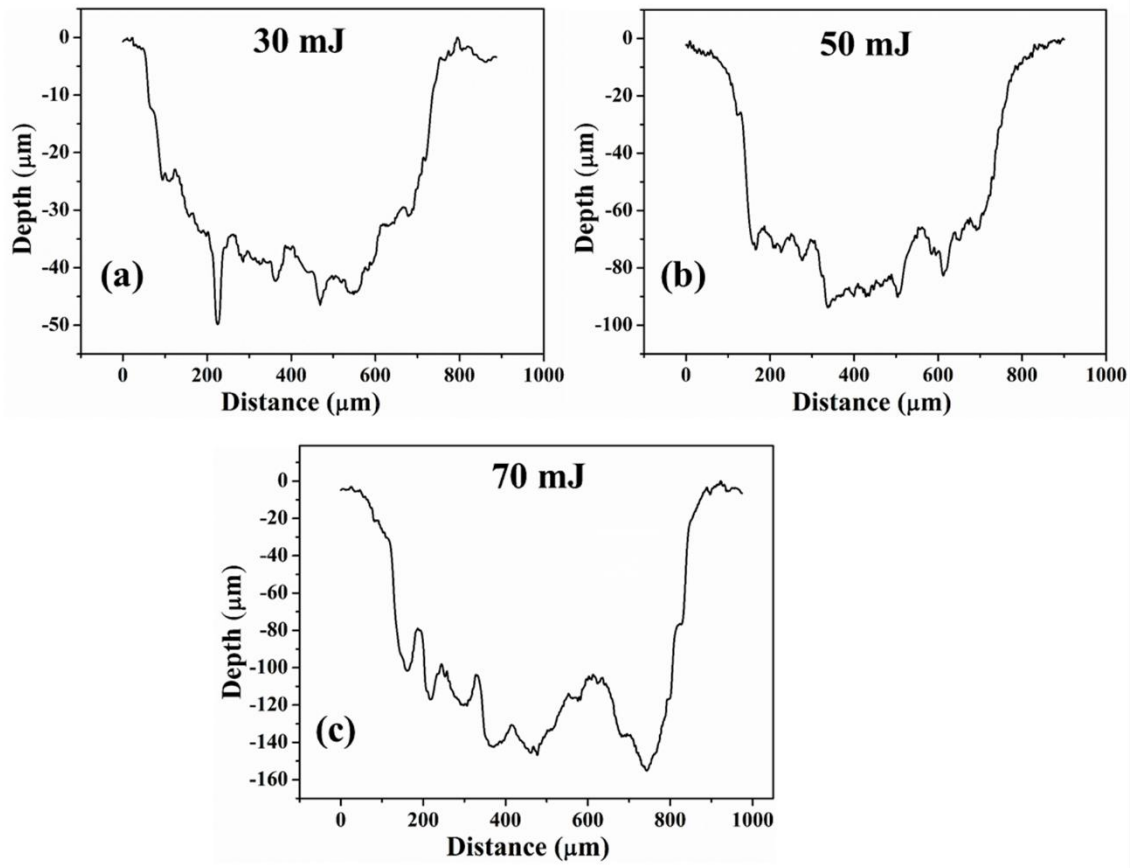

Figure 4.2 *Depth profiles of crater produced at* **(a)** *30 mJ,* **(b)** *50 mJ and* **(c)** *70 mJ.*

From the integrated ablated volume of the crater, measured via the surface profilometer, the mass ablation rate was estimated. Fig 4.3 depicts the ablation rate (μg/shot) versus the incident laser energy. The ablation rate increases with the increase in the laser energy which facilitates the release of more material in the form of NPs in the

surrounding liquid. The higher ablation rate in the case of Ag as compared to Cu under similar conditions is attributed mainly to the lower melting point (961.8 °C) and ablation threshold (0.354 J/cm^2) of Ag than that of Cu (1085 °C, 1.6 J/cm^2) at 532 nm [15, 16]. In fact, this is the reason for choosing a maximum ablation duration of 30 minutes in the synthesis of Ag NPs (unlike 60 minutes for Cu NPs) in order to avoid excessive agglomeration among the NPs due to very high concentration.

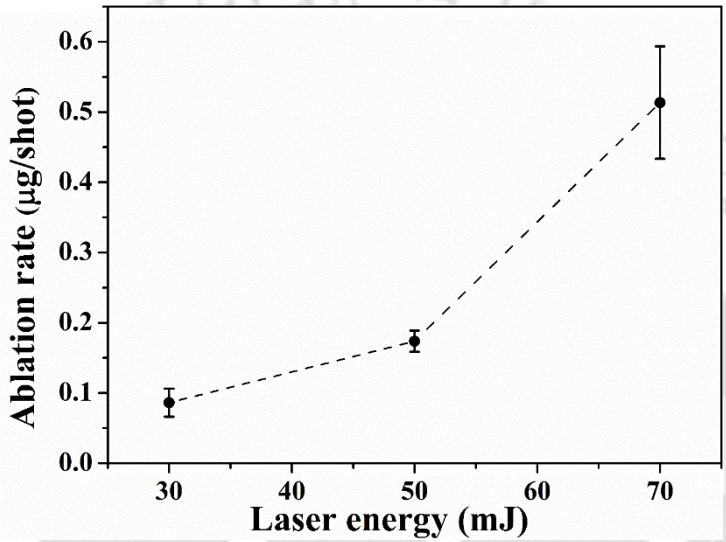

Figure 4.3 *Variation of ablation rate as a function of incident laser energy.*

4.3.3 Particle size analysis by transmission electron microscope

The transmission electron microscope (TEM) images and the corresponding size distributions (inset) of the samples A1-A5 are shown in Fig. 4.4(a)-(e), respectively. The particles are nearly spherical in shape and the average particle size is found to be ~ 20, 19, 15, 12 and 10 nm for samples A1-A5, respectively as shown in Fig. 4.4(f).

For A1-A3, the decrease in the average particle size with the increase in the laser ablation duration from 5 to 30 minutes is mainly attributed to the redistribution of the size of the NPs as a result of longer interaction with the incident laser beam. Similar to the case of Cu NPs, as discussed in chapter 3, the absorption of laser energy by the initially formed NPs lying in the path of the laser beam leads to thermal heating. This leads to melting and

fragmentation of the NPs resulting in the decrease in particle size with the increase in exposure time of the laser [17].

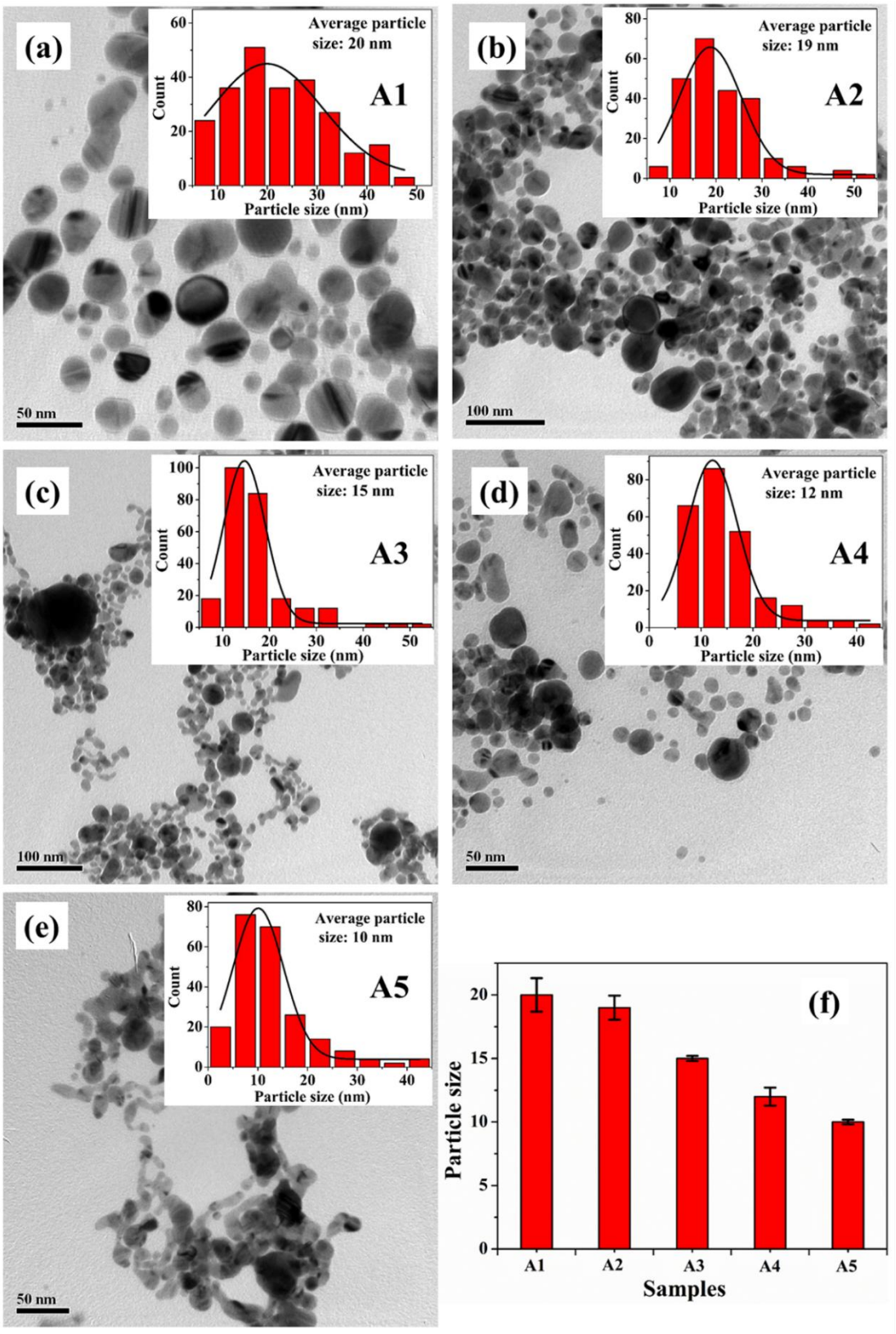

Figure 4.4 (a)-(e) *TEM image of samples A1-A5 with the particle size distribution shown in the inset,* **(f)** *Variation of average particle size from A1-A5.*

From the histogram of the particle size distributions for samples A1-A3, it is observed that the reduction in the size of the NPs is accompanied by a significant narrowing of the size distribution. For sample A1, Fig. 4.4(a), for least ablation duration of 5 minutes only, a broad size distribution is observed. But as the ablation duration increases, the initially formed larger sized NPs get fragmented into smaller ones resulting in the narrowing down of the particle size distribution which is observed for samples A2 and A3.

For samples A3-A5, there is a slight broadening in the particle size distribution with the increase in incident laser energy as depicted in Fig. 4.4(c)-(e), respectively which may be due to the increase in the concentration of the NPs.

The reasons for the reduction in the size of the NPs are the same as those cited for Cu NPs in section 3.3.3. Firstly, the large absorption of laser energy by the initially formed NPs and less dissipation of heat to the surrounding liquid medium raises its temperature which results in disintegration of the particles. This is expected to be more probable for higher laser energies [18]. Secondly, the kinetic energy of the particles ejected via ablation increases with the laser energy which in turn increases the collisions among the particles before the condensation phase leading to fragmentation of the larger particles into smaller ones [19]. Lastly, photoejected electrons which assemble near the NP surface leads to the disintegration of the initially formed NPs because of charging thus causing the reduction of the size [20]. All the three mechanisms are equally probable for the observed decrease in size with the increase in incident laser energy.

4.3.4 Structural and compositional studies

4.3.4.1 SAED and HRTEM analysis

The selected area electron diffraction (SAED) patterns of samples A1-A5 are depicted in Fig. 4.5(a)-(e), respectively.

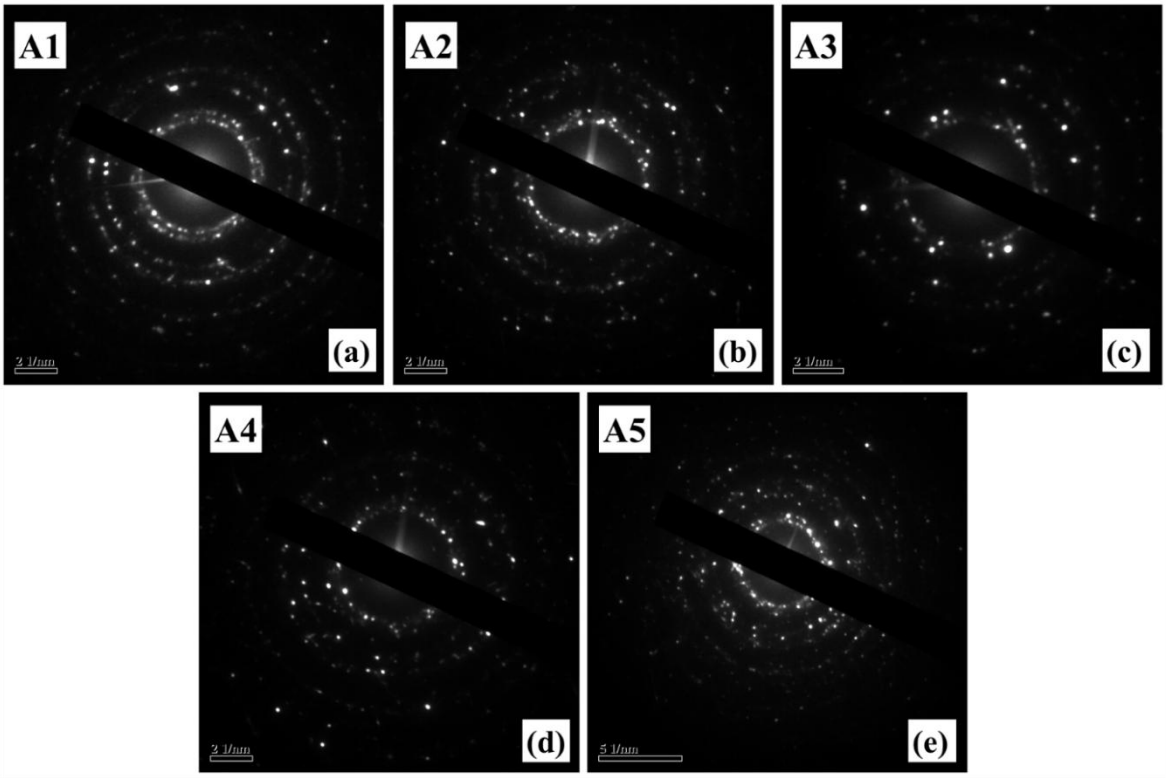

Figure 4.5 (a)-(e) *SAED patterns of samples A1-A5, respectively.*

Distinct diffraction patterns clearly confirm the formation of crystalline phases in all the samples. The *d*-values obtained from the SAED patterns for various phases of Ag as well as its oxides along with the corresponding *hkl*-planes are listed in table 4.2. From the SAED patterns, it is confirmed that the NPs formed are actually $Ag@Ag_xO_y$(x=1, 2; y=0, 1, 3). The formation of oxidized NPs is due to the breakdown of water molecules during the ablation in the neighbourhood of the focal volume. In all the samples, (111), (200), (220) and (311) planes of pure Ag phase are observed. In addition to these, in samples A1 and A2, two planes corresponding to oxide phases of Ag viz., Ag_2O(110) and AgO(110) are also detected. For samples A3-A5, there is the appearance of oxygen-rich Ag_2O_3 and the oxygen-deficient Ag_2O phase is absent. At high incident laser energy, large number of water molecules undergo dissociation thus facilitating the formation of oxygen-rich phase of Ag oxide.

Table 4.2 *Lattice d-spacing of synthesized NPs calculated from SAED patterns along with the corresponding planes.*

		Observed in sample				
***hkl* plane**	***d* (nm)**	**A1**	**A2**	**A3**	**A4**	**A5**
Ag(311)	0.12	✓	✓	✓	✓	✓
Ag(220)	0.15	✓	✓	✓	✓	✓
Ag(200)	0.20	✓	✓	✓	✓	✓
Ag(111)	0.24	✓	✓	✓	✓	✓
AgO(110)	0.29	✓	✓	✓	✓	✓
Ag_2O(110)	0.33	✓	✓	-	-	-
Ag_2O_3(311)	0.22	-	-	-	✓	✓
Ag_2O_3(110)	0.35	-	-	✓	✓	✓

The high resolution TEM (HRTEM) images of samples A1-A5, Fig. 4.6(a)-(e), respectively, along with the Inverse Fast Fourier Transform (IFFT) of the selected regions shown in the insets, further confirm the formation of oxidized NPs. The observed *d*-values from the HRTEM images for the samples A1, Fig. 4.6(a) and A2, Fig. 4.6(b) correspond to (200) and (111) planes, respectively of pure Ag phases. For sample A3, the HRTEM image, Fig. 4.6(c), shows two planes corresponding to AgO(110) and Ag_2O_3(110). Fig. 4.6(d), for sample A4, shows the presence of Ag_2O_3(311) phase while the planes observed for sample A5, Fig. 4.6(e), corresponds to Ag(200) and Ag_2O_3(311) phases, respectively. Thus, it is observed that the SAED and HRTEM results complement each other in terms of the elucidation of the structural features and presence of oxide phases of the Ag NPs.

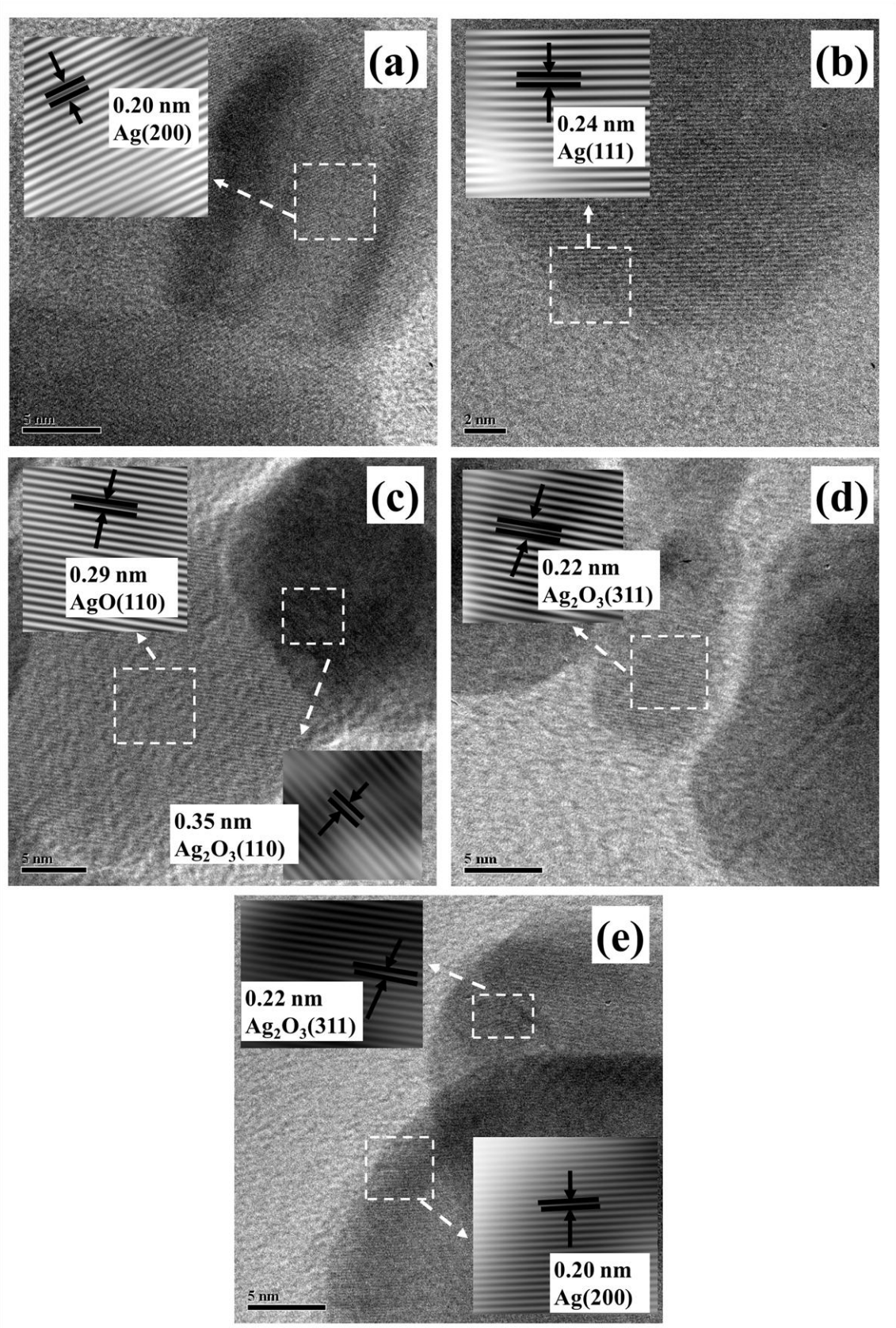

Figure 4.6 (a)-(e) *HRTEM image with the IFFT of selected region of samples A1-A5.*

4.3.4.2 XRD analysis

Fig. 4.7 shows the X-ray diffraction (XRD) patterns for all the five samples, A1-A5. The observed peaks at 38.16, 44.37, 64.47 and 77.46° correspond to (111), (200), (220) and (311) planes, respectively of the fcc structure of metallic Ag [21]. This is in agreement with the SAED analysis. However, the XRD could not detect any trace of Ag oxide as predicted by the SAED and HRTEM analysis which could be due to its presence in extremely small quantity in the probed regions and also due to the low sensitivity of XRD as compared to SAED. The intensity of the XRD peaks is very weak for the samples A1 and A2 which have been synthesized under the exposure of laser for lesser duration yielding the low concentration compared to those of the other samples.

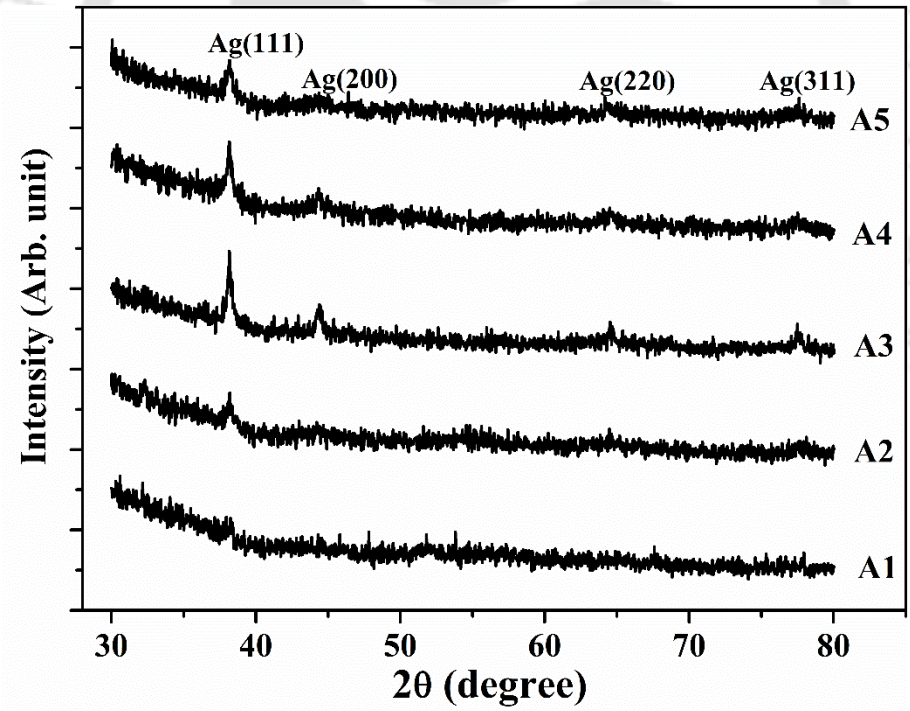

Figure 4.7 *XRD patterns of the samples A1-A5.*

4.3.5 Surface plasmon resonance of the NPs

The absorption spectra of samples A1-A5 are shown in Fig. 4.8(a)-(e), respectively. It clearly depicts the SPR peak in these samples around ~ 400 nm as well as signature of inter

band (IB) transition peak at ~ 280 nm. A closer look at the absorption maxima reveals that there is a slight blue-shift in the SPR peak position from ~ 403 to 398 nm for samples A1-A3, respectively.

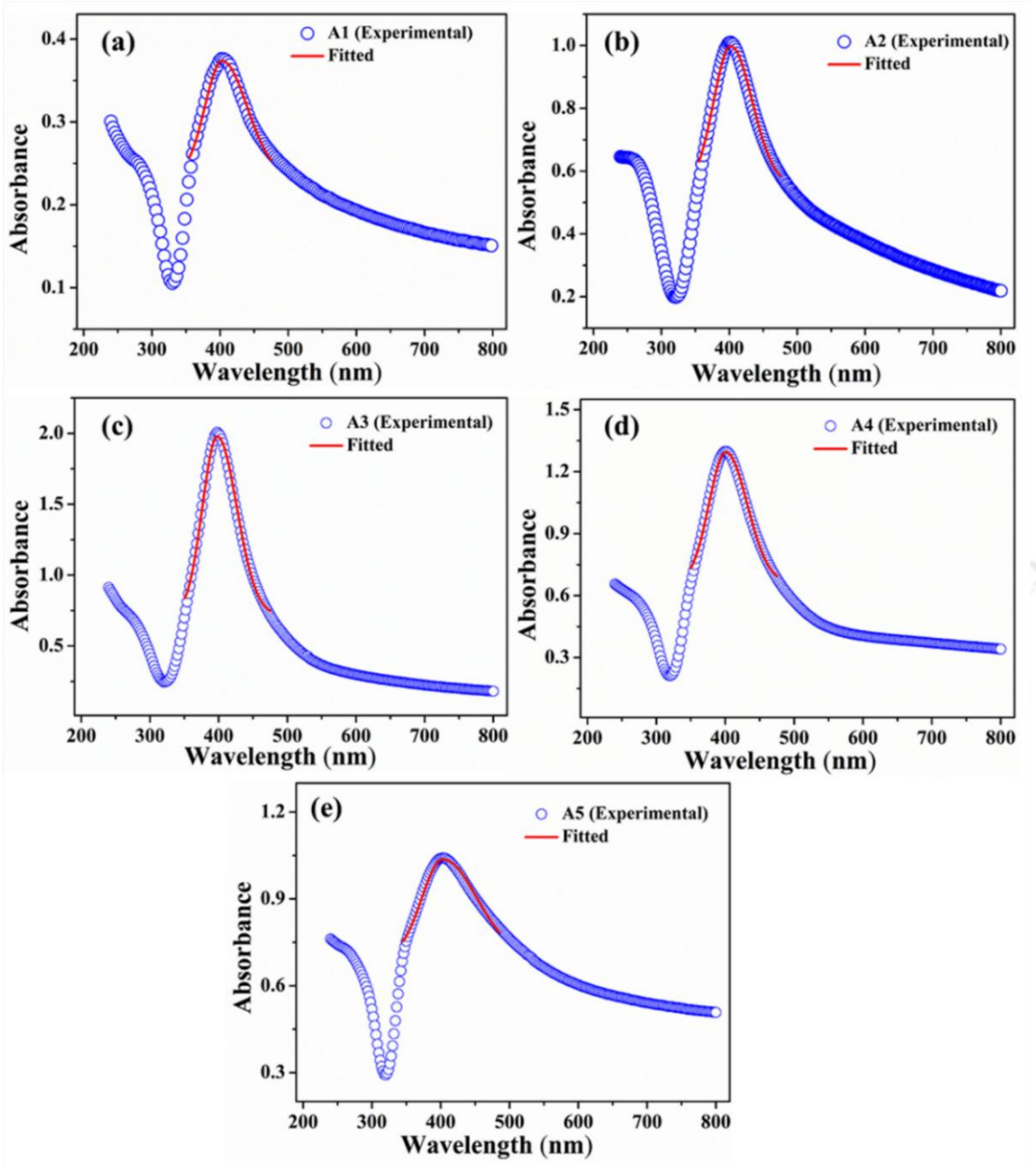

Figure 4.8 (a)-(e) *Absorption spectra of the colloidal solution of samples A1-A5 along with the corresponding curve fitted using Bi-Gaussian function.*

The shift in the SPR peak towards shorter wavelength with the increase in laser ablation duration from 5 to 30 minutes could possibly be due to the reduction in the size of the NPs. The change in the plasmonic bandwidth is clearly visible in the absorption spectra for these samples. The bandwidth is found to decrease from ~ 66 to 51 nm for samples A1-

A3, respectively. The origin of this decrease in the plasmonic bandwidth from A1-A3 may be due to the decrease in the particle size distribution for these samples as discussed in section 4.3.3. Similar to the case of Cu NPs, the SPR peak position and bandwidth have been determined by fitting the experimental absorbance plots with the Bi-Gaussian function [22].

For the samples A3-A5 which form the set of samples for the study of the effect of incident laser energy, there is a slight red-shift in the SPR peak position from ~ 398 to 403 nm with the increase in the incident laser energy from 30 to 70 mJ, respectively. The red-shift of the plasmonic peak position is usually an indication of the increase in the size of the NPs [23]. However, in the present case, from the TEM images discussed earlier in section 4.3.3, it is observed that the average particle size of the NPs decreases from A3-A5. This appears to be in contradiction with the usual behaviour of plasmonic peak shift (red/blue) with the size (increase/decrease) of the NPs [6]. A similar trend of reversing the size-effects of the SPR of Ag NPs synthesized by chemical method was reported by Peng *et al.* [24]. A so-called "exceptional" behaviour of the NPs in the size range of 2-20 nm was observed. It was reported that as the size of the NPs decreases below 20 nm, the SPR band blue-shifts but near 12 nm there is a turn-over and the band displays a red-shift. This behaviour was explained on the basis of multilayer Mie theory model. The model consists of several layers, a central spherical metal core, a surrounding shell corresponding to a layer of reduced conductivity, a shell corresponding to surfactant layer and a solvent layer [24]. A lowered electron conductivity in the outermost atomic layer is found to be the reason for this red-shift. Interestingly, it was also mentioned that surface oxidation of the NPs may result in a reduced conductivity of the surface and hence a red-shift of the SPR band. The NP samples synthesized in the present work indeed possess an oxide layer as predicted by the SAED and HRTEM results. Hence, the observed red-shift with the decrease in the

particle size for A3-A5 in the present work may be well justified. The turnover to a red-shift in the SPR band as the size of the NPs decreases has also been reported in other works [25, 26] .

From the absorption spectra, the plasmonic bandwidth for A3-A5 is also observed to increase from ~ 51 to 80 nm. Unlike for the case of samples A1-A3 where the decrease in the size distribution is believed to be contributing towards the narrowing of the SPR bandwidth, for the samples A3-A5 there is no appreciable change in the size distribution. These samples have been synthesized for longer ablation duration of 30 minutes, so the concentration of the NPs synthesized is higher. Also, as the incident laser energy is varied from 30 to 70 mJ, the concentration increases from sample A3 to A5, respectively. Thus, there is a fair chance of the aggregation of the NPs with the increase in concentration resulting in the larger bandwidth of the SPR spectra along with the presence of more oxide phase of Ag [27].

For samples A3-A5, the broadening in the plasmonic bandwidth may also be related to the size-dependent material dielectric constant described by the Mie theory, as described elaborately in section 3.3.5. The Drude term in the material dielectric constant describing the free electrons is given by equation 3.5. For a perfect free electron gas, the damping constant γ becomes equal to the plasmon bandwidth. The dependence of γ on the particle radius is given by equation 3.6. From these, the inverse behaviour of the plasmonic bandwidth with the particle radius is established.

The SPR peak position, bandwidth and the average NP size for the samples A1-A5 are listed in table 4.3.

Table 4.3 SPR peak position, bandwidth and average NP size for the samples A1-A5.

Sample	SPR peak position (nm)	SPR peak width (nm)	Average particle size (nm)
A1	403	66	20
A2	402	58	19
A3	398	51	15
A4	401	57	12
A5	403	80	10

4.3.6 Photoluminescence spectra from Ag NPs

As already mentioned, the PL emission associated with Ag NPs has led to its use in several applications [5]. In order to check if the Ag NPs synthesized in the present work also exhibit PL, the NP samples were subjected to PL studies. The PL spectra of the synthesized NPs were recorded at an excitation wavelength of 300 nm. The samples A1 and A2 being of low concentration of Ag NPs did not display any PL emission. For the remaining samples, A3-A5, a broad distinct PL emission band was observed at ~ 407 nm close to the absorption band of Ag NPs as shown in Fig. 4.9(a). As the concentration of the NPs increases for A3-A5, the PL emission becomes significant and is found to be maximum for the sample A5, having the maximum NP concentration pertaining to its synthesis conditions of maximum laser energy (70 mJ) and longest ablation duration (30 minutes) [28]. The increase in the intensity may also be attributed to the decrease in the particle size for A3-A5 from ~ 15 to 10 nm, respectively [29].

In order to ascertain the origin of the PL emission, the PL spectra were deconvoluted via multiple peak fitting using Gaussian line shape function. The deconvoluted spectra clearly display the two distinct peaks as shown in Fig. 4.9(b)-(d) for samples A3-A5,

respectively. It is observed that the first peak matches well with the wavelength range of SPR excitation. This is due to the radiative decay (RD) of SPR excited in the NPs [29, 30]. This band, denoted as P_{RD}, is found to be slightly red-shifted from 399 to 404 nm with the decrease in particle size from ~ 15 to 10 nm for samples A3-A5, respectively and is in accordance with the observed SPR spectra for samples A3-A5, Fig. 4.8(c)-(e). The second peak (P_{RR}) observed around 440 nm for the samples is due to the radiative recombination (RR) of Fermi level electrons with *sp*- or *d*- band holes [31]. However, unlike the P_{RD} band, no shift in the peak position is observed for P_{RR}.

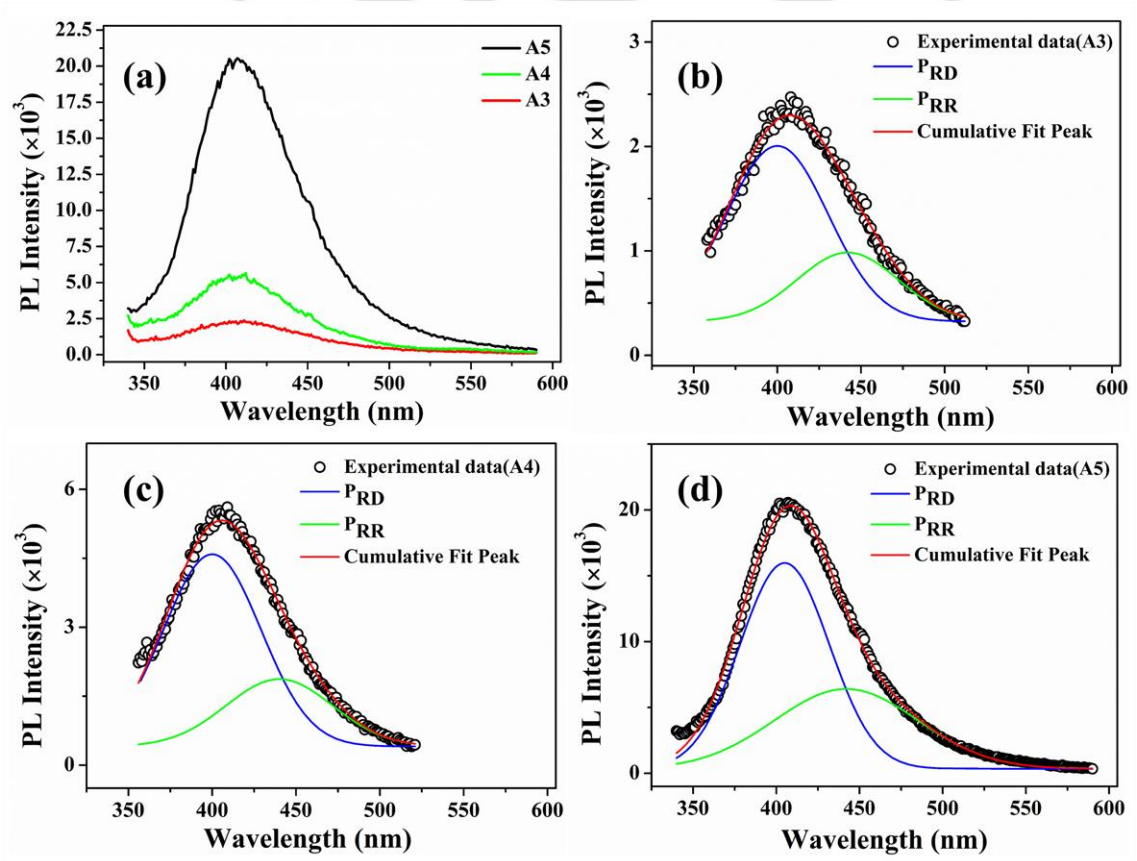

Figure 4.9 (a) *PL spectra of samples A3-A5,* **(b)-(d)** *Deconvoluted peaks corresponding to P_{RD} and P_{RR} bands for samples A3-A5, respectively.*

4.4 Conclusion

$Ag@Ag_xO_y$(x=1, 2; y=0, 1, 3) NPs were synthesized by the pulsed laser ablation of Ag in DW. An increase in the laser ablation duration from 5 to 30 minutes at a fixed laser energy

of 30 mJ decreases the size of the NPs from ~ 20 to 15 nm, respectively while an increase in the incident laser energy to 70 mJ for ablation duration of 30 minutes further decreases the size to ~ 10 nm. The initial decrease in the average particle size upto ~ 15 nm is accompanied by a blue-shift in the SPR peak but with even smaller NPs the plasmonic peak is red-shifted. The decrease in the average size of the Ag NPs with the increase in laser ablation duration and incident laser energy is similar to that obtained in the case of NPs of Cu, as discussed in chapter 3. The Ag NPs exhibited PL emission having peak around 399-404 nm corresponding to the radiative decay of SPR and another peak around 440 nm attributed to the radiative recombination of Fermi level electrons and *sp*- or *d*- band holes.

References

[1] C.-Y. Li, M. Meng, S.-C. Huang, L. Li, S.-R. Huang, S. Chen, L.-Y. Meng, R. Panneerselvam, S.-J. Zhang, B. Ren, "Smart" Ag nanostructures for plasmon-enhanced spectroscopies, Journal of the American Chemical Society, **137** (2015) 13784-13787.

[2] C.M. Cobley, S.E. Skrabalak, D.J. Campbell, Y. Xia, Shape-Controlled Synthesis of Silver Nanoparticles for Plasmonic and Sensing Applications, Plasmonics, **4** (2009) 171-179.

[3] Y. Zhang, Q. Zhang, X. Ouyang, D.Y. Lei, A.P. Zhang, H.-Y. Tam, Ultrafast Light-Controlled Growth of Silver Nanoparticles for Direct Plasmonic Color Printing, ACS nano, **12** (2018) 9913-9921.

[4] W.-J. Yoon, K.-Y. Jung, J. Liu, T. Duraisamy, R. Revur, F.L. Teixeira, S. Sengupta, P.R. Berger, Plasmon-enhanced optical absorption and photocurrent in organic bulk heterojunction photovoltaic devices using self-assembled layer of silver nanoparticles, Solar Energy Materials and Solar Cells, **94** (2010) 128-132.

[5] V. Kravets, Z. Almemar, K. Jiang, K. Culhane, R. Machado, G. Hagen, A. Kotko, I. Dmytruk, K. Spendier, A. Pinchuk, Imaging of biological cells using luminescent silver nanoparticles, Nanoscale research letters, **11** (2016) 30.

[6] S. Agnihotri, S. Mukherji, S. Mukherji, Size-controlled silver nanoparticles synthesized over the range 5–100 nm using the same protocol and their antibacterial efficacy, Rsc Advances, **4** (2014) 3974-3983.

[7] A. Garcia-Leis, I. Rivera-Arreba, S. Sanchez-Cortes, Morphological tuning of plasmonic silver nanostars by controlling the nanoparticle growth mechanism: Application in the SERS detection of the amyloid marker Congo Red, Colloids and Surfaces A: Physicochemical and Engineering Aspects, **535** (2017) 49-60.

[8] M.H. Mahdieh, B. Fattahi, Size properties of colloidal nanoparticles produced by nanosecond pulsed laser ablation and studying the effects of liquid medium and laser fluence, Applied Surface Science, **329** (2015) 47-57.

[9] D. Reyes-Contreras, M. Camacho-López, M.A. Camacho-López, S. Camacho-López, R.I. Rodríguez-Beltrán, M. Mayorga-Rojas, Influence of the per pulse laser fluence on the optical properties of carbon nanoparticles synthesized by laser ablation of solids in liquids, Optics & Laser Technology, **74** (2015) 48-52.

[10] V. Amendola, M. Meneghetti, What controls the composition and the structure of nanomaterials generated by laser ablation in liquid solution?, Physical chemistry chemical physics : PCCP, **15** (2013) 3027-3046.

[11] E. Solati, M. Mashayekh, D. Dorranian, Effects of laser pulse wavelength and laser fluence on the characteristics of silver nanoparticle generated by laser ablation, Applied Physics A, **112** (2013) 689-694.

[12] D. Dorranian, S. Tajmir, F. Khazanehfar, Effect of laser fluence on the characteristics of ag nanoparticles produced by laser ablation, Soft Nanoscience Letters, **3** (2013) 93.

[13] C.G. Moura, R.S.F. Pereira, M. Andritschky, A.L.B. Lopes, J.P. de Freitas Grilo, R.M. do Nascimento, F.S. Silva, Effects of laser fluence and liquid media on preparation of small Ag nanoparticles by laser ablation in liquid, Optics & Laser Technology, **97** (2017) 20-28.

[14] R. Mahfouz, F.J. Cadete Santos Aires, A. Brenier, B. Jacquier, J.C. Bertolini, Synthesis and physico-chemical characteristics of nanosized particles produced by laser ablation of a nickel target in water, Applied Surface Science, **254** (2008) 5181-5190.

[15] T. Palomar, M. Oujja, I. Llorente, B. Ramírez Barat, M.V. Cañamares, E. Cano, M. Castillejo, Evaluation of laser cleaning for the restoration of tarnished silver artifacts, Applied Surface Science, **387** (2016) 118-127.

[16] K.S. Singh, A.K. Sharma, Effect of variation of magnetic field on laser ablation depth of copper and aluminum targets in air atmosphere, Journal of Applied Physics, **119** (2016) 183301.

[17] M.H. Mahdieh, B. Fattahi, Effects of water depth and laser pulse numbers on size properties of colloidal nanoparticles prepared by nanosecond pulsed laser ablation in liquid, Optics & Laser Technology, **75** (2015) 188-196.

[18] A. Takami, H. Kurita, S. Koda, Laser-Induced Size Reduction of Noble Metal Particles, Journal of Physical Chemistry B, **103** (1999) 1226-1232.

[19] A.F.M.Y. Haider, S. Sengupta, K.M. Abedin, A.I. Talukder, Fabrication of gold nanoparticles in water by laser ablation technique and their characterization, Applied Physics A, **105** (2011) 487-495.

[20] P.V. Kamat, M. Flumiani, G.V. Hartland, Picosecond dynamics of silver nanoclusters. Photoejection of electrons and fragmentation, The Journal of Physical Chemistry B, **102** (1998) 3123-3128.

[21] T. Ahmad, I.A. Wani, O.A. Al-Hartomy, A.S. Al-Shihri, A. Kalam, Low temperature chemical synthesis and comparative studies of silver oxide nanoparticles, Journal of Molecular Structure, **1084** (2015) 9-15.

[22] T.S. Buys, K. de Clerk, Bi-Gaussian Fitting of Skewed Peaks, Analytical Chemistry, **44** (1972) 1273-1275.

[23] K.L. Kelly, E. Coronado, L.L. Zhao, G.C. Schatz, The optical properties of metal nanoparticles: the influence of size, shape, and dielectric environment, The Journal of Physical Chemistry B, **107** (2003) 668-677.

[24] S. Peng, J.M. McMahon, G.C. Schatz, S.K. Gray, Y. Sun, Reversing the size-dependence of surface plasmon resonances, Proceedings of the National Academy of Sciences, **107** (2010) 14530-14534.

[25] K.P. Charlé, F. Frank, W. Schulze, The optical properties of silver microcrystallites in dependence on size and the influence of the matrix environment, Berichte der Bunsengesellschaft für physikalische Chemie, **88** (1984) 350-354.

[26] S. Fedrigo, W. Harbich, J. Buttet, Collective dipole oscillations in small silver clusters embedded in rare-gas matrices, Physical Review B, **47** (1993) 10706.

[27] M. Baalousha, M. Sikder, A. Prasad, J. Lead, R. Merrifield, G.T. Chandler, The concentration-dependent behaviour of nanoparticles, Environmental Chemistry, 13 (2016).

[28] O.P. Siwach, P. Sen, Synthesis and fluorescence properties of Ag nanoparticles, Solid State Communications, **148** (2008) 221-225.

[29] O.A. Yeshchenko, I.M. Dmitruk, A.A. Alexeenko, M.Y. Losytskyy, A.V. Kotko, A.O. Pinchuk, Size-dependent surface-plasmon-enhanced photoluminescence from silver nanoparticles embedded in silica, Physical Review B, **79** (2009) 235438.

[30] A. Zhang, J. Zhang, Y. Fang, Photoluminescence from colloidal silver nanoparticles, Journal of Luminescence, **128** (2008) 1635-1640.

[31] Y. Zhao, Y. Jiang, Y. Fang, Spectroscopy property of Ag nanoparticles, Spectrochimica Acta Part A: Molecular and Biomolecular Spectroscopy, **65** (2006) 1003-1006.

Chapter 5

Role of Confining Liquids on the Properties of Nanoparticles Synthesized via PLAL

5.1 Introduction

In chapter 3, we observed the formation of Cu@Cu_xO(x=1, 2) nanoparticles (NPs). Both Cu_2O and CuO have their importance and the choice depends on the particular application. In addition to its implementation in sensing [1] and photocatalytic [2] applications, oxides of Cu are also being used as electrode materials in supercapacitors [3], as semiconductors in renewable energy production [4], as hole-transport layers in perovskite solar cells [5], etc. As the degree of oxidation taking place in the NPs affects its plasmonic response, there is a need to control the oxidation of Cu NPs [6]. Controlled oxidation of NPs has been achieved mostly by chemical techniques like chemical vapour synthesis, and also by adjusting the molecular weight of capping molecules [7, 8]. As most of these chemical techniques require the use of strong chemical reagents which may prove to be harmful to the environment, therefore, alternate environment friendly techniques are consistently being looked for.

Pulsed laser ablation in liquid (PLAL) is normally devoid of any harmful chemicals, and is an excellent technique for the synthesis of NPs [9, 10]. However, the synthesis of Cu NPs via PLAL results in NPs which are prone to oxidation, especially when the synthesis of the NPs is carried out in water as discussed in chapter 3 and also reported in literature [11]. Liu *et al.* reported the reduction in the oxidation of Cu NPs synthesized in oxygen-deficient organic solvents [12]. The formation of an encapsulated carbon layer

from the organic liquid over the surface of Cu NPs is believed to be the reason behind the reduced oxidation. Although there is a report on blue-shift in the surface plasmon resonance (SPR) peak in the case of ablation in organic solvents as compared to that in pure water, a better and comprehensive study in this area is further required which may be useful in the understanding of the oxidation in the NPs [12]. It may also be interesting to study the effect of the ambient on the surface of the target itself as the interaction of the laser beam with the target surface is the heart of the entire process. There have been numerous correlative studies on the formation mechanism of NPs and the synthesis conditions via plasma spectroscopic technique, but no attempt has been made to unveil the mechanism of NP synthesis through a proper ablation study of the target surface [13, 14].

In this chapter, synthesis of Cu NPs has been reported in two organic liquids viz., methanol and 2-propanol. The properties of the NPs synthesized in these liquids are also compared to that of NPs synthesized in distilled water (DW), reported in chapter 3. The change in the size and structure of the NPs as a function of laser ablation duration is also investigated. In addition, the effect of various ambients on the target surface due to laser irradiation is studied and the material ablation rate is compared. An attempt is made to correlate the observed changes in the target surface due to laser ablation in different ambients and the properties of the NPs.

5.2 Experimental details

Cu NPs were synthesized by pulsed laser ablation of a pure Cu target in methanol and 2-propanol. The same procedure as described in section 2.2 was followed for the synthesis of NPs. Samples M1-M3 and P1-P3 were prepared by varying the ablation duration for 15, 30 and 60 minutes in methanol and 2-propanol, respectively while keeping the laser energy fixed at 30 mJ. Unlike the synthesis of Cu NPs in DW, the NPs in the organic solvents were not synthesized for higher incident laser energy due to the volatile nature of these liquids

which results in ignition during ablation. The conditions under which the NPs were synthesized are summarized in table 5.1.

Table 5.1 *Nanoparticle samples prepared under different conditions.*

Sample	Laser energy (mJ)	Duration (minutes)
M1, P1	30	**15**
M2, P2	30	**30**
M3, P3	30	**60**

In order to investigate the structural and morphological changes of the laser irradiated target surface in various ambients, laser ablation of the Cu surface was performed in air, DW, methanol and 2-propanol. The single shot of laser pulse hardly leaves any imprint of laser ablation on the target. Therefore, repeated shots of laser were fired at the same spot for 5 minutes to produce a prominent crater. The reason for using more number of laser shots, in the present work, to produce the craters as compared to craters discussed in chapter 3 and 4 lies in the lower mass ablation rate in the organic solvents as will be discussed in section 5.3.2.4.

5.3 Results and discussion

The synthesis of Cu NPs in DW as a function of laser ablation duration was discussed in a detailed manner in chapter 3. The SPR peak of Cu NPs was red-shifted to ~ 626-641 nm range from its usual reported range of ~ 570-580 nm. This red-shift was attributed mainly to the formation of oxidized NPs due to the release of oxygen during ablation in DW. It was also observed that an increase in laser ablation duration resulted in the formation of smaller and finer NPs. This reduction in the size of NPs was accompanied by a blue-shift in the SPR peak of the samples. The formation of oxidized NPs was also confirmed by Raman studies and the selected area electron diffraction (SAED) patterns which showed

definite formation of Cu@Cu_xO(x=1, 2) NPs. For lesser ablation duration, Cu_2O is the main phase while for longer ablation duration of 60 minutes there is an additional CuO phase. The characterization of the NPs synthesized in methanol and 2-propanol is discussed in the following sections.

5.3.1 Characterization of nanoparticles

5.3.1.1 Particle size distribution and structure of Cu NPs

The transmission electron microscope (TEM) images along with the SAED patterns (insets) of the samples M1-M3 synthesized in methanol for laser ablation duration of 15, 30 and 60 minutes are shown in Fig. 5.1(a)-(c), and the corresponding particle size distribution are depicted in Fig. 5.1(d)-(f), respectively. The particles formed are of nearly spherical shape and the average size of the NPs are found to be ~ 7, 15 and 19 nm for samples M1-M3, respectively. The increase in the size of the NPs with ablation duration is an interesting observation and this variation in size is in contrast to that observed in the case of ablation in DW. For the NPs synthesized in DW, the decrease in its average size with the increase in the laser ablation duration is due to the fragmentation of the initially formed larger particles but the same doesn't hold for methanol. The growth of the NPs with the laser ablation duration, in this case, may be explained on the basis of the mechanism proposed by Zeng *et al.* [15]. In their work, the variation in the size of the NPs in terms of the laser ablation duration was explained by considering three stages. In the initial stage, fragmentation of the NPs take place and in the second stage a growth in the size of the NPs is observed. The final stage is characterized by only a slight increase in the size of the NPs. In the present case, for the NPs synthesized in methanol, with the increase in laser ablation duration, growth of the NPs is followed by an increase in the average size of the NPs. At the growth stage, the initially formed particles are transformed into hot plasma with repeated irradiation of laser. When the plasma cools down, nucleation and growth of NP

takes place. Coalescence of the ablated species may result in bigger sized particles. This results in an increase in the particle size with longer ablation duration. Thus, the 2nd stage as reported by Zeng *et al.* is found to be the effective stage for the growth of NPs in the present case.

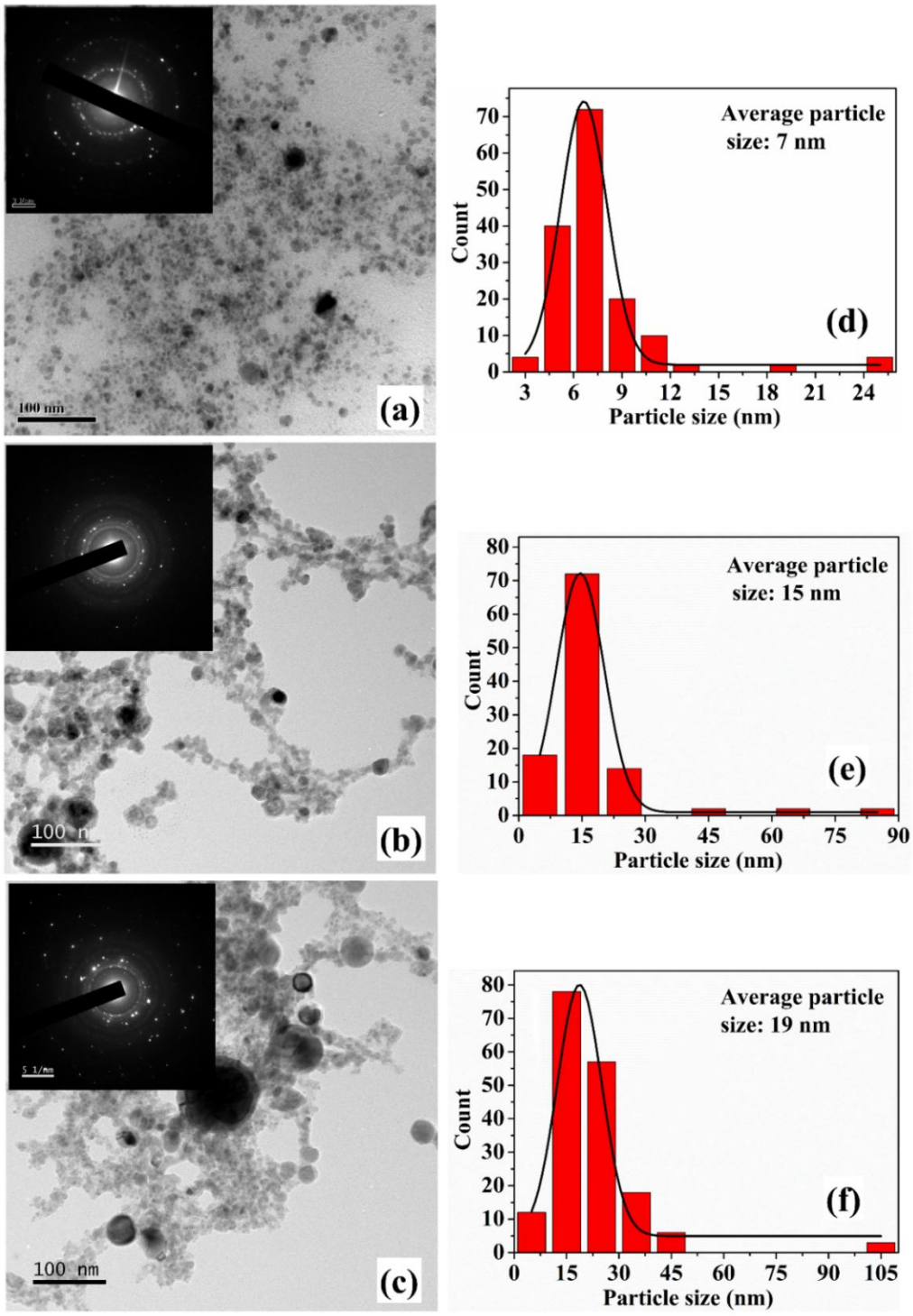

Figure 5.1 (a)-(c) *TEM images along with the SAED pattern (inset) for samples M1-M3, respectively;* **(d)-(f)** *corresponding particle size distribution.*

The difference in the formation mechanism in methanol and DW also lies in the fact that the density of methanol is less than that of DW as listed in table 5.2. The higher density of DW provides a more confined atmosphere during laser ablation facilitating more collisions and as a result fragmentation among the ablated species is dominant in DW. Hence, although there is fragmentation taking place in methanol, the growth of the NPs as mentioned earlier dominates over the fragmentation.

Table 5.2 *Properties of the chosen liquid in the present study.*

Ambient	Density (g/mL)	Thermal conductivity (W/mK)	Acoustic impedance (g cm^{-2} s^{-1})
Air	0.001	0.025	42.8
DW	0.998	0.591	1.48×10^5
Methanol	0.791	0.200	0.89×10^5
2-Propanol	0.785	0.135	0.92×10^5

The TEM images and SAED patterns (insets) of samples P1-P3 synthesized in 2-propanol for an ablation duration of 15, 30 and 60 minutes are displayed in Fig. 5.2(a)-(c), respectively. The corresponding particle size distribution of the samples are shown in Fig. 5.2(d), 5.2(e) and inset of 5.2(c), respectively. The average particle size of these samples are found to be ~ 9, 12 and 17 nm, respectively. Similar to the NPs synthesized in methanol, an increase in the average size of the NPs is observed with the increase in the laser ablation duration from 15 to 60 minutes which is again attributed to the lower density of 2-propanol as compared to that of DW.

The SAED patterns of the NPs in both the liquids reveal the polycrystalline nature. The *d*-values calculated from the diffraction patterns indicate the presence of planes corresponding to Cu_2O phase of the NPs in all the samples in addition to the Cu(111) plane. The details of the crystalline planes observed in the SAED patterns are listed in table 5.3.

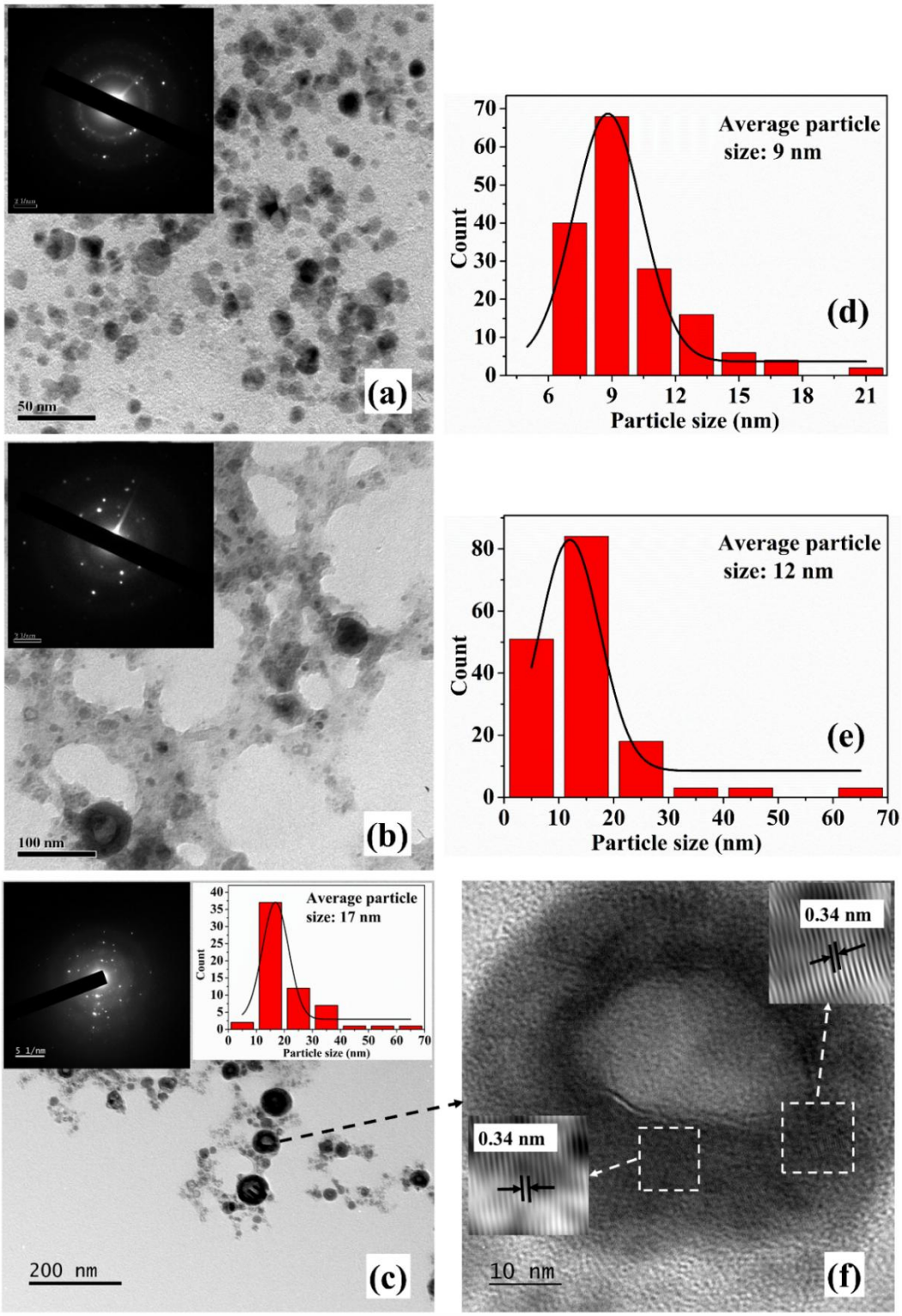

Figure 5.2 (a)-(c) *TEM images along with the SAED pattern (inset) of samples P1-P3 respectively;* **(d), (e)**, *and inset of* **(c)** *corresponding particle size distributions;* **(f)** *HRTEM image of sample P3.*

For the NPs synthesized in DW, there was formation of Cu_2O as well as CuO phases of NPs. However, in the case of ablation in the methanol and 2-propanol, although there is

aerobic transformation of Cu to Cu_2O, no further oxidation to CuO was observed. This confirms that the ablation carried out in oxygen-deficient solvents is useful in reducing the degree of oxidation of the NPs synthesized via PLAL.

Table 5.3 *d-values obtained from the SAED patterns along with corresponding planes for the NPs synthesized in methanol and 2-propanol.*

***hkl* planes**	***d*-value (nm)**	**Cu NPs in methanol**			**Cu NPs in 2-propanol**		
		M1	**M2**	**M3**	**P1**	**P2**	**P3**
Cu(111)	0.20	-	✓	✓	✓	✓	✓
Cu_2O (110)	0.29	✓	-	-	✓	-	-
Cu_2O (111)	0.24	-	-	✓	-	✓	✓
Cu_2O (211)	0.17	✓	-	-	✓	-	-
Cu_2O (220)	0.16	-	-	✓	-	✓	-
Cu_2O (310)	0.13	✓	✓	✓	✓	-	-
Cu_2O (321)	0.11	✓	✓	✓	-	-	-
Cu_2O ($12\bar{4}$)	0.08	-	✓	✓	-	-	-

From the TEM images, it is also observed that there is a formation of core-shell kind of NPs for the samples synthesized for higher ablation duration of 30 and 60 minutes. The formation of core-shell NPs is believed to be due to the encapsulation of the NPs formed initially by the carbon from the surrounding liquid [12]. When laser ablation is carried out in the organic solvents, the number of hydrogen and carbon species generated is more than that of oxygen species due to the lower bond energies of C-C (347 kJ/mol) and C-H (413 kJ/mol) as compared to that of O-H (467 kJ/mol). The carbon from the solvent encapsulates the Cu NPs formed by the ablation of the Cu target thus favouring the

formation of insufficiently oxidized NPs in organic solvents. The carbon encapsulation of the NPs in the synthesis of NPs via pulsed laser ablation in organic solvents has been widely reported [12, 16, 17].

In order to confirm the carbon encapsulation, the high resolution TEM (HRTEM) image of one of the core-shell NPs in sample P3 is depicted in figure 5.2(f). The HRTEM image clearly shows the lattice fringes corresponding to graphitic carbon (d ~ 0.34 nm) surrounding the NPs confirming the carbon encapsulation of the Cu@Cu_2O NPs.

The X-ray diffraction (XRD) spectra of the Cu NP samples synthesized in methanol and 2-propanol for an ablation duration of 60 minutes, Fig. 5.3, show the peak corresponding to Cu(111) plane only, which was also detected in the SAED patterns. The absence of oxide phase of the synthesized NPs indicates comparatively small amount of oxidation. However, the SAED patterns due to the electrons is more sensitive as compared to XRD and is able to detect the various orientations of oxide phase though it is present in minutest quantity [18].

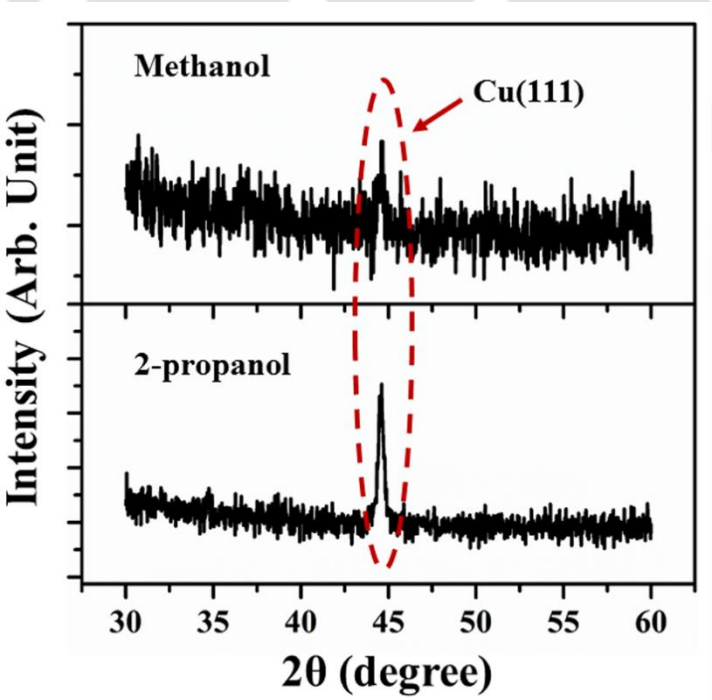

Figure 5.3 *XRD spectra of Cu NP samples synthesized in methanol and 2-propanol for an ablation duration of 60 minutes.*

5.3.1.2 Surface plasmon resonance of Cu NPs

The UV-visible absorption spectra of the colloidal solutions of Cu NPs, M1-M3 and P1-P3 synthesized in methanol and 2-propanol, respectively are depicted in Fig. 5.4(a) and (b). The SPR peak of the samples are clearly observed in both the figures.

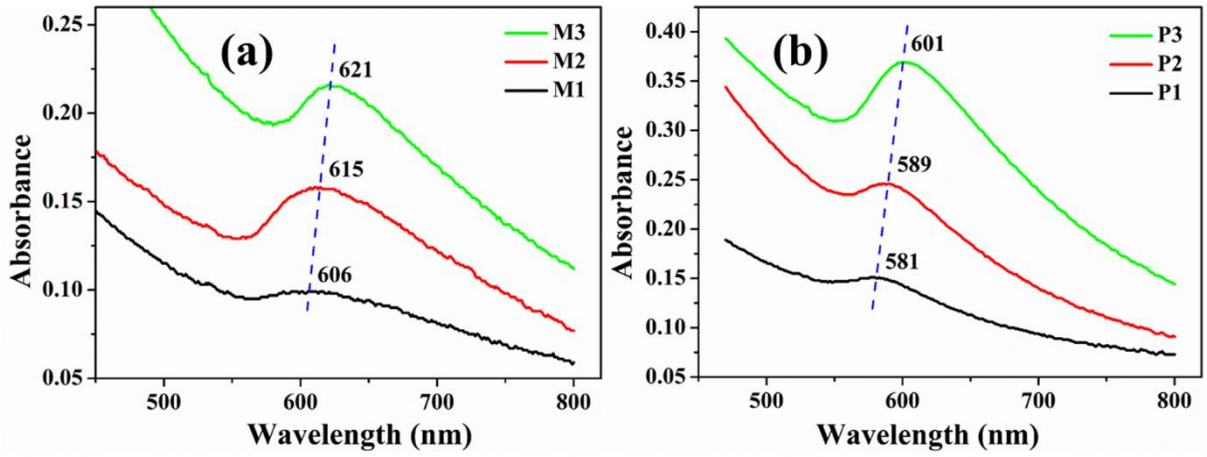

Figure 5.4 *UV-Visible absorption spectra of samples* **(a)** *M1-M3 and* **(b)** *P1-P3.*

The absorption spectra vividly reveal a red-shift in the SPR peak with the increase in ablation duration for the NPs synthesized in both the liquids. For the samples M1-M3, the SPR peak shifts from ~ 606 to 621 nm with the increase in ablation duration from 15 to 60 minutes, respectively. This shift is due to the increase in the average size of the NPs from ~ 7 to 19 nm, which was confirmed by the TEM images, Fig. 5.1. As already discussed in chapter 3, according to Mie theory, there is a peak-shift in an absorption spectrum with the change in the size distribution of the particles [19]. A red shift in the absorption spectrum is generally pertaining to the increase in size of the NPs [20].

In the case of samples P1-P3, the SPR peak shifts from ~ 581 to 601 nm with the increase in ablation duration from 15 to 60 minutes, respectively which is again due to increase in the average size of the NPs from ~ 9 to 17 nm (Fig. 5.2). The NPs synthesized by pulsed laser ablation in DW, as already mentioned in chapter 3, exhibited a blue-shift in the SPR peak position with the increase in the laser ablation duration which was confirmed

to be due to the reduction in the size of the NPs due to fragmentation for the longer exposure of laser.

From these observations, it is clear that the characteristics of NPs synthesized via PLAL is to a great extent dependent on the surrounding liquid medium. Thus, in order to understand the factors responsible for such observations, there is a need to study the effect of the various ambients on the target surface itself due to laser irradiation. Starting exactly from this, the laser ablated Cu target surface in different ambients is analysed and presented in the following sections.

5.3.2 Surface characterization of the laser ablated Cu target in different ambients

Once the target is ablated via laser, the ablated material condenses in the form of NPs, leaving behind the cavity or crater on the target in the focal region of the laser beam. To study the effect of surrounding liquid, the laser produced craters were fabricated, as described in section 5.2, in four different ambients, air, DW, methanol and 2-propanol.

5.3.2.1 Optical microscope images of laser produced crater

The optical micrographs of the laser produced craters in air, DW, methanol and 2-propanol are depicted in Fig. 5.5(a)-(d), respectively. The crater produced in air, Fig. 5.5(a), is surrounded by a thick blackish envelope. This black envelope is due to the formation of CuO in the sample as a result of excessive aerobic oxidation taking place during ablation in air ambient. The crater produced in DW, Fig. 5.5(b), also shows a darker layer in the peripheral region of the crater but the degree of oxidation is visibly less as compared to that in air.

In the peripheral regions of the craters produced in methanol and 2-propanol, Fig. 5.5(c) and (d), respectively, there is hardly any blackish layer indicating the absence of CuO phase. However, in both the cases, a blueish envelope along the periphery of the crater is observed which may be due to the formation of oxygen deficient phase of Cu_2O (known

to be blue in color). Thus, optical micrographs distinctly indicate the effect of the surrounding medium during laser ablation on the extents of oxidation on the target surface. A better understanding on the formation of Cu_2O and CuO phases could be possible by subjecting the samples to Raman spectroscopic studies as described in the next subsection, 5.3.2.2.

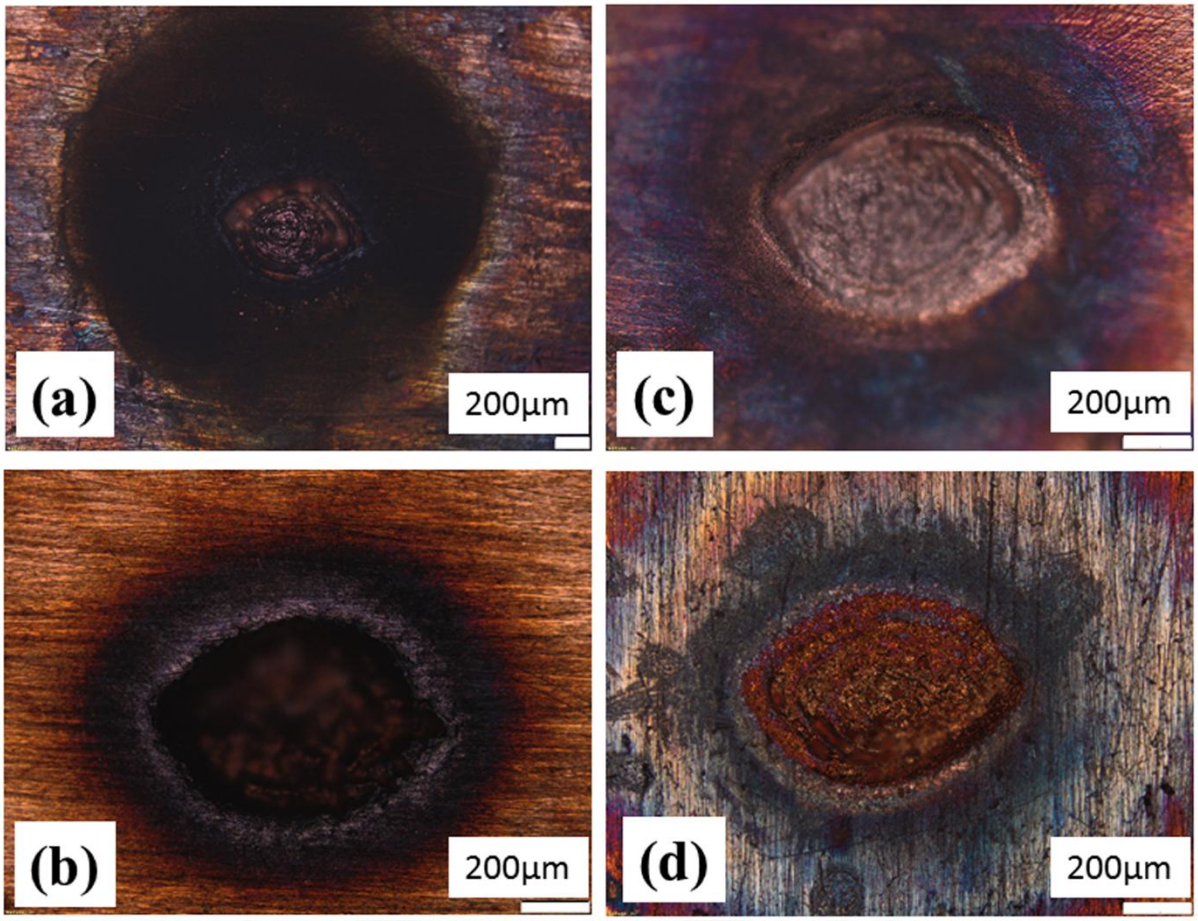

Figure 5.5 *Optical micrographs of laser ablated crater produced in* **(a)** *air,* **(b)** *DW,* **(c)** *methanol and* **(d)** *2-propanol.*

5.3.2.2 Raman analysis of the craters

In order to verify the observations from the optical micrographs, the ablated surfaces were subjected to Raman spectroscopic measurements. The central region of the crater did not exhibit any Raman peak. However, the peripheral regions of the craters confirmed the presence of Cu_2O and CuO phases of NPs. For the sample ablated in air, prominent Raman

peaks at 292 and 340 cm^{-1} corresponding to A_g and B_g mode, respectively of CuO phase are observed as depicted in Fig. 5.6(a) [21].

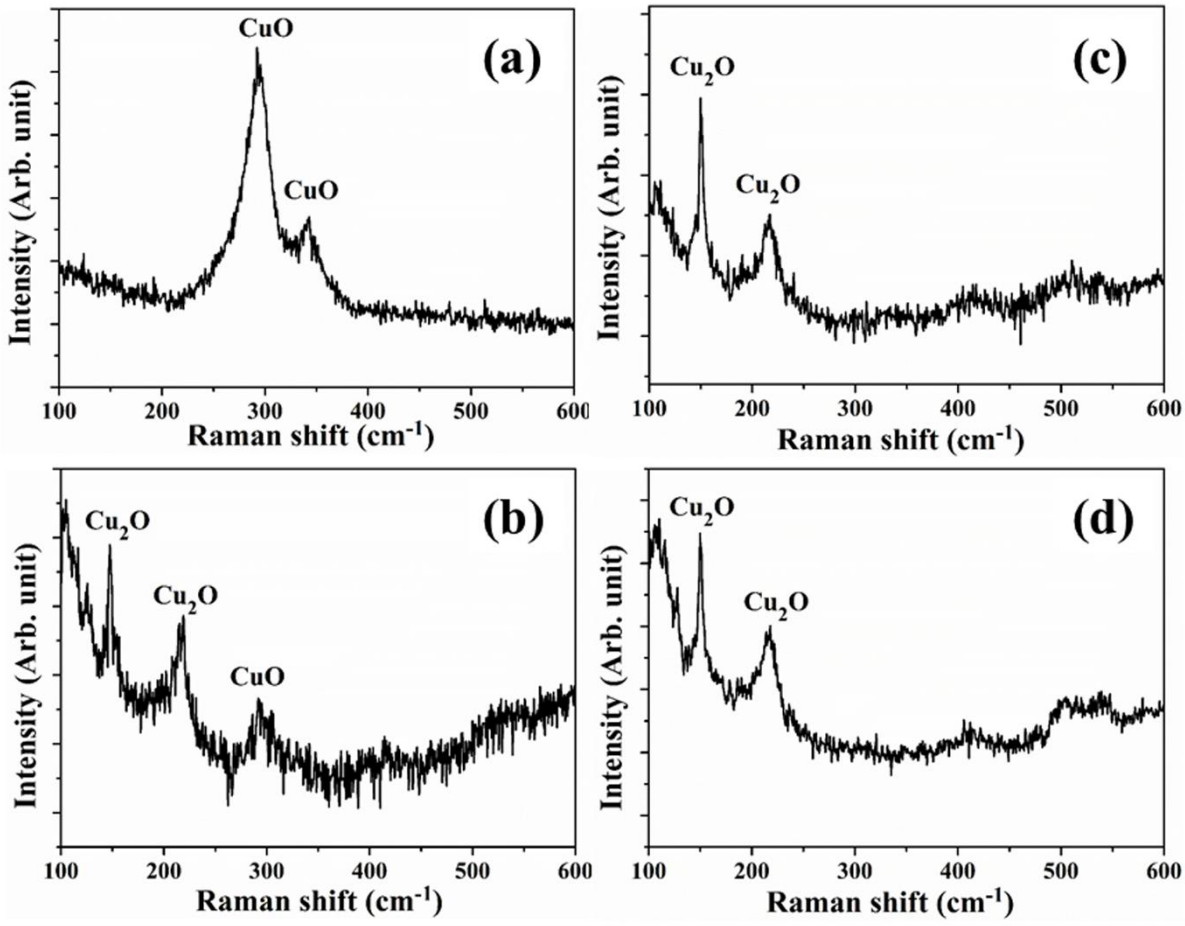

Figure 5.6 *Raman spectrum in the peripheral region of the laser ablated crater produced in* **(a)** *air,* **(b)** *DW,* **(c)** *methanol and* **(d)** *2-propanol.*

The Raman spectrum from the peripheral region of the crater produced in DW, Fig. 5.6(b), shows peaks at 149, 215 and 293 cm^{-1} [21]. The first two peaks correspond to Cu_2O, while the peak at 293 cm^{-1} corresponds to A_g mode of CuO. The Raman spectra of craters produced in the organic solvents, methanol and 2-propanol, shown in Fig. 5.6(c) and (d), respectively, exhibit peaks at 149 and 215 cm^{-1} corresponding to Cu_2O phase. It can be inferred that the periphery of the crater produced in air undergoes maximum oxidation followed by the one produced in DW. Organic solvents being oxygen deficient (along with large bond energy of O-H), the peripheral regions of the craters produced in methanol and 2-propanol are least oxidized and exhibited the oxygen deficient phase of Cu oxide. The

reproducibility of the observed result was verified by probing different regions of the crater with the micro-Raman laser. Thus, the Raman spectra of the different craters strongly support the predictions based on the optical micrographs of the craters regarding the formation of oxide phases.

5.3.2.3 Energy dispersive X-ray of the craters

The optical micrographs of the laser produced craters elucidate the oxide formation around the crater periphery but does explain the oxide formation in the entire crater region. Also, no Raman signal could be detected at the central portion of the craters. Hence, in order to assess the degree of oxidation in the complete crater region, all the samples were subjected to energy dispersive X-ray (EDX) analysis. The percentage of oxygen in different regions of the crater can be a good indication of the degree of oxide formation. For this, the craters produced in all the four ambients have been divided into four different regions viz., one central and three peripheral as shown in Fig. 5.7 (as an example, for the crater produced in air). Similar division of region was also implemented while analysing the craters formed on the Cu target immersed in various liquids.

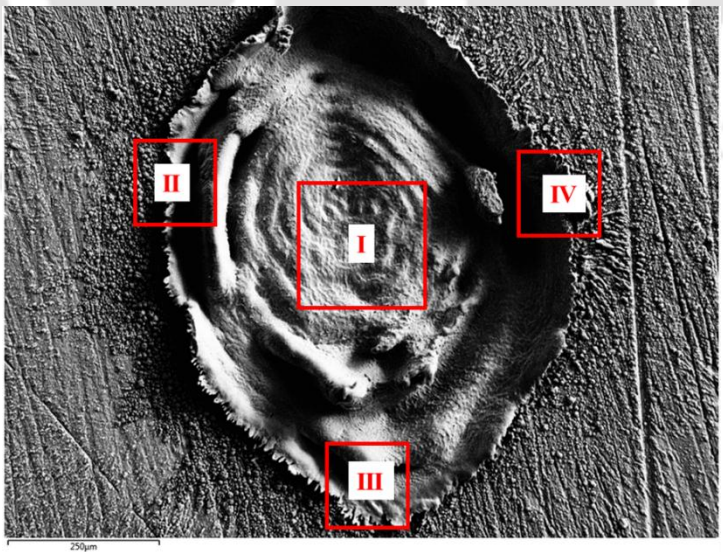

Figure 5.7 *FESEM image of laser produced crater in air exhibiting the different regions chosen for EDX analysis.*

The % composition of Cu and O along with the EDX spectra of all the four regions of the crater in all the samples are shown in Fig. 5.8-5.11.

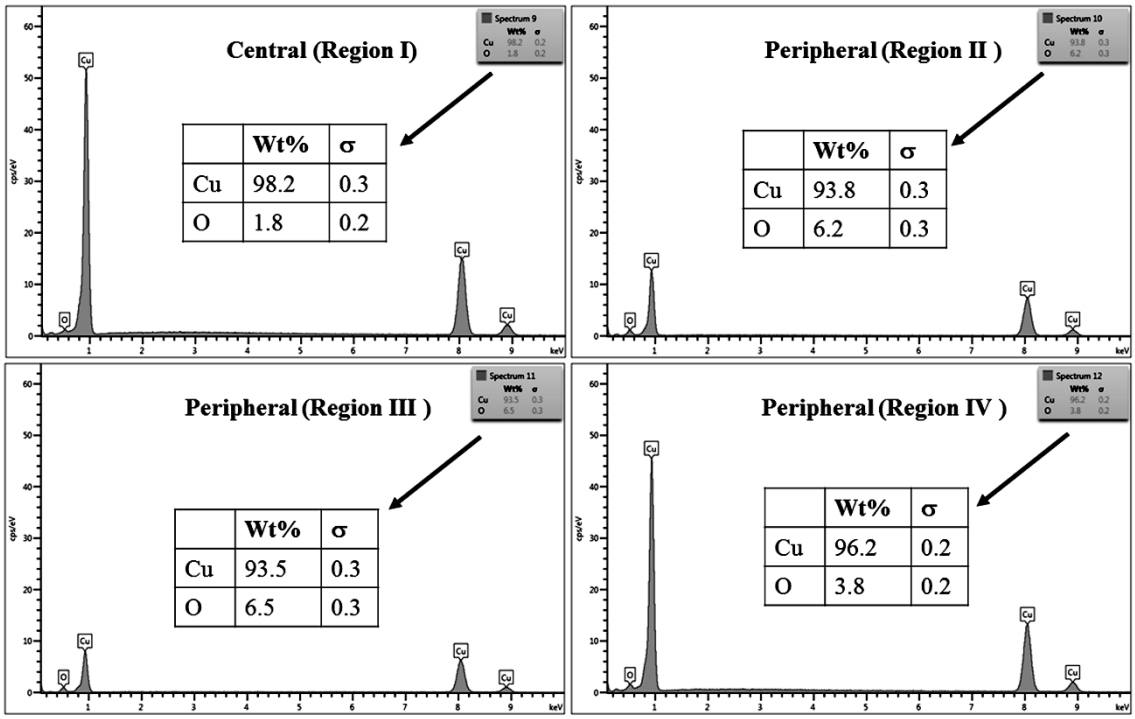

Figure 5.8 *EDX spectra from different regions of crater produced in air.*

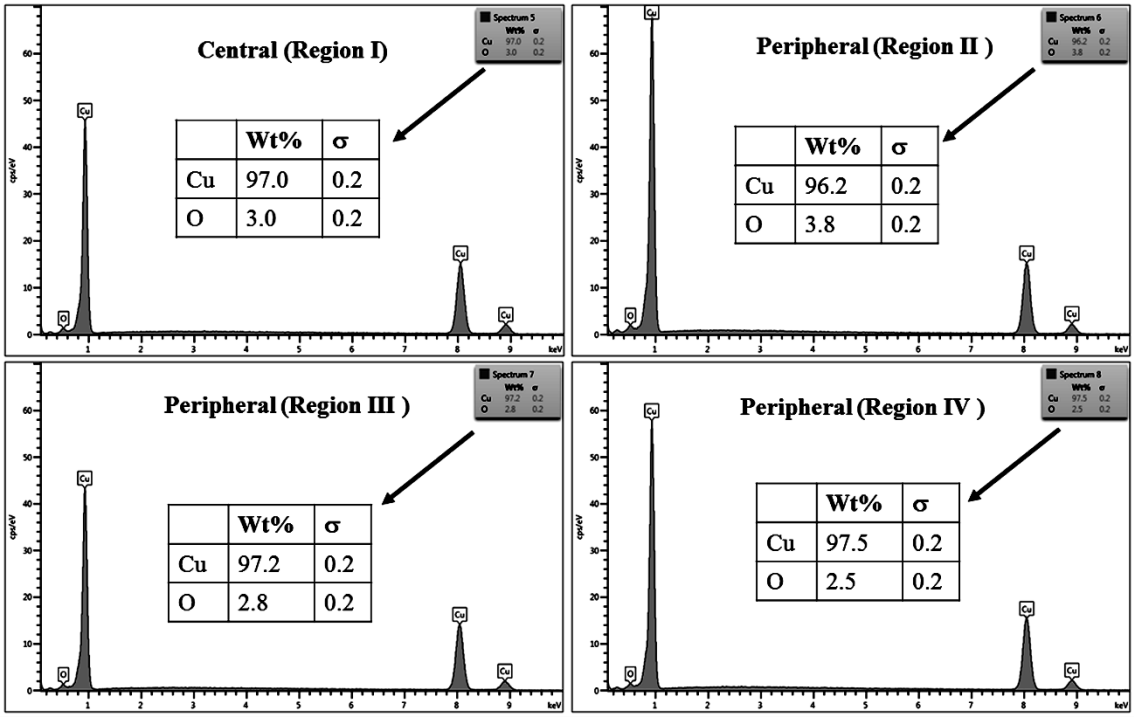

Figure 5.9 *EDX spectra from different regions of crater produced in distilled water (DW).*

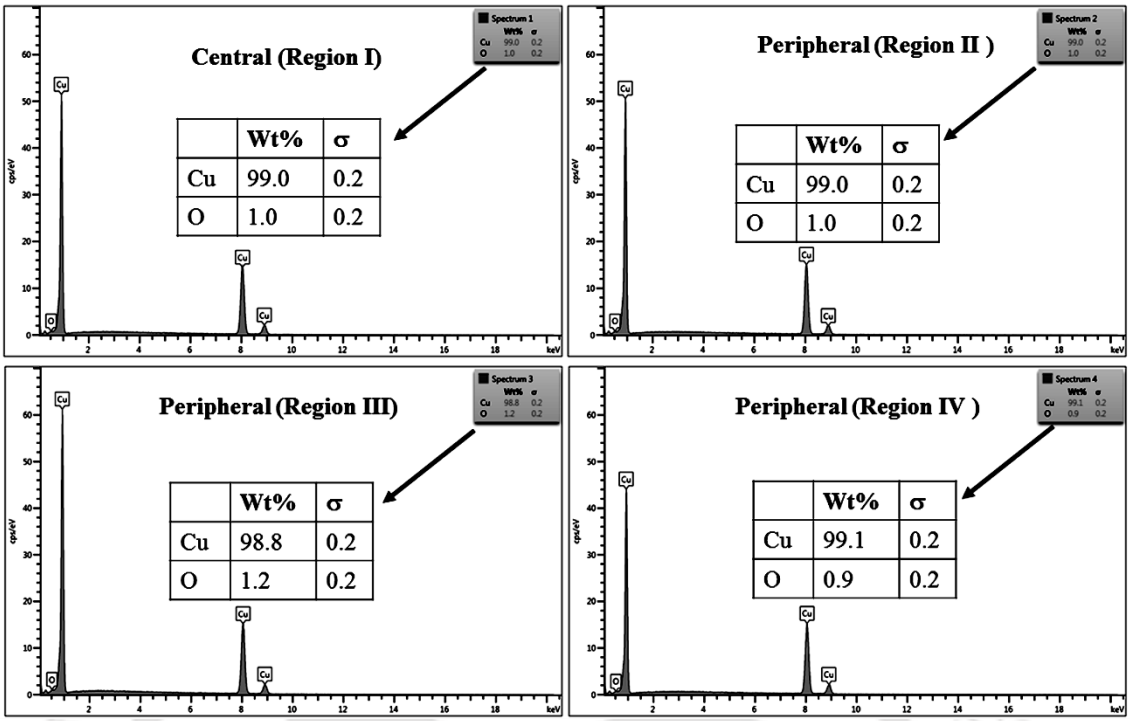

Figure 5.10 *EDX spectra from different regions of crater produced in methanol.*

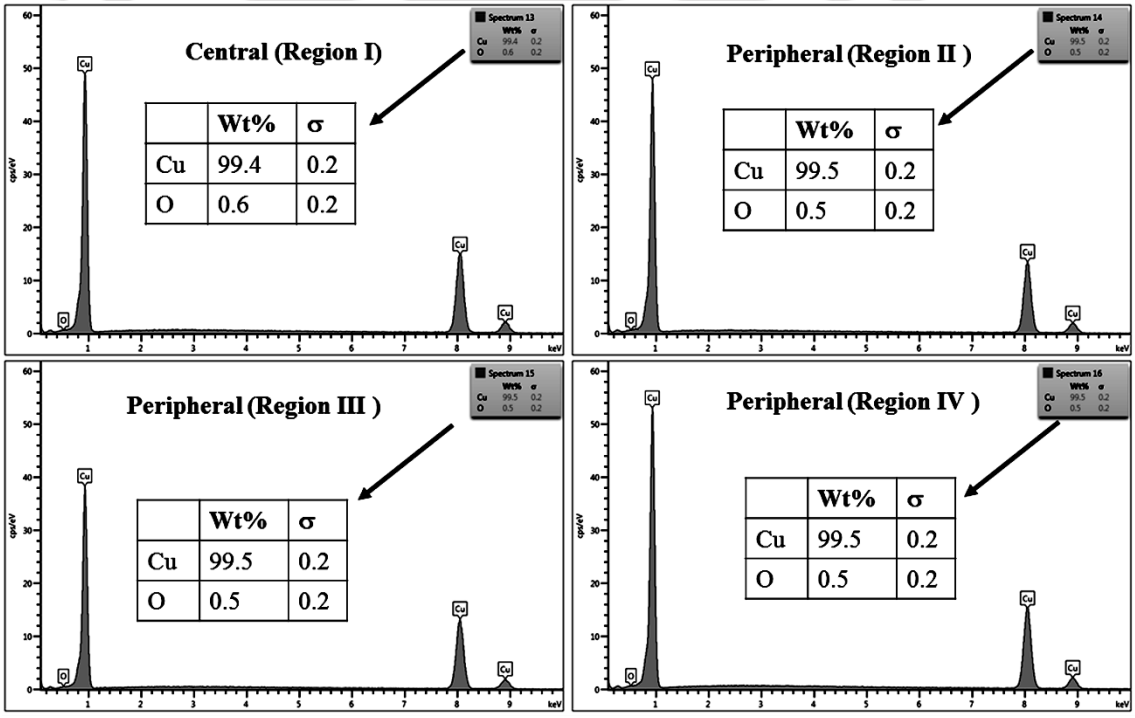

Figure 5.11 *EDX spectra from different regions of crater produced in 2-propanol.*

For clarity, the EDX data is also represented graphically in Fig. 5.12(a)-(d) for the ablation carried out in air, DW, methanol and 2-propanol, respectively. In the central portion of the crater i.e. region I, the oxygen content is 1.8, 3.0, 1.0 and 0.6 wt% for air, DW, methanol and 2-Propanol, respectively. In the other three regions, the oxygen content is the maximum for ablation in air followed by DW and methanol, and is found to be the least for 2-propanol. The amount of oxygen present in the four representative regions of the laser ablated craters in different ambients complements the optical micrographs and Raman spectroscopic analysis.

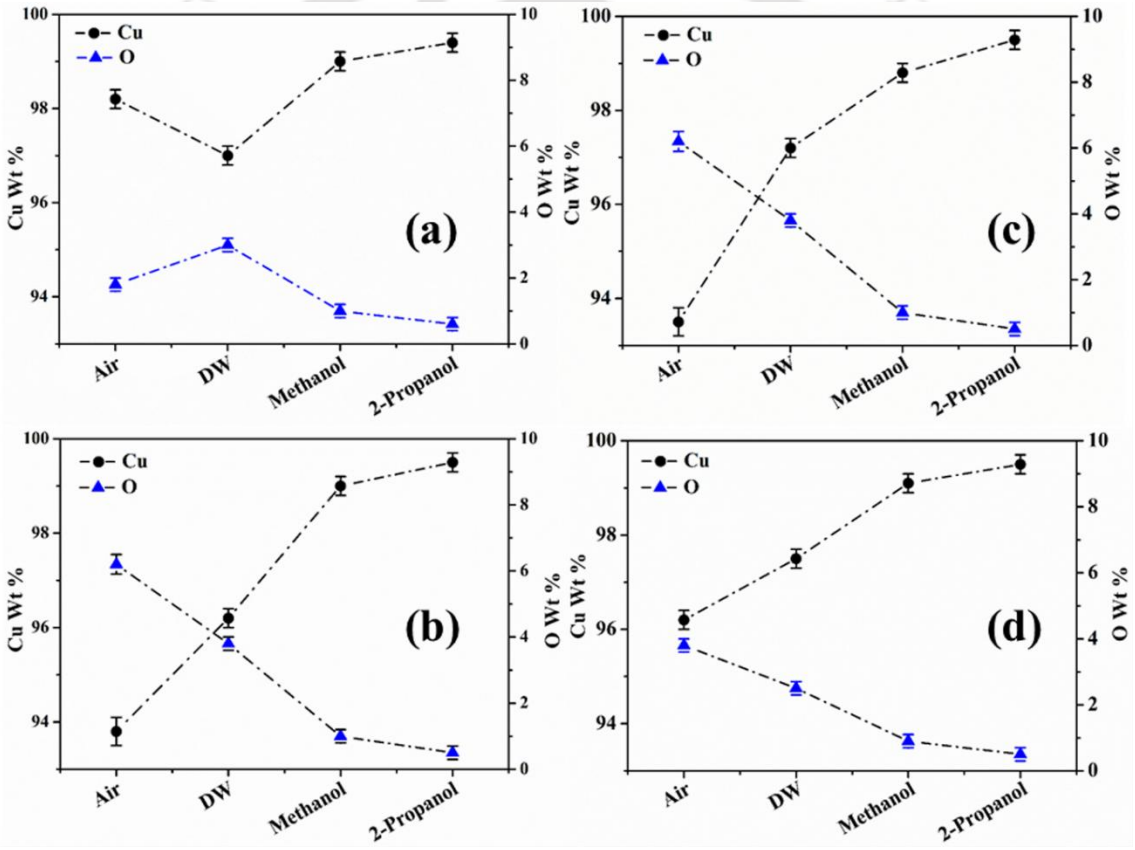

Figure 5.12 *Graphical representation of the EDX result of craters produced in different ambient for* **(a)** *region I,* **(b)** *region II,* **(c)** *region III and* **(d)** *region IV.*

Except for the central region of the craters, the oxygen content in the peripheral regions decreases in the order: air, DW, methanol, 2-propanol. The % of oxygen for the case of ablation performed in 2-propanol is the least which is due to less oxidation taking

place on the target surface. In order to understand this, it is important to investigate the ablation efficiency in each ambient. With this in view, the craters were also subjected to surface profilometer to ascertain the amount of material ablated and hence the ablation rate which is described in the following subsection.

5.3.2.4 Surface profilometer analysis of the craters

The depth profiles of the craters produced in various ambients are shown in Fig. 5.13(a)-(d).

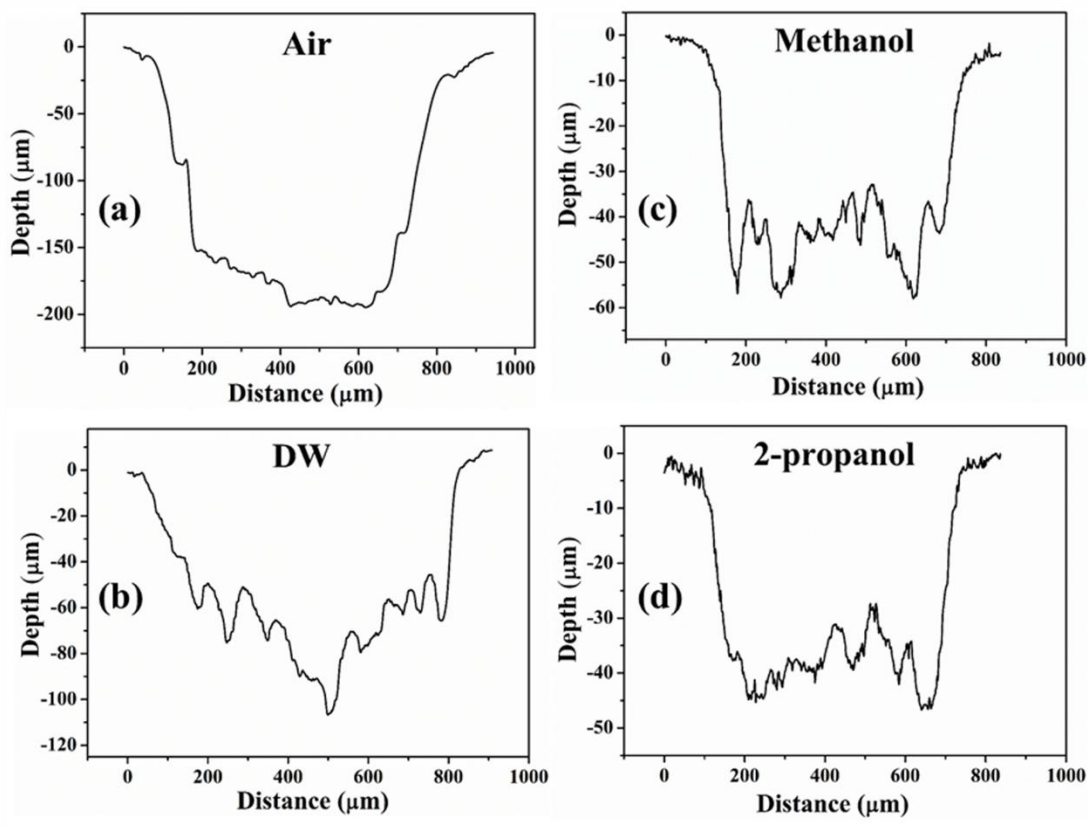

Figure 5.13 *Depth profiles of the craters produced in* **(a)** *Air,* **(b)** *DW,* **(c)** *Methanol, and* **(d)** *2-propanol.*

The depth of the crater produced in air is found to be the maximum, followed by the craters produced in DW, methanol and 2-propanol. In order to assess the mass ablation rate, the volume of the craters was measured by the surface profilometer. The volumes of the craters produced in air, DW, methanol and 2-propanol are found to be 2.91×10^{7}, 1.00×10^{7}, 0.47×10^{7} and 0.25×10^{7} μm^{3}, respectively. From this, the mass of the material

ablated from the target and hence the mass ablation rate (mass ablated per laser shot) was estimated.

The mass ablation rate in various ambients is depicted in Fig. 5.14. The ablation rate is maximum for ablation carried out in air and is minimum for that of in 2-propanol.

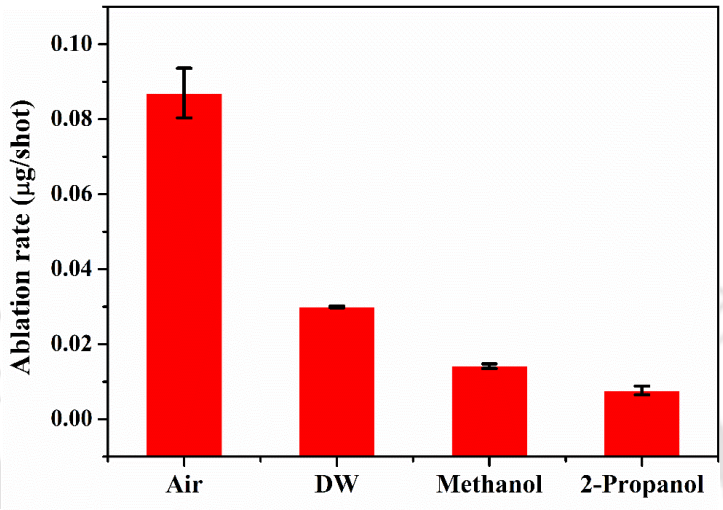

Figure 5.14 *Variation of mass ablation rate in different ambients.*

There are various factors responsible for the observed reduction in the ablation rate in liquid. With the presence of liquid column above the target, the ablation rate decreases as there is increased heat loss during as well as after the laser irradiation [22]. This results in a decrease in the temperature and pressure on the target and eventually the process of ablation becomes weaker. In the present case, the height of the liquid column was deliberately kept large as the focussing of the laser beam on the target surface through lower column height of liquid resulted in ignition of methanol and 2-propanol which are flammable liquids. So, the liquid level was maintained at ~ 4 mm above the target surface for all the three liquids.

The other factors which may equally affect the ablation rate are the various physical properties viz., density, thermal conductivity, etc. of the surrounding environment. The density of liquids decrease in the order: DW, methanol, 2-propanol. The difference in the density of DW and the two organic solvents is significant while there is only a marginal

difference among the densities of the two organic solvents. Due to stronger confinement of liquid having high density, the laser-produced plasma drives the molten surface layer of the target into superheated state [23]. As distilled water has higher density than methanol and 2-propanol, the mass ablation rate is highest in the case of ablation in distilled water.

Another reason behind higher ablation rate in DW may be explained by considering the plasma induced recoil pressure. The maximum pressure generated by liquid-confined plasma is given by the following equation: [23, 24]

$$P(GPa) = 0.01\sqrt{\frac{\alpha}{\alpha+3}} \times \sqrt{Z\ (g.cm^{-2}.s^{-1})} \times \sqrt{I_0(GW.cm^{-2})} \qquad (5.1)$$

where α is the fraction of internal energy devoted to thermal energy for ionization (typically α = 0.1), I_0 is the incident intensity. The reduced shock impedance, Z between the target and the liquid medium is defined as [23, 24]

$$\frac{2}{Z} = \frac{1}{Z_{liquid}} + \frac{1}{Z_{target}} \qquad (5.2)$$

where Z_{liquid} *and* Z_{target} are the acoustic impedances of the surrounding liquid and target, respectively. Thus, the parameter Z takes into consideration the effect of both the surrounding liquid and the target. As α and I_0 are typically same for the ablation carried out in the different liquids, the maximum pressure generated may be considered to be changing with Z as

$$P(GPa) \propto \sqrt{Z} \qquad (5.3)$$

The acoustic impedance of Cu is 4.16×10^6 g cm^{-2} s^{-1} and that of DW, methanol and 2-propanol are listed in table 5.2 shown earlier in section 5.3.1.1. Using these values, the value of $\sqrt{Z}$ is evaluated to be ~ 535, 417 and 424 g$^{1/2}$cm^{-1}s$^{-1/2}$, respectively. Thus, the maximum pressure generated by DW-confined plasma is very high as compared to that

generated by methanol and 2-propanol confined plasmas. Higher plasma induced recoil pressure facilitates more mass removal thereby increasing the ablation rate. Thus, the mass ablation rate is maximum in DW as compared to the two organic liquids and there isn't much difference in the rate of ablation for methanol and 2-propanol.

5.3.2.5 Surface morphology of the craters using FESEM

The surface morphology of craters in each case was investigated using the Field emission scanning electron microscope (FESEM). Fig. 5.15(a)-(c) shows the central, the peripheral and magnified image of the peripheral region, respectively of the crater produced in air, while that of in DW are shown in Fig. 5.15(d)-(f), respectively.

As the laser beam is focussed onto the target surface, the temperature of the surface increases. Laser ablation in the nanosecond regime is mainly due to photo-thermal process. This may be understood by considering free electrons in the metal target which absorbs the optical energy from the laser radiation and gets excited. The excited electrons impart its excess energy as thermal energy to the lattice via non-radiative electron-phonon coupling instantaneously for a nanosecond laser pulse. This results in the propagation of energy into the solid target and consequently the temperature of the surface increases [25]. Once the ablation threshold of Cu is achieved, the material starts getting ablated in the form of hot plasma plume. The laser fluence used in the present case of ablation for Cu in air is ~ 10 J/cm^2 which is much above its ablation threshold of 1.6 J/cm^2 at laser wavelength of 532 nm [26]. The plasma temperature at this stage is as high as ~ 9270 and 5798 K in air and water, respectively [27, 28]. Due to the attainment of extremely high temperature and pressure, evaporation of the target surface takes place leaving behind the molten pool of mass at the centre of the crater. Hence, once the plasma plume is over, for the crater produced in air, the central region consists of mostly melted layers of Cu which solidifies back at later stage after the termination of the laser pulse. This is evident in the FESEM

image (Fig. 5.15(a)). The fraction of material that ejected out during ablation gets re-deposited onto the target which then re-solidifies and lie along the periphery of the crater in the form of particles as observed in Fig. 5.15(b) and (c).

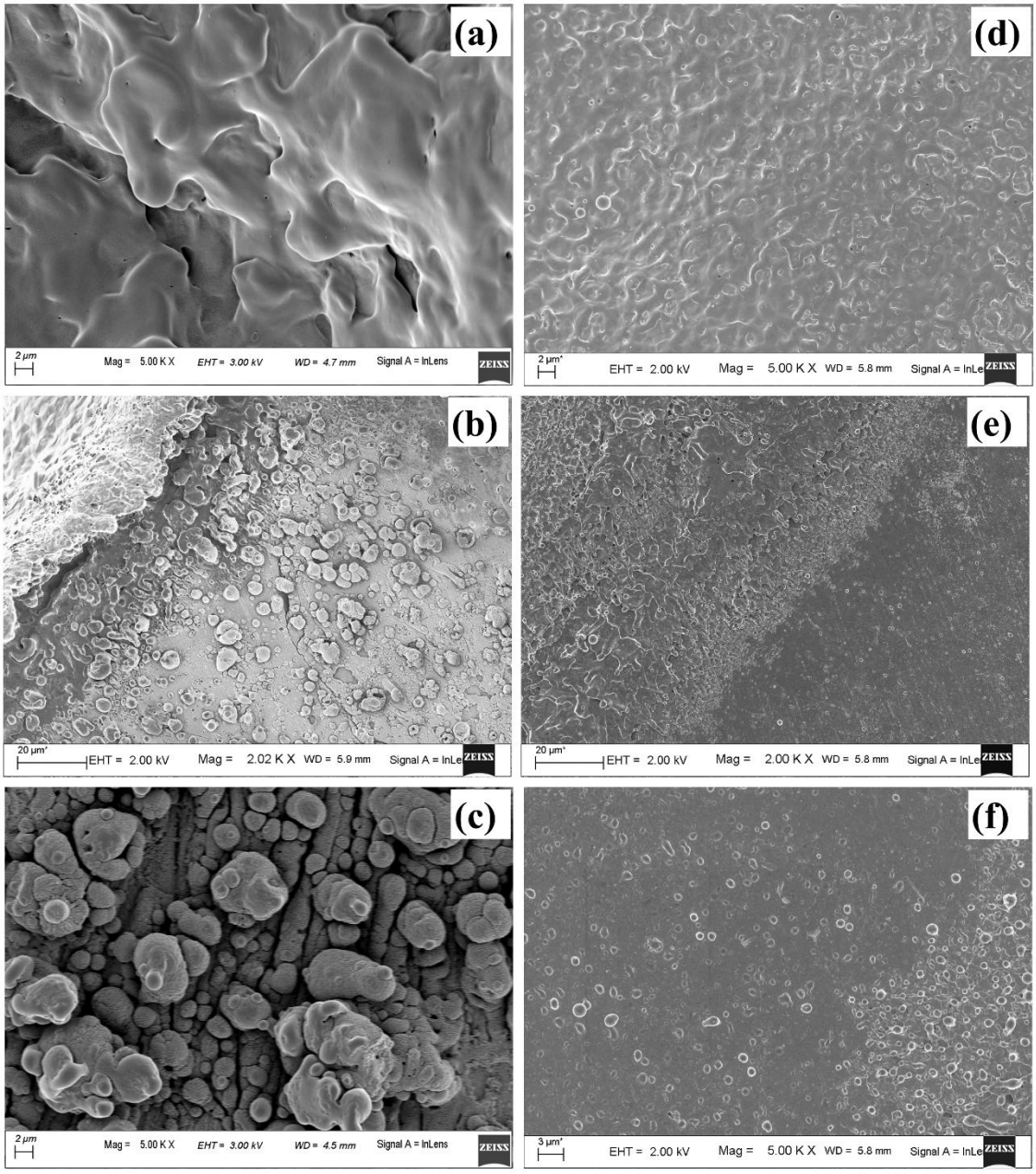

Figure 5.15 *FESEM images of* **(a)-(c)** *central, peripheral and the magnified image of the peripheral region, respectively of laser produced crater in air,* **(d)-(f)** *respective images of the crater produced in DW.*

The central portion of the crater produced in DW shows similar structure as in air but the melt-like structure is less prominent (Fig. 5.15(d)). This is because the surrounding

DW cools down the target surface much faster by dissipating most of the heat from the target surface [23]. The origin of this rapid decrease of temperature lies in the high thermal conductivity of water compared to that of air which results in more heat transfer in DW and hence a decrease in the plasma temperature. During ablation in DW, dissociation of the water molecules produces hydrogen and oxygen gas. As the thermal conductivity of hydrogen gas (0.187 W/mK) is much larger than that of air (0.026 W/mK) so the release of hydrogen gas facilitates faster cooling in DW [27]. So, the heat affected zone formed in the case of ablation in DW is less, thereby making the molten structures, formed in the central part of the crater, less prominent. The molten material at the centre of the crater splashes out due to the high pressure and is redeposited in the radially outward direction which is visible in the peripheral region of the crater shown in Fig. 5.15(e) and 5.15(f). Also, unlike in air, there are only a few particles present along the periphery of the crater in DW as most of the molten material is washed away and remain suspended in the DW in the form of NPs.

Fig. 5.16(a)-(b) and Fig. 5.16(c)-(d) depict the central and peripheral regions, of the crater produced in methanol and 2-propanol, respectively. For the craters produced in both these organic solvents, the central region is dominated by thin layers of solidified melt similar to that observed in DW. However, there is appearance of small micro pores as observed in Fig. 5.16(a) and 5.16(c). There are reports on the formation of micro pores due to etching action of organic solvents on the target surface during laser ablation [29]. This strong etching property of methanol and 2-propanol may result in the formation of micro-pores on the surface of the target. Again, it is observed that the number of such micro pores are slightly more in the case of 2-propanol than in methanol. During plasma formation, the pressure created in the focal volume of the laser beam is enormously high and at higher pressure, 2-propanol is known to have higher etch rate than methanol [30]. This must be

the possible reason for observing more number of micro-pores for the ablation carried in 2-propanol. The periphery of the craters in methanol and 2-propanol are found to exhibit similar structure to that of the crater produced in DW. Moreover, the micro- pores which were observed in the central part are also found in the peripheral regions.

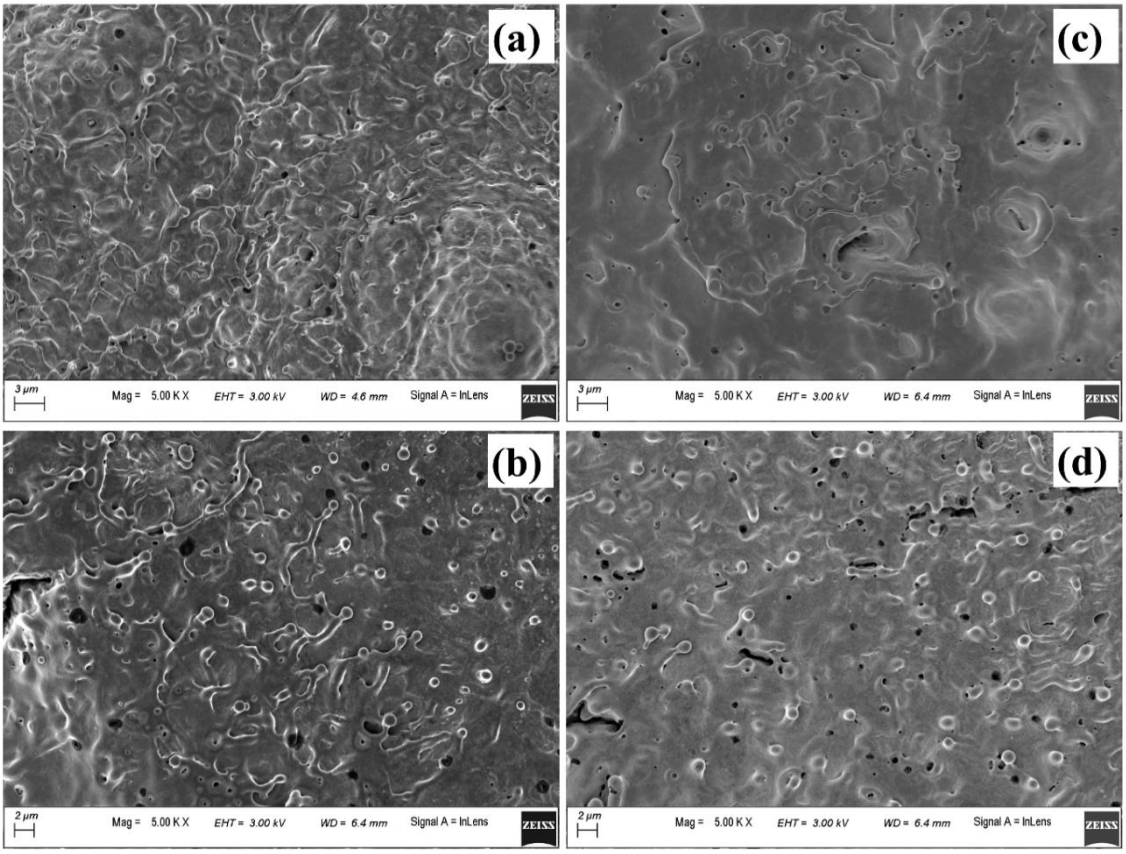

Figure 5.16 *FESEM images of* **(a)-(b)** *central and peripheral region, respectively of laser produced crater in methanol,* **(c)-(d)** *respective images of the crater produced in 2-propanol.*

Another possible reason for the formation of the micro-pores could be the volatile nature of the organic solvents. Due to this, during laser ablation, as the laser beam passes through the organic liquids, it was observed that the target plasma sometimes induces excess breakdown of the liquid and there is a cracking sound. This is due to a phase explosion taking place and as a result there is violent turbulence in the ejected material in the molten state. The molten mass cools and re-solidifies immediately but the imprint of the violent disturbance in the form of micro-pores remains embedded on it.

5.4 Conclusion

Insufficiently oxidized Cu NPs were synthesized by pulsed laser ablation of Cu target immersed in methanol and 2-propanol. The size of the NPs increases with the increase in the laser ablation duration and there is corresponding red-shift in the plasmonic peak in both the solvents. This behaviour is in sharp contrast to the NPs synthesized in DW. Oxidation of the NPs is found to be minimal for the synthesis of NPs in the organic solvents than that in DW. Carbon encapsulation of the NPs resulting in core-shell NPs is a reason behind the decrease in the oxidation occurring in the organic solvents. The ablation study of the laser produced crater in different ambient reveals that the process of laser ablation is dependent on the properties of the surrounding medium to a great extent. The ablation in air resulted in the formation of big sized NPs deposited on the target surface. In liquid ambient, the synthesized NPs remain suspended in the surrounding liquid. It is also observed that cleaner surface with minimum amount of micro or nanoparticles are obtained for the laser ablated surface in liquids as compared to that of air. From the viewpoint of NP synthesis, the variation in the degree of oxidation of the NPs may be related to the less oxidation of the target surface in organic solvents as compared to DW and air, in addition to its encapsulation by carbon.

References

[1] J. Zhang, J. Liu, Q. Peng, X. Wang, Y. Li, Nearly monodisperse Cu_2O and CuO nanospheres: preparation and applications for sensitive gas sensors, Chemistry of materials, **18** (2006) 867-871.

[2] J. Choi, H. Oh, S.-W. Han, S. Ahn, J. Noh, J.B. Park, Preparation and characterization of graphene oxide supported Cu, Cu_2O, and CuO nanocomposites and their high photocatalytic activity for organic dye molecule, Current Applied Physics, **17** (2017) 137-145.

[3] S. Shinde, H. Dhaygude, D.-Y. Kim, G. Ghodake, P. Bhagwat, P. Dandge, V. Fulari, Improved synthesis of copper oxide nanosheets and its application in development of

supercapacitor and antimicrobial agents, Journal of Industrial and Engineering Chemistry, **36** (2016) 116-120.

[4] X. Liu, J. Chen, P. Liu, H. Zhang, G. Li, T. An, H. Zhao, Controlled growth of CuO/Cu_2O hollow microsphere composites as efficient visible-light-active photocatalysts, Applied Catalysis A: General, **521** (2016) 34-41.

[5] S. Chatterjee, A.J. Pal, Introducing Cu_2O thin films as a hole-transport layer in efficient planar perovskite solar cell structures, The Journal of Physical Chemistry C, **120** (2016) 1428-1437.

[6] Y. Han, R. Lupitskyy, T.-M. Chou, C.M. Stafford, H. Du, S. Sukhishvili, Effect of oxidation on surface-enhanced Raman scattering activity of silver nanoparticles: a quantitative correlation, Analytical Chemistry, 83 (2011) 5873-5880.

[7] J. Ruusunen, M. Ihalainen, T. Koponen, T. Torvela, M. Tenho, J. Salonen, O. Sippula, J. Joutsensaari, J. Jokiniemi, A. Lähde, Controlled oxidation of iron nanoparticles in chemical vapour synthesis, Journal of Nanoparticle Research, **16** (2014) 2270.

[8] S. Jeong, K. Woo, D. Kim, S. Lim, J.S. Kim, H. Shin, Y. Xia, J. Moon, Controlling the Thickness of the Surface Oxide Layer on Cu Nanoparticles for the Fabrication of Conductive Structures by Ink-Jet Printing, Advanced Functional Materials, **18** (2008) 679-686.

[9] H. Zeng, X.W. Du, S.C. Singh, S.A. Kulinich, S. Yang, J. He, W. Cai, Nanomaterials via laser ablation/irradiation in liquid: a review, Advanced Functional Materials, **22** (2012) 1333-1353.

[10] D. Zhang, B. Gökce, S. Barcikowski, Laser synthesis and processing of colloids: fundamentals and applications, Chemical reviews, **117** (2017) 3990-4103.

[11] R.M. Tilaki, A. Iraji zad, S.M. Mahdavi, Size, composition and optical properties of copper nanoparticles prepared by laser ablation in liquids, Applied Physics A, **88** (2007) 415-419.

[12] P. Liu, H. Wang, X. Li, M. Rui, H. Zeng, Localized surface plasmon resonance of Cu nanoparticles by laser ablation in liquid media, RSC Advances, **5** (2015) 79738-79745.

[13] B. Kumar, D. Yadav, R.K. Thareja, Growth dynamics of nanoparticles in laser produced plasma in liquid ambient, Journal of Applied Physics, **110** (2011) 074903.

[14] J. Lam, D. Amans, F. Chaput, M. Diouf, G. Ledoux, N. Mary, K. Masenelli-Varlot, V. Motto-Ros, C. Dujardin, γ-Al 2 O 3 nanoparticles synthesised by pulsed laser ablation in liquids: a plasma analysis, Physical Chemistry Chemical Physics, **16** (2014) 963-973.

[15] H. Zeng, S. Yang, W. Cai, Reshaping formation and luminescence evolution of ZnO quantum dots by laser-induced fragmentation in liquid, The Journal of Physical Chemistry C, **115** (2011) 5038-5043.

[16] A. Baladi, R. Sarraf Mamoory, Investigation of different liquid media and ablation times on pulsed laser ablation synthesis of aluminum nanoparticles, Applied Surface Science, **256** (2010) 7559-7564.

[17] A. Kanitz, J.S. Hoppius, M. del Mar Sanz, M. Maicas, A. Ostendorf, E.L. Gurevich, Synthesis of magnetic nanoparticles by ultrashort pulsed laser ablation of iron in different liquids, ChemPhysChem, **18** (2017) 1155-1164.

[18] D.B. Williams, C.B. Carter, Diffraction in TEM, in: Transmission Electron Microscopy: A Textbook for Materials Science, Springer US, Boston, MA, 2009, pp. 197-209.

[19] G. Mie, Contributions to the optics of turbid media, particularly of colloidal metal solutions, Annalen der Physik, **25** (1908) 377-445.

[20] A. Takami, H. Kurita, S. Koda, Laser-Induced Size Reduction of Noble Metal Particles, Journal of Physical Chemistry B, **103** (1999) 1226-1232.

[21] A.S. Zoolfakar, R.A. Rani, A.J. Morfa, A.P. O'Mullane, K. Kalantar-zadeh, Nanostructured copper oxide semiconductors: a perspective on materials, synthesis methods and applications, Journal of Materials Chemistry C, **2** (2014) 5247-5270.

[22] H.W. Kang, A.J. Welch, Effect of liquid thickness on laser ablation efficiency, Journal of Applied Physics, **101** (2007) 083101.

[23] P. Ouyang, P. Li, E. Leksina, S. Michurin, L. He, Effect of liquid properties on laser ablation of aluminum and titanium alloys, Applied Surface Science, **360** (2016) 880-888.

[24] S. Zhu, Y. Lu, M. Hong, X. Chen, Laser ablation of solid substrates in water and ambient air, Journal of Applied Physics, **89** (2001) 2400-2403.

[25] J. Yu, Q. Ma, V. Motto-Ros, W. Lei, X. Wang, X. Bai, Generation and expansion of laser-induced plasma as a spectroscopic emission source, Frontiers of Physics, **7** (2012) 649-669.

[26] K.S. Singh, A.K. Sharma, Effect of variation of magnetic field on laser ablation depth of copper and aluminum targets in air atmosphere, Journal of Applied Physics, **119** (2016) 183301.

[27] B. Kumar, R.K. Thareja, Laser ablated copper plasmas in liquid and gas ambient, Physics of Plasmas, **20** (2013) 053503.

[28] M. Sabsabi, P. Cielo, Quantitative analysis of copper alloys by laser-produced plasma spectrometry, Journal of Analytical Atomic Spectrometry, **10** (1995) 643-647.
[29] V. Tangwarodomnukun, H.-Y. Chen, Laser ablation of PMMA in air, water, and ethanol environments, Materials and Manufacturing Processes, **30** (2015) 685-691.
[30] K. Torek, J. Ruzyllo, R. Grant, R. Novak, Reduced pressure etching of thermal oxides in anhydrous HF/alcoholic gas mixtures, Journal of the electrochemical Society, **142** (1995) 1322-1326.

Chapter 6

Dynamics of the Process of Laser Ablation in Liquid: Cavitation Bubbles and Shock Waves

6.1 Introduction

The mechanism behind the formation of nanoparticles (NPs) via pulsed laser ablation in liquid (PLAL) is an active area of research which although has been rigorously studied, never fails to raise curiosity in the researchers [1-3]. In order to understand the variation in the properties of the NPs in PLAL, it is extremely important to have a clear picture of the underlying mechanism [4, 5]. Once the laser beam is incident onto the target immersed in liquid, plasma formation of the target occurs which is followed by the release of shock waves (SWs) and subsequent formation of the cavitation bubbles. The behaviour of the SWs and the cavitation bubbles determines the properties of the NPs formed. As such, there have been many endeavours to study the dynamics of the SWs and the cavitation bubbles [5, 6].

For better understanding of the nucleation and growth of NPs synthesized via PLAL, studying the thermodynamical aspect of PLAL has been one approach. In order to delve into the thermodynamics of the processes involved, the determination of the pressure and temperature in the vicinity of the target due to the emitted SWs and also the same within the cavitation bubbles is essential. Diagnostic techniques like the shadowgraphy and the beam deflection techniques can be employed to characterize the exuberant nature of the SWs and the cavitation bubbles. In the shadowgraphy technique, image of the bubble and also the SW front as a function of time w. r. t. the laser pulse is captured to obtain the radius

of the bubble and the speed of propagation of the SW to understand the dynamical behaviour [7]. In contrast, in the beam deflection technique the entire time evolution of the SW and cavitation bubble can be obtained in a single shot of the laser [7]. The beam deflection technique is the simplest technique owing to the low-cost and high sensitivity associated with it. However, the technique is limited by its inability to get visualization of the dynamical evolution of the processes occurring in PLAL. Other techniques such as stroboscopic imaging and X-ray radiography to investigate the dynamics of PLAL and X-ray small angle scattering to study the particle formation inside the cavitation bubble have also been demonstrated by Reich *et al.* [5].

There are numerous reports on the study of the bubble expansion and the subsequent release of the NPs from it [8, 9]. However, the thermodynamics within the bubble is still largely unknown [10]. Hence, in the present work, an attempt has been made to study the dynamics of the cavitation bubbles and the SWs using shadowgraphy and beam deflection techniques. The bubble thermodynamics has been studied analytically by the cavitation based model developed by Lam *et al.* [10]. The SWs have been extensively studied by the beam deflection technique and the thermodynamical parameters estimated from it have been utilized to understand the nucleation of Cu@Cu_2O NPs synthesized via pulsed laser ablation of Cu in distilled water (DW). In chapter 3, it was reported that the laser fluence can be varied to tune the size of Cu@Cu_xO(x=1, 2) NPs. Hence, all the measurements in the work presented in this chapter have been carried out to draw conclusions regarding the impact of laser fluence on the bubble and SW dynamics and hence on the nucleation of NPs.

6.2 Experimental details

The experimental details for the study of the dynamics of the cavitation bubbles and SWs via shadowgraphy and beam deflection techniques are illustrated in chapter 2, section 2.5.

In the shadowgraphy set up, the temporal evolution of the bubbles was recorded by a charge coupled device (CCD) camera triggered appropriately at different interval of time w. r. t. the laser pulse. The dynamics of both the cavitation bubbles and SWs is studied via the beam deflection set up by recording the deflection in the probe cw He:Ne laser beam. The probe beam was made to fall onto a photodiode aligned for maximum signal. The experiment was performed in single shot mode of the laser. The laser fluences used were ~ 10, 16 and 22 J/cm^2, same as those used for the synthesis of NPs as reported in chapter 3.

6.3 Results and discussion

The shadowgraphic images of the cavitation bubbles captured at various delays w. r. t. the laser pulse are shown in Fig. 6.1, 6.2 and 6.3 for laser fluences of ~ 10, 16 and 22 J/cm^2, respectively. Each and every image in these figures is 1376×1040 pixel^2 and the distance was calibrated using a standard scale.

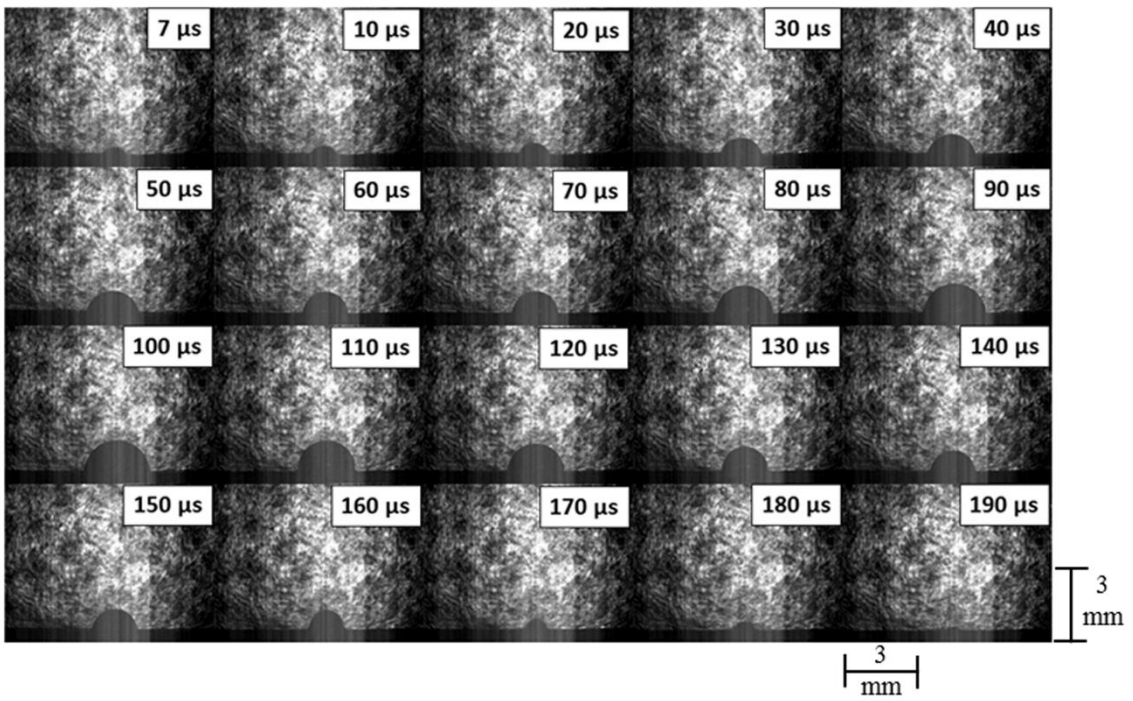

Figure 6.1 *Shadowgraphs of the cavitation bubbles at laser fluence of ~ 10 J/cm^2.*

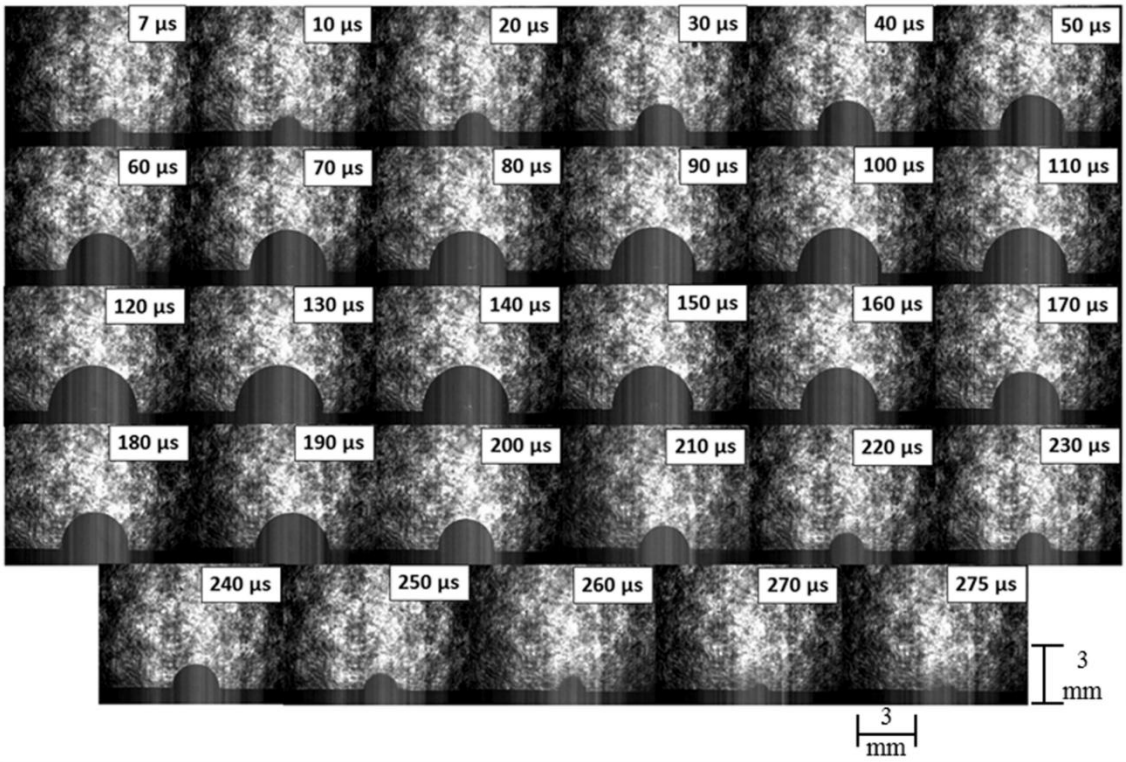

Figure 6.2 *Shadowgraphs of the cavitation bubbles at laser fluence of ~ 16 J/cm^2.*

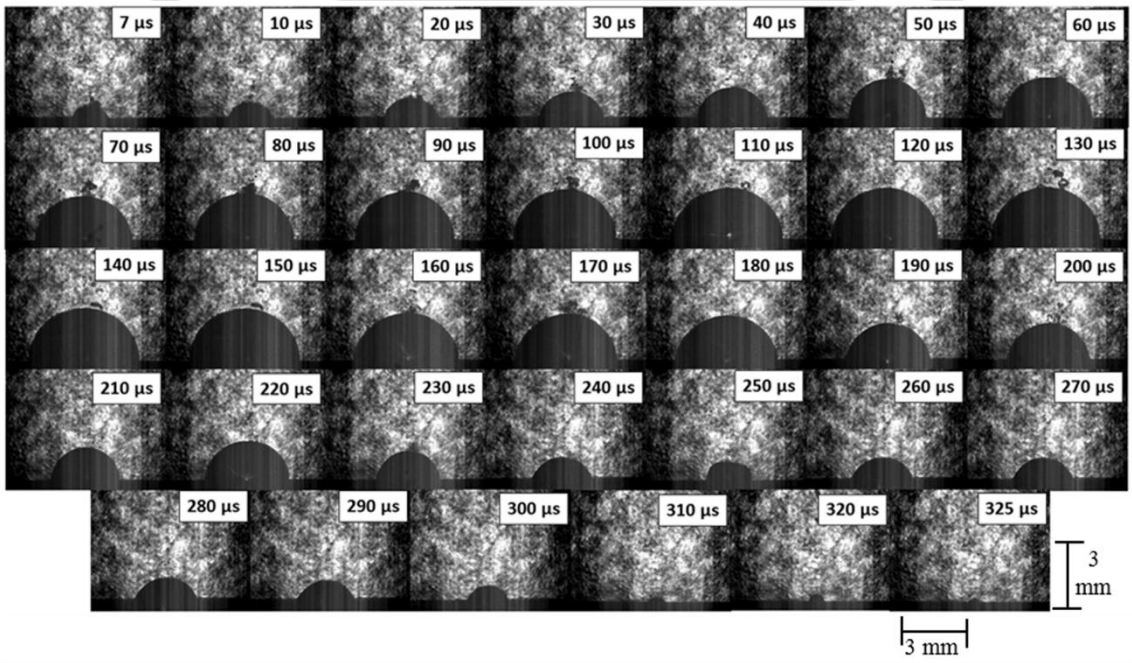

Figure 6.3 *Shadowgraphs of the cavitation bubbles at laser fluence of ~ 22 J/cm^2.*

From these images, the bubble radius was measured and its variation as a function of the delay time w. r. t. the laser pulse is shown in Fig. 6.4 for all the three laser fluences. The values shown in the figure are the average over images taken for 20 shots of laser. For

~ 10 J/cm^2, it is observed that the bubble starts expanding due to the inertia of the vaporized species present inside and reaches a maximum radius of 1.5 mm at a delay time of 100 µs w. r. t. the laser pulse. This is followed by a stage in which the bubble starts compressing in order to maintain the pressure with the hydrostatic pressure of the surrounding liquid. During this stage, the radius of the bubble continues to decrease and it decays completely after 190 µs. The same trend of increase upto a maximum radius followed by compression is also observed for higher fluences of ~ 16 and 22 J/cm^2.

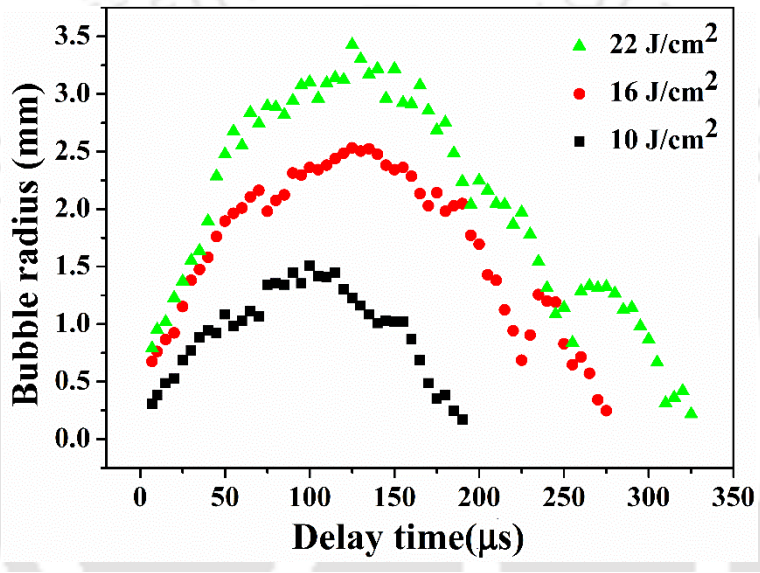

Figure 6.4 *Variation of bubble radius with time at various laser fluences.*

For the higher fluences of ~ 16 and 22 J/cm^2, the bubble expands upto a maximum radius of 2.5 and 3.4 mm, respectively at the same delay time of 125 µs. However, for both the fluences of ~ 16 and 22 J/cm^2, after attainment of maximum bubble radius, the bubble radius decreases and then increases again before decaying completely beyond 275 and 325 µs, respectively. The first increase in the bubble radius and its collapse is referred to as the first oscillation of the bubble [11, 12]. The subsequent increase followed by a decrease in the bubble radius which is observed in the case of higher fluences is the second oscillation of cavitation bubble [11, 12]. Collapse of each bubble gives rise to a new bubble and is the origin of a secondary oscillations. The secondary oscillation is much more pronounced for

laser fluence of ~ 22 J/cm^2 as compared to ~ 16 J/cm^2. No such oscillation was observed at lower fluence of ~ 10 J/cm^2.

In order to confirm the shadowgraphy results of the slight increase in the bubble radius towards the later stage of the cavitation bubble followed by its complete decay for the higher laser fluences, the beam deflection signals at these conditions were analyzed. The beam deflection traces at laser fluences of ~ 10, 16 and 22 J/cm^2, depicted in Fig. 6.5, show that the bubble lifetime from the shadowgraphy and beam deflection signal are in reasonably good agreement. For the fluence of ~ 10 J/cm^2, beam deflection trace does not show any second oscillation of the bubble which is in accordance with that of obtained from the corresponding shadowgraphic images. Interestingly, for ~ 16 and 22 J/cm^2, the speculation about the second oscillation obtained from the shadowgraphs of the bubbles is confirmed by the beam deflection signal which clearly shows the second oscillation. The oscillations are more prominent for the highest fluence of ~ 22J/cm^2.

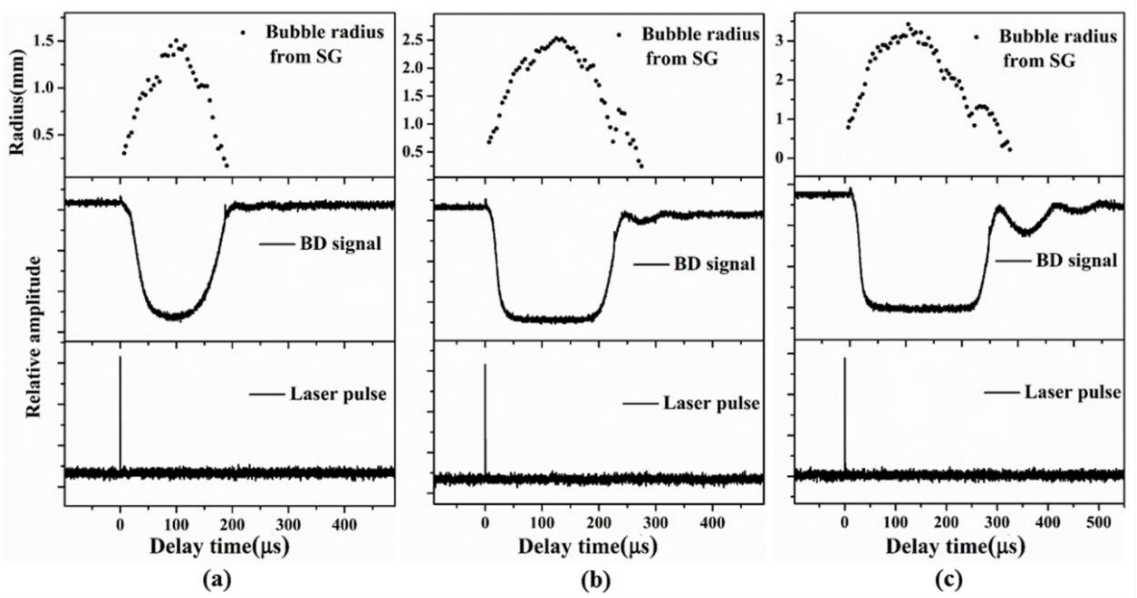

Figure 6.5 *Comparison of the temporal evolution of cavitation bubbles by shadowgraphy and beam deflection technique at laser fluence of* **(a)** *10,* **(b)** *16 and* **(c)** *22 J/cm^2; SG: Shadowgraphy, BD: Beam deflection.*

In the generation of NPs by the process of PLAL, the properties of NPs, its size in particular, is dependent on the dynamics of the cavitation bubble [6]. So, in order to

investigate the influence of laser fluence on the size of the NPs, the temperature and pressure inside the cavitation bubble should be estimated at various fluences. Depending on the magnitude of the pressure and temperature, an idea about the role of laser fluence on the size of the NPs can be ascertained.

The temporal evolution of the cavitation bubbles can be utilized to get the pressure profile of the bubbles. Analytically, the dynamics of the cavitation bubble is discussed based on the Rayleigh-Plesset (R-P) equation given by [10, 13, 14]

$$R\ddot{R} + \frac{3}{2}\dot{R}^2 = \frac{1}{\rho}\left[P_B(t) - P_l - \frac{2\sigma'}{R} - \frac{4\eta\dot{R}}{R} \right] \tag{6.1}$$

where R, ρ, P_B, P_l, σ', η represent the bubble radius, mass density of the liquid, internal pressure of the bubble, pressure of the surrounding liquid, liquid surface tension and viscosity of the liquid, respectively. $\dot{R} = \frac{dR}{dt}$ and $\ddot{R} = \frac{d^2R}{dt^2}$. Lam *et al.* have modified the R-P equation by neglecting the viscous term and the surface effects in the original equation [10]. For the case of water, it was shown that the ratio of inertial to viscous forces is ~ 10^3 and hence the contribution of the viscous term is negligible [10]. Moreover, the contribution of the inertial term as compared to surface tension is ~ 10^2 and can be neglected. Thus, the modified R-P equation is reduced to [10]

$$R\ddot{R} + \frac{3}{2}\dot{R}^2 = \frac{1}{\rho}\left[P_B(t) - P_l \right] \tag{6.2}$$

The bubble pressure, P_B as a function of time can be obtained by carrying out an integration of the R-P equation (6.2) w. r. t. time, which finally gives [10]

$$P_B(t) = (1-\gamma')\left[P_l + \frac{3\rho}{2}(\dot{R}^2 - \frac{C}{R^3}) \right] \tag{6.3}$$

where γ' is the ratio of the heat capacity and C is a constant of integration. Here, it has been assumed that the bubble evolution is adiabatic and the mass transfer to and from the bubble is neglected.

After estimating the pressure profile of the cavitation bubble, the temperature T_B of the bubble as a function of time was derived by using the isentropic equation for an ideal gas which is given by [10, 15]

$$T_B(t) = T_0 \left(\frac{P_B(t)}{P_0} \right)^{\frac{\gamma'-1}{\gamma'}} \tag{6.4}$$

where T_0 and P_0 are the temperature and pressure corresponding to the time from which the bubble expansion is considered i.e. t = 7 µs, in the present study. The value of P_0 was taken from the plot of $P_B(t)$ vs delay time and T_0 = 647 K was taken to be the critical temperature of the liquid i.e. water [10]. The value of P_0 is 3.02×10^8, 1.48×10^8 and 1.54×10^8 Pa for laser fluences of ~ 10, 16 and 22 J/cm^2, respectively. The reason behind taking the critical temperature as T_0 is that as the bubble is formed, the temperature inside the bubble is below the critical temperature of water and so the critical temperature is considered as the upper limit for T_0 [10]. The value of γ' was taken to be 1.22 for water [16].

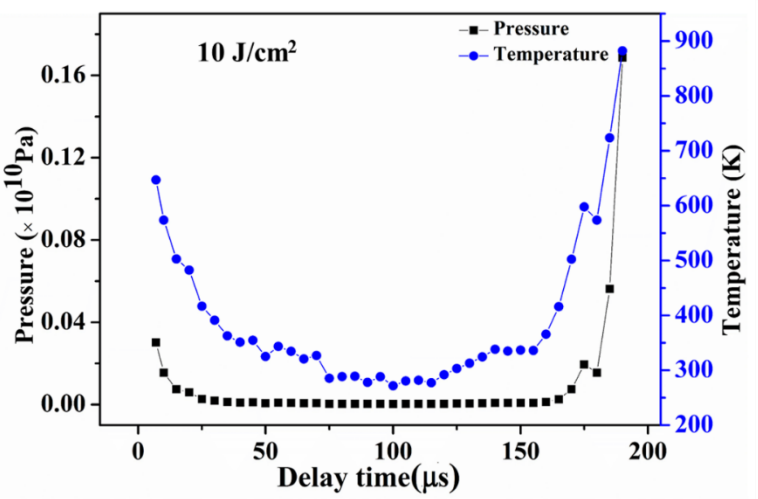

Figure 6.6 *Pressure and temperature profiles inside the cavitation bubble as a function of time at laser fluence of ~ 10 J/cm^2.*

The pressure and temperature profiles of the cavitation bubbles at laser fluences of ~ 10, 16 and 22 J/cm^2 are depicted in Fig. 6.6, 6.7 and 6.8, respectively.

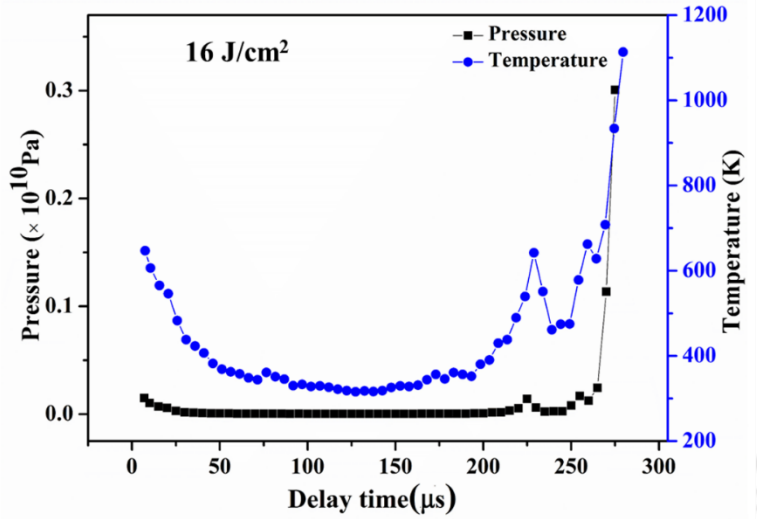

Figure 6.7 *Pressure and temperature profiles inside the cavitation bubble as a function of time at laser fluence of ~ 16 J/cm^2.*

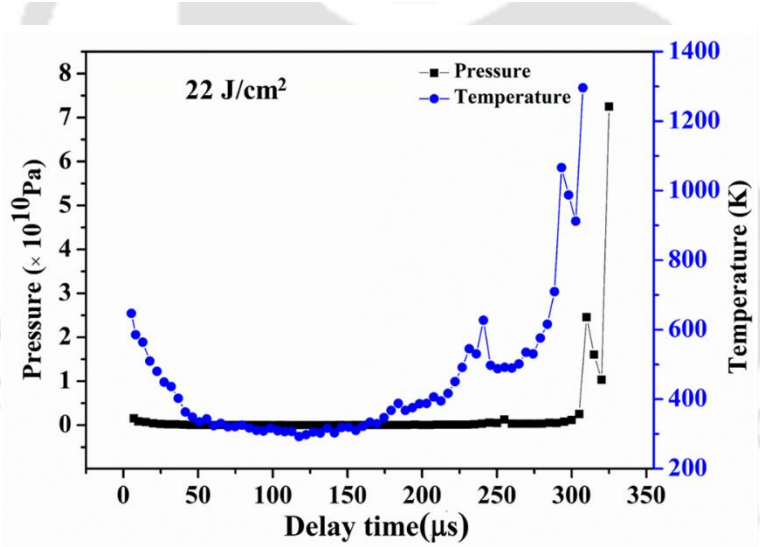

Figure 6.8 *Pressure and temperature profiles inside the cavitation bubble as a function of time at laser fluence of ~ 22 J/cm^2.*

Considering the dynamics of the bubble at the laser fluence of ~ 10 J/cm^2, the bubble pressure starts decreasing from ~ 3.0×10^8 Pa (at t = 7 μs) and reaches a value of ~ 1.2×10^7 Pa (at t = 35 μs). After this, the pressure of the bubble varies slowly and reaches a minimum of ~ 2.4×10^6 Pa at a delay of 100 μs (corresponding to the maximum size of the bubble) w. r. t. the laser pulse. Thereafter, the pressure starts increasing slowly upto ~ 1.7 ×10^7 Pa at

160 μs and then sharply increases upto ~ 1.7×10^9 Pa at 190 μs which denotes the collapse of the bubble.

At the fluences of ~ 16 and 22 J/cm^2, the pattern of pressure variation is similar but the low pressure regime is for a prolonged duration of 155 and 165 μs, respectively as compared to 135 μs for the fluence of ~ 10 J/cm^2. The minimum bubble pressure for ~ 16 J/cm^2 is found to be ~ 2.7×10^6 Pa at 125 μs and that for ~ 22 J/cm^2 is found to be ~ 1.9×10^7 Pa at 125 μs.

As far as the temperature evolution of the bubble as a function of delay time is concerned, the similar trend of decrease in the temperature of the bubble with the increase in delay time is observed. The temperature attains a minimum value at the same time as that of minimum pressure, after which the temperature of the bubble starts rising again till it reaches a maximum of nearly 1000 K in the case of ~ 10 J/cm^2 and more than 1000 K for fluences of ~ 16 and 22 J/cm^2. The variation of pressure and temperature values inside the cavitation bubbles estimated in the present study is of the same order of magnitude as those reported in pioneering works on cavitation bubbles carried out under similar conditions [16].

Another factor playing the role in the synthesis of NPs by PLAL, in addition to the cavitation bubbles, is the SWs [4, 6]. Laser ablation of the target immersed in liquid induces SWs in its vicinity which propagates away from the target [17]. The expanded view of beam deflection signal in the early phase as a function of distances above the target for the three laser fluences of ~ 10, 16 and 22 J/cm^2 are shown in Fig. 6.9, 6.10 and 6.11, respectively. The variation in the position of the SW front as a function of distance from the target along the direction of incident laser beam, implies the slowing down of the SWs as it moves away from the target.

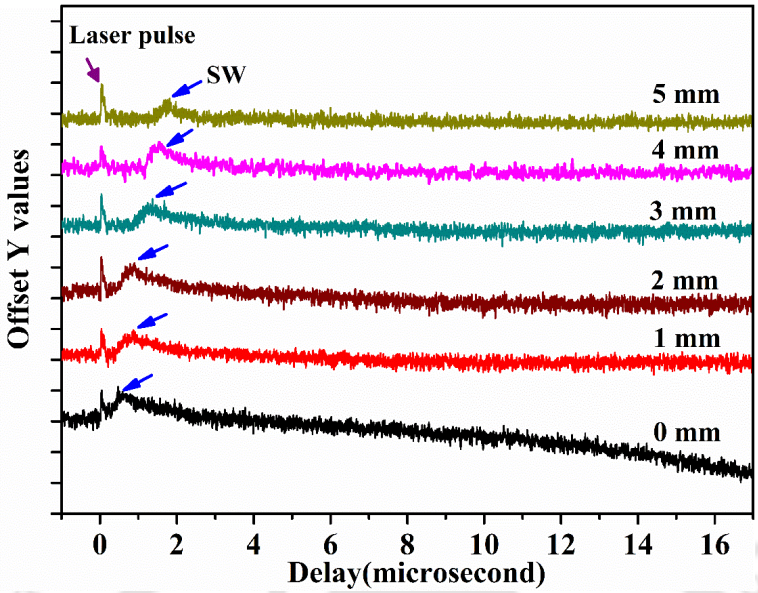

Figure 6.9 *Beam deflection trace showing the deflection corresponding to the first SW after the laser pulse at laser fluence of ~ 10 J/cm^2.*

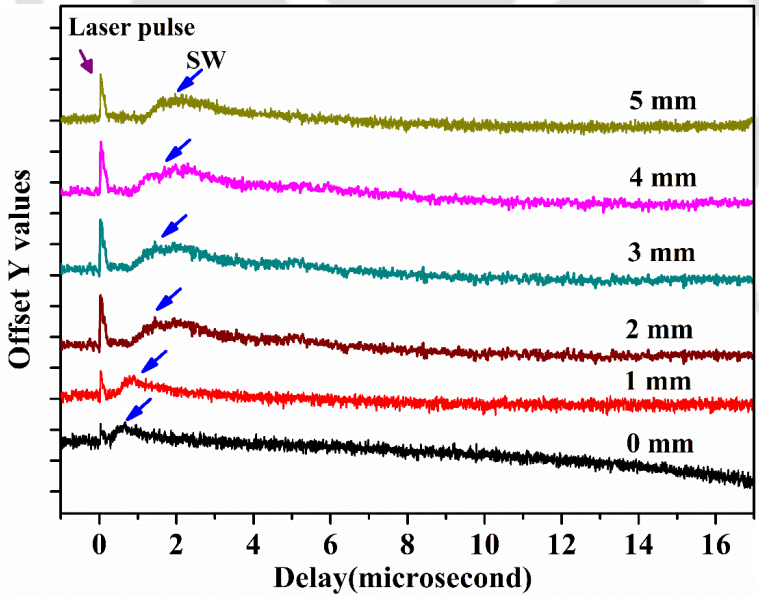

Figure 6.10 *Beam deflection trace showing the deflection corresponding to the first SW after the laser pulse at laser fluence of ~ 16 J/cm^2.*

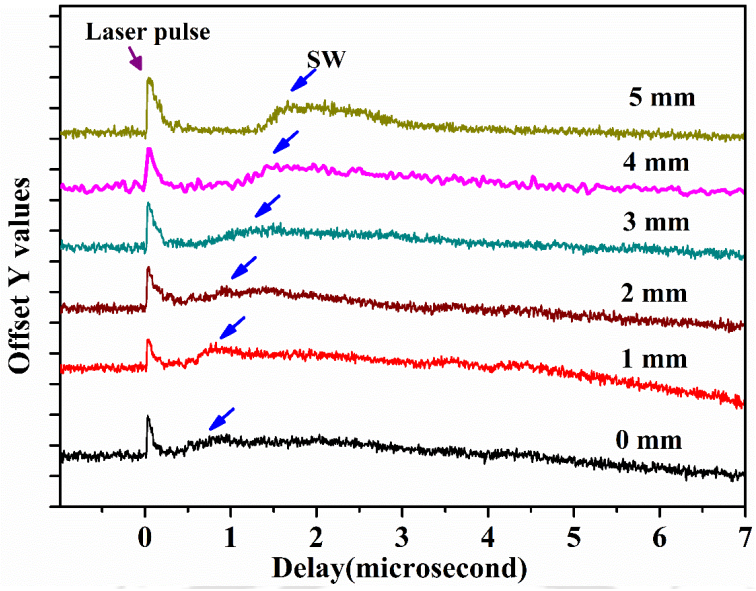

Figure 6.11 *Beam deflection trace showing the deflection corresponding to the first SW after the laser pulse at laser fluence of ~ 22 J/cm^2.*

The SW velocity, v_s was determined by considering the temporal evolution of the SW front as a function of positions w. r. t. the target surface. From the SW velocity, an estimate of the SW pressure can be obtained by the application of Newton's second law across a SW discontinuity. This is given by [18]

$$P_s - P_h = v_s v_p \rho \tag{6.5}$$

where P_s, P_h, v_s, v_p and ρ are the SW pressure, hydrostatic pressure, SW velocity, particle velocity and density of water, respectively.

The equation of state relates v_s and v_p and this relation is empirically stated as [18, 19]

$$v_S = a + bv_p \tag{6.6}$$

where a = 1.48 km/s is the velocity of sound in water and b = 2.07 is a constant.

The SW velocity as a function of distances from the target is shown in Fig. 6.12 (a)-(c) for laser fluences of ~ 10, 16 and 22 J/cm^2, respectively. As the SW propagates away from the target, its velocity decreases in all the three cases. The maximum SW velocity

estimated for ~ 10, 16 and 22 J/cm^2 are ~ 8.1 × 10^3, 9.5 × 10^3 and 12.1 × 10^3 m/s, respectively.

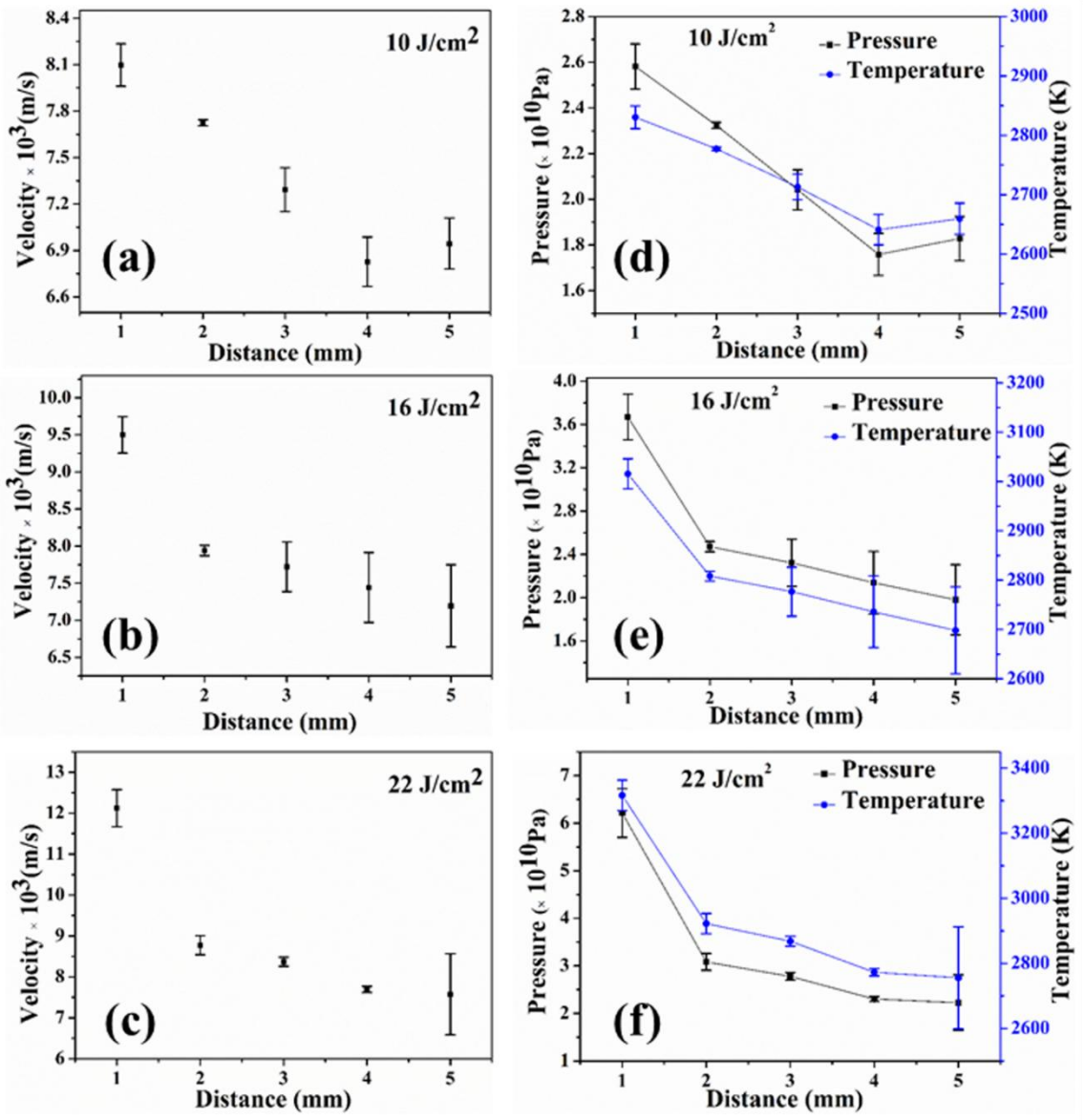

Figure 6.12 *Shock wave velocity as function of distance from the target at laser fluence of* **(a)** *10,* **(b)** *16 and* **(c)** *22 J/cm^2; Variation of pressure and temperature as a function of distance from the target at laser fluence of* **(d)** *10,* **(e)** *16 and* **(f)** *22 J/cm^2.*

The corresponding SW pressures were evaluated using equation (6.5). Now, considering the SW propagation as a compressible one, the temperature can be estimated from equation (6.4) [15]. The variation of the SW pressure and temperature with distance from the target for different laser fluences are depicted in Fig. 6.12 (d)-(f). While the maximum SW pressure is ~ 6.21×10^{10} Pa, the maximum temperature is found to be as high

as ~ 3316 K. These extreme conditions favour the formation of NPs and hence a proper understanding of the dynamics of both cavitation bubble and SWs is an absolute necessity to understand well the mechanism of NP synthesis via PLAL.

The SW emitted initially by the laser produced plasma during PLAL is closely associated to the nucleation phenomenon of the NPs. Hence, the pressure and temperature estimated from the SW can be used to understand the nucleation mechanism. Taking the theoretical kinetic model proposed by Wang *et al.* as the base, a study of the nucleation of Cu NPs was attempted [20]. In this model, a theoretical kinetic approach was adopted to understand the nucleation and growth of nanocrystals synthesized via PLAL by considering the synthesis of nanodiamond by pulsed laser ablation of graphite in water.

As the laser beam interacts with the Cu target immersed in DW, there is the plasma formation of Cu as well as DW. The interaction between the plasmas followed by its subsequent cooling heralds the nucleation and growth stage of the NPs. In the case of ablation of Cu in DW, the release of oxygen molecule from the dissociation of DW during laser induced breakdown favours the formation of insufficiently oxidized Cu@Cu_2O NPs initially, as discussed in chapter 3. In the initial stage of the nucleation process, as the temperature and pressure drops, condensation of the ablated species during laser ablation results in the formation of clusters of the target material, Cu and oxidized Cu in the present case. The strong interaction among these clusters leads to its aggregation and the clusters grow to reach a size called the critical nucleus, r^* given by [20]

$$r^* = \frac{2\gamma_s\left(\frac{2}{3} + \frac{V_m}{\Delta V}\right)}{p_{sat}(T) - p} \tag{6.7}$$

where γ_s and V_m are the surface energy and molar volume of Cu_2O NPs, respectively and ΔV is the molar volume difference between Cu and Cu_2O NPs, respectively. p, T and $p_{sat}(T)$ are the pressure, temperature and the saturated vapour pressure, respectively at the interface

of the Cu target and the surrounding DW. The time taken for this onset of nucleation was assessed by the isothermal nucleation time, τ, given by [20]

$$\tau = \sqrt{2\pi m k_B T}\,\frac{k_B T \gamma_s}{p_{sat}(T)(\Delta\mu)^2} \tag{6.8}$$

where $\Delta\mu$ and m are the chemical potential difference and mass of Cu_2O NPs, respectively. k_B is the Boltzmann constant. The values of m (0.143 kg/mol for Cu_2O) and γ_s (0.78 J/m^2) were taken from the literature [21]. The temperature T and pressure p were taken to be the one corresponding to the highest SW pressure at the closest proximity of the target during laser ablation. For, the laser fluences of ~ 10, 16 and 22 J/cm^2, the highest SW pressure and the corresponding temperature, as depicted in Fig. 6.12, are found to be ~ 2.6 × 10^{10}, 3.7 × 10^{10} and 6.2 × 10^{10} Pa and ~ 2830, 3016 and 3316 K, respectively. The phase diagram of Cu shows a maximum pressure of 6 GPa [22]. This maximum pressure was assumed to be the $p_{sat}(T)$ in all the cases.

The chemical potential difference, $\Delta\mu$ is given by [20]

$$\Delta\mu = \frac{\Delta V[p - p_{sat}]}{V_m N_A} \tag{6.9}$$

where N_A is the Avogadro's number. The values of V_m and ΔV are 23.9 cm^3/mol and 16.79 cm^3/mol, respectively which were taken from available reports [23].

After the formation of the critical nucleus, the growth of the NPs occur till the time which is almost the double of the laser pulse duration (t_l = 7 ns) [20]. The growth velocity of crystalline nucleus in the process of formation of the NPs is given by [20, 24]

$$V = \zeta\upsilon \exp(-\frac{E_a}{RT})[1 - \exp(-\left|\frac{\Delta G_m}{RT}\right|) \tag{6.10}$$

where ζ, v, E_a, R, T, and ΔG_m are the lattice spacing in the growth direction, thermal vibration frequency, activation energy for the formation of Cu_2O NPs, gas constant,

temperature and Gibbs free energy difference per mole (given by equation 6.11), respectively. The value of ζ was taken to be the lattice spacing (0.24 nm) corresponding to the most common phase of Cu_2O, as discussed in chapter 3. The frequency of thermal vibration is given as $\nu = \frac{k_B T}{h}$, where h is the Planck's constant. The activation energy, E_a for the formation of oxides of Cu reportedly varies in the range of ~ 40-224 kJ/mol [25]. In the present work, the value of E_a was fixed at 200 kJ/mol and was found to give results that matches well with the experimental findings as reported in chapter 3. The Gibbs free energy difference per mole is given as [20]

$$\Delta G_m = -RT \ln\left(\frac{p}{p_{sat}(T)}\right) \tag{6.11}$$

From the growth velocity, an estimate of the size of the NPs, r, was obtained which is given as [20]

$$r = V(2t_l - \tau) + 2r^* \tag{6.12}$$

where t_l is the laser pulse duration and τ is the nucleation time defined in equation (6.8). For ~ 10 J/cm^2, the nucleation time is estimated to be 1.8×10^{-12} s during which a critical nucleus size of ~ 0.16 nm is formed. Once the critical nucleus is formed, depending on the growth velocity, NPs of different sizes are formed. The growth velocity for ~ 10 J/cm^2 was calculated to be ~ 2.21 nm/ns. Using this, the size of the NPs formed was estimated to be ~ 31 nm which is fairly close to that of obtained experimentally in chapter 3.

The nucleation time, growth velocity, critical size and the NP size as a function of the laser fluence are depicted in Fig. 6.13. The nucleation time τ is found to decrease from 1.8×10^{-12} to 0.3×10^{-12} s with the increase in the laser fluence from ~ 10 to 22 J/cm^2, respectively and this is accompanied by a decrease in the size of the critical nucleus from

~ 0.16 to 0.05 nm, respectively. With the increase in the laser fluence from ~ 10 to 22 J/cm^2, the growth velocity is estimated to increase from ~ 2.2 to 10.5 nm/ns, respectively.

The estimate of the size of the NPs is based on the cumulative effect of all the above mentioned parameters and is found to increase as ~ 31, 60 and 147 nm for the laser fluences of ~ 10, 16 and 22 J/cm^2, respectively.

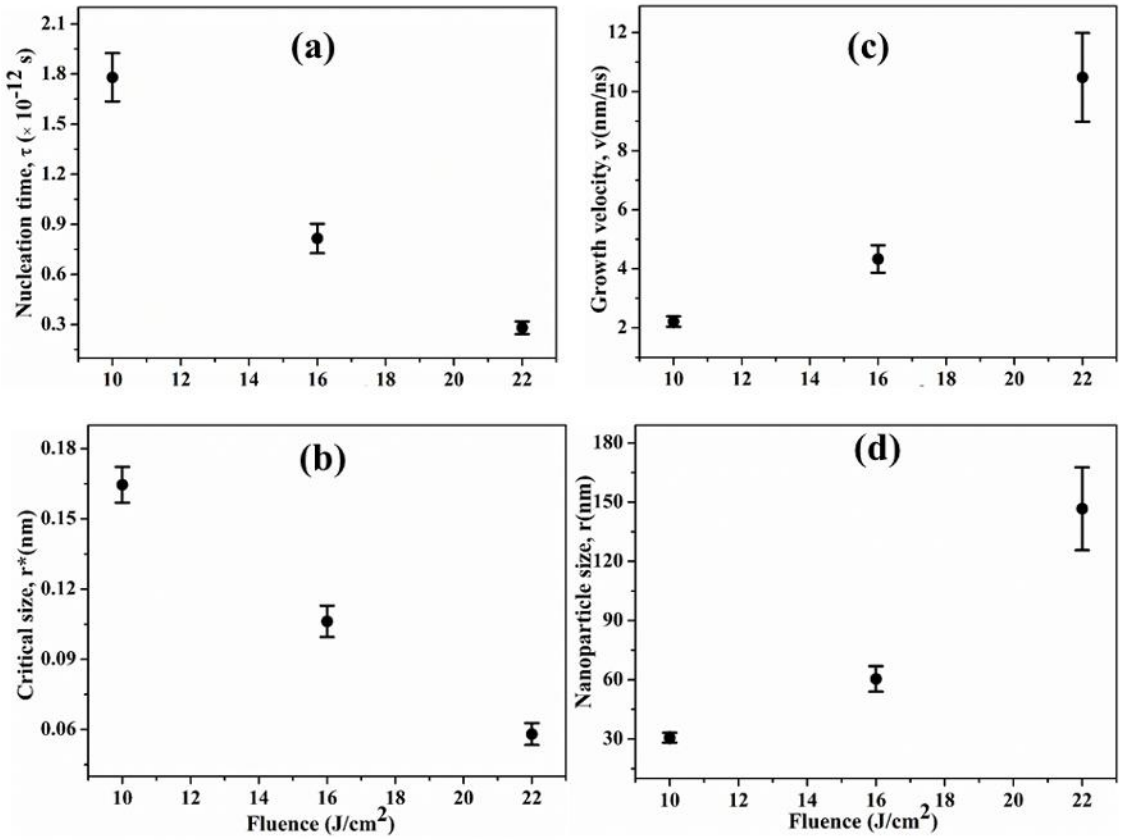

Figure 6.13 *Variation of* **(a)** *nucleation time,* **(b)** *critical size,* **(c)** *growth velocity and* **(d)** *nanoparticle size as a function of laser fluence.*

The increase in size of the NPs with the increase in laser fluence is in contrast to the experimental findings, in which a decrease in the size of the NPs was reported with higher fluence, as shown in chapter 3. However, it should be noted that the entire nucleation study in the present work is based on data derived from a single laser shot. In chapter 3, the experimental findings of decrease in the size of the NPs for higher fluence was for an ablation duration of 60 minutes in which multiple shots of laser induced fragmentation

among the initially formed NPs and thereby lead to a reduction in the average size of the NPs.

In the present case, the increase in the size of the NPs with laser fluence is attributed to the high temperature and pressure conditions at higher fluence as already discussed. Such conditions not only lead to the release of more NPs in the ambient liquid but also favours longer life of the cavitation bubble before it collapses [26]. This longer duration of the cavitation bubble is already confirmed by the shadowgraphy as well as beam deflection results in this work. Longer duration of cavitation bubbles is responsible for the formation of larger sized particles by coalescence [26, 27]. Thus, the dependence of the size of the NPs synthesized via pulsed laser ablation of Cu in DW on the dynamics of the cavitation bubble and SWs is vividly observed in the present work.

6.4 Conclusion

Cavitation bubbles and SWs produced during pulsed laser ablation of copper immersed in DW were extensively studied in this work. The thermodynamics of the cavitation bubble derived using the temporal evolution of the bubble reveal the variation of high pressure (~ 10^8-10^9 Pa) and temperature (~ 400-1200 K) inside the bubble. The SWs emitted by the laser produced plasma travel at the speed of the order of ~ 10^3 m/s. The pressure and temperature at the interface of Cu and DW were estimated from the SWs and is found to be as high as ~ 10^{10} Pa and ~ 3000 K, respectively. The pressure and temperature estimated for both cavitation bubbles and SWs are found to increase with the increase of incident laser fluence. From the nucleation study, it is observed that the size of Cu@Cu_2O NPs increases from ~ 31 to 147 nm with the increase in the incident laser fluence from ~ 10 to 22 J/cm^2, respectively. The size of ~ 31 nm obtained at laser fluence of ~ 10 J/cm^2 is fairly close to the size obtained experimentally as described in chapter 3. However, the deviation

from the experimentally observed particle size for higher fluences is due to the higher degree of fragmentation taking place at higher fluence.

References

[1] J. Tomko, S. O'Malley, C. Trout, J. Naddeo, R. Jimenez, J.C. Griepenburg, W. Soliman, D. Bubb, Cavitation bubble dynamics and nanoparticle size distributions in laser ablation in liquids, Colloids and Surfaces A: Physicochemical and Engineering Aspects, **522** (2017) 368-372.

[2] T. Tsuji, Y. Tsuboi, N. Kitamura, M. Tsuji, Microsecond-resolved imaging of laser ablation at solid–liquid interface: investigation of formation process of nano-size metal colloids, Applied Surface Science, **229** (2004) 365-371.

[3] P. Wagener, S. Ibrahimkutty, A. Menzel, A. Plech, S. Barcikowski, Dynamics of silver nanoparticle formation and agglomeration inside the cavitation bubble after pulsed laser ablation in liquid, Physical Chemistry Chemical Physics, **15** (2013) 3068-3074.

[4] S. Ibrahimkutty, P. Wagener, T. dos Santos Rolo, D. Karpov, A. Menzel, T. Baumbach, S. Barcikowski, A. Plech, A hierarchical view on material formation during pulsed-laser synthesis of nanoparticles in liquid, Scientific reports, **5** (2015) 16313.

[5] S. Reich, P. Schönfeld, P. Wagener, A. Letzel, S. Ibrahimkutty, B. Gökce, S. Barcikowski, A. Menzel, T. dos Santos Rolo, A. Plech, Pulsed laser ablation in liquids: Impact of the bubble dynamics on particle formation, Journal of colloid and interface science, **489** (2017) 106-113.

[6] J. Chen, X. Li, Y. Gu, H. Wang, X. Song, H. Zeng, Probing mesoscopic process of laser ablation in liquid by integrated method of optical beam deflection and time-resolved shadowgraphy, Journal of colloid and interface science, **489** (2017) 38-46.

[7] P. Gregorčič, R. Petkovšek, J. Možina, Investigation of a cavitation bubble between a rigid boundary and a free surface, Journal of Applied Physics, **102** (2007) 094904.

[8] R. Tanabe, T.T. Nguyen, T. Sugiura, Y. Ito, Bubble dynamics in metal nanoparticle formation by laser ablation in liquid studied through high-speed laser stroboscopic videography, Applied Surface Science, **351** (2015) 327-331.

[9] M. Dell'Aglio, R. Gaudiuso, O. De Pascale, A. De Giacomo, Mechanisms and processes of pulsed laser ablation in liquids during nanoparticle production, Applied Surface Science, **348** (2015) 4-9.

[10] J. Lam, J. Lombard, C. Dujardin, G. Ledoux, S. Merabia, D. Amans, Dynamical study of bubble expansion following laser ablation in liquids, Applied Physics Letters, **108** (2016) 074104.

[11] P. Gregorcic, J. Mozina, A beam-deflection probe as a method for optodynamic measurements of cavitation bubble oscillations, Measurement Science and Technology, **18** (2007) 2972.

[12] R. Petkovšek, P. Gregorčič, A laser probe measurement of cavitation bubble dynamics improved by shock wave detection and compared to shadow photography, Journal of Applied Physics, **102** (2007) 044909.

[13] R. Lord, On the pressure developed in a liquid during the collapse of a spherical cavity, Phil. Mag, **34** (1917) 94-98.

[14] M.S. Plesset, The dynamics of cavitation bubbles, Journal of applied mechanics, **16** (1949) 277-282.

[15] J.D. Anderson Jr, Fundamentals of aerodynamics, Tata McGraw-Hill Education, 2010.

[16] A. De Giacomo, M. Dell'Aglio, A. Santagata, R. Gaudiuso, O. De Pascale, P. Wagener, G. Messina, G. Compagnini, S. Barcikowski, Cavitation dynamics of laser ablation of bulk and wire-shaped metals in water during nanoparticles production, Physical Chemistry Chemical Physics, **15** (2013) 3083-3092.

[17] G. Yang, Laser ablation in liquids: principles and applications in the preparation of nanomaterials, CRC Press, 2012.

[18] A. Doukas, A. Zweig, J. Frisoli, R. Birngruber, T. Deutsch, Non-invasive determination of shock wave pressure generated by optical breakdown, Applied Physics B, **53** (1991) 237-245.

[19] P. Harris, H.N. Presles, Reflectivity of a 5.8 kbar shock front in water, The Journal of Chemical Physics, **74** (1981) 6864-6866.

[20] C. Wang, P. Liu, H. Cui, G. Yang, Nucleation and growth kinetics of nanocrystals formed upon pulsed-laser ablation in liquid, Applied Physics Letters, **87** (2005) 201913.

[21] A. Soon, M. Todorova, B. Delley, C. Stampfl, Thermodynamic stability and structure of copper oxide surfaces: A first-principles investigation, Physical Review B, **75** (2007) 125420.

[22] D.A. Young, Phase diagrams of the elements, Univ of California Press, 1991.

[23] J. Ruzyłło, E.S.E. Division, E.S.D. Science, T. Division, E.S. Meeting, Cleaning Technology in Semiconductor Device Manufacturing VIII: Proceedings of the International Symposium, Electrochemical Society, 2004.

[24] A. Nath, P. Sharma, A. Khare, Laser-induced metastable phases in liquids, Laser Physics Letters, **15** (2018) 026001.

[25] Y. Zhu, K. Mimura, M. Isshiki, Oxidation mechanism of copper at 623-1073 K, Materials transactions, **43** (2002) 2173-2176.

[26] M.H. Mahdieh, B. Fattahi, Size properties of colloidal nanoparticles produced by nanosecond pulsed laser ablation and studying the effects of liquid medium and laser fluence, Applied Surface Science, **329** (2015) 47-57.

[27] K. Sugioka, M. Meunier, A. Piqué, Laser precision microfabrication, Springer, 2010.

Chapter 7

SERS and Antibacterial Activities of PLAL Synthesized Nanoparticles of $Cu@Cu_xO$ and $Ag@Ag_xO_y$

7.1 Introduction

Metallic nanoparticles (NPs) have tremendous applications due to their surface enhanced Raman scattering (SERS) and antibacterial activities. SERS is a vibrational spectroscopic technique that uses the localized surface plasmon resonance (LSPR) property of noble metal NPs to increase the intensity of Raman signal of compounds having intrinsically low Raman signal [1, 2]. Although a large amount of work has been carried out towards the development of reliable and efficient SERS substrates but even today the quest for cheaper and reliable substrates is still on [3-5]. Thus, the selection of the SERS substrate and the species to be detected is of utmost importance in SERS study. Gold (Au), silver (Ag) and copper (Cu) possess LSPR in the visible range and are widely used as SERS substrates [6, 7]. There are various factors that may affect the efficiency of an SERS substrate but the most important aspect is the proper plasmonic interaction between the probe and the substrate and once this criteria is satisfied the substrate may be manipulated for optimum utilization.

For the improvement of SERS substrates it is important to understand the factors that affect its efficiency and accordingly the work on the relevant parameters for optimization is required to be undertaken. Starting exactly from this point, in the present chapter, a study was carried out to use the Cu and Ag NPs synthesized via pulsed laser ablation in liquid (PLAL) in distilled water (DW) without adding any reagent and tested its

effectiveness as an SERS substrate to increase the Raman signal of a bio-active furanoflavonoid, karanjin (3-methoxy furano-2, 3, 7, 8-flavone) extracted from the seeds of *Pongamia Pinnata* [8]. The chemical structure of karanjin is shown in Fig. 7.1. Flavonoids have important medicinal properties owing to its polyphenolic nature and are therefore a part of many pharmaceutical products [9]. Karanjin which is also a part of this class of compounds is used in alternative medicines and is known to have anti-oxidant, anti-ulcerogenic and analgesic effects [10]. The sensitive structural detection of such compounds having intrinsically low Raman signal is extremely important. In this work, the effect of Cu and Ag NP concentration, average size of the NPs, its aggregation state as well as its oxidation on the SERS activity is discussed. Taking into account all these factors, the optimization of the prepared NPs as a viable SERS substrate has been reported.

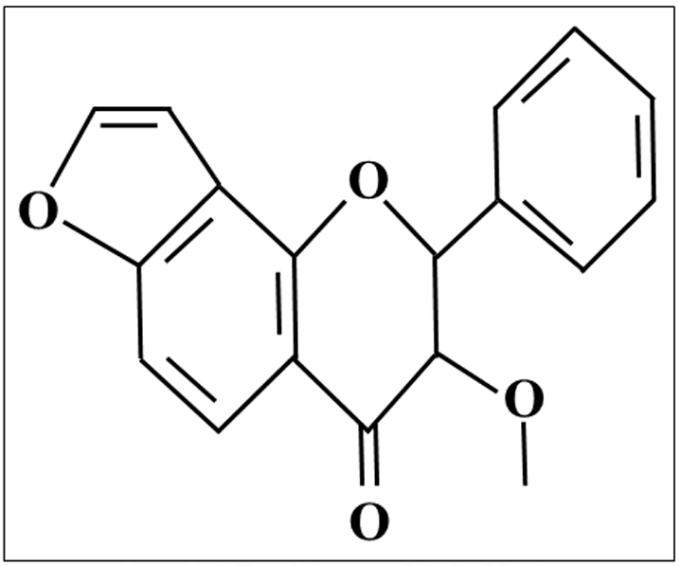

Figure 7.1 *Chemical structure of karanjin.*

Another very important property associated with metallic NPs is its excellent antibacterial activity [11-13]. Both Cu and Ag NPs are known to possess antimicrobial properties, and hence the addition of these NPs to a particular material can act as a protective layer against bacteria. Natural silk is one such material which has immense importance in textile industries. Some of the natural silks are known to possess medicinal

properties and are therefore used in biomedical applications [14]. Of late, addition of NPs to silk have shown increased anti-bacterial properties [15]. The importance of silk and the need to develop an effective antibacterial protective coating motivated a study on the effect of treatment of Ag and Cu NPs synthesized via PLAL on three common silks viz., Eri, Pat and Muga. These natural varieties of silks are woven from the silkworms *Philosomia ricini*, *Bombyx mori* and *Antheraea assamensis*, respectively.

The antibacterial properties of Cu and Ag NPs can also be used to devise easy and convenient methods to rid drinking water, especially during emergencies, from harmful pathogenic bacteria. With this in view, the synthesized NPs were also applied to check its viability on the treatment of filter paper for the annihilation of bacteria from contaminated water.

7.2 Basics of Surface enhanced Raman scattering (SERS)

The amplification of the signal in SERS can be explained through two main mechanisms [16, 17]. In the first mechanism, the electromagnetic enhancement, light interacts with metal NPs to form plasmons and its energy causes the enhancement of Raman signal of the adsorbed molecule [16].

When a suitable electric field E_0, in the form of a laser light having a frequency, ω_0 is incident on a metal and there is resonant excitation of the free conduction electrons present in it, LSPR oscillations occur. These oscillations are dipolar in nature and the oscillating induced dipole moment, μ, depends on the polarizability of the metal, α_{met}, and the strength of the incident field, E_0, and is given by $\mu = \alpha_{met} E_0(\omega_0)$. The oscillating dipole results in the emission of radiation at the same frequency ω_0. Thus, there is an enhanced local field E_1 relative to E_0 in the vicinity of the metal NP. In addition to this, the incident electric field also induces a dipole moment in the molecule which is given by $\mu = \alpha_{mol} E_1(\omega_0)$.

There is vibration of the molecule at a frequency ω_1 which results in the inelastic scattering of E_1 by the vibrating molecule [16].

The increase in the intensity in SERS is dependent on both the incoming as well as outgoing radiation. Thus, the difference in the mechanism of SERS from that of traditional Raman scattering lies in the generation of the enhanced local field due to the presence of the metal NPs.

The other main mechanism, the chemical enhancement, is attributed to the charge transfer between the metal and the molecule [17]. There is transfer of charge between the molecule in its electronic ground state and the metal NP. This can change the polarizability of the molecule which changes the cross section for Raman scattering of the molecule and hence an enhancement in the Raman signal.

7.3 Mechanism of antibacterial property of NPs

The exact mechanism for the antibacterial properties of metallic NPs has eluded scientists for a long time. However, there are a few factors believed to be responsible for the antibacterial properties [11, 13]. Firstly, the change in the permeability of the bacterial membrane due to the accumulation of NPs leads to the uncontrolled exchange of cellular organelles which disrupts the normal functioning of the cells. Secondly, the generation of oxidative species from the NPs leads to oxidative damage to cellular structures. Then, there is also a possibility of the NPs entering the cell and depleting the Adenosine triphosphate (ATP) production and disrupting the replication of the deoxyribonucleic acid (DNA).

7.4 Experimental details

The SERS capability of the synthesized Cu and Ag NP samples C3-C5 and A1-A5, listed in tables 2.1 and 2.2, respectively, for which uniform particle size distribution was observed, was tested for karanjin. For NP samples C1 and C2, the particle size distribution was highly non-uniform and hence these samples were excluded from the SERS study. The

details of the SERS substrate preparation and measurements were elaborated in section 2.6.1. Briefly, 10 µL of karanjin solution was mixed with 500 µL of each NP sample and then sonicated for uniform mixing and drop casted onto silicon (Si) wafers. The dried samples were subjected to the Raman spectrophotometer with an excitation wavelength of 488 nm to record the Raman spectra.

The NP concentrations of the as-synthesized Cu and Ag NP samples used in the SERS study, as listed in table 7.1, were estimated from the mass ablation rate described in chapter 3 and 4, respectively.

Table 7.1 *NP concentration for the as-synthesized samples for SERS study.*

Sample	Concentration (mg/mL)	Sample	Concentration (mg/mL)
C3	0.338	A1	0.032
C4	0.485	A2	0.097
C5	0.588	A3	0.194
-	-	A4	0.391
-	-	A5	1.155

For the antibacterial studies, samples C5 and A5 pertaining to their respective high concentrations were taken. The colloidal NP samples were treated to pellets of Eri, Pat and Muga silk and the antibacterial activity was tested using the agar diffusion method. The experimental details for the testing of the NP samples as a protective layer for the natural silks were elaborated in section 2.6.2.1. These NP samples were also treated with filter paper and its antibacterial activity is tested in the annihilation of bacteria from contaminated

water. The experimental details for the NP treated filter paper were provided in section 2.6.2.2.

7.5 Results and discussion

7.5.1 SERS activity of Cu and Ag NPs synthesized via PLAL

The SERS activity of Cu and Ag NPs tested for karanjin is discussed in the following sections.

7.5.1.1 SERS activity of Cu NPs for karanjin

In order to study the effect of Cu NP concentration on the SERS enhancement for karanjin, the as-synthesized samples of the Cu NPs were suitably diluted to obtain 5 different concentrations of Cu NPs. The SERS spectra for the samples C3-C5 having average particle size of ~ 20, 11 and 7 nm (discussed in chapter 3), respectively, along with the corresponding NP concentrations are shown in Fig. 7.2, 7.3 and 7.4, respectively. For comparison, the Raman spectrum of untreated karanjin is also depicted in each of these figures. As the samples in liquid form were drop casted and then taken for recording the Raman spectra, to minimize the effect due to formation of aggregates as a result of drying, the drop casted samples were probed with the micro Raman set up at different locations of each sample. The SERS plots presented in this chapter are averaged over eight most intense spectra with the intensity variation among them within 10%.

For sample C3, as observed in Fig. 7.2, the intensity of the Raman spectra increases with the decrease in Cu NP concentration from ~ 0.338 to 0.203 mg/mL and with further decrease in concentration to ~ 0.068 mg/mL, the Raman intensity is found to decrease. However, in all the samples a remarkable increase in Raman intensity is clearly visible as compared to that of untreated karanjin, shown in Fig. 7.2(f).

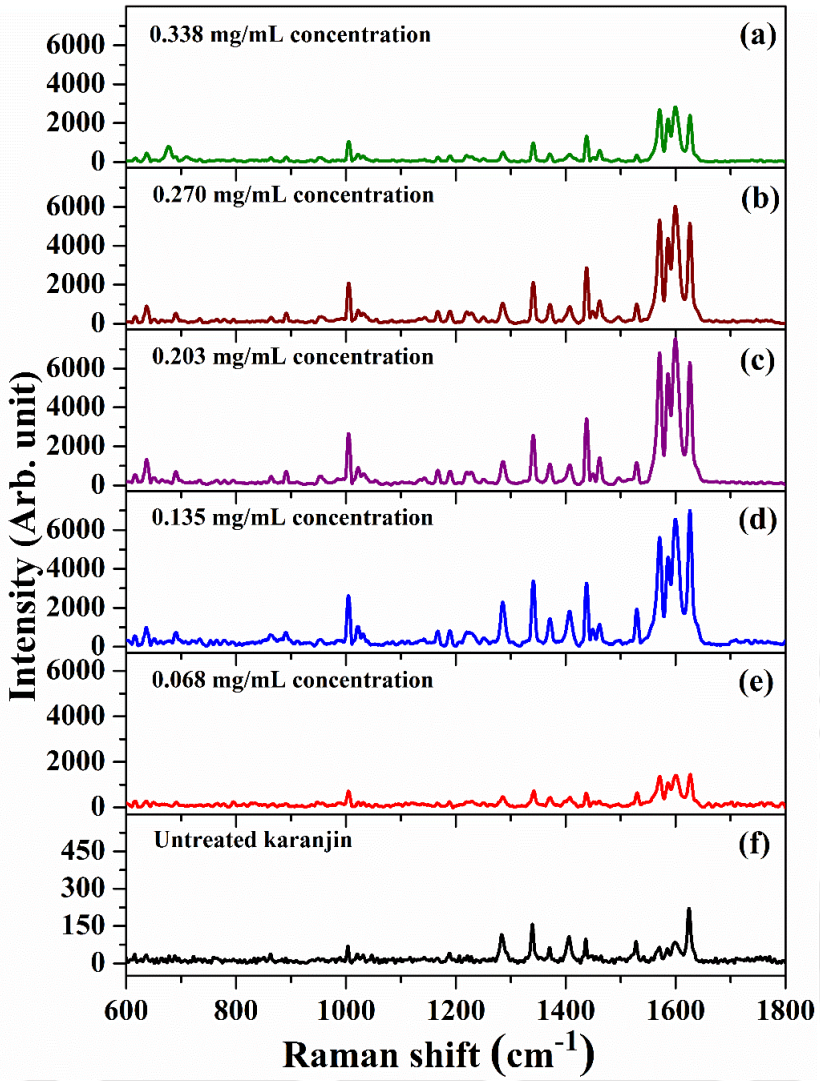

Figure 7.2 *Raman spectra of karanjin treated with different dilutions of sample C3 having NP concentration of* **(a)** *0.338 mg/mL,* **(b)** *0.270 mg/mL,* **(c)** *0.203 mg/mL,* **(d)** *0.135 mg/mL,* **(e)** *0.068 mg/mL;* **(f)** *Raman spectrum of untreated karanjin.*

The increase in Raman signal is attributed to the excitation of localized surface plasmons of the Cu NPs present in the vicinity of karanjin. The lower SERS intensity at highest concentration of NPs is an interesting observation and it may be explained on the basis that at higher concentration the signal from karanjin itself is getting decreased due to aggregation of the NPs which may have covered the analyte, karanjin to a great extent. The absorption of light by the plasmon resonance of suspended NPs, affects both the incident and the scattered Raman emission [18]. For sample C3, the concentration of ~ 0.203 mg/mL is the optimum for which the enhancement in Raman signal is maximum. At values below

this optimum concentration, the Raman enhancement goes down again as the effect of localized surface plasmons decreases due to the presence of fewer NPs in the vicinity of the compound.

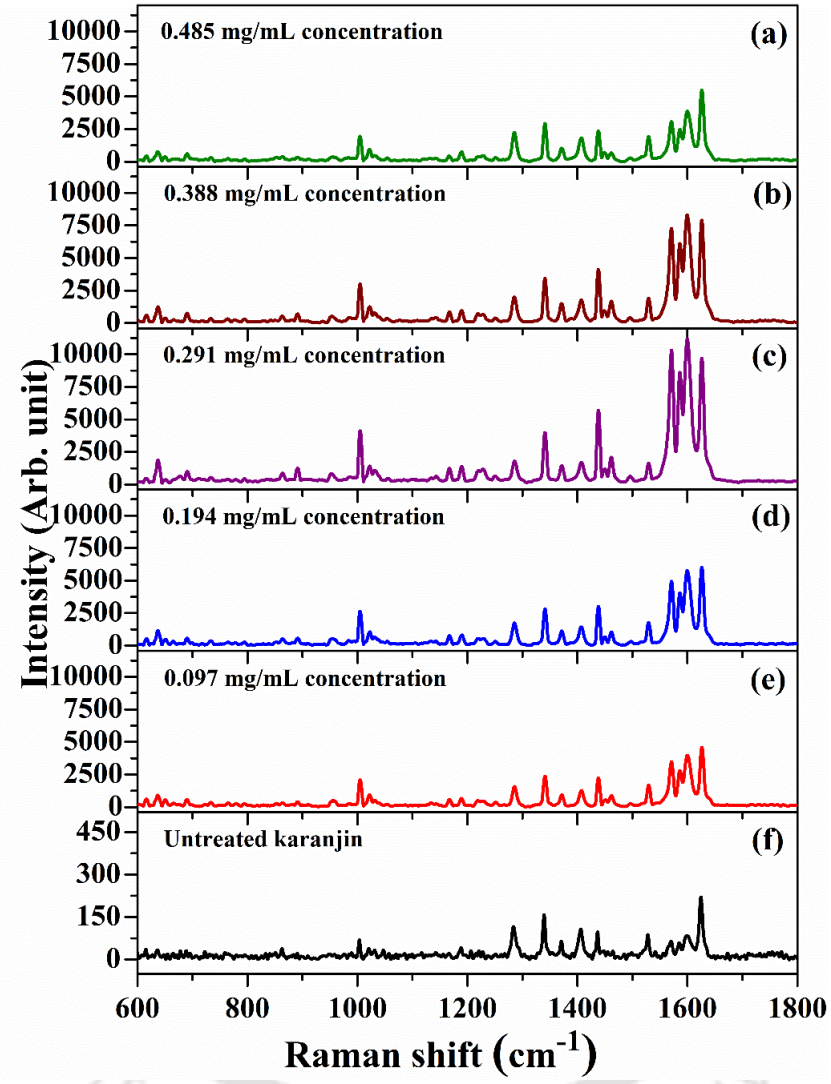

Figure 7.3 *Raman spectra of karanjin treated with different dilutions of sample C4 having NP concentration of* **(a)** *0.485 mg/mL,* **(b)** *0.388 mg/mL,* **(c)** *0.291 mg/mL,* **(d)** *0.194 mg/mL,* **(e)** *0.097 mg/mL;* **(f)** *Raman spectrum of untreated karanjin.*

For the samples C4 and C5, a similar trend as that of C3 in the enhancement of Raman signal with the change in concentration of NPs is observed and is depicted in Fig. 7.3 and 7.4, respectively. The optimum concentration for these two sets of samples at which maximum enhancement is obtained, is found to be ~ 0.291 and 0.353 mg/mL, respectively.

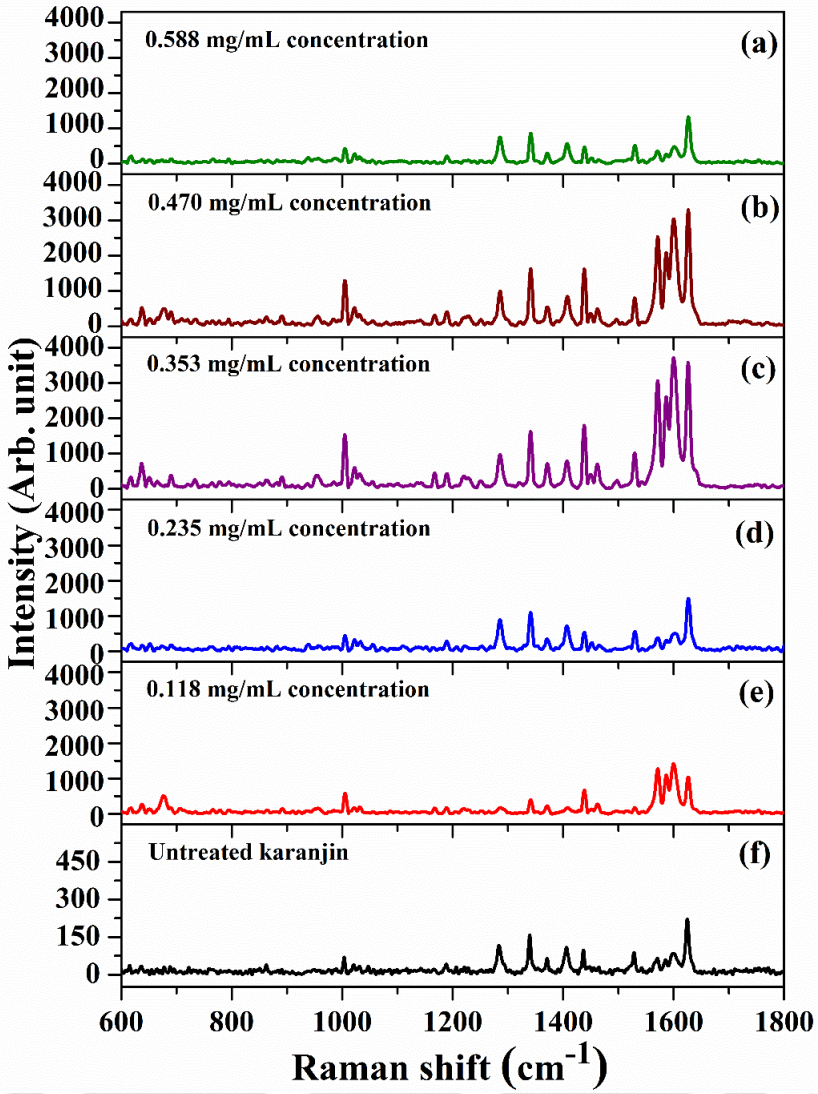

Figure 7.4 *Raman spectra of karanjin treated with different dilutions of sample C5 having NP concentration of* **(a)** *0.588 mg/mL,* **(b)** *0.470 mg/mL,* **(c)** *0.353 mg/mL,* **(d)** *0.235 mg/mL,* **(e)** *0.118 mg/mL;* **(f)** *Raman spectrum of untreated karanjin.*

The identified Raman bands of karanjin as well as their vibrational assignments are listed in table 7.2 [8]. In order to ensure that there is no overlapping of bands of the NPs with karanjin, the Raman spectrum of drop casted Cu NPs only, in the range of 1000-1800 cm^{-1} is shown in Fig. 7.5. There is hardly any identifiable Raman band in this spectrum and thus it is confirmed that for the selected range of 1000-1800 cm^{-1}, the observed Raman peaks correspond to karanjin itself.

Table 7.2 *Vibrational assignments of known Raman bands of karanjin.*

Raman shift (cm^{-1})	Assignments
1004	Trigonal stretch of flavone B ring
1019	CH- vibration in the furan ring
1189	Bending of CH-plane
1286	Bending of CH-plane
1342	CH- vibration in the furan ring
1372	Presence of CH_3 group
1437	CH- vibration in the furan ring
1530	Bending of CH-plane
1600	Strong C=O stretching of flavone ring
1627	

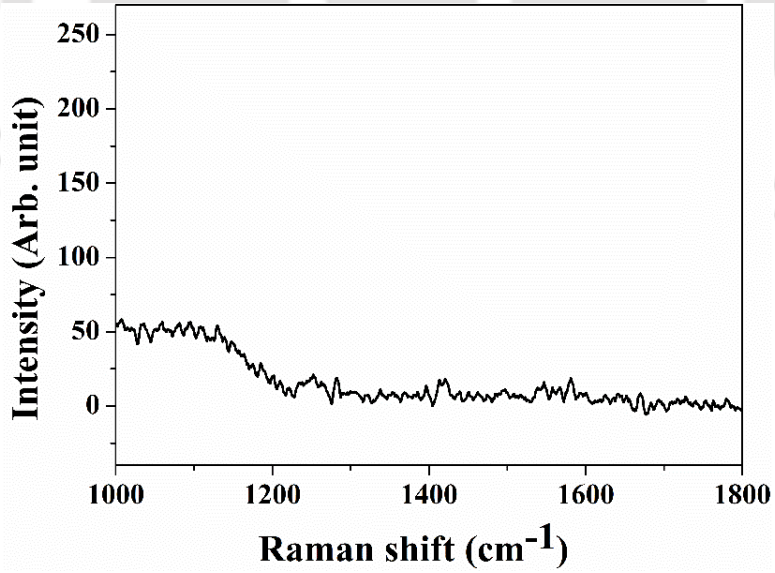

Figure 7.5 *Raman spectrum of Cu NPs in the range of 1000-1800 cm^{-1}.*

Thus, it is clear from the above sets of data that the concentration of synthesized NPs plays a pivotal role in the SERS of Cu for karanjin. Although there is marked

enhancement in all the samples, the most intense enhancement is seen for sample C4 for a concentration of ~ 0.291 mg/mL. However, to understand this enhancement better it is important to note how the addition of Cu NPs has affected different bands of karanjin. With this in view, the ratio of the Raman intensity of karanjin treated with the sample for which maximum enhancement is observed (R_T) and that of untreated karanjin (R_U) for all the known bands of karanjin, as listed in table 7.2, was determined and is demonstrated in Fig. 7.6. It is observed that among all the bands, the band appearing at 1600 cm^{-1} which is attributed to the strong C=O stretching of flavone ring, appears to be the most enhanced. Also, this band is very sharp and there is hardly any shift in its peak position in all the samples treated with Cu NPs.

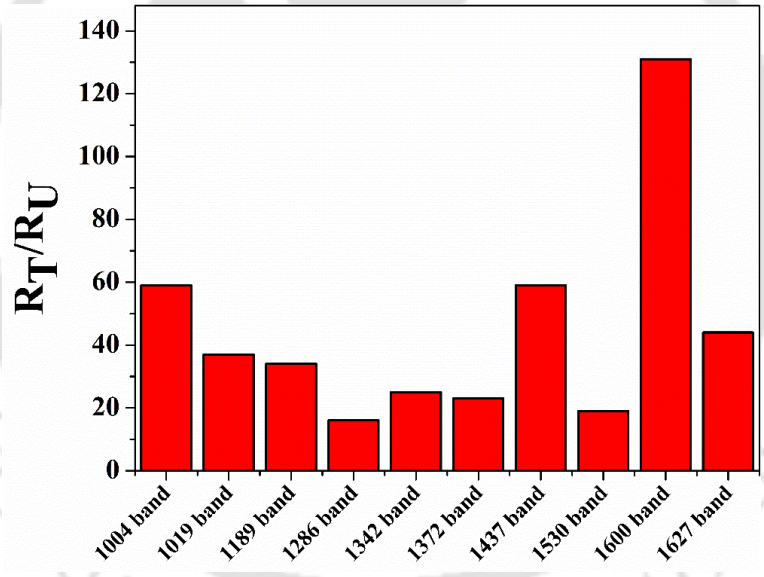

Figure 7.6 *Ratio of the Raman intensity of karanjin treated with optimum concentration and particle size of Cu NPs (R_T) and that of untreated karanjin (R_U) for the known bands of karanjin.*

The value of R_T/R_U was evaluated for all the samples for this particular band appearing at 1600 cm^{-1} and its variation with the concentration is shown in Fig. 7.7(a)-(c). Fig. 7.7(a) shows that for sample C3, this value is ~ 33 for an initial Cu NP concentration of ~ 0.338 mg/mL and it reaches a maximum value of ~ 89 at the concentration of ~ 0.203 mg/mL. With further decrease in the NP concentration upto ~ 0.068 mg/mL, the value of

R_T/R_U falls down to ~ 17. As mentioned earlier, this behaviour is probably due to fact that the samples with different concentration of the NPs lie around and cover karanjin to different extents thereby influencing the enhancement of the Raman signal. The R_T/R_U calculated for all the known bands of karanjin, as listed in table 7.2, for the other sets of samples also follow similar behaviour with the change in concentration of the NPs.

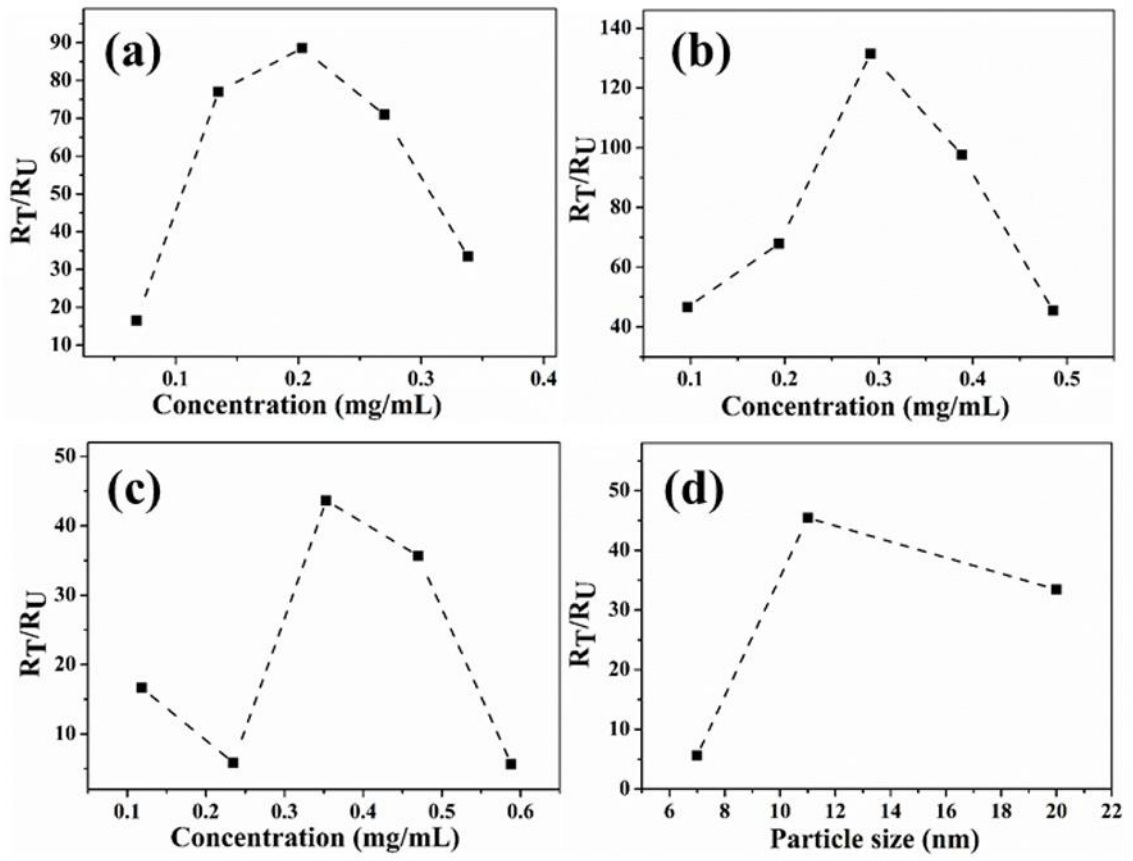

Figure 7.7 (a)-(c) *Plot of R_T/R_U as a function of concentration of Cu NPs for samples C3-C5, respectively* **(d)** *Plot of R_T/R_U vs average particle size.*

In order to quantify the degree of SERS enhancement, the analytical enhancement factor (E) for all the samples was also calculated for the same most intense 1600 cm^{-1} band by using the following expression: [18, 19]

$$E = \frac{I_{SERS} \times C_{SOL}}{I_{SOL} \times C_{SERS}} \qquad (7.1)$$

where I_{SERS} is the intensity of this band in the SERS spectrum, I_{SOL} is the intensity in the normal (untreated) Raman spectrum, C_{SERS} is the concentration of karanjin in the colloid and C_{SOL} is the concentration of karanjin in the solution (DMSO).

The SERS enhancement is observed to be maximum for the optimum concentration of sample C4 which has an average particle size of ~ 11 nm. The corresponding enhancement factor is calculated to be ~ 6.6×10^3. For the samples C3 and C5, with average particle size of ~ 20 and 7 nm, respectively, the maximum enhancement factors at their respective optimum NP concentrations are found to be ~ 4.4×10^3 and ~ 2.2×10^3, respectively.

Although the size range of 7-20 nm in the present case (for samples C3-C5) is not large but it is adequate to have a rough idea of the effect of Cu NP size on its SERS ability for karanjin. The change in the SERS enhancement with the average particle size is depicted in Fig. 7.7(d). The decrease in the SERS enhancement for larger sized NPs can be explained on the basis of the local electromagnetic field due to LSPRs. As the size of the NPs increases beyond a certain value, the convex shape of the surface becomes flatter and hence the absorption of light by the NPs as well as the inelastic scattering of light on the surface reduces [20]. This diminishes the local electromagnetic enhancement thereby reducing the SERS intensity.

The decreased enhancement for smaller sized particles of ~ 7 nm can be explained again on the basis of the local electromagnetic enhancement due to collective oscillations of the localized surface plasmons of the Cu NPs. This local enhancement is also known to decrease with decreasing particle size. When the size of the particle is too small, its light scattering capability, which is essential for SERS enhancement, decreases. As the localized surface plasmons are strongly dependent on the number of electrons excited and hence on the volume of the NPs so a decrease in size of NPs can surely decrease the SERS

enhancement [21, 22]. The reason for this decrease in enhancement for smaller NPs may also be attributed to the formation of large aggregates of the NPs with the smallest average particle size of ~ 7 nm. Aggregation of NPs has been reported to have reduced the SERS efficiency which is due to the trade-off of the inter- and intra- particle plasmonic fields [23]. As mentioned previously, in chapter 3, the decrease in NP size was achieved as a result of the increase in incident laser energy during the synthesis of the NPs. Along with this size reduction, increase in laser energy also resulted in an increase in concentration of the NPs in colloidal form, as discussed in chapter 3. There are reports of increased aggregation among NPs due to an increase in its concentration [24]. Thus, in addition to the size of the NPs, its aggregation also plays a very crucial role in the application of the synthesized Cu NPs as effective SERS substrates.

Another reason for the variation in the SERS enhancement could be due to the presence of NPs with oxidized phase in the samples. Oxidation of Ag NPs was reported to markedly diminish the SERS enhancement [25]. Although no such effect of oxidation of Cu NPs on the SERS enhancement is reported, still a similar behaviour cannot be ruled out in the case of Cu NPs as these are more prone to oxidation. As discussed in chapter 3, the Raman spectrum of the sample C3, synthesized at the lowest laser energy of 30 mJ, contained only Cu_2O phase. For the sample C4, the Raman spectrum (Fig. 3.8(d)) indicates the presence of both Cu_2O as well as CuO, the latter being the dominating phase. The selected area electron diffraction (SAED) patterns shown in Fig. 3.6 also complements these observations. But for sample C5, only CuO phase could be detected. Thus, it was inferred that sample C5 comprises of NPs which has undergone the maximum oxidation. Thus, in the present study, for sample C5, along with the particle size, the higher degree of oxidation of the NPs is another factor behind the lower SERS enhancement as compared to the samples C3 and C4.

Finally, it can be concluded that Cu NPs having average size of ~ 11 nm (sample C4) with a corresponding optimum concentration of ~ 0.291 mg/mL has been found to give the maximum enhancement in Raman intensity for karanjin.

In order to investigate the presence of Cu NPs around the analyte, karanjin, the transmission electron microscope (TEM) image of the sample for which the enhancement in the Raman signal is maximum was captured and is shown in Fig. 7.8. It clearly demonstrates that the Cu NPs are notably at close proximity to the karanjin crystal. It attests the fact that the localized surface plasmons of the NPs are actually responsible for the remarkable enhancement in the Raman signal of karanjin.

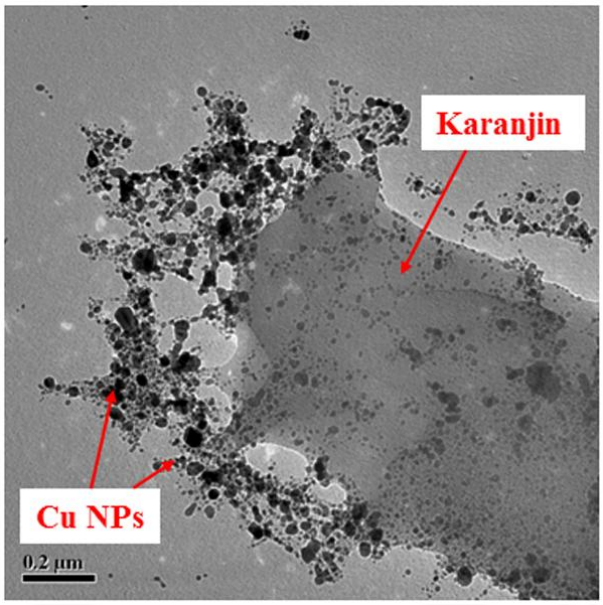

Figure 7.8 *TEM image of karanjin treated with Cu NPs (optimized sample).*

7.5.1.2 SERS activity of Ag NPs for karanjin

In this section, the SERS efficiency of the colloids of Ag NPs synthesized via PLAL is presented. The SERS spectra of Ag NP treated karanjin for the samples A1-A5 are illustrated in Fig. 7.9. For comparison, the Raman spectrum of pure karanjin (untreated) is also shown in this figure. For the Ag NPs, all the 5 samples, A1-A5 were found to have uniform size distribution and hence the SERS enhancement is first discussed on the basis

of the average particle size followed by the effect of NP concentration. Similar to the preceding study on SERS of Cu NPs, the experimental SERS plots shown in Fig. 7.9 are averaged over eight most intense spectra having less than 10% variation in the intensity among them.

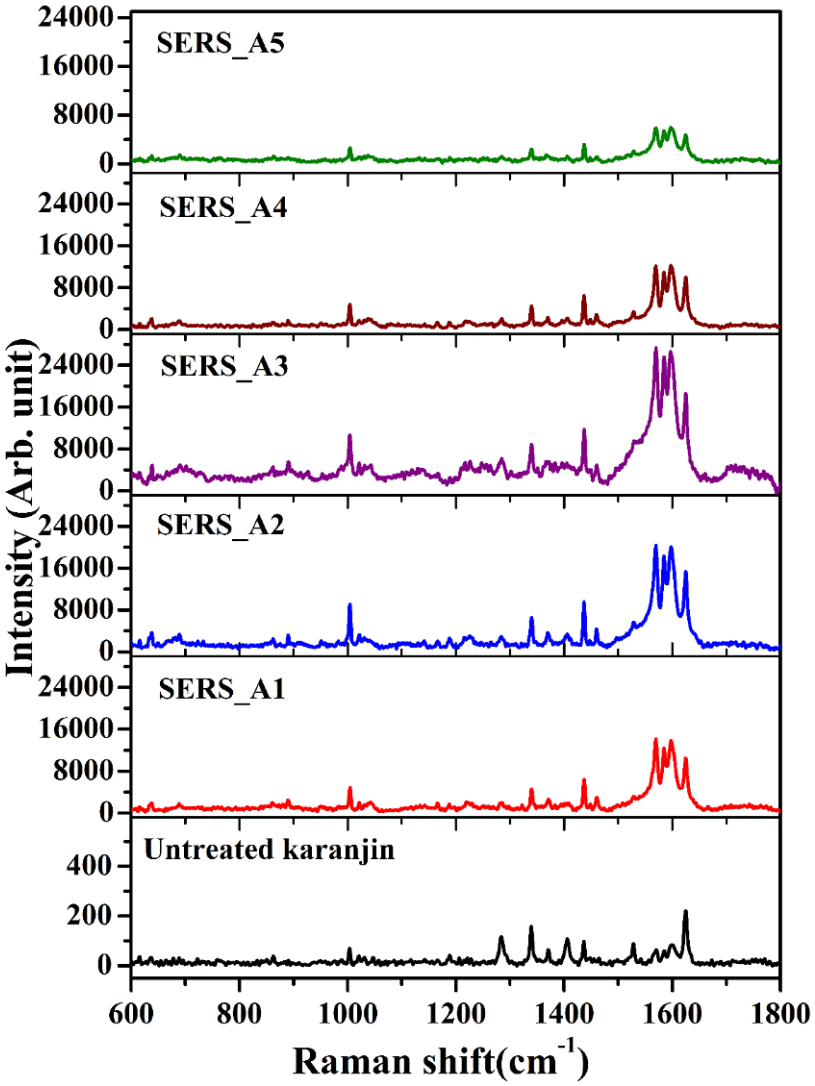

Figure 7.9 *SERS spectra for karanjin treated with Ag NPs (samples A1-A5) along with its normal Raman spectrum.*

From Fig. 7.9, it is evident that the SERS enhancement is maximum for karanjin treated with colloid sample A3. In order to understand, how the presence of the Ag NPs affects the different bands of karanjin, the ratio R_T/R_U, defined earlier, for all the known bands was calculated for sample A3 and is shown in Fig. 7.10(a). In the case of Ag NPs as

well, the band appearing at 1600 cm^{-1} is found to be the most enhanced. It is also observed that this band is sharp and there is negligible shift in its peak position for all the samples, A1-A5.

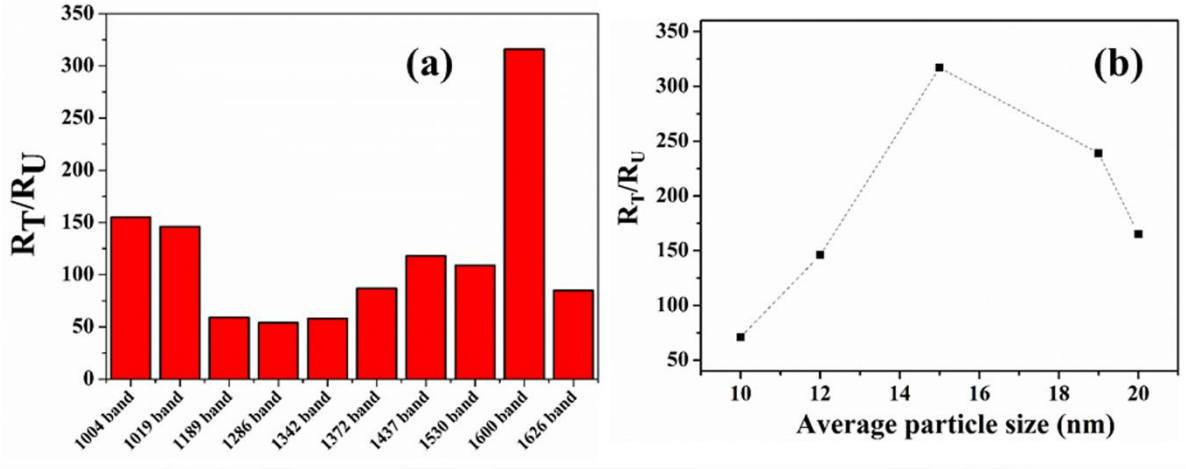

Figure 7.10 (a) *R_T/R_U for the identified bands of karanjin,* **(b)** *R_T/R_U vs particle size.*

The value of R_T/R_U was evaluated for all the samples for this particular band appearing at 1600 cm^{-1} and its variation with the average particle size is shown in Fig. 7.10(b). It is observed that as the particle size increases from ~ 10 to 15 nm, the SERS enhancement is found to increase but with further increase in the particle size up to ~ 20 nm, the SERS enhancement decreases. The maximum enhancement is obtained for sample A3 corresponding to the average particle size of ~ 15 nm and this corresponds to an analytical enhancement factor of ~ 1.6×10^4.

The relatively low enhancement for samples having smaller average particle size of ~ 10 and 12 nm as compared to that of the sample with average size ~15 nm, can be explained in similar manner as for Cu NPs. As the size of the NPs decreases, its capability to scatter light also decreases. The localized surface plasmons being dependent on the number of the electrons excited, a decrease in the size of the NPs, which is equivalent to a decrease in the volume of the NP, can decrease the SERS enhancement [21, 22]. Another explanation for this decrease in enhancement for smaller NPs is the formation of large

aggregates for the NPs with the smallest average particle size of ~ 10 nm (sample A5) which also has the highest concentration. As mentioned previously, aggregated NPs result in reduction of SERS enhancement [23].

The maximum SERS intensity for sample A3 may also be attributed to its narrow size distribution (Fig. 4.4(c)) which is found to be the minimum among all the other NP samples. This indicates that uniformly sized NPs behave as better SERS substrates. Also, the SPR peak for sample A3 (Fig. 4.8(c)) is the sharpest and hence a stronger plasmonic effect contributes to the maximum SERS enhancement in this case.

Also, as the size of NP increases beyond a critical value its absorption of light reduces and hence there is a decrease in the inelastic scattering of light on the surface of the NPs [24]. This results in the lowering of the local electromagnetic enhancement thereby reducing the SERS intensity for the samples A1 and A2 with average size of ~ 19 and 20 nm, respectively.

The SERS capability of the optimized Ag NPs (sample A3) as shown in Fig. 7.10 is nearly 2.5 times more as compared to that of the optimized Cu NP sample. In the study of Cu NPs as SERS substrate, it was observed that the concentration of Cu NPs plays a crucial role in the SERS enhancement for karanjin. To check the effect of concentration of the Ag NPs on SERS enhancement, sample A3 (concentration ~ 0.194 mg/mL), for which maximum SERS enhancement is observed, was diluted to make three more samples having concentration of ~ 0.116, 0.078 and 0. 039 mg/mL. The R_T/R_U as a function of concentration of Ag NPs is shown in Fig. 7.11(a). It is observed that there is a notable decrease in the enhancement for the diluted samples as indicated by the decrease in R_T/R_U with the decrease in concentration. This is in sharp contrast to that of Cu NPs, for which there was initially an increase followed by a decrease in the SERS enhancement with the decrease in concentration of the samples.

However, it is important to ensure that the effect of average size of the Ag NPs is valid and that it is not the concentration of the NPs alone which is dominant in the SERS enhancement of Ag NPs for karanjin. To validate this, the sample A5 which has the highest concentration of ~ 1.155 mg/mL was diluted to make three more samples having concentration of ~ 0.693, 0.231 and 0.115 mg/mL and treated for the SERS in karanjin.

From the R_T/R_U graph for these diluted samples of A5, Fig. 7.11(b), it is observed that there is not much change in its values for these three concentrations. On comparing the R_T/R_U ratio for A3 with that of A5 at nearly the same concentration of ~ 0.2 mg/mL, this ratio is almost five times higher in the former confirming that the sample A3 having an average particle size of ~ 15 nm is the optimum.

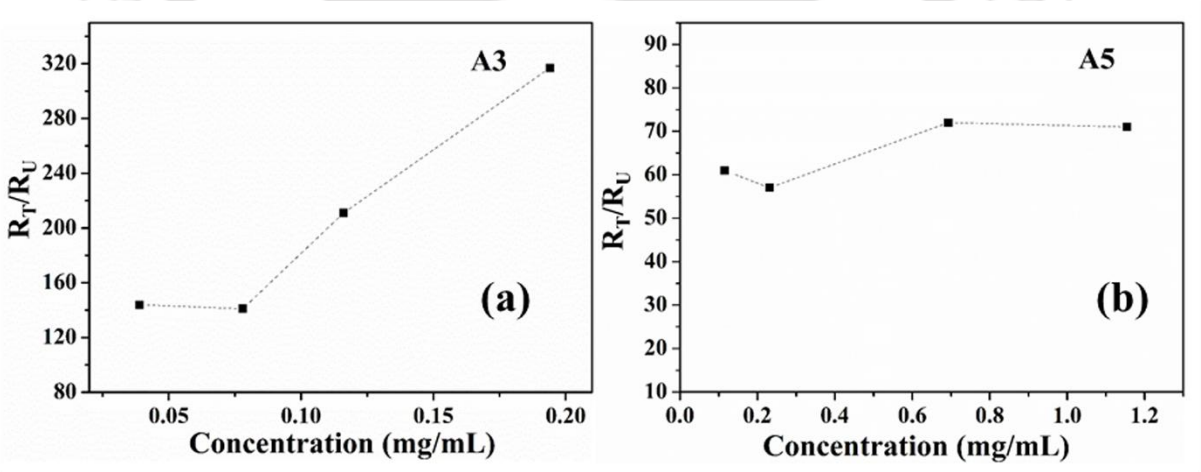

Figure 7.11 *R_T/R_U vs concentration of sample* **(a)** *A3 and* **(b)** *A5.*

The presence of Ag NPs around karanjin, investigated via TEM shows the Ag NPs in close proximity to the karanjin crystal as depicted in Fig. 7.12.

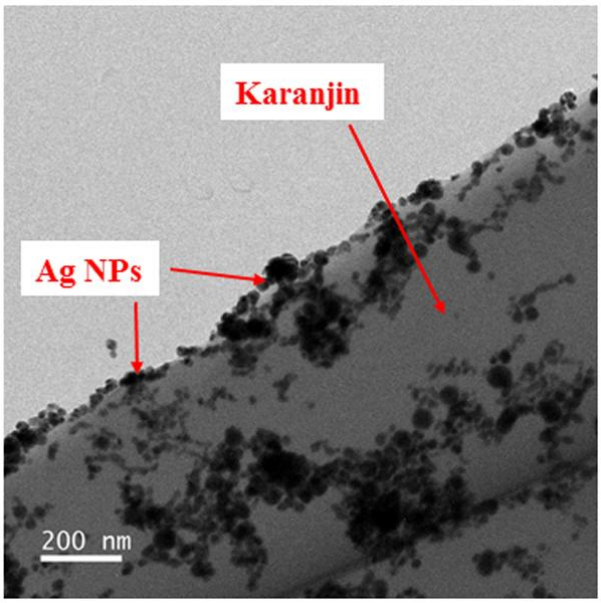

Figure 7.12 *TEM image of karanjin treated with Ag NPs (optimized sample).*

7.5.1.3 Comparison of Cu and Ag NPs as SERS substrate for karanjin

The SERS capability of the Cu and Ag NPs was discussed in the preceding sections. The Raman signal of karanjin which has intrinsically low Raman signal is remarkably enhanced by the presence of NPs of Cu and Ag synthesized via PLAL. A comparison of the enhancement efficiency of both the NPs can be drawn from the results obtained and a few of the important differences are listed in table 7.3.

Table 7.3 Some important values from the SERS study of Cu and Ag NPs.

	Cu NPs	**Ag NPs**
Optimum Particle size (nm)	11	15
Optimum concentration (mg/mL)	0.291	0.194
Maximum R_I/R_U	131	316
Maximum Enhancement factor	6.59×10^{3}	1.58×10^{4}

The optimum particle size for SERS enhancement is found to be ~ 11 and 15 nm for Cu and Ag NPs, respectively. It is also found that the concentration of the NPs is a very important factor in the SERS enhancement and the optimum concentration for Cu and Ag NPs is found to be ~ 0.291 and 0.194 mg/mL, respectively. The maximum enhancement in the case of Cu NPs is around 131 times that of untreated karanjin while that in the case of Ag is as high as almost 316 times.

The difference in the SERS enhancement for different metals can be explained on the basis of the electromagnetic model proposed by Gersten *et al.*, according to which the polarizability of small metal sphere with dielectric function ε and radius r surrounded by vacuum is given by [2, 26-28]

$$\alpha' = \frac{r^3(\varepsilon_b\omega^2 - \omega_p{}^2) + i\omega\gamma\varepsilon_b}{[(\varepsilon_b + 3)\omega^2 - \omega_p^2] + i\omega\gamma(\varepsilon_b + 3)} \qquad (7.2)$$

where ε_b is the interband transition contribution to the dielectric constant, ω_p is the plasmon frequency resonance of the metal and γ is the electron-scattering rate. The real and imaginary parts of the above expression have a pole when the frequency ω is equal to $\omega_p/\sqrt{(\varepsilon_b+3)}$. The width of the resonance is given by $\gamma\ (\varepsilon_b+3)$ [2, 26]. Hence, the resonance and SERS enhancement is reduced when the electron scattering rate, γ is large. The large value of γ may be either due to poor conductivity of the metal or because of dominant electronic scattering at the particle's surface. Also for metals whose value of ε_b is large, the resonance-width increases and hence there is a decrease in SERS enhancement. In the case of Cu, ε_b i.e. the contribution of interband transition to the dielectric constant is more as compared to that of Ag [26]. Thus, the SERS enhancement has been observed to be greater in the case of Ag.

7.5.2 Antibacterial applications of Cu and Ag Nanoparticles

The antibacterial activity of the synthesized Cu and Ag NPs was tested for two cases. These were tested as a protective layer for natural silk against bacterial attack and in the treatment of filter paper for bacterial annihilation in contaminated water. The details of these studies are discussed in the following subsections.

7.5.2.1 Antibacterial activity of silk treated with NPs

The preparation of silk pellets and the protective coating of Cu and Ag NPs were detailed in chapter 2, section 2.6.2.1 and also briefly in section 7.4. The results of the antibacterial assay carried on Eri, Pat and Muga silks treated with Cu and Ag NPs are shown in Fig. 7.13(a)-(c).

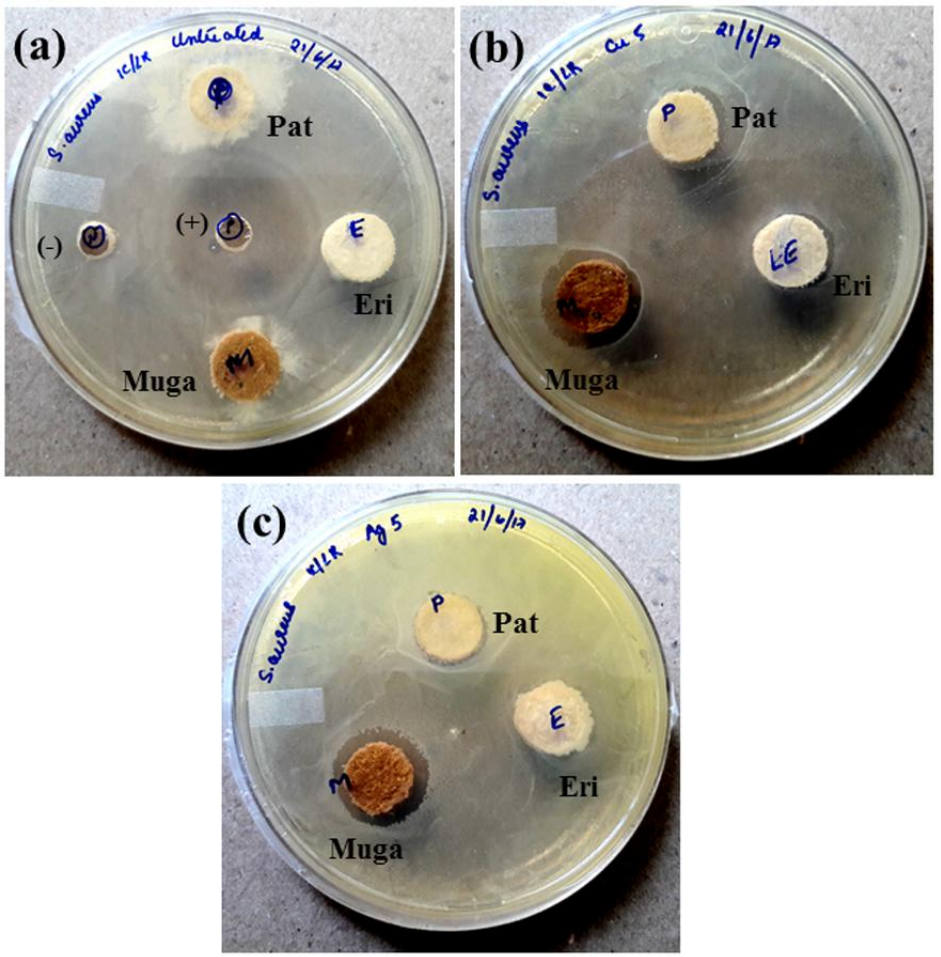

Figure 7.13 *Agar diffusion test on* **(a)** *untreated Eri (E), Pat (P) and Muga (M) silk pellets along with negative (-) and positive (+) control,* **(b)** *silk pellets treated with Cu NPs, and* **(c)** *silk pellets treated with Ag NPs.*

Fig. 7.13(a) shows the untreated pellets of each silk along with positive (antibiotic, Kanamycin) and negative control (water). From the image, it is clear that there is no inhibition zone for the pellets that have not been treated with NPs. This confirms that the silk used did not possess any antibacterial property of its own in the present experimental conditions. The negative control (-) also shows no inhibition zone around it, while for the positive control (+), there is an inhibition zone of approximately 10 mm. The null effect of negative control and the maximum inhibition zone for the positive control shows that the test is correct.

From Fig. 7.13(b) and 7.13(c), it is observed that in both the cases of treatment with Cu and Ag NPs, Muga silk shows more antibacterial activity against the bacteria *S. aureus* than Pat silk while Eri silk shows the least antibacterial activity. In fact, the Eri silk treated with Ag NPs did not show any antibacterial activity. However, in all the other cases the observed inhibition zones strongly suggest that the addition of the NPs has definitely played the role of a protective layer against the bacteria used. The details of the inhibition zone in each case are listed in table 7.4.

Table 7.4 *Results of agar diffusion test on Cu and Ag NP treated Eri (E), Pat (P) and Muga (M) silk pellets with S. aureus bacteria.*

Silk samples	**Inhibition zone (in mm)**		
	Eri (E)	**Pat (P)**	**Muga (M)**
Cu NP treated	1.2 ± 0.4	2.3±1.3	5.1 ± 2.3
Ag NP treated	0	1.1 ± 0.5	4.2± 2.1
Untreated	0	0	0

Thus, the preliminary experiments conducted show that different types of silk treated with metallic NPs exhibit different extent of antibacterial activities. The silks chosen

in the present work have high commercial value in the textile industry and hence its protection from bacterial attack is important [29]. The present procedure of treating the silks with the NPs can be a useful solution in this direction.

7.5.2.2 Bactericidal efficacy of filter paper treated with NPs

A filter paper when treated with metallic NPs can be used for the annihilation of bacteria present in contaminated water. However, the efficiency of such a NP treated filter paper depends on the attachment of the NPs to the filter paper. In the present work, the adhesion of the synthesized NPs onto the filter papers was confirmed by recording the FESEM images of the NP treated filter papers as shown in Fig. 7.14.

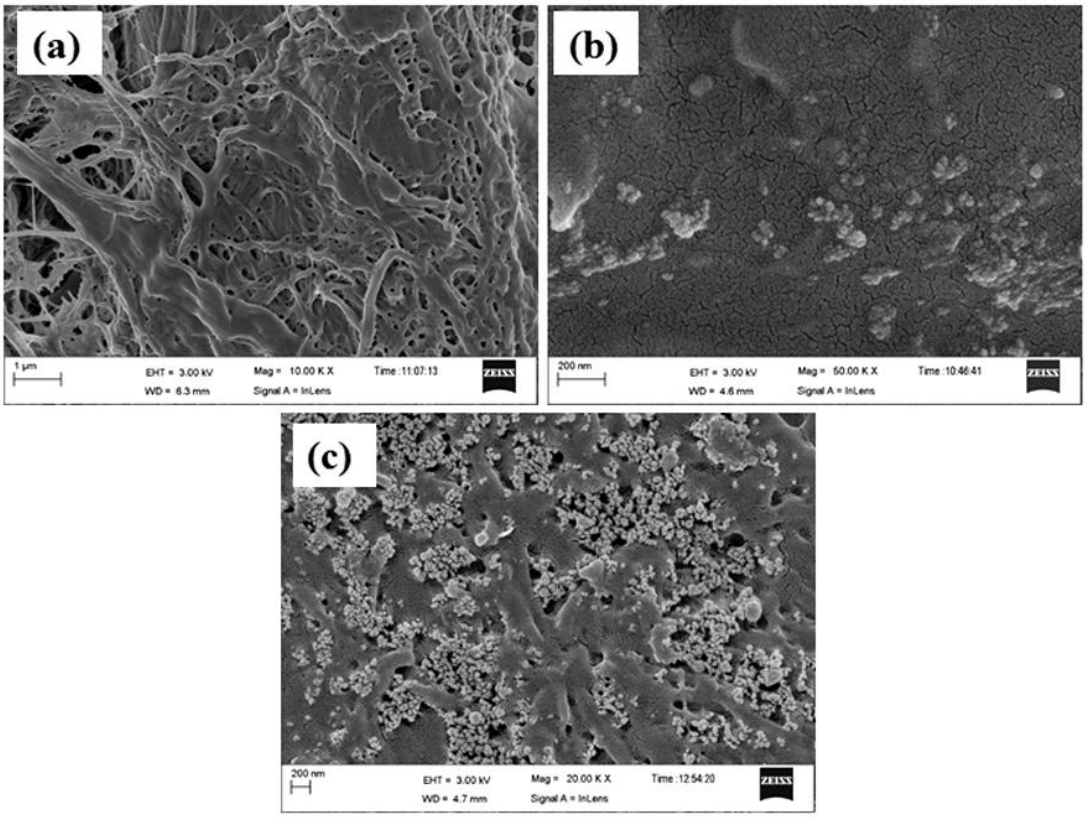

Figure 7.14 *FESEM images of* **(a)** *untreated filter paper; and filter paper treated with* **(b)** *Cu NPs, and* **(c)** *Ag NPs.*

Fig. 7.14(a) shows the FESEM image of the untreated paper while the filter papers treated with the Cu and Ag NPs are shown in Fig. 7.14(b) and (c), respectively. In the FESEM

images, the NPs getting attached to the filter paper are clearly observed.

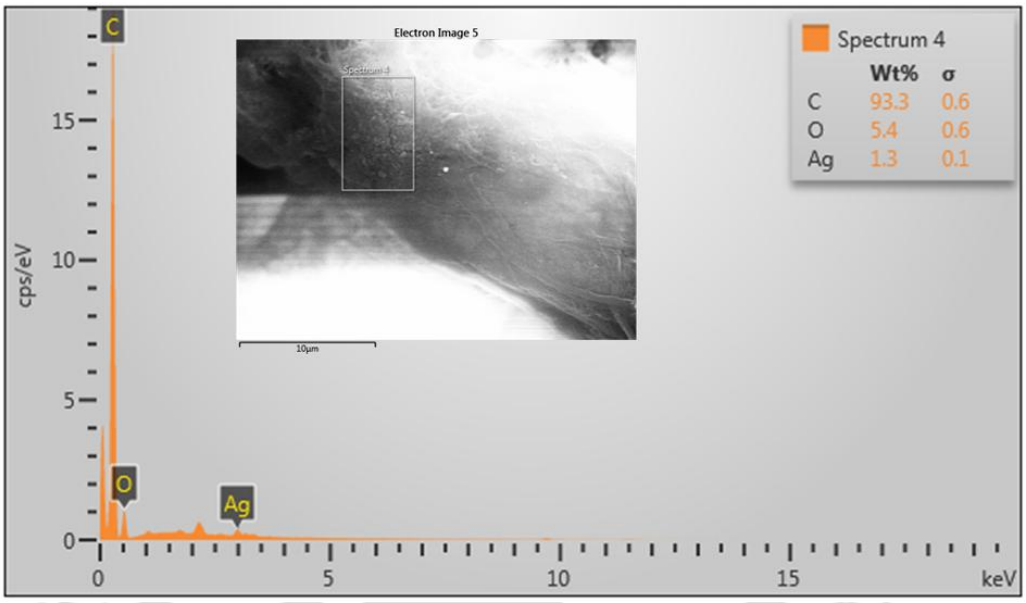

Figure 7.15 *EDX spectrum of a region of Ag NP treated filter paper; inset shows the selected region on the paper.*

The filter paper treated with Ag NPs was also subjected to the energy dispersive X-ray (EDX) for elemental analysis, which confirmed the presence of trace amount of Ag in the sample as shown in Fig 7.15. The image of the probed region of the filter paper is shown in the inset of Fig. 7.15.

In this study, in addition to gram positive bacteria, *S. aureus*, gram negative bacteria, *E. coli* was also used as *E. coli* is one of the most common bacteria found in contaminated drinking water [30]. Presence of *E. coli* in water is an indicator of faecal pollution in water.

The result of the antibacterial assay is shown in Fig 7.16. Fig. 7.16(a)-(c) shows the agar plates (for the case of *S. aureus*) on which the filtrate was inoculated after passing through the untreated, Cu NP treated and Ag NP treated filter papers, respectively. The same for the case of *E. coli* are shown in Fig. 7.16(d)-(f), respectively. As observed in Fig. 7.16(a), there is growth of *S. aureus* bacteria in the agar from the filtrate that was passed through the untreated filter paper. However, interestingly enough, no trace of bacterial

growth was observed on the agar plates that were spread with the filtrate obtained after passing through the Cu and Ag NP treated filter papers, as shown in Fig 7.16(b) and (c), respectively. Similar results are observed for the case of *E. coli* bacteria as illustrated in Fig. 7.16(d)-(f). These results strongly indicate that the water obtained after passing through NP treated filter paper is free from bacterial contamination. Thus, the filter paper treated with the synthesized NPs has the potential to behave as an effective tool for the treatment of bacteria contaminated water.

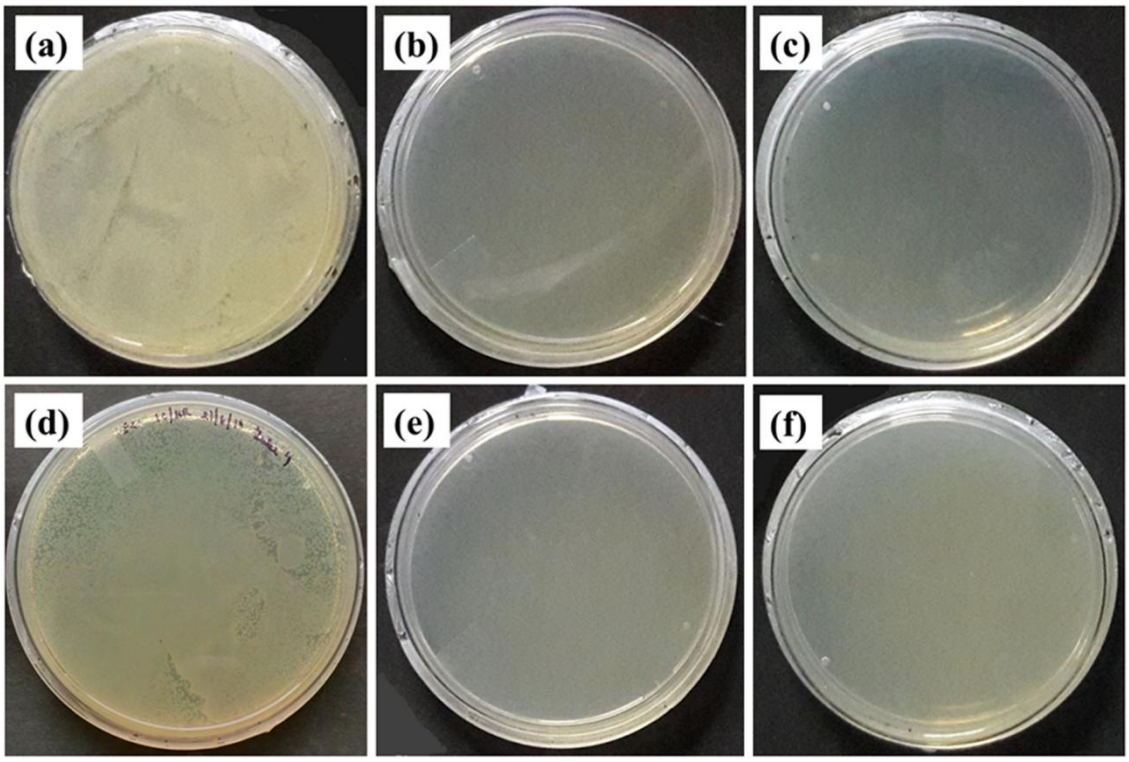

Figure 7.16 *Agar diffusion test on* **(a)-(c)** *filtrate (containing S. aureus) obtained by passing through untreated, Cu and Ag NP treated filter paper, respectively,* **(d)-(f)** *filtrate (containing E. coli) obtained by passing through untreated, Cu and Ag NP treated filter paper, respectively.*

In order to substantiate the results obtained by the agar test, a systematic growth kinetics study of the bacteria that was accumulated on the filter papers was performed. The growth curves of both the bacteria, *S. aureus* and *E. coli* monitored for 24 hours are shown in Fig. 7.17(a) and (b), respectively.

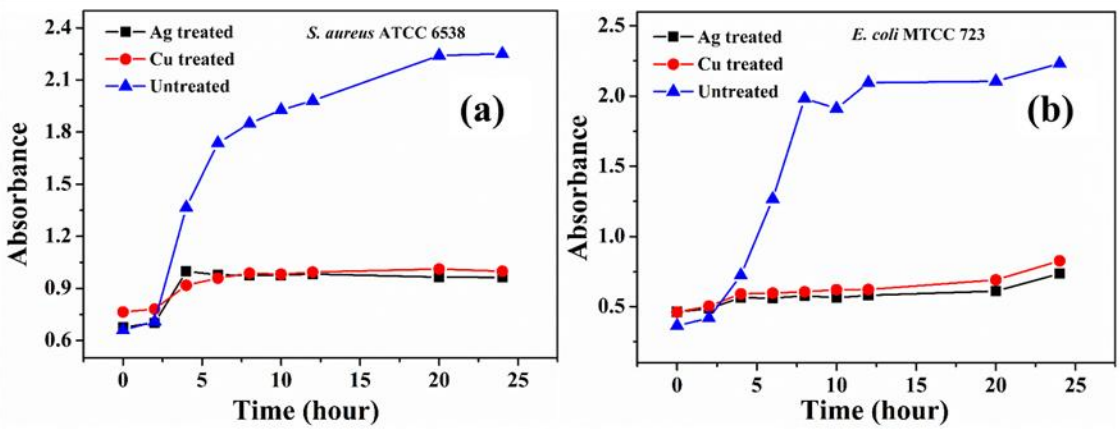

Figure 7.17 *Growth curves of bacteria* **(a)** *S.aureus, and* **(b)** *E.coli.*

The growth curves clearly show that the bacteria that came into contact with the NPs in the NP-treated filter papers did not show any substantial increase in the optical density which confirms that the activity of the bacteria was reduced thereby hindering its growth. Almost identical growth curves for the case of Cu and Ag NPs indicate similar antibacterial efficacy of both the metallic NPs. In contrast to this, for the bacteria that got separated in the untreated filter papers, the growth curves show a significant increase in the optical density indicating the growth of bacteria in the nutrient broth.

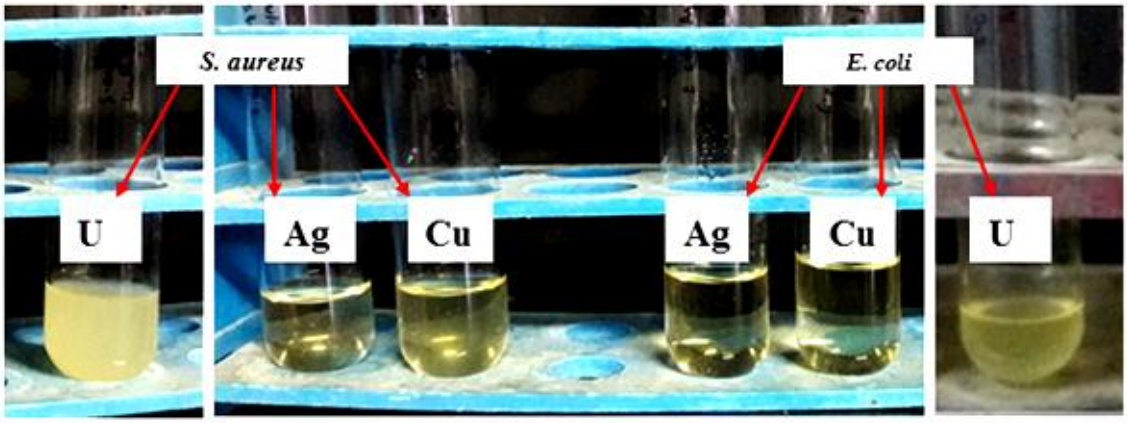

Figure 7.18 *Photographs of the bacteria in the nutrient broth taken at the end of the kinetic growth study (after 24 hours).*

Fig. 7.18 shows the photographs of the bacteria in the nutrient broth taken at the end of 24 hours (in the growth study). The turbidity in the nutrient broth is an indicator of

the growth of bacteria [31]. The very high turbidity in the media inoculated with bacteria on untreated filter papers implies the presence of large amount of actively growing bacteria, which is in coherence with the results obtained in the growth kinetics study. On the other hand, no turbidity and hence, no growth of bacteria in the media was observed with the bacteria that came in contact with the NPs on filter paper, thus, indicating the annihilation of bacteria.

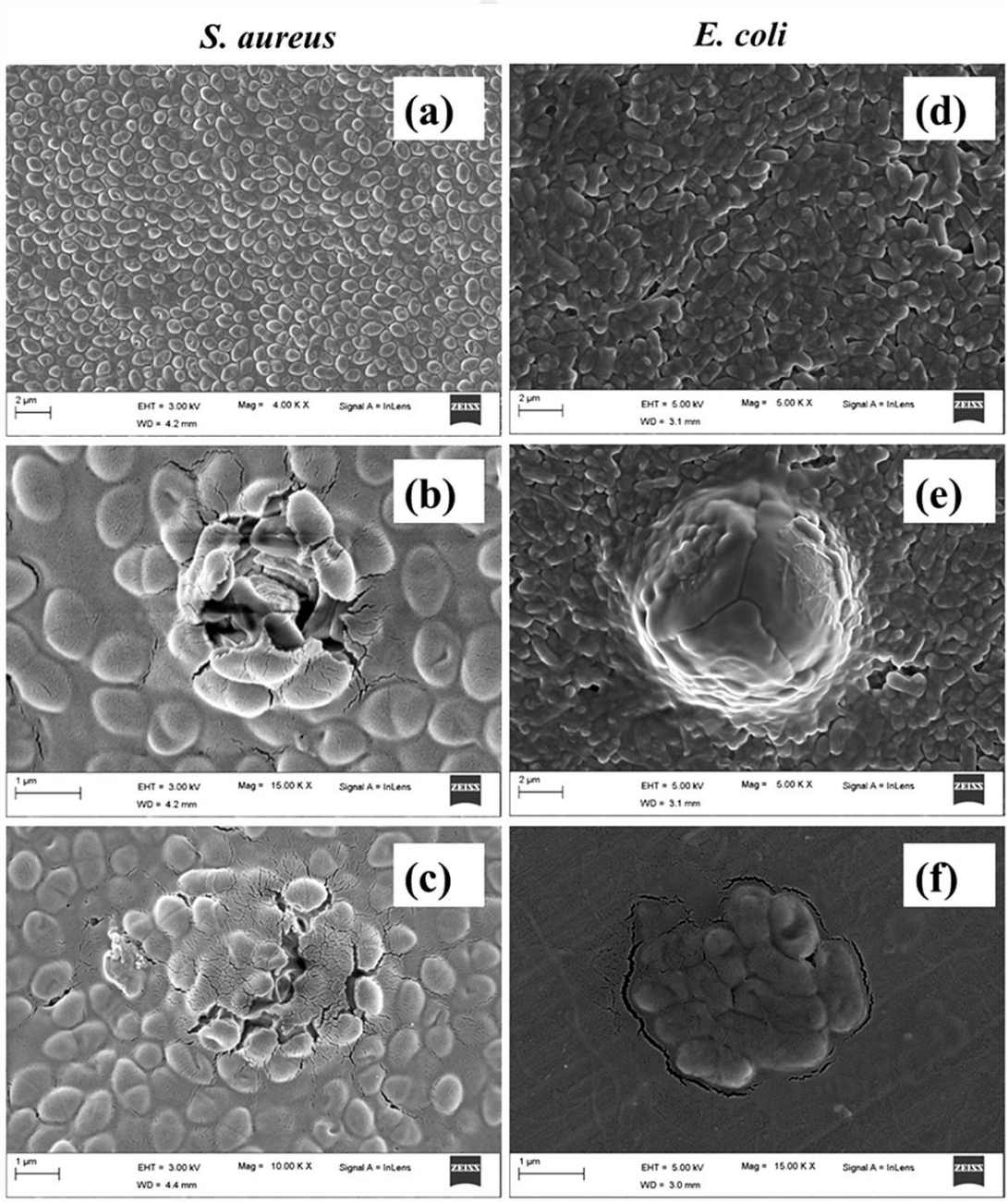

Figure 7.19 *FESEM images of* **(a)-(c)** *S. aureus bacteria that was passed through untreated, Ag and Cu NP treated filter paper, respectively,* **(d)-(f)** *E.coli bacteria that was passed through untreated, Ag and Cu NP treated filter paper, respectively.*

In order to check the condition/morphology of the bacteria left on the NP treated filter paper, it was subjected to the FESEM. Fig. 7.19(a)-(c) shows the FESEM images of *S.aureus* bacteria that were passed through untreated, Ag NP and Cu NP treated filter papers, respectively, while the same for the *E.coli* bacteria are shown in Fig. 7.19(d)-(f). It is observed that the bacteria that did not come in contact with the NPs are healthy and intact; *S. aureus* exhibited spherical morphology whereas rod-shaped, elongated cells were observed in case of untreated *E. coli*. The bacterial cells that came in contact with the NPs underwent lysis and exhibited ruptured or distorted morphology.

Thus, the present study confirms that the treatment of filter paper with Cu and Ag NPs synthesized via PLAL is a very effective method in the annihilation of bacteria from drinking water. However, there is a need to check the amount of Ag NPs in the filtered water due to the toxicity associated with it [32]. So, the filtrates in the present study were subjected to a UV-Visible spectrophotometer to check for the detection of the surface plasmon resonance (SPR) signature. No SPR signal could be detected in the filtrates which suggest that the presence of NPs in the filtered water is quite low. This is a crude way to test the presence of NPs in the filtrate and better methods to quantify the amount of NPs present in necessary. But, a study conducted by Praveena *et al.* provides a very positive insight in this direction [33]. In their work, a comparison of cellulose paper with other materials used as antibacterial water filter was done. It was found that the Ag concentration in the filtered water using cellulose paper is lesser and in compliance with the drinking water quality standards as compared to other materials like blotting papers or ceramic materials.

Filter papers treated with NPs can be especially useful during emergencies where a point-of-use water treatment is more convenient and easy as compared to the supply of trucked water from a treatment plant as was reported for CuO NPs by Booshehri *et al.* [34].

The low cost and easy availability of these filter papers negates the issues of maintenance and replacement. In the present work, the use of Whatman Grade 1 cellulose filter paper with particle retention (in liquid) of size 11 μm ensured the medium flow rate which is sufficient to meet the minimum drinking water requirement of 7.5 L for a person per day as prescribed by the WHO (World Health Organization) [35].

7.6 Conclusion

Cu and Ag NPs synthesized via PLAL were successfully tested as excellent SERS substrate for the detection of furanoflavonoid, karanjin. The factors affecting the SERS enhancement including NP size, concentration and aggregation were investigated. In addition to finding the optimum size and concentration of the Cu and Ag NPs, a comparison of the enhancement capability of both the NPs is also discussed. The synthesized Cu and Ag NP samples having the maximum concentration and the smallest average particle size were successfully applied to act as an antibacterial coating for three locally available natural silks, Eri, Pat and Muga. The Cu and Ag NP samples treated to filter papers are also found to be efficient in the annihilation of bacteria from contaminated drinking water.

References

[1] B. Sharma, R.R. Frontiera, A.-I. Henry, E. Ringe, R.P. Van Duyne, SERS: Materials, applications, and the future, Materials Today, **15** (2012) 16-25.

[2] M. Moskovits, Surface-enhanced Raman spectroscopy: a brief retrospective, Journal of Raman Spectroscopy: An International Journal for Original Work in all Aspects of Raman Spectroscopy, Including Higher Order Processes, and also Brillouin and Rayleigh Scattering, **36** (2005) 485-496.

[3] B. Sharma, M.F. Cardinal, S.L. Kleinman, N.G. Greeneltch, R.R. Frontiera, M.G. Blaber, G.C. Schatz, R.P. Van Duyne, High-performance SERS substrates: Advances and challenges, MRS bulletin, **38** (2013) 615-624.

[4] J.F. Betz, W.Y. Wei, Y. Cheng, I.M. White, G.W. Rubloff, Simple SERS substrates: powerful, portable, and full of potential, Physical Chemistry Chemical Physics, **16** (2014) 2224-2239.

[5] S. Wang, J. Jiang, H. Wu, J. Jia, L. Shao, H. Tang, Y. Ren, M. Chu, X. Wang, Self-assembly of silver nanoparticles as high active surface-enhanced Raman scattering substrate for rapid and trace analysis of uranyl (VI) ions, Spectrochimica Acta Part A: Molecular and Biomolecular Spectroscopy, **180** (2017) 23-28.

[6] M. Dendisová-Vyškovská, V. Prokopec, M. Člupek, P. Matějka, Comparison of SERS effectiveness of copper substrates prepared by different methods: what are the values of enhancement factors?, Journal of Raman Spectroscopy, **43** (2012) 181-186.

[7] M. Vinod, K.G. Gopchandran, Au, Ag and Au:Ag colloidal nanoparticles synthesized by pulsed laser ablation as SERS substrates, Progress in Natural Science: Materials International, **24** (2014) 569-578.

[8] A. Singh, I. Jahan, M. Sharma, L. Rangan, A. Khare, A.N. Panda, Structural Characterization, In Silico Studies and In Vitro Antibacterial Evaluation of a Furanoflavonoid from Karanj, Planta Medica Letters, **3** (2016) e91-e95.

[9] C. Corredor, T. Teslova, M.V. Canamares, Z. Chen, J. Zhang, J.R. Lombardi, M. Leona, Raman and surface-enhanced Raman spectra of chrysin, apigenin and luteolin, Vibrational spectroscopy, **49** (2009) 190-195.

[10] W.S. Eipeson, J. Manjunatha, P. Srinivas, T.S. Kanya, Extraction and recovery of karanjin: A value addition to karanja (Pongamia pinnata) seed oil, Industrial Crops and Products, **32** (2010) 118-122.

[11] S.M. Dizaj, F. Lotfipour, M. Barzegar-Jalali, M.H. Zarrintan, K. Adibkia, Antimicrobial activity of the metals and metal oxide nanoparticles, Materials Science and Engineering: C, **44** (2014) 278-284.

[12] T. Yuranova, A. Rincon, A. Bozzi, S. Parra, C. Pulgarin, P. Albers, J. Kiwi, Antibacterial textiles prepared by RF-plasma and vacuum-UV mediated deposition of silver, Journal of Photochemistry and Photobiology A: Chemistry, **161** (2003) 27-34.

[13] A.K. Chatterjee, R. Chakraborty, T. Basu, Mechanism of antibacterial activity of copper nanoparticles, Nanotechnology, **25** (2014) 135101.

[14] A. Leal-Egaña, T. Scheibel, Silk-based materials for biomedical applications, Biotechnology and Applied Biochemistry, **55** (2010) 155-167.

[15] G. Zhang, Y. Liu, X. Gao, Y. Chen, Synthesis of silver nanoparticles and antibacterial property of silk fabrics treated by silver nanoparticles, Nanoscale research letters, **9** (2014) 216.

[16] S. Schlücker, Surface-Enhanced raman spectroscopy: Concepts and chemical applications, Angewandte Chemie International Edition, **53** (2014) 4756-4795.

[17] P.L. Stiles, J.A. Dieringer, N.C. Shah, R.P. Van Duyne, Surface-enhanced Raman spectroscopy, Annual Review Analytical Chemistry, **1** (2008) 601-626.

[18] M. Canamares, J. Garcia-Ramos, S. Sanchez-Cortes, M. Castillejo, M. Oujja, Comparative SERS effectiveness of silver nanoparticles prepared by different methods: A study of the enhancement factor and the interfacial properties, Journal of colloid and interface science, **326** (2008) 103-109.

[19] E. Le Ru, E. Blackie, M. Meyer, P.G. Etchegoin, Surface enhanced Raman scattering enhancement factors: a comprehensive study, The Journal of Physical Chemistry C, **111** (2007) 13794-13803.

[20] S. Hong, X. Li, Optimal size of gold nanoparticles for surface-enhanced Raman spectroscopy under different conditions, Journal of nanomaterials, 2013 (2013) 49.

[21] S. Abalde-Cela, P. Aldeanueva-Potel, C. Mateo-Mateo, L. Rodríguez-Lorenzo, R.A. Alvarez-Puebla, L.M. Liz-Marzán, Surface-enhanced Raman scattering biomedical applications of plasmonic colloidal particles, Journal of the Royal Society Interface, **7** (2010) S435-S450.

[22] N.D. Israelsen, C. Hanson, E. Vargis, Nanoparticle properties and synthesis effects on surface-enhanced Raman scattering enhancement factor: an introduction, The Scientific World Journal, 2015 (2015).

[23] M. Mahmoud, M. El-Sayed, Aggregation of gold nanoframes reduces, rather than enhances, SERS efficiency due to the trade-off of the inter-and intraparticle plasmonic fields, Nano letters, **9** (2009) 3025-3031.

[24] M. Baalousha, M. Sikder, A. Prasad, J. Lead, R. Merrifield, G.T. Chandler, The concentration-dependent behaviour of nanoparticles, Environmental Chemistry, **13** (2016).

[25] Y. Han, R. Lupitskyy, T.-M. Chou, C.M. Stafford, H. Du, S. Sukhishvili, Effect of oxidation on surface-enhanced Raman scattering activity of silver nanoparticles: a quantitative correlation, Analytical Chemistry, **83** (2011) 5873-5880.

[26] T.K.T. Vu, Q.D. Nguyen, T.D. Nguyen, T.H. Trinh, Preparation of metal nanoparticles for surface enhanced Raman scattering by laser ablation method, Advances in Natural Sciences: Nanoscience and Nanotechnology, **3** (2012) 025016.

[27] J.I. Gersten, The effect of surface roughness on surface enhanced Raman scattering, The Journal of Chemical Physics, **72** (1980) 5779-5780.

[28] J. Gersten, A. Nitzan, Electromagnetic theory of enhanced Raman scattering by molecules adsorbed on rough surfaces, The Journal of Chemical Physics, **73** (1980) 3023-3037.

[29] U.K. De, M. Das, Economics of Sericulture in Assam: A Comparative Analysis of Three Cultivars, South Asia Economic Journal, **11** (2010) 309-336.

[30] S. Edberg, E. Rice, R. Karlin, M. Allen, Escherichia coli: the best biological drinking water indicator for public health protection, Journal of applied microbiology, **88** (2000) 106S-116S.

[31] S. Ma, H. Li, C. Yan, D. Wang, H. Li, X. Xia, X. Dong, Y. Zhao, T. Sun, P. Hu, Antagonistic effect of protein extracts from Streptococcus sanguinis on pathogenic bacteria and fungi of the oral cavity, Experimental and therapeutic medicine, **7** (2014) 1486-1494.

[32] S. Prabhu, E.K. Poulose, Silver nanoparticles: mechanism of antimicrobial action, synthesis, medical applications, and toxicity effects, International nano letters, **2** (2012) 32.

[33] S.M. Praveena, L.S. Han, L.T.L. Than, A.Z. Aris, Preparation and characterisation of silver nanoparticle coated on cellulose paper: evaluation of their potential as antibacterial water filter, Journal of Experimental Nanoscience, **11** (2016) 1307-1319.

[34] A.Y. Booshehri, R. Wang, R. Xu, Simple method of deposition of CuO nanoparticles on a cellulose paper and its antibacterial activity, Chemical Engineering Journal, **262** (2015) 999-1008.

[35] W. H. Organization, How much water is needed in emergencies, Technical Notes on Drinking-Water, Sanitation and Hygiene in Emergencies, **9** (2013) 1-4.

Chapter 8

Conclusion and Future Scope

The aim of the present research work was to implement the technique of pulsed laser ablation in liquid (PLAL) for the synthesis of nanoparticles (NPs) of copper (Cu) and silver (Ag) by the ablation of the respective targets in distilled water (DW). The 2nd harmonic of a Q-switched Nd:YAG laser having a pulse duration of ~ 7 ns was used to synthesize the NPs. Laser ablation duration and incident laser energy were the process parameters employed to tailor the properties of the NPs in both the cases. In the case of Cu NPs synthesized via PLAL, an increase in the laser ablation duration from 15 to 60 minutes at a fixed incident laser energy of 30 mJ resulted in the reduction in the size of the NPs. While an ablation duration of 15 and 30 minutes resulted in particles of highly non-uniform size distribution consisting of mostly bigger sized NPs, an increased duration of 60 minutes resulted in the formation of NPs with uniform size distribution having an average particle size of ~ 20 nm. The UV-visible absorption spectra of the NPs revealed a broad peak in the visible region of the electromagnetic spectrum attributed to the localized surface plasmon resonance (LSPR) of Cu NPs. The decrease in the size of the NPs with the increase in ablation duration from 15 to 60 minutes induced a blue-shift of the SPR peak from ~ 641 to 626 nm and also a broadening of the plasmonic bandwidth from ~ 127 to 165 nm, respectively. With the increase in incident laser energy as 30, 50 and 70 mJ, for a fixed ablation duration of 60 minutes, the average particle size of the NPs decreased as ~ 20, 11 and 7 nm, respectively. Here, the laser energy of 30, 50 and 70 mJ corresponds to laser fluence of ~ 10, 16 and 22 J/cm^2, respectively. The reduction in the size of the NPs from ~ 20 to 7 nm induced a similar blue-shift in the plasmon peak from ~ 626 to 617 nm and an

increase in the bandwidth from ~165 to 209 nm, respectively. The selected area electron diffraction (SAED) and Raman spectroscopy revealed that the extent of oxidation taking place in the NPS is also dependent on the laser ablation duration and incident energy. The samples synthesized for an ablation duration of upto 30 minutes with an incident laser energy of 30 mJ has Cu_2O as the dominant oxide phase whereas for an ablation duration of 60 minutes at the same energy, the CuO phase is also observed. With further increase in the incident laser energy to 70 mJ for 60 minutes, the oxygen-rich CuO is the dominant phase. Thus, the NPs formed in the case of Cu are actually found to be $Cu@Cu_xO(x=1, 2)$.

In order to substantiate the effect of laser ablation duration and incident energy on the NPs, Ag NPs were also synthesized as a function of the two process parameters. In addition to the huge importance associated with Ag NPs, the choice of Ag also allows a good comparison of the efficiency of the synthesized Cu NPs with respect to Ag NPs. For the synthesis of Ag NPs, increase in the ablation duration from 5 to 30 minutes at fixed laser energy of 30 mJ resulted in the decrease of the average particle size from ~ 20 to 15 nm, respectively. By increasing the incident laser energy from 30 to 70 mJ the average particle size of the NPs further decreased from ~ 15 to 10 nm, respectively. Similar to the case of Cu, the decrease in the average size of the NPs from ~ 20 to 15 nm induced a blue-shift of the SPR peak from ~ 403 to 398 nm but for the samples with even smaller average particle size upto ~ 10 nm, a reversing of the SPR peak to ~ 403 nm was observed. The reversing of the SPR peak towards longer wavelength for smaller particles is attributed to surface oxidation of the NPs which is reported to reduce the conductivity of the surface and hence causes a red-shift of the SPR band. As for the bandwidth of the SPR peaks, increase in the laser ablation duration from 5 to 30 minutes, decreases the bandwidth from ~ 66 to 51 nm which is due to the narrowing of the particle size distribution as confirmed via TEM images. For the samples synthesized at higher incident laser energy from 30 to 70 mJ, the

plasmonic bandwidth is found to increase from ~ 51 to 80 nm, respectively. This behaviour is explained on the basis of the increased aggregation among the NPs and also by incorporating a size-dependent material dielectric constant described by the Mie theory. The structural features of the NPs investigated using the X-ray diffraction, SAED and high resolution transmission electron microscope (HRTEM) images, reveal that longer duration of ablation and higher incident laser energy resulted in the formation of more oxidized phases of Ag NPs. Similar to the case of Cu NPs, the NPs formed in the case of Ag are actually $Ag@Ag_xO_y$(x=1, 2; y=0, 1, 3). The NPs of Ag were also found to be photo-luminescent and exhibited emission peak around 399-404 nm attributed to radiative decay of the SPR and another peak around 440 nm corresponding to the radiative recombination of Fermi level electrons with *sp*- and *d*- band holes.

For the investigation of the effect of confining liquid on the properties of the synthesized NPs in PLAL, NPs of Cu were also synthesized in two organic solvents, methanol and 2-propanol. In contrast to the NPs synthesized in DW, the increase in the laser ablation duration from 15 to 60 minutes at fixed incident energy of 30 mJ in methanol and 2-propanol resulted in an increase in the average size of the NPs from ~ 7 to 19 nm and ~ 9 to 17 nm, respectively. The increase in the size of the NPs with an increase in the ablation duration is accompanied by a red-shift in the SPR peak from ~ 606-621 nm and ~ 581-601 nm for methanol and 2-propanol, respectively. The red-shift in the SPR peak with the increase in average particle size is in accordance with results reported in the available literature. Another interesting observation for the NPs synthesized in these solvents for higher ablation duration is the formation of core-shell kind of NPs with carbon encapsulation. The SAED patterns indicate that the Cu NPs synthesized in the oxygen-deficient organic solvents have undergone only slight oxidation to form a few phases of Cu_2O. But unlike in the case of DW, no CuO phases were found. These observations lead

to the conclusion that the NPs synthesized in methanol and 2-propanol are insufficiently oxidized and are actually Cu@Cu_2O NPs.

The study of the effect of liquid on the properties of the NPs is complemented with a correlative study of the laser produced crater in various ambients. The crater produced in air has large sized NPs deposited on the target surface while for those produced in the liquids, the maximum amount of the NPs remain suspended in the surrounding liquid. The mass ablation rate is found to decrease in the various ambients in the order of air, DW, methanol and 2-propanol. The investigation of the target surface in the crater region via optical microscope, energy dispersive X-ray (EDX) and Raman spectrophotometer reveals that less oxidation occurs in the case of ablation in methanol and 2-propanol as compared to DW while there is excessive oxidation for the ablation taking place in air. The explanation for the decreased oxidation taking place in the organic solvents is given based on the properties of the liquid like density, acoustic impedance, etc. These factors in addition to the carbon encapsulation of the NPs is responsible for the formation of insufficiently oxidized NPs in methanol and 2-propanol.

In the synthesis of NPs vial PLAL, the role of the dynamics of the cavitation bubbles and shock waves (SWs) is extremely important. These two very important phenomena have been studied by employing two techniques viz., the shadowgraphy and the beam deflection. The laser fluences of ~ 10, 16 and 22 J/cm^2 used for these studies are same as that used for the synthesis of the NPs, discussed earlier. In the shadowgraphy technique, a fast, gated charge coupled camera (CCD) camera was used to record the temporal evolution of the cavitation bubbles. The bubbles are found to grow upto a maximum size after which the compression of the bubble occurs. The maximum bubble radius is measured to be ~ 1.5, 2.5 and 3.4 mm at the laser fluence of ~ 10, 16 and 22 J/cm^2, respectively. Also, for the higher laser fluence of ~ 16 and 22 J/cm^2, the bubbles are found to exhibit secondary

oscillations which is not observed for the lower fluence of ~ 10 J/cm^2. These observations are found to be matching well with the results obtained via beam deflection technique. From the temporal evolution of the cavitation bubbles obtained from the shadowgraphs, the pressure and temperature of the bubbles, derived analytically, are found to be ~ 10^8-10^9 Pa and ~ 400-1200 K. The dynamics of the SWs emitted by the laser produced plasma, studied using the beam deflection technique, reveal that the SWs travel at the speed of the order of ~ 10^3 m/s. The velocity of the SWs increases with the increase in the laser ablation fluence and it slows down as it propagates away from the target. The extremely high temperature and pressure conditions prevailing during the SW emission is estimated by considering the propagation of the SWs using the beam deflection technique. The maximum SW pressure and temperature are found to be ~ 2.6 × 10^{10}, 3.7 × 10^{10} and 6.2 × 10^{10} Pa and ~ 2830, 3016 and 3316 K at laser fluence of ~ 10, 16 and 22 J/cm^2, respectively. These high values of pressure and temperature at the interface of Cu and DW were applied to understand the nucleation of Cu@Cu_2O NPs. An estimate of the size of the NPs was obtained from the nucleation study and it was found that the size of the NPs increases from ~ 31 to 147 nm with the increase in fluence from ~ 10 to 22 J/cm^2. These results were explained in correlation with the experimental observations based on the dynamics of the cavitation bubbles and the NPs synthesized. The overestimated particle size from the dynamics study is due to the single shot of laser. Actual particle size was smaller due to the fragmentation of the NP as a result of repeated shots of laser.

As part of the application of the present work, the surface enhanced Raman scattering (SERS) and antibacterial activity of the Cu and Ag NPs synthesized via pulsed laser ablation in DW were studied. The synthesized NPs were tested to behave as an excellent SERS substrate for a furanoflavonoid, karanjin. The optimum conditions for the maximum SERS enhancement in the case of both Cu and Ag NPs are assessed by studying

the effect of particle size and concentration of the NPs. The optimum samples for Cu and Ag NPs were found to have average particle size of ~ 11 and 15 nm and concentration of ~ 0.291 and 0.194 mg/mL, respectively.

The antibacterial properties of the synthesized NPs were also applied to develop a protective layer for three varieties of natural silks, Eri, Pat and Muga, found mostly in the north-eastern part of India. The agar plate method was used for this study and the bacteria used was gram positive, *Staphylococcus aureus*. The antibacterial effect of the NPs resulted in the formation of clear inhibition zones around the pellets of silk treated with the NPs while no such activity of the untreated pellets were observed. The antibacterial properties of the NPs were also applied to check its viability on the treatment of filter paper for the annihilation of bacteria from contaminated drinking water. In this study, a common gram negative bacteria, *Escherichia coli* found in contaminated water was also used in addition to gram positive, *Staphylococcus aureus.* The agar method showed positive antibacterial effect for both Cu and Ag NPs. The growth kinetics study of the bacteria that came in contact with the NPs in the NP-treated filter papers demonstrated extremely slow growth of the bacteria as compared to the ones that were passed through untreated filter papers.

Future scope

The technique of PLAL has been implemented for the synthesis of large variety of NPs. However, work on the fabrication of bi-metallic NPs of Cu and Ag via PLAL and tuning of their plasmonic response is not explored much and has the potential in various plasmonic applications. The properties of such NPs can be further tailored by using both organic as well as inorganic solvents as the confining liquid in PLAL. It could also be interesting to get insights into the stage of ablation process by considering the degree of oxidation of the synthesized NPs. The further study on the dynamics of cavitation bubbles and SWs for different target materials and in different liquids is another area which is expected to

provide interesting insights in the mechanism of PLAL. Also, the emission of secondary SW during the collapse of the cavitation bubble has not be analysed in the present thesis and needs to be investigated in a detailed manner. The laser induced breakdown spectroscopy (LIBS) can be implemented in liquid to test the presence of heavy elements in the contaminated water.

As for the application of the NPs, the SERS capability of the NPs can be tried for other important compounds having biological importance and the same may be implemented at the commercial level. The antibacterial study, in the present work, has been carried out using the synthesized Cu and Ag NP samples having the maximum concentration. A detailed study in the same direction incorporating the effect of NP concentration and average size will be very useful. In fact, the NPs synthesized in different solvents can also be used for similar antibacterial applications for the optimization. It has been found that the treatment of silk with Cu and Ag NPs acts as a protective coating, hence efforts may be put for collaborative work with the textile industry which may lead to an increase in the longevity of the textile fabrics with the treatment of NPs as well as for some of the clinical applications. The fabrication of the filter paper treated with Cu and Ag NPs has tremendous potential especially during emergencies. Commercialization of such NP treated filter papers on a large scale and at a low cost may prove to be extremely beneficial for the society at large.

List of Publications

Publication/Proceeding

1. **Prahlad K. Baruah**, Ashwini K. Sharma, Alika Khare, *Role of confining liquids on the properties of Cu@Cu_2O nanoparticles synthesized by pulsed laser ablation and a correlative ablation study of the target surface,* RSC Advances, **9**, 15124-15139, 2019.
2. **Prahlad K. Baruah**, Anuma Singh, Latha Rangan, Ashwini K. Sharma and Alika Khare *Optimization of copper nanoparticles synthesized by pulsed laser ablation in distilled water as a viable SERS substrate for karanjin,* Materials Chemistry and Physics, **220**, 111-117, 2018.
3. **Prahlad K. Baruah**, Ashwini K. Sharma, Alika Khare, *Effective control of particle size, surface plasmon resonance and stoichiometry of Cu@Cu_xO nanoparticles synthesized by laser ablation of Cu in distilled water,* Optics and Laser Technology **108**, 574–582, 2018.
4. **Prahlad K. Baruah**, Moghe A. Raman, Ishani Chakrabartty, Latha Rangan, Ashwini K. Sharma, Alika Khare, *Antibacterial Effect of Silk Treated with Silver and Copper Nanoparticles Synthesized by Pulsed Laser Ablation in Distilled Water,* AIP Conference Proceedings **1953**, 030064, 2018.
5. **Prahlad K. Baruah**, Ashwini K. Sharma, Alika Khare, *Effect Of Laser Energy On The SPR And Size Of Silver Nanoparticles Synthesized By Pulsed Laser Ablation In Distilled Water*, AIP Conference Proceedings **1942**, 050036, 2018.
6. **Prahlad K. Baruah**, Anuma Singh, Iffat Jahan, Latha Rangan, Aditya N. Panda, Ashwini K. Sharma and Alika Khare, *Surface-enhanced Raman scattering from copper nanoparticles treated furanoflavonoid Karanjin*, Advanced Materials Letters, Volume **8**, Issue 10, 971-976, 2017.
7. **Prahlad K. Baruah**, Ashwini K. Sharma, Alika Khare, *Dependence of the Size of Copper Nanoparticles on Laser Energy Synthesized by Pulsed Laser Ablation in Liquid*, Advanced Materials Proceedings, Volume **2**, Issue 4, 264-268, 2017.
8. **Prahlad K. Baruah**, Anuma Singh, Latha Rangan, Ashwini K. Sharma and Alika Khare, *Comparison of surface enhanced Raman scattering of silver and copper nanoparticles on furanoflavanoid karanjin*, International Conference on Fiber Optics

and Photonics – PHOTONICS, IIT Kanpur, December 04-08, OSA Technical Digest (online) (Optical Society of America, 2016), paper Th4E.2, 2016.

9. **Prahlad K. Baruah**, Anuma Singh, Latha Rangan, Ashwini K. Sharma and Alika Khare, "*Elucidation of Size, Structure, Surface Plasmon Resonance and Photoluminescence of Ag Nanoparticles Synthesized by Pulsed Laser Ablation in Distilled Water and its Viability as SERS Substrate*." (Under review)
10. **Prahlad K. Baruah**, Ishani Chakrabartty, Latha Rangan, Ashwini K. Sharma, Alika Khare, "*Efficacy of cellulose paper treated with Cu and Ag nanoparticles synthesized via pulsed laser ablation in distilled water in the annihilation of bacteria*." (Under review)
11. **Prahlad K. Baruah**, Ashwini K. Sharma, Alika Khare, "*Investigating the exuberant properties of cavitation bubbles and shockwaves and its implications on the nucleation of laser produced copper nanoparticles.*" (To be submitted)

Publication outside thesis work

1. Sanasam Sunderlal Singh, **Prahlad K. Baruah**, Alika Khare, Shrikrishna N. Joshi *Incubation studies and the threshold for surface damage and cavity formation in the processing of Polycarbonate by Nd:YAG laser,* Optics and Laser Technology **108**, 592–601, 2018.
2. Rasmi R. Behera, Mamilla R. Sankar, **Prahlad K. Baruah**, Ashwini K. Sharma, Alika Khare, *Experimental investigations of nanosecond-pulsed Nd:YAG laser beam micromachining on 304 stainless steel,* Journal of Micromanufacturing, **1**, Issue 1, 1–14, 2018.
3. Sanasam S. Singh, **Prahlad K. Baruah**, Alika Khare, Shrikrishna N. Joshi, *Effect of laser beam conditioning on fabrication of clean micro-channel on stainless steel 316L using second harmonic of Q-switched Nd:YAG laser,* Optics and Laser Technology **99**, 107–117, 2018.
4. Ishani Chakrabartty, **Prahlad K. Baruah**, Aditya N. Panda, Alika Khare, and Latha Rangan, *Hybrid formulation of Cu nanoparticles and Labdane Diterpene from Alpinia Nigra: a vibrational spectroscopic study,* Journal of Applied Spectroscopy, **85**, No. 5, 2018.

Book chapter

1. *Surface Enhanced Raman Scattering and Antibacterial Capability of Pulsed Laser Ablated Metal/Metal Oxide Nanoparticles,* Advances in Science and Technology, Volume **1,** ISBN: 978-81-908910-9-7, 2019, i-manager Publications.

Conferences/Symposia attended

1. **Prahlad K. Baruah**, *Elucidation of Surface Plasmon Resonance, Size and Structure of* $Cu@Cu_xO$ *and* $Ag@Ag_xO_y$ *Nanoparticles Synthesized by Pulsed Laser Ablation in Liquid, Dynamics of the Process and Applications*, 3 Minute Thesis Presentation, Research conclave 2019, IIT Guwahati, Guwahati (2019). (Oral)
2. **Prahlad K. Baruah**, Ashwini K. Sharma and Alika Khare, *Particle size, surface plasmon resonance and stoichiometry of silver nanoparticles synthesized by pulsed laser ablation in distilled water*, National Conference on Recent Advances in Science and Technology **(**NCRAST-2018), Assam Science and Technology University, Guwahati (2018). (Poster)
3. **Prahlad K. Baruah**, Ashwini. K. Sharma and Alika Khare, *Effect of laser energy on the SPR and size of silver nanoparticles synthesized by pulsed laser ablation in distilled water*, 62^{nd} DAE Solid State Physics Symposium (DAE SSPS-2017), BARC, Mumbai (2017). (Poster)
4. **Prahlad K. Baruah**, M. A. Raman, I. Chakrabarty, L. Rangan, Ashwini K. Sharma and Alika Khare, *Antibacterial effect of silk treated with silver and copper nanoparticles synthesized by pulsed laser ablation in distilled water*, 2nd International conference on condensed matter and applied physics (ICC-2017), Govt. Engineering College, Bikaner, Rajasthan (2017). (Poster)
5. **Prahlad K. Baruah**, Ashwini K. Sharma, Alika Khare, *Characterization of noble metal nanoparticles synthesized via pulsed laser ablation in liquid,* International Conference on Sophisticated Instruments in Modern Research (ICSIMR-2017), IIT Guwahati, Guwahati (2017). (Poster)
6. **Prahlad K. Baruah**, Kh. Shantakumar Singh, Sumit Goswami, Eshita Mal, Ashwini K. Sharma and Alika Khare, *Application of laser induced breakdown for nanoparticle synthesis and as a powerful spectroscopic technique,* Research Conclave 2017, IIT Guwahati, Guwahati (2017). (Poster)

7. **Prahlad K. Baruah**, Anuma Singh, Latha Rangan, Ashwini K. Sharma, Alika Khare, *Comparison of surface enhanced Raman scattering of silver and copper nanoparticles on furanoflavanoid karanjin*, Photonics-2016, The International Conference on Fiber Optics and Photonics, IIT Kanpur, Kanpur (2016). (Oral)
8. **Prahlad K. Baruah**, Eshita Mal, Kh. Shantakumar Singh, Ashwini K. Sharma and Alika Khare, *Laser produced plasma and its applications, Research Conclave 2016*, IIT Guwahati, Guwahati (2016). (Poster)
9. **Prahlad K. Baruah**, Ashwini K. Sharma and Alika Khare, *Dependence of laser energy on the size of copper nanoparticles synthesized by pulsed laser ablation in liquid*, International Conference on Materials Science & Technology (ICMTech), University of Delhi, Delhi (2016). (Poster)
10. **Prahlad K. Baruah**, Ashwini K. Sharma, Alika Khare, *Preliminary investigation on the expansion dynamics of laser produced graphite plasma in air*, 30th National Symposium on Plasma Science & Technology (Plasma-2015), Saha Institute of Nuclear Physics (SINP), Kolkata (2015). (Poster)
11. **Prahlad K. Baruah**, Ashwini K. Sharma, Alika Khare, *Basics and applications of the process of Laser induced breakdown,*TEQIP Symposium to celebrate the 2015 International Year of Light, Department of Physics, IIT Guwahati, Guwahati (2015). (Poster)
12. **Prahlad K. Baruah**, Kh. Shantakumar Singh, Ashwini K. Sharma and Alika Khare, *Effect of laser energy on nanoparticles produced by laser ablation of copper in distilled water*, 29th National Symposium on Plasma Science & Technology and the International Conference on Plasma & Nanotechnology (PLASMA 2014), Mahatma Gandhi University, Kottayam, Kerala (2014). (Poster)
13. Kh. Shantakumar Singh, **Prahlad K. Baruah**, Eshita Mal, Alika Khare and Ashwini K. Sharma**,** *Effect of uniform magnetic field on laser drilling*, National Laser Symposium, Sri Venkateswara University, Tirupati (2014). (Poster)
14. **Prahlad K. Baruah**, N. S. Mallick, I. Kumar, Ashwini K. Sharma, and Alika Khare, *Dynamics of laser induced breakdown at solid-liquid interface by imaging technique*, 3rd PSSI-PLASMA Scholars Colloquium (PSC-2014) & National workshop on Exploring Plasma Technology on Material Processing, VIT Chennai, Chennai (2014). (Oral)
15. I. Kumar, **Prahlad. K. Baruah**, Ashwini K. Sharma, and Alika Khare, *Laser induced graphite plasma in liquid by ccd imaging*, 28th National Symposium on Plasma

Science & Technology (PLASMA 2013), KIIT University, Bhubaneswar (2013). (Poster)

Workshop/School/Exhibition

1. "One-Day Workshop on Vacuum Technology and Its application In Optical Science" organized by SPIE IITG student chapter in association with Pfeiffer vacuum, 19th August, 2017.
2. "Research Conclave 2017" organized by Students' Academic Board (SAB), IIT Guwahati, 16th to 19th March, 2017.
3. "Intra IIT Latex Workshop" organized by RSF, Mathematics and Students' Academic Board, IIT Guwhati, 18th February, 2017.
4. "ACS on Campus" organized by the American Chemical society at IIT Guwahati, 16th January, 2017.
5. "Light: not a light matter-a students' symposium" organized by SPIE IIT Guwahati student chapter, Dibrugarh University, Dibrugarh, 12th November, 2016.
6. "Research Conclave 2016" organized by Students' Academic Board (SAB), IIT Guwahati, 17th to 20th March, 2016.
7. "National Workshop on Advanced Probing Techniques in TEM (APTTEM-2016)" organized by Indian Institute of Technology Guwahati (IITG) and Electron Microscopy Society of Indian (EMSI), 15th and 16th February, 2016.
8. "Feel the light-on optics outreach" organized by SPIE IIT Guwahati student chapter, Cotton College, Guwahati, 6th February, 2016.
9. South Asian Workshop on Optics & Photonics "SAWOP-2015"organized by Indian Institute of Technology Guwahati, 17th to 18th November, 2015.
10. "Research Conclave" organized by the PhD council of the Students' Academic Board (SAB), IIT Guwahati, 23rd to 26th March, 2015.
11. "Science Fair 2015" held at IASST, Guwahati, 28th February to 1st March, 2015.
12. "DST-SERC School on Nonlinear Optics and Materials" organized by SSN College of Engineering and Pondicherry University, Chennai, 3rd to 21st February 2014.
13. "IEEE Workshop on Compressive Sensing and Technical writing" organized by IEEE Student Branch, IIT Guwahati, 6th to 7th April 2013.

Awards/Honors

1. Best poster award in the 62nd DAE Solid State Physics Symposium (DAE SSPS-2017), BARC, Mumbai (2017).
2. Best Poster award in the 2nd Position in the TEQIP symposium to celebrate the 2015 International Year of Light organized by the Department of Physics, IIT Guwahati, Guwahati (2015).
3. Winner of the Test on Nonlinear Optics in "DST-SERC School on Nonlinear Optics and Materials" organized by SSN College of Engineering and Pondicherry University, Tamil Nadu (2014).
4. Winner of the Crystal Growth Activities Session in "DST-SERC School on Nonlinear Optics and Materials" organized by SSN College of Engineering and Pondicherry University, Tamil Nadu (2014).